Nagoya University

Doctoral Thesis

The physical properties of star-forming galaxies and their environments at intermediate redshifts

Author:
Daichi Kashino

Supervisor:
Dr. Naoshi Sugiyama

A thesis submitted in fulfillment of the requirements for the degree of Doctor of Philosophy

in the

Division of Particle and Astrophysical Science
Graduate School of Science

August 1, 2016

NAGOYA UNIVERSITY

Abstract

Division of Particle and Astrophysical Science
Graduate School of Science

Doctor of Philosophy

The physical properties of star-forming galaxies and their environments at intermediate redshifts

by Daichi KASHINO

Recent galaxy surveys have provided us with large data containing multi-wavelength photometry, images, spectra, and spatial distributions of a large number of galaxies. The redshift frontier has amazingly expanded towards almost the epoch of the formation of the first galaxies. Such data have enabled us to investigate the nature of galaxies over the cosmic time, and then have successfully built up a clear picture on how galaxies form and evolve in the Universe. They also have unveiled the cosmic star formation history, i.e., the total amount of newborn stars per unit volume as a function of cosmic time. These studies, in particular, show that the global star formation in the Universe was most intense at $z \sim 1$–3, when individual galaxies actively form stars with rates that are 20–50 times higher than those as seen in local galaxies.

This thesis is aimed at comprehensively studying the properties of star-forming galaxies at a intermediate redshift range, $1.4 \lesssim z \lesssim 1.7$, an important epoch close to the peak of the cosmic star formation history. We carry out a near infrared spectroscopic galaxy survey using the Fiber Multi-Object Spectrograph (FMOS) mounted on the Subaru telescope. This survey is designed to collect near infrared band spectra of more than 3000 galaxies in the Cosmological Evolution Survey (COSMOS) field. Several rest-frame optical emission lines (e.g., Hα, [N II]λ6584, Hβ, [O III]λ5007) from galaxies at $z \sim 1.6$ are redshifted into the H and J spectral windows.

The first part of this thesis focuses on the intrinsic properties of high-z star-forming galaxies. We use a sample of color selected star-forming galaxies that yield an Hα detection to measure their star formation rates (SFRs). Then, we establish the star forming main sequence (i.e., the relation between SFRs and stellar masses) of $z \sim 1.6$ galaxies. With further J-band spectroscopy, the level of dust extinction is assessed by measuring the Balmer decrement (Hα/Hβ) using co-added spectra. We find that differential extinction between stellar and nebular emission is smaller than that typically seen at low redshift, and that the amount of extinction towards nebular emission is comparable to those in local galaxies on average. This might indicate that stars, star-forming regions, and dust are spatially well mixed. After correcting the observed Hα flux for dust extinction, we derive an Hα-based main sequence with SFRs being about 10–20 times larger than those of local galaxies at a fixed stellar mass.

Next, we present results on the physical conditions of the interstellar medium. We use a sample of galaxies that cluster along the star-forming main sequence over a range of stellar mass $10^{9.6} \lesssim M_*/M_\odot \lesssim 10^{11.6}$, with those at $M_* > 10^{11}$ $M_\odot$ well sampled. The excitation state and chemical enrichment of the ionized gas are investigated using diagnostic diagrams based on the ratios of emission line strengths, including Hα, [N II]λ6584, [S II]$\lambda\lambda$6717,6731, Hβ, and [O III]λ5007. Our data confirm an offset of the star-forming sequence on the Baldwin, Phillips & Terlevich (BPT) diagram ([O III]/Hβ vs. [N II]/Hα), primarily towards higher [O III]/Hβ, compared with local star-forming galaxies. Based on the [S II] doublet ratio, we measure an electron density, which turns out to be higher than that of local galaxies. Based on the comparison with theoretical models, we comclude that the changes in emission line properties in high-z galaxies

are caused primarily by a higher ionization parameter, enhanced as compared to local galaxies at fixed metallicity, as supported by a lower-than-expected [S II]/Hα ratio and comparison with a theoretical model.

We also measure the mass–metallicity relation by using a conventional [N II]/Hα-based indicator and a newly-introduced calibration based on the [N II]/[S II] ratio. Our data confirm that the most massive galaxies ($M_* \gtrsim 10^{11}\ M_\odot$) are fully chemically enriched, while lower mass galaxies have metallicities considerably lower than local galaxies. We further investigate the SFR dependence of the mass–metallicity relation, and find that this dependence is well reproduced by a physically motivated model of chemical evolution with gas processes.

Finally, we also study the connection between our galaxy sample and dark matter halos. We measure the projected two-point correlation function of a spectroscopic sample that consists of 516 galaxies with a significant Hα detection, while carefully taking complicated observational biases into consideration. The observed correlation function indicates a significant clustering amplitude at scales 0.05–20 h^{-1} Mpc with a correlation length of $5.2 \pm 0.7\ h^{-1}$ Mpc, consistent with past studies at similar redshifts. We interpret our clustering measurement using a halo occupation distribution (HOD) model and successfully constrain the model parameters. We successfully measure the one-halo term, a contribution from galaxy-galaxy pairs in the same halos, and find the transition scale to be $\simeq 0.6\ h^{-1}$Mpc, at which the one-halo term equals the two-halo term. We find that, on average, our sample galaxies inhabit halos with $M_{\rm h} = 4.62^{+1.14}_{-1.63} \times 10^{12}\ h^{-1}\ M_\odot$ at $z \sim 1.6$, which eventually grow into group-scale halos ($\sim 2 \times 10^{13}\ h^{-1} M_\odot$) at the present epoch. We also measure the stellar-to-halo mass ratio $M_*/M_{\rm h} \approx 5 \times 10^{-3}$ at $M_h = 10^{11.9}\ M_\odot$, thus providing a new constraint on the low mass side of the stellar-to-halo mass relation at this epoch. Our result is in good agreement with the extrapolation of the relation derived from past measurements based on the HOD modeling.

Acknowledgements

First, I would like to express my sincere gratitude to my supervisor, Professor Naoshi Sugiyama, for providing me this precious opportunity. He always encouraged me and gave helpful advice when I got stuck on difficulties in research and in my life. I am very fortunate to spent my Ph.D years in his research group.

I especially would like to express my deepest gratitude to John D. Silverman of Kavli IPMU, the University of Tokyo, for his elaborated guidance, encouragement and invaluable discussions that made my research a great achievement and my time of study unforgettable. He taught me a number of important skills with respect to observations, data analysis, English writing, and also expanded my world by providing opportunities to communicate with many researchers from around the world.

I would like to show my deep appreciation to Surhud More of Kavli IPMU for his kind encouragement and helpful discussions, which were indispensable for completing my Ph.D research. I have learned a lot, especially concerning the analysis and the theoretical treatment of the galaxy clustering and its interpretation.

Very fortunately, I had the chance to work with many researchers throughout the world, especially, Alvio Renzini, Emanuele Daddi, Simon Lilly, Lisa Kewley, Masato Onodera, Jeyhan Kartaltepe, Tohru Nagao, Stephanie Juneau, Jabran H. Zahid, Jason Chu, Dave Sanders, Nobuo Arimoto through the FMOS-COSMOS project. I have learned a lot from them. I also got precious advice from Kiyoto Yabe, Tadayuki Kodama, Masami Ouchi, Chiaki Hikage, and many of researchers and graduate students at other institutes.

I would like to express my special appreciation to Tsutomu T. Takeuchi at Nagoya University. I have learned a lot from him, from the basics of the galaxy evolution to the skills of observations and data analysis. I also thank him for reading this thesis carefully and giving me a lot of suggestions.

I greatly thank Kentaro Aoki, a support astronomer at the Subaru telescope, for his strong support and expertise with carrying out our observations. I have learned a lot from him, and also had a number of happy nights, even if cloudy, with him at the summit of Mauna Kea. I also would like to express my gratitude to staffs at National Astronomical Observatory of Japan (NAOJ), the Subaru office, and especially persons who were responsible for the development and maintenance of Subaru/FMOS.

I deeply thank the faculty members and postdoctoral fellows of the Cosmology Group in Nagoya University, Takahiko Matsubara, Kiyotomo Ichiki, Hiroyuki Tashiro, Atsushi Nishizawa, Kenji Hasegawa, Yuko Urakawa, Sachiko Kuroyanagi, Daisuke Nitta, and my colleagues, Shinsuke Asaba, Shohei Saga, and all the graduate students for precious discussions and a lot of fun through my PhD life. I especially thank our office administrator, Ms. Hitomi Tanaka, for all her help and kindness.

I have been supported by Grant-in-Aid for the Japan Society for the promotion of Science Fellows for three years, which has enabled me to focus on my research activity. Works in this Thesis had been supported in part by program for Leading Graduate Schools "PhD Professional: Gateway to Success in Frontier Asia" commissioned by the Ministry of Education, Culture, Sports, Science and Technology of Japan. This work is based on data collected at the Subaru telescope, which is operated by NAOJ.

I am full of feelings of gratefulness to Momoko Ogino. She always gives me a lot of emotional support, encouragement, and understanding.

Finally, I would like to express my indebtedness and deep gratitude to my dear parents for their endless love, understanding, constant support and sacrifice over my life.

Contents

Chapter 1

Introduction

Essentially everything of astronomical interest is either part of a galaxy, or from a galaxy, or otherwise relevant to the origin and evolution of galaxies. — B. M. Tinsley

We study galaxies to ultimately understand the fate of all the matter in the Universe. Galaxies are giant complex systems that essentially drive the evolution of baryons in the Universe. Heavy elements are generated through star formation in galaxies, and compose every visible structures we see in the Universe, including the readers and myself. If you seek for the origin of ourselves, essentially we cannot avoid understanding the formation and evolution of galaxies.

1.1 Galaxies in the Universe

Galaxies consist of stars and the interstellar medium. The Sun and other stars seen in the sky belongs to one such system. We call it *the Milky Way Galaxy* (usually, simply refereed to as *the Galaxy*), which includes an order of 10^{11} stars. In the Universe, a lot of (at least 10^{11}) galaxies ubiquitously exist, ranging from systems of $\sim 10^6$ stars to those including more than 10^{14} stars, which show a variety of size, luminosity, color, shape, morphology, and other properties.

Galaxies are also the fundamental building blocks of structure in the Universe, forming various structures such as galaxy groups (a few $\times$10–100 galaxies), clusters ($\gtrsim 10^2$), filamentary structures that connects clusters, and huge empty regions called *voids*. Some of groups and clusters are concentrated and form even a larger structure, called a *supercluster*. Our Milky Way Galaxy is a member of *the Local Group*, and located in the outskirts of *Virgo Supercluster*. Such structures made out of galaxies trace the underlying cosmological large-scale structure of *dark matter*, which governs the structure formation in the Universe.

Luminous galaxies can be observed with large telescopes even if they exist at very large distances from us. Because the speed-of-light is finite, distant things appear younger than what they are today. Observing more distant objects is seeing an earlier epoch of the Universe. Therefore, galaxies are also an important tool to investigate the Universe and its evolution. Large galaxy surveys in recent years, surprisingly, have revealed enormous information with respect to the nature of galaxies and the Universe. Given that a hundred years ago, we as human beings did not even know the existence of other galaxies, this progress has been achieved at a breathtaking pace.

Four hundred years ago, Galileo Galilei trained a telescope on the night sky, and discovered the unevenness of the moon, four satellites going around Jupiter, and found that the wispy Milky Way comprises a myriad of individual stars. However, in those days, people commonly believed that things we can see in the sky, i.e., the Milky Way and other objects make up the Universe itself, and had not recognized yet that the Milky Way is an enormous numbers of galaxies present in the Universe.

In the middle of the 18th century, Thomas Wright considered that we are located within a huge spherical shell that consists of numerous stars, as the reason why we see a sequence of stars across the sky. William Herschel provided a quantitative picture of the structure of the Galaxy for the first time, from a technique referred to as *star gauging* (see in Figure 1.1; Herschel 1785).

Until 1784, Charles Messier has published a catalog that includes astronomical objects that have an extended shape (nebulae and star clusters), which came to be known as the 110 *Messier objects*[1]. William Persons (Lord Rosse) discovered spiral structures in some nebulae in 1845–1850. Such numerous exploits owe much to the development of reflecting telescopes invented by Isaac Newton. Despite such numerous observational efforts, however, it still remained to be seen whether such objects were *inside* or *outside* the Milky Way. Opinions were divided into two opposing camps among astronomers.

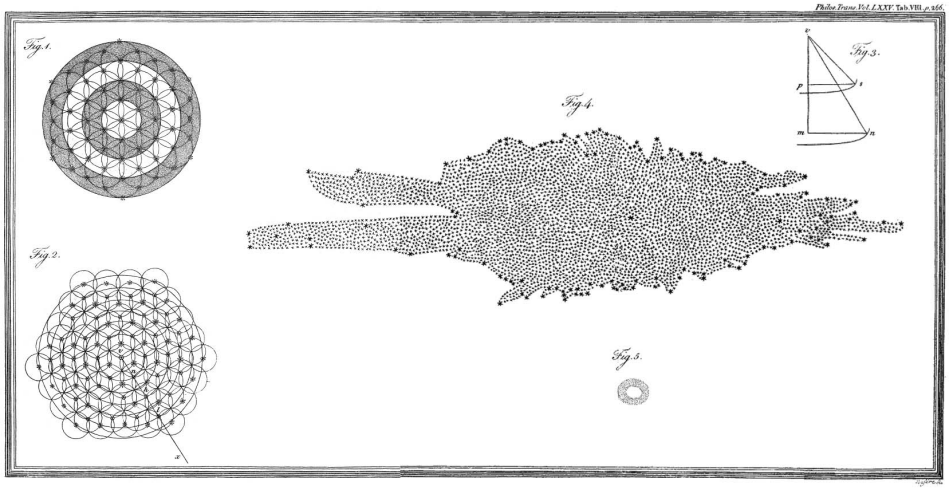

Figure 1.1: Illustration of the Milky Way Galaxy by W. Hershel. This figure is taken from "On the Construction of the Heavens" (Herschel 1785).

In the early 1900s, the intense controversy continued among astronomers between the two directly-opposed ideas. To settle the dispute, a debate was held on 26 April 1920 between Harlow Shapley and Heber Curtis, concerning the nature of spiral nebulae and the size of the Universe. Shapley claimed that such spiral nebulae belong to the Milky Way Galaxy, and that the size of the Galaxy is 10^6 light years, while Curtis claimed that those objects independently exist outside our Galaxy, and its size is 10^5 light years. This debate impacted many astronomers, and came to be called *the Great Debate* (or *the Shapley-Churtis debate*). However, the dispute remained unsettled at that time. Later, in 1923, Edwin Hubble found that M31 (Andromeda galaxy) is separated by at least 300 kpc from us by observing Cepheid variables in it, and has a size comparable to our Milky Way Galaxy. Simultaneously, he found Cepheid variables in other nebulae and measured distances of them, and concluded that space continues beyond the Milky Way Galaxy, where a lot of extragalactic objects, i.e., galaxies exist.

With recent advances of large galaxy surveys, properties of galaxies have been statistically investigated, and then established using large samples. In particular, the Sloan Digital Sky Survey (York et al. 2000), which was the most ambitious project in the history of modern astronomy, has accumulated the data of an order of 10^6 galaxies, and thus has provided the essential contribution to our understanding of galaxies and the Universe.

1.2 Galaxy evolution driven by star formation

The galaxies that we see in the Universe are continuously undergoing transformations. Like a huge creature, they show a variety of complex phenomena in their body that change their appearance and intrinsic nature with time. They also sometimes interact and merge with neighbors.

[1]The number of objects in the lists published by Messier reached 103, but other few objects though to be observed by him have been added by other astronomers later. There is an opinion that M102 are M101 duplicates.

We can find various evolutionary stages in different galaxies at different redshifts, whereas we can see only a snapshot at the moment for individual galaxies.

In this thesis, we particularly focus on the time evolution of the compositions of galaxies that includes stars and interstellar medium (gas), which is primarily driven by formation of stars. Galaxies form new stars. Stars compose heavy elements from hydrogen and helium through nuclear fusion. Some fraction of metals is stored in long-lived stars and the other is returned into interstellar space through mass-loss like supernovae and stellar winds. Therefore, the amount of heavy elements in galaxies is an important indicator of the evolutionary stage of a galaxy. Such an evolution caused by star formation is particularly referred to as the *chemical evolution* of galaxies.

In late 1970's, Beatrice Tinsley introduced the concept of the evolution of the stellar populations and gas content of galaxies and established the theoretical framework (see Tinsley 1980 for a review). Thereafter, there have been numerous efforts to explore the galaxy evolution both observationally and theoretically. Let us suppose that a huge gas cloud begins to form stars now. By observing such a system, we should see young newborn stars with various mass. Some time later, massive short-lived stars explode, while less massive stars still stay alive. Thus, the fraction of less massive, long-lived stars increases, i.e., the stellar population gradually becomes older. Galaxies continuously form stars with a fixed distribution of the initial masses of stars (initial mass function; IMF), which describes the probability distribution of initial mass of stars that form simultaneously from a gas cloud. Simultaneously, the abundance of heavy elements both in stars and interstellar gas increases. This is a very simple, but one of the fundamental aspects of the galaxy evolution.

In response to the evolution of the stellar population, the luminosity and the spectral energy distribution (SED) of a galaxy vary, which reflects the relative fraction of stars of different types. SEDs of stars are strongly correlated with the mass. Massive stars are short-lived, more luminous and have higher effective temperature, thus being luminous with the ultraviolet (UV) emission. In contrast, long-lived less massive stars are rather luminous in optical–near infrared. While they are actively forming stars, the galaxies sustain a UV–blue component in their SED. Once the star formation stops, only less massive long-lived stars continuously stay alive, and then the galaxy becomes redder. An SED of a galaxy can be calculated with an *evolutionary population synthesis* model. Preparing a library of SEDs of various stars, we can construct a galaxy-wide SED at an arbitrary evolutionary phase by composing the individual spectra of stars, with a star formation history and an assumed IMF. If we have multi-wavelength luminosity measurements of a galaxy, we can evaluate the physical properties, such as stellar mass, SFR, age, by fitting modeled SEDs to an observed data. Shifting wavelengths of spectral features to fit the data of a galaxy, the redshift of the galaxy can also be estimated. This is called the *photometric redshift* method. Such a technique, called an *SED-fitting*, is ubiquitously applied for astrophysical studies today. So far, various population synthesis models, SED libraries, techniques, and softwares have been developed (e.g., Bruzual A. 1983; Bruzual A. & Charlot 1993; Fioc & Rocca-Volmerange 1997; Bruzual & Charlot 2003; Maraston 2005).

As mentioned above, star formation is the most important activity that primarily governs the evolution of a galaxy. Stars form in the cores of molecular gas clouds through the gravitational instability, where gas cooling mechanisms are also important. Once stars enter the main sequence, massive hot stars (type-O and B) emit the UV radiation, thus ionize the surrounding gas clouds, and form H II regions, where a variety of spectral emission lines are emitted. The galaxy-wide star formation rate (SFR), which is defined as the mass converted into stars per year ($M_\odot$ yr^{-1}), is one of the fundamental quantities of a galaxy. While there are various diagnostics of the galactic star formation rate based on the related processes (such as total far-infrared luminosity, 1.4 GHz radio flux, X-ray emission, etc...; see Kennicutt & Evans 2012 for a review), the SFR is most commonly estimated with indicators based on the amount of massive young stars such as the rest-frame UV emission or flux of recombination lines (e.g., Hα). Using such indicators,

we can assess a temporary formation rate of stars, averaged over the typical lifetime of OB stars ($\sim 10^{6\text{–}8}$ yr) that is much shorter than the evolutionary time scale of a galaxy itself ($\gtrsim 10^9$ yr). The total amount of newborn stars is estimated from the amount of massive stars by assuming an IMF.

In a galaxy, the star formation activity never continues eternally. While a galaxy contains an abundance of gas, new stars form continuously, and consumes the gas. Such star-forming galaxies may be often undergoing the accretion of pristine gas from the intergalactic space. Once the gas accretion stops and the restored gas is consumed, new stars can no longer form. When the galaxy acquires additional gas from outside through the gas accretion or galaxy mergers, the star formation can happen again temporarily. In the Universe, there are galaxies with various SFRs. The majority of elliptical galaxies have SFRs almost equal to zero, i.e., do not form stars in their body, and thus they are red. In contrast, spiral or irregular galaxies usually form stars actively.

1.3 Star-forming main sequence and cosmic star formation history

Recent large data sets have resulted in the discovery of a bimodal distribution on the galactic color-magnitude diagram for galaxies at $z \lesssim 1$ (or more), showing two groups; a *red sequence* that is a relatively tight sequence dominated by non–star-forming galaxies and a *blue cloud* of star-forming galaxies (e.g., Strateva et al. 2001; Blanton et al. 2003; Bell et al. 2004; Baldry et al. 2004). It has also been shown that galaxies can be well separated in color-color space into star-forming and quiescent populations. The development in redshift estimation and thus accurate rest-frame color measurement has been crucial for arriving at these conclusions (e.g., Daddi et al. 2004; Wuyts et al. 2007). With such advances, many studies have shown a strong correlation between SFR and stellar mass of star-forming galaxies up to $z \sim 3$ or more ($z \lesssim 6$; e.g., Brinchmann et al. 2004; Daddi et al. 2007; Elbaz et al. 2007; Noeske et al. 2007; Wuyts et al. 2011), and that such a *star-forming main sequence* at a fixed redshift is well expressed by a power-law as

$$\log \mathrm{SFR} = \alpha \log M_* + \beta \tag{1.1}$$

where α is a power-law slope and β denotes a global normalization value of the sequence. In the Local Universe, the slope α is measured to be ~ 0.6–1 with some variations from one study to another depending on the SFR indicator and the sample selection. The normalization is $\mathrm{SFR} \sim 1\ M_\odot\ \mathrm{yr}^{-1}$ at $M_* = 10^{10}\ M_\odot$. The scatter of the sequence is known to be 0.25–0.35 dex (e.g., Noeske et al. 2007). The presence of such a well-organized tight correlation of galaxies indicates the existence of a specific mode of star formation, which the majority of galaxies follow, and the rapid transition from star-forming to quiescent phases (*quenching* of star formation).

The location of a galaxy on the M_* versus SFR diagram with respect to the main sequence is a good diagnostic to separate different modes of the star formation in galaxies. We see minor populations that are located below and above the main sequence. The former includes galaxies that are now in the process of being quenched. The latter population is starburst galaxies, which are considered to temporarily enhance their SFRs as compared to the main-sequence galaxies. Starburst galaxies usually show the existence of a large amount of cool molecular gas and an enhancement of star formation resulting from the instability of the gas clouds triggered by galaxy-galaxy interaction or some mechanisms that supply gas into the galactic nucleus. In the local Universe, starburst galaxies have $\mathrm{SFR} \sim 10$–$100\ M_\odot\ \mathrm{yr}^{-1}$ (e.g., Sargsyan & Weedman 2009; Kennicutt & Evans 2012).

Measuring the stellar mass and SFR of galaxies at all redshifts provides essential information for our understanding of galaxy formation and evolution. As mentioned above, many studies have

established the star-forming main sequence at high redshifts using a wide variety of SFR indicators. Particularly, in the last decade, the advance of near-infrared multi-object spectroscopic spectrographs on the world's largest telescopes (Keck/MOSFIRE, VLT/KMOS, Subaru/FMOS) has led to significant progress, permitting us to access an well-understood SFR indicator, i.e., the Hα emission line, for galaxies beyond redshift $z \sim 0.5$, where Hα is redshifted to the IR window and there is no choice but to rely on other SFR indicators. With many efforts based on the near-IR spectroscopy (and also narrow-band imaging), the main sequence has been accurately established at high redshifts, and it has been clear that the slope is almost independent of redshift, while the normalization β remarkably increases with redshift at least up to $z \sim 4$ (e.g., Whitaker et al. 2012; Bouwens et al. 2012; Kashino et al. 2013; Steinhardt et al. 2014; Speagle et al. 2014, and references therein). The average SFR at a given stellar mass at $z \sim 2$ has been measured to be larger by a factor of ~ 20 than that of the present day.

The evolution of the star-forming main sequence is linked to the cosmic star formation history, which has been established with many efforts on large telescopes, expanding the redshift frontier of galaxy surveys. Around 1980, a series of studies by H. R. Butcher and A. Oemler, Jr. have found that the fraction of blue galaxies is significantly larger in clusters at $0.3 < z < 0.5$ as compared to local clusters (e.g., Butcher & Oemler 1978, 1984), where most member galaxies are red and have early-type morphology (elliptical or S0), i.e., non–star-forming. This obviously indicates that the majority of cluster galaxies have stopped star formation over the last ~ 5 Gyr.

The concept of the history of cosmic star formation rate was introduced by Tinsley & Danly (1980), who theoretically studied the evolution of the comoving density of gas associated with galaxies, which increases with redshift up to $z \sim 4$. Gallego et al. (1995) measured the star formation rate density (SFRD) per unit cosmic volume ($M_\odot$ yr^{-1}Mpc^{-3}) based on the Hα luminosity density. Lilly et al. (1996) explore the cosmic star formation history up to $z \sim 1$ by measuring the evolution of the galactic luminosity density. Madau et al. (1996) measured SFRs of high-redshift galaxies utilizing Keck telescope and *Hubble Space Telescope* (launched in 1990), and presented the SFRD as a function of redshift (lookback time) that rapidly increase from $z = 0$ to $z \sim 1$. Such a diagram is now referred to as *Madau plot*. Hopkins & Beacom (2006) provided an extensive compilation of SFRD measurements, and established an accurate star formation history over a range of redshift $0 < z < 6$. With very deep imaging and spectroscopic campaigns, there have been many studies that provide SFRD measurements at high redshifts, beyond $z \sim 4$ up to $z \sim 11$ (e.g., Bouwens et al. 2011; Coe et al. 2013; Finkelstein et al. 2013; Oesch et al. 2013, 2014; Bouwens et al. 2014, 2015). With these efforts, the cosmic star formation history has been quantitatively well constrained, and it supports the conclusion that the SFRD had increased since the first galaxies formed with cosmic time, with a peak SFRD ≈ 0.13 $M_\odot$ yr^{-1}Mpc^{-3} at $z \sim 2$, and then has decreased to SFRD ≈ 0.015 $M_\odot$ yr^{-1}Mpc^{-3} at the present day (Figure 1.2; see Madau & Dickinson 2014 for a review).

1.4 Chemical evolution

Heavy elements are synthesized in stars, then partially returned into the ISM from stars as a result of winds and supernovae or confined in long-lived stars. Therefore, measuring metal abundance provides important clues for understanding the evolutionary stage and the star formation history of galaxies. The metallicity is also influenced by gas flows which galaxies have undergone. The inflows of pristine (or metal-poor) gas dilutes the metal fraction of the ISM, while outflows transport metals into the circumgalactic environment (e.g., Köppen & Edmunds 1999; Dalcanton 2007; Ellison et al. 2008; Erb 2008; Finlator & Davé 2008; Mannucci et al. 2010; Cresci et al. 2010; Peeples & Shankar 2011; Bouché et al. 2012; Lilly et al. 2013). A fundamental theoretical

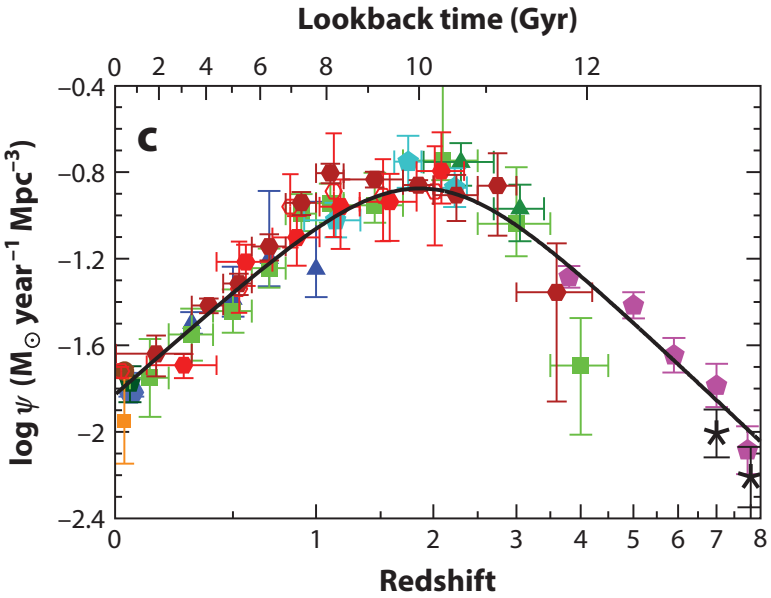

Figure 1.2: SFRD as a function of redshift. This figure is taken from Madau & Dickinson (2014).

framework of the chemical enrichment was introduced by a pioneering study by Schmidt (1963), which is described in Appendix A. Tinsley (1980) provided a good review on this matter.

There are two primary methods to determine the gas-phase metallicity of H II regions: the direct method and the strong line method. In the direct method, the determination of the electron temperature of gas is crucial, which utilizes the line ratios of faint auroral to strong nebular lines (e.g., [O III]λ4363/[O III]λ5007; e.g., Aller 1984). Such a line ratio is a function of the electron temperature because the auroral and nebular lines originate from the second and first excited states, respectively. Once the electron temperature is measured, the metallicity can be determined from the flux ratios of metal lines to a Balmer line of hydrogen (e.g., Hβ). However, auroral lines are usually very faint to detect for extragalactic objects with a reasonable observational cost. Therefore, there is no choice but to make use of the so-called strong line method (e.g., Denicoló et al. 2002; Nagao et al. 2006) to explore distant galaxies. The strong line method determines the metallicity using the line ratios of strong nebular lines which are relatively easier to detect. Indicators commonly used include the [N II]λ6584/Hα ratio ($N2$ index) and ([O II]+[O III])/Hβ (R_{23} index). The line ratios are calibrated empirically based on the metallicities from the direct method (e.g., Pettini & Pagel 2004; Nagao et al. 2006), or theoretically with photoionization models (e.g., Kewley & Dopita 2002). Such calibrations implicitly assume a constant electron temperature or an invariable relation between metallicity and electron temperature. Historically, a number of calibrations have been proposed, but which do not usually produce consistent metallicities. In particular, it is commonly known that metallicities determined from theoretical strong line calibrations are systematically higher than those from empirical calibration or direct methods (Kewley & Ellison 2008; Moustakas et al. 2010). Therefore, caution is warranted when one compares the absolute values of metallicity between studies that use different indicators or calibrations. A relative evaluation for galaxies in a sample based on a consistent calibration show a clear correlation between metallicity and galactic properties.

Star formation directly impacts both the buildup of stellar mass and chemical enrichment of a galaxy. Thus, the relation between galactic stellar mass and metallicity is essentially dependent on the galaxy evolution models, and measuring the mass–metallicity (MZ) relation across cosmic time provide crucial observational constraints. Lequeux et al. (1979) found a correlation between total mass and metallicity for nearby irregular and blue compact galaxies. The advance

of evolutionary population synthesis models (e.g., Bruzual & Charlot 2003) has dramatically improved the accuracy of the stellar mass determination. Based on large data sets such as SDSS, Tremonti et al. (2004) and subsequent studies (e.g., Andrews & Martini 2013; Zahid et al. 2011) have robustly established the existence of a tight correlation between stellar mass and metallicity over the stellar mass range $8 \lesssim \log M_* \lesssim 11$, and it has been explored down to $M_* \sim 10^6\ M_\odot$ (Lee et al. 2006). In which, the metallicity significantly increase with increasing stellar mass, being almost constant at the maximum value above $10^{11}\ M_\odot$ (see Figure 1.3). Beyond the Local Universe, the existence of the MZ relation has been extended up to $z \sim 3$ or more (e.g., Erb et al. 2006; Maiolino et al. 2008; Yabe et al. 2012, 2014, 2015; Zahid et al. 2014a,b; Wuyts et al. 2014). The observed MZ relations show an evolution where the metallicity decreases with redshift at a fixed stellar mass. However, the exact shape has not been established yet at high redshifts, and there still remains some discrepancies between various studies that implement different sample selection methods and/or metallicity determinations.

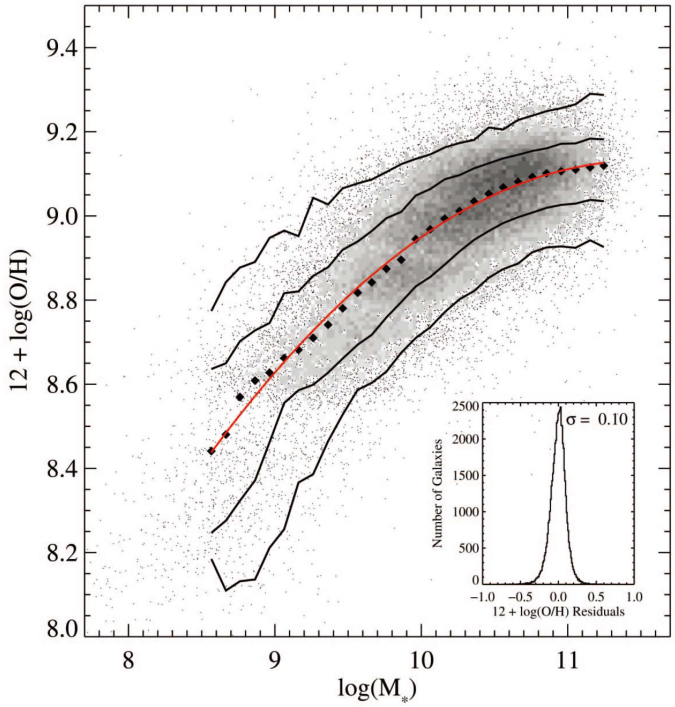

Figure 1.3: The mass–metallicity relation of $\sim 10^5$ SDSS galaxies. This figure is taken from Tremonti et al. (2004).

An anti-correlation between metallicity and SFR at a fixed stellar mass was first reported by Ellison et al. (2008), and then has been further explored in many subsequent studies (e.g., Lara-López et al. 2010b, 2013; Mannucci et al. 2011; Yates et al. 2012; Andrews & Martini 2013; Wuyts et al. 2014; Zahid et al. 2014b). In particular, Mannucci et al. (2010) proposed the so-called *fundamental metallicity relation* (FMR), as a redshift-invariant surface in the (M_*, SFR, Z), with SFR being a third axis in the MZ relation. Such an FMR was then meant to describe both anti-correlated SFR and Z fluctuations at fixed mass, and the redshift evolution of metallicity and SFR, where with increasing lookback time the specific SFR goes up and Z goes down, thus keeping galaxies on the FMR.

In a physical interpretation of such an FMR, upward fluctuations in the amount of pristine infalling gas would boost star formation while diluting the metal abundance of the ISM. There have been some physically motivated models where star formation and chemical evolution is regulated by inflow of metal-poor gas and outflow of metal-rich gas (Dayal et al. 2013; Lilly et al. 2013). Such an idea has also been suggested from cosmological hydrodynamical simulations

(e.g., Davé et al. 2012). On physical grounds, one expects an FMR to exist, but observations are still somewhat contradictory with large discrepancies existing in determining the exact shape of the FMR. These discrepancies largely arise from the use of different metallicity indicators, or different galaxy selection criteria adopted in different studies(see e.g., Andrews & Martini 2013). Beyond the local Universe, there have been many efforts to examine whether an observed MZ relation is consistent with non-evolving FMR or not (e.g., Wuyts et al. 2014; Zahid et al. 2014b; Yabe et al. 2014; Kashino et al. 2016; Guo et al. 2016a). However, the dependence of on SFR of the MZ relation has not been well established yet at higher redshifts.

1.5 Physical conditions of H II gas

Besides the metallicity, there are a number of factors (such as ionization parameter, gas density, shape of the radiation field, metal compositions, etc...) that describe the physical conditions of the ISM. Measuring them provides clues to understand the current state and past activity of galaxies. Studies of ionized gas and its excitation state in star-forming (i.e., H II) regions have been carried out through a number of previous observational efforts (e.g., Aller 1942; Pagel et al. 1979, 1980). At the same time, the underlying physics has been studied theoretically with photoionization models (e.g., Evans & Dopita 1985; Dopita et al. 2000; Kewley & Dopita 2002). A variety of diagnostic techniques have been empirically and theoretically established, especially based on spectral features in the rest-frame optical window, to investigate the gas properties and the origin of gas excitation.

Baldwin et al. (1981) proposed a diagnostic diagram that compares line ratios [N II]/Hα and [O III]/Hβ to classify galaxies according to their principal excitation mechanisms: massive stars (normal H II regions), white dwarfs (planetary nebulae), a power-law continuum, and shock-wave heating. Subsequently, Veilleux & Osterbrock (1987) adopted this diagnostic to classify emission-line galaxies into normal star-forming or narrow-line active galaxies. Today, this diagram is referred to as the Baldwin–Phillips–Terlevich (BPT) diagram, and commonly used as a tool to distinguish star-forming galaxies from those hosting and/or dominated by an active galactic nucleus (AGN). Local star-forming galaxies form the tight *abundance sequence* on the BPT diagram (see Figure 1.4; e.g., Kauffmann et al. 2003b) with line excitation attributed to radiation from young massive stars (type O and B). In contrast, AGNs deviate from this sequence due to their harder power-law radiation field from an accretion disk. Large data sets such as SDSS have established the precise location of star-forming galaxies and AGNs, thus facilitating a relatively clean selection of these populations (e.g., Kauffmann et al. 2003b; Kewley et al. 2006; Stasińska et al. 2006; Lara-López et al. 2010a).

However, the physical conditions of galaxies at higher redshifts ($z \gtrsim 1$), where most key rest-frame optical lines are redshifted into infrared, are still unclear. One would expect the properties of ionized gas in high-z galaxies (around the *peak* epoch of the cosmic star formation history) to be dissimilar to local galaxies given their higher star-forming activity (for a review, see Madau & Dickinson 2014) and gas fractions (e.g., Genzel et al. 2010; Magdis et al. 2012; Scoville et al. 2014). In particular, in the last decade, it has been reported that high-z galaxies are located far off on the BPT diagram from the local star-forming galaxies and have higher [O III]/Hβ and/or [N II]/Hα ratios (see Figure 1.5; e.g., Zahid et al. 2013; Shirazi et al. 2014; Shapley et al. 2015; Hayashi et al. 2015; Cowie et al. 2016; Kartaltepe et al. 2015; Onodera et al. 2016). There have been many studies that investigate the properties of ionized gas regions, suggesting more extreme conditions, i.e., high gas pressure, large ionization parameter and harder spectrum of radiation field, based on multiple diagnostic techniques mainly using rest-frame optical emission lines (see e.g., Zahid et al. 2013; Kewley et al. 2013b, 2015; Nakajima & Ouchi 2014; Steidel et al. 2014; Shirazi et al. 2014; Shapley et al. 2015; Shimakawa et al. 2015; Onodera et al. 2016; Sanders et al. 2016), which are considered also as the origins of the BPT offset. We will extensively explore

the conditions of H II gas in high-z star-forming galaxies in Chapter 4.

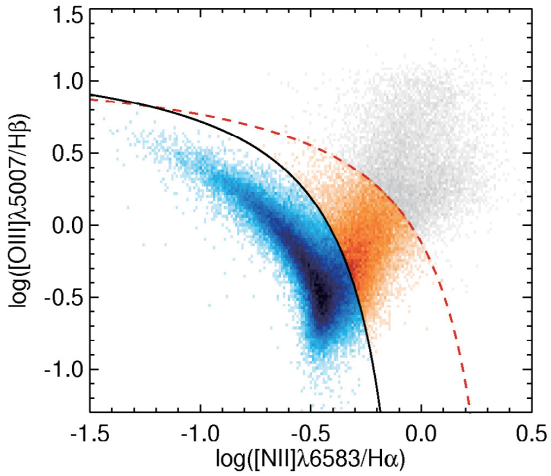

Figure 1.4: log([N II]/Hα) vs. log([O III]/Hβ) BPT diagram. Solid line shows the Kauffmann et al. (2003b) empirical division between star-formign and composite galaxies, and the dashed line represents the Kewley et al. (2001) starburst limit This figure is taken from Lara-López et al. (2010a).

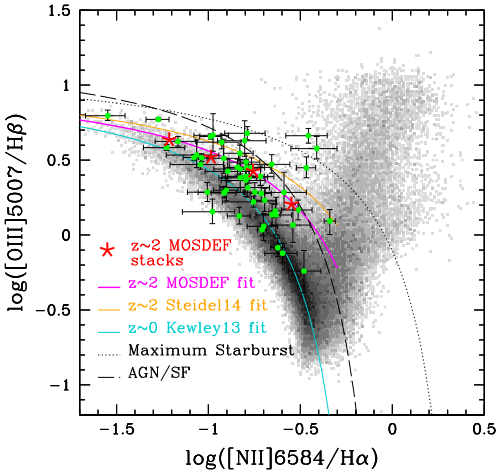

Figure 1.5: BPT diagram for $z \sim 2.3$ galaxies. Green points indicate the sample of 53 galaxies from the MOSDEF survey. The grayscale histogram corresponds to the distribution of local SDSS galaxies. Large red stars represent measurements of stacks, binned by stellar mass. This figure is taken from Shapley et al. (2015).

1.6 Environmental effects

Large galaxy surveys have shown that galaxies form a variety of structures, from clusters to voids (de Lapparent et al. 1986; Colless et al. 2001). This means that galaxies inhabit various environments. A simple indicator that quantifies the environment is the number density of galaxies measured locally. In cluster regions, the number density is much higher (a factor of $> 10^2$) than the cosmic average, while it is equal or less than the background density in *field* regions. Do galactic properties depend on the environment in which galaxies exist?

Dressler (1980) found, by investigating more than 50 nearby clusters, a significant correlation between the abundance fractions of different type of galaxies and the environment; the fractions of elliptical and S0 galaxies (i.e., non–star-forming passive galaxies) is higher at denser regions, while the fraction of spiral and irregular galaxies (i.e., star-forming galaxies) are higher at less dense regions (see Figure 1.6). Giovanelli et al. (1986) mapped the distribution of galaxies for different types separately, then found elliptical and S0 galaxies are concentrated along a filament structure, while late-type galaxies are scattered, showing featureless distribution, as shown in Figure 1.7.

These observations have raised an essential question on the origin of the relation between galactic type and environments. Why galactic properties do depend on the environment where they exist? Two hypotheses have been advocated; nature or nurture. In the "nature" hypothesis, the characteristics of galaxies were determined when they are born. One would suppose that elliptical galaxies form earlier at denser regions while spirals form later in the field.

In the "nurture" hypothesis, the environment changes some properties of galaxies in the process of galaxy clustering. Spiral galaxies actively form new stars, whereas elliptical and S0

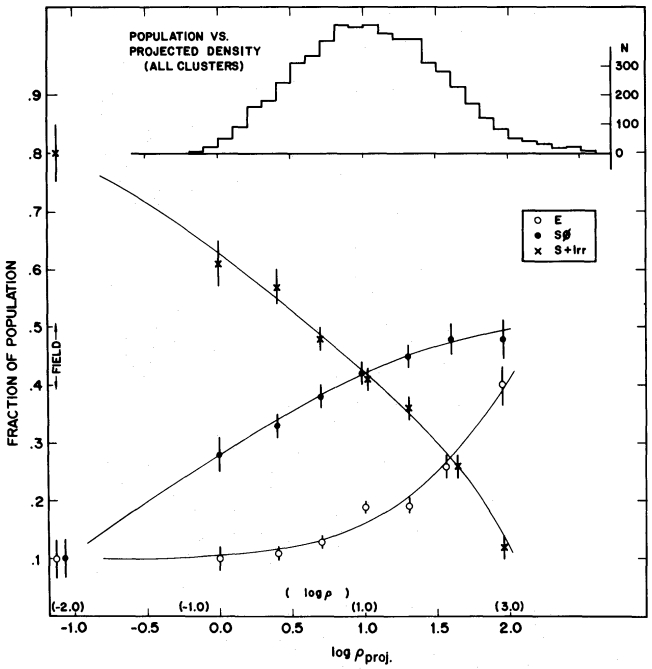

Figure 1.6: The fraction of elliptical (E), S0, and spiral+irregular (S+Irr) galaxies as a function of the log of the projected number density of galaxies (Mpc^{-2}). Spiral and irregular galaxies are dominant at lower density regions, while the fraction of elliptical (open circles) and S0 (filled circles) galaxies increases at high density regions. This figure is taken from Dressler (1980).

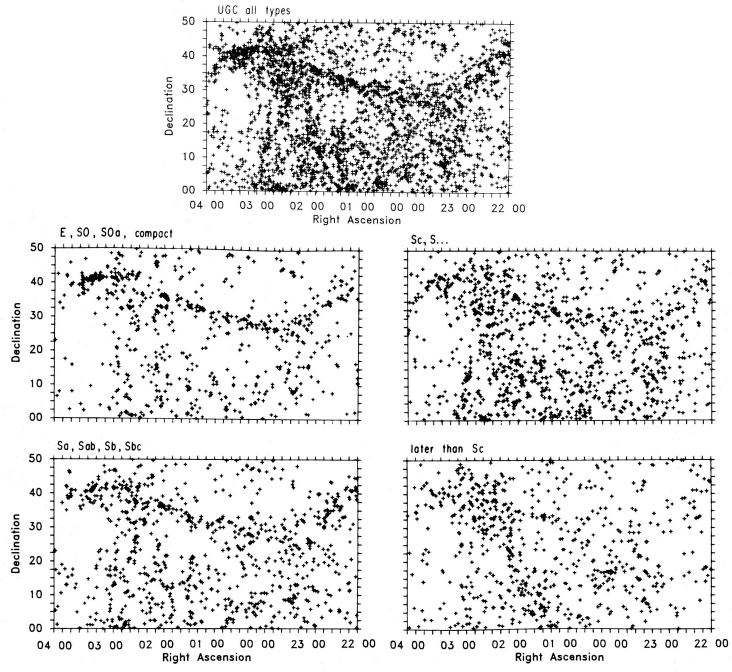

Figure 1.7: The fraction of elliptical (E), S0, and spiral+irregular (S+Irr) galaxies as a function of the log of the projected number density of galaxies (Mpc^{-2}). Spiral and irregular galaxies are dominant at lower density regions, while the fraction of elliptical (open circles) and S0 (filled circles) galaxies increases at high density regions. This figure is taken from Giovanelli et al. (1986).

galaxies are non–star-forming. Thus, it is considered that, in over-dense regions, star formation of galaxies was quenched earlier due to some environmental effects, then spiral galaxies evolved into ellipticals or lens galaxies. A number of sites have been found where galaxies are interacting and/or merging in such dense regions. It is likely that interacting galaxies lose and/or exhaust their gas through starburst, then evolve into red, bulge-dominated passive galaxies. Clusters are filled with hot ionized gas. Thus, galaxies falling into the potential wells of clusters are exposed under strong pressure of hot gas, so that their gas is stripped. Such galaxies have also been found.

As above, it is certain that the extragalactic environment plays some role in galaxy evolution in the nearby Universe. However, we are still far from well understanding the environmental effects and how do galactic properties naturally depend on the environment where they were born. The correlation between galactic properties and local number density is relatively significant at $z \lesssim 1$, while less at higher redshift. In other words, the environmental effects may be especially important in the last several Gyrs. Probably, this is because cluster-scale structures have become prominent after $z \sim 1$.

1.7 Dark matter

Nowadays, physicists believe that the matter in the Universe is dominated by invisible dark matter and that such matter is commonly considered to be some kind of non-baryonic particles, which have a mass but almost does not interact with the electromagnetic force. However, the identity of dark matter (–undetected astronomical objects? undetected gas? unknown particles? or...) has been unknown for a long time since an indication of invisible matter was reported. Here, we look back the discovery of the dark matter, prior to describing the cosmological structures and the connection between galaxy evolution. Dark matter was proposed to solve some astronomical problems with respect to the inconsistency of mass measurement.

In 1933, Fritz Zwicky found evidence of unseen matter on galaxy cluster scales by adopting the virial theorem to the Coma cluster; its virial mass estimated from the velocity dispersion of member galaxies was much higher than the mass measured from luminous objects[2] (Zwicky 1933, 1937). He called such invisible matter *dunkle Materie = dark matter*. The advance of X-ray astronomy has provided an additional indication of cluster-scale dark matter through observations of hot gas surrounding clusters, which indicates the existence of a large amount of gas of $T \sim 10^{7-8}$ K with mass about ten times higher than the total mass of galaxies. The mass required to gravitationally confine such hot gas within a cluster is about ten times larger than the sum of masses of gas and galaxies.

Another evidence of dark matter was obtained by measuring the rotation curve of galaxies. Babcock (1939) measured a rotation curve of M31 that is flat from the inner to outer region. Such an observed *flat* rotation curve can not be explained the mass distribution estimated from the luminous objects, and requires that the total-to-luminous mass ratio increase with radius. He, however, did not attribute it to the existence of invisible matter, but to other astronomical effects. Rubin & Ford (1970) re-measured an accurate rotation curve of M31, and Rubin et al. (1980) established its universality; most galaxies have such a flat rotation curve as shown in Figure 1.8. Given these observational efforts, astronomers had widely recognized the necessity of dark matter as a major unsolved problem in astronomy. In contrast, some modifications of the gravitational law were proposed as an alternative idea that do not consider dark matter.

Measuring the gravitational lensing, predicted by Albert Einstein's *general theory of relativity*, provides a mass estimate of all the matter that exists there independent of astronomical uncertainties with respect to conversion between observed flux and mass and/or non-detection of

[2]Note that the ratio of total to visible masses that he measured (about 400) were much overestimated by more than an order of magnitude, mainly due to the uncertainties in the Hubble constant.

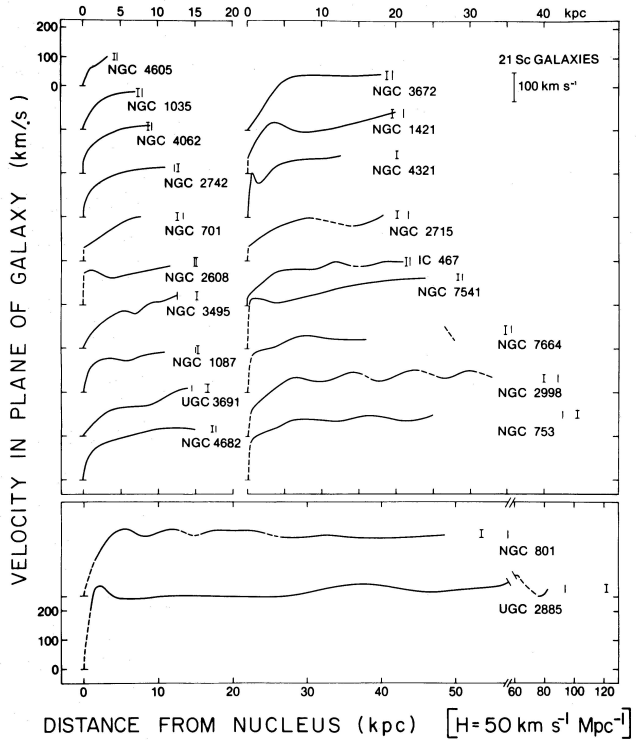

Figure 1.8: Rotation curves of 21 nearby Sc-type galaxies. The flat behavior is ubiquitously seen in most galaxies. This figure is taken from Rubin et al. (1980).

faint objects. The *bullet* cluster is an interacting cluster, which consists of a large cluster and a smaller one that has passed through the other like a bullet. Such a situation was confirmed from X-ray observations of hot cluster gas; galaxies of each cluster do pass each other almost without collision, but the gas interacts and lags behind the collision-less galaxies, distributed between these clusters. Clowe et al. (2004) and Markevitch et al. (2004) measured the weak lensing effects of this cluster and found that the mass distribution is coincident with the distribution of galaxies, and off from the gas distribution (see Figure 1.9). This evidently indicates that a large amount of invisible unknown *matter* that interacts only with gravity exists because modified theories of gravitation can not explain such an observed mass distribution (Clowe et al. 2006).

Currently, dark matter is generally considered to be massive non-baryonic particles that weakly (or non) interact through the weak force (Weakly Interacting Massive Particles; WIMP), although historically astronomical objects that consist of baryons (Massive Compact Halo Object; MACHO) also have been considered as candidates of dark matter. Cosmological surveys of large scale structures have also suggested the existence of dark matter and cosmological models with dark matter have been advocated. Around the same time, the acceleration of the expansion of the Universe has been found by measuring distances of type-Ia supernovae (Riess et al. 1998), and unknown energy is hypothesized to explain it, which is called *dark energy*. Finally, an accurate measurement of the Cosmic Microwave Background (CMB) with the *Wilkinson Microwave Anisotropy Probe (WMAP)* satellite has established the standard cosmological model with non-baryonic dark matter of approximately $\approx 22\%$ of the critical density of the Universe and dark energy of $\approx 74\%$ (Spergel et al. 2007; Komatsu et al. 2009). The latest constraint of the composition of the Universe (baryon, 4.8%; non-baryonic dark matter, 26%; dark energy, 69%) has obtained from *Planck* satellite observations (Planck Collaboration 2015).

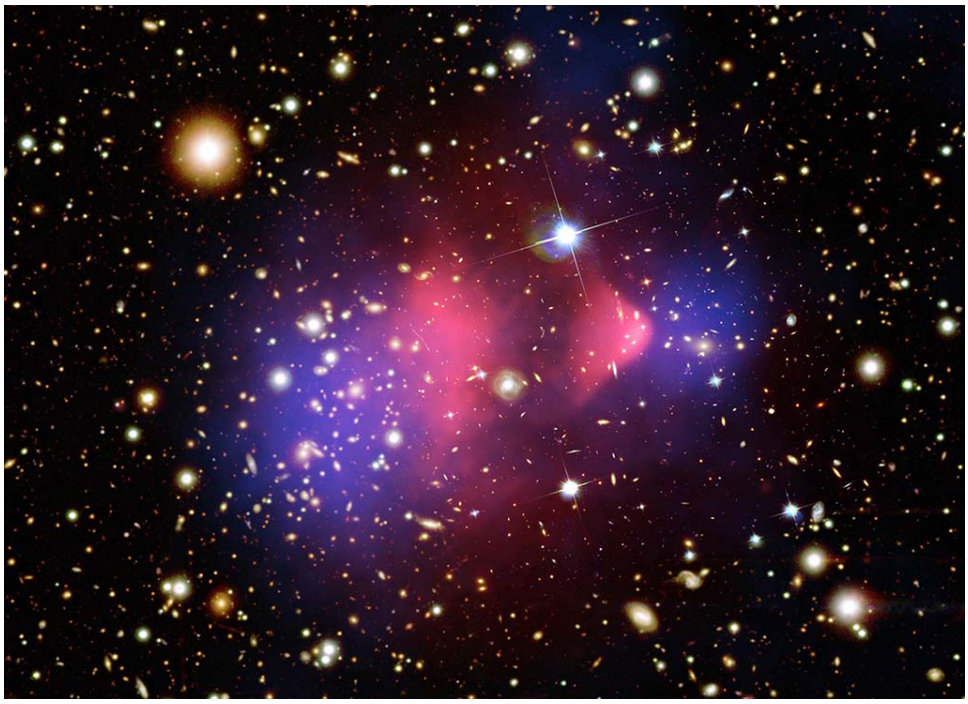

Figure 1.9: A galaxy cluster 1E 0657-56, known as the Bullet Cluster. The cluster's two clouds of X-ray emitting gas shown in red are offset from the primary concentrations of mass shown in blue, which is measured from gravitational lensing. Individual galaxies of the cluster are shown in the optical image, which are concentrated following the mass distribution. Image credit: X-ray: NASA/CXC/CfA/M.Markevitch et al.; Optical: NASA/STScI; Magellan/U.Arizona/D.Clowe et al.; Lensing Map: NASA/STScI; ESO WFI; Magellan/U.Arizona/D.Clowe et al.

1.8 Structure formation and dark halos

The formation of galaxies can be separated into two aspects: the evolution of dark matter and baryonic matter. Galaxies form from baryonic gas cooling in the gravitational potential wells of extended halos of dark matter. The evolution of baryons is a messy process, including a number of complex physical mechanisms, which still remains unclear. In contrast, the evolution of dark matter has been relatively well understood theoretically because only gravity is important. Here, we provide an overview of the formation of cosmological large scale structures and dark matter halos.

Structures in the Universe originate from the quantum fluctuations during the inflation. The structure formation of the Universe is dominated by dark matter; here we consider the standard *cold* dark matter, whose velocity dispersion is almost negligible. Let δ be the density contrast as

$$\delta(\boldsymbol{r}, t) \equiv \frac{\rho(\boldsymbol{r}, t) - \bar{\rho}(t)}{\bar{\rho}(t)} \tag{1.2}$$

where $\rho(\boldsymbol{r}, t)$ and $\bar{\rho}(t)$ are the local and average density of the Universe at time t, respectively. Just after the Big Bang, the density contrast was very small, i.e., $\delta \ll 1$. As the Universe expands, the density contrast grows up because gravity is relatively strong at denser regions, thus the cosmic expansion is slightly suppressed. In the matter-dominant Universe, δ is proportional to the scale factor a of the Universe. When δ approaches 1, the growth of the density contrast becomes faster than $\delta \propto a$. Then, the regions where δ approaches ≈ 5 begin to collapse overcoming the expansion. Such regions eventually form gravitationally-bounded systems, which are called *dark halos*.

Regions with a higher initial density overcome expansion earlier, then form relatively small collapsed structures. As time passes, larger regions begin to collapse, then form larger dark halos, which usually contains smaller dark halos that were already collapsed earlier. Dark halos also attract each other by gravity and/or fall into the potential wells of larger structures, then form larger structures. Such a manner of the structure formation has been also demonstrated from cosmological N-body simulations (Kravtsov et al. 2004; Springel et al. 2005). We call this the *bottom-up* structure formation.

All individual galaxies are expected to form in their own dark matter halos. Larger dark halos sometimes contain multiple halos. In clusters, each member galaxy has its own smaller dark halo, called a *subhalo*, while the cluster itself is a single large dark halo as a whole, thus can be considered as a single astronomical object. Massive halos can have masses as large as $10^{15}\ M_\odot$. Further larger structures such as superclusters and cosmic large scale structures, however, have only $\delta \sim 1$, thus they are not bound gravitationally.

There are some important statistical quantities of dark halos that are predicted by a given cosmological model. The mass function of dark halos is a fundamental quantity that describes the number density of halos as a function of halo mass. Press & Schechter (1974) established a analytical framework that predicts the halo mass function from extrapolation of the linear perturbation theory. Thereafter, the formalism has been improved to reproduce results from a series of numerical simulations better (see Figure 1.10; e.g., Bond et al. 1991; Sheth & Tormen 1999; Lee & Shandarin 1998; Sheth et al. 2001; Jenkins et al. 2001; Tinker et al. 2008).

The two-point correlation function (or power spectrum) is a powerful tool to describe the statistical properties of the distribution of dark matter and dark halos (and also galaxies). Dark halos, of course, follow the distribution of the underlying dark matter, but the distinct halos and fluid dark matter are clustered in different manners. The clustering of halos is biased relative to that of the underlying mass distribution by an amount that depends on halo mass scale. The correlation function of dark halos $\xi_{\rm h}$ is related to that of dark matter $\xi_{\rm DM}$ as

$$\xi_{\rm h} = b_{\rm h}^2 \xi_{\rm DM} \tag{1.3}$$

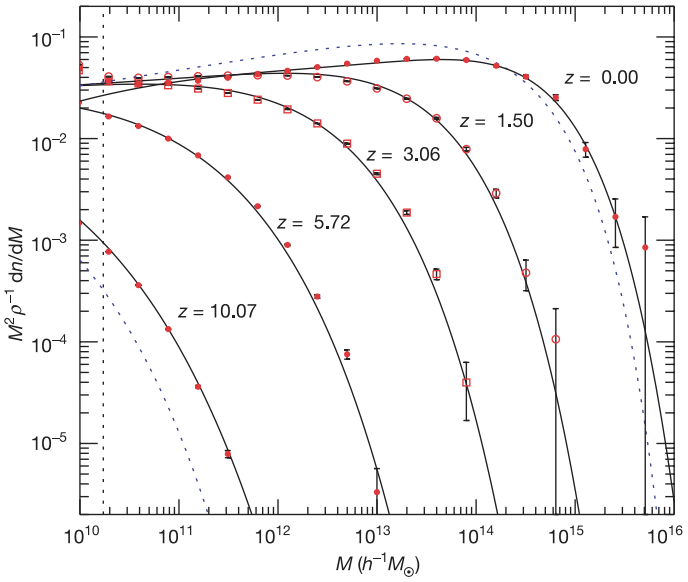

Figure 1.10: Halo mass function at various redshifts from the Millennium Simulation. Solid lines are predictions from an analytic fitting function proposed by Jenkins et al. (2001). Dotted lines provide the Press-Schechter mass function. This figure is taken from (Springel et al. 2005).

where $b_{\rm h}$ is called the *halo bias*. Pioneering studies of the formalism of the halo bias were conducted by Cole & Kaiser (1989) and Mo & White (1996), and subsequent studies have improved the formulation by using cosmological simulations (e.g., Sheth & Tormen 1999; Sheth et al. 2001; Tinker et al. 2005, 2010)

1.9 Connection between galaxies and dark matter halos

In the current paradigm, galaxies form through baryonic gas cooling in dark halos. Thus, studying the formation and evolution of dark halos is essential for understanding the formation and evolution of galaxies. For this purpose, cosmological N-body simulations are very powerful, and have enriched our understanding, from the evolution of matter fluctuation to the formation of dark halos, as mentioned above. Observationally, we can study the connection between galaxies and their dark halos with multiple methods, including gravitational lensing, satellite kinematics, the X-ray observations of the intracluster medium (e.g., Mandelbaum et al. 2006; Rykoff et al. 2008; More et al. 2009). With large surveys, we have mapped the three-dimensional distribution of galaxies. The large-scale distribution of dark matter has also been mapped based on the week lensing effects (e.g., Massey et al. 2007). Another powerful method is to compare observed statistical properties (such as a two-point correlation function) of galaxies to those of dark matter, which are predicted by cosmological models or numerical simulations, to investigate the characteristics of halos which the galaxies inhabit. The halo correlation function depends on the halo mass; more massive halos are more strongly clustered. Galaxies inherit the clustering of the halos in which they reside. Thus the clustering of galaxies can inform us about their dark matter halo masses.

Pioneering studies by Neyman and Scott et al. (e.g., Neyman & Scott 1952) established a theoretical context for studying galaxy density fluctuation with the two-point correlation function. Thereafter, It has been found by Totsuji & Kihara (1969), and later by Peebles et al. (e.g., Groth & Peebles 1977), that the correlation function is well expressed by a power-law function

as

$$\xi_{\rm g}(r) = \left(\frac{r}{r_0}\right)^{-\gamma} \tag{1.4}$$

where r_0 is called the correlation length, which depends on a galaxy sample, and the slope γ is known to be ~ 1.7 for optical sample. Afterwords, large data sets from galaxy redshift surveys have enabled us to measure galaxy clustering accurately and established a quantitative characterization of its dependence on galactic properties, including luminosity, stellar mass, color, morphology, and spectral type (see Figure 1.11; e.g., Davis & Geller 1976; Hamilton 1988; Norberg et al. 2001, 2002; Zehavi et al. 2005; Li et al. 2006; Zehavi et al. 2011). Luminous, massive galaxies are generally clustered more strongly than faint, less massive galaxies. Red, bulge-dominant galaxies are also more strongly clustered than blue, disk galaxies. The advance of galaxy surveys has made significant progress in measuring galaxy clustering at higher redshift (e.g., Daddi et al. 2003; Ouchi et al. 2004; Meneux et al. 2008, 2009).

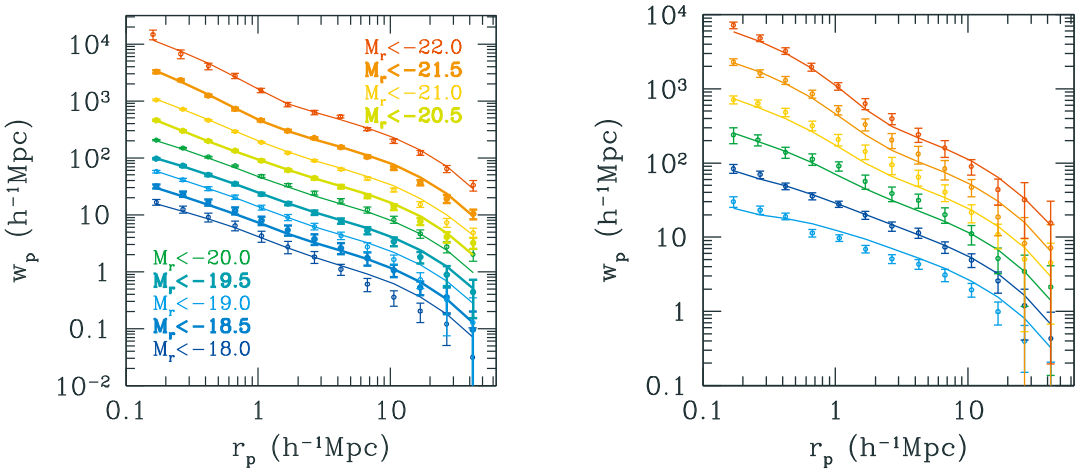

Figure 1.11: Luminosity (right) and color (left) dependence of the correlation function of galaxies from the SDSS. The solid lines show the best-fit predictions from the HOD modeling. These figures are taken from Zehavi et al. (2011).

Observed dependence of galaxy clustering on the galactic properties evidently indicates that intrinsic properties of galaxies depend on which dark matter halos they reside. In other words, subsamples of galaxies are biased relative to dark halos in different manners. Comparing observed galaxy clustering to the dark halo clustering provides clues to understand what rules galaxies obey to inhabit dark halos. Galaxy clustering is biased relative to that of the underlying dark matter or dark halos. Similarly to Equation (1.3), the correlation function of galaxy $\xi_{\rm g}$ is related to $\xi_{\rm DM}$ as

$$\xi_{\rm g} = b_{\rm g}^2 \xi_{\rm DM} \tag{1.5}$$

where $b_{\rm g}$ is called the *galaxy bias*, which is generally scale-dependent.

The framework of halo occupation distribution (HOD) has been advocated to describe galaxy bias and to model galaxy clustering (Seljak 2000; Peacock & Smith 2000; Berlind & Weinberg 2002; Zheng et al. 2005). It models the galaxy correlation function in terms of the probability distribution $P(N|M)$ that a halo of mass M contains N galaxies of a given type. A pioneering study by Benson et al. (2000) demonstrated that the observed galaxy clustering can be reproduced by populating N-body halos with a predicted $P(M|N)$. Thereafter, through many observations and simulations, the HOD framework have been commonly considered as a powerful tool to study the connection between galaxies and dark halos, with a variety of models of $P(N|M)$ advocated

(e.g., Kravtsov et al. 2004). In Figure 1.11, the HOD models of the galaxy correlation function are shown with the observational data.

Another method linking galaxies with halos is the abundance matching technique (e.g., Kravtsov et al. 2004; Tasitsiomi et al. 2004). It assumes a tight correlation between properties of galaxies and (sub)halos, for example, galaxy luminosity L and maximum circular velocity of halos $V_{\rm max}$. Such an assumption basically rests on the expectation that larger halos should host larger galaxies. For a luminosity-limited galaxy sample, a corresponding halo sample is constructed by setting a threshold value of $V_{\rm max}$ such that the number density of halos matches with that of the galaxy sample as

$$n_{\rm halo}(> V_{\rm max}^{\rm thresh}) = n_{\rm galaxy}(> L). \tag{1.6}$$

By comparing observed clustering of the galaxy sample to that of the halo sample, one can test the relation between galaxies and halos that they assume. It has been shown that the predictions from abundance matching techniques can well reproduce the observed correlation functions of luminosity-limited (or stellar mass limited) galaxy samples (e.g., Conroy et al. 2006; Trujillo-Gomez et al. 2011; Moster et al. 2010; Reddick et al. 2013). Currently, the abundance matching techniques have been widely used (e.g. Behroozi et al. 2013a; Masaki et al. 2013; Saito et al. 2015).

Measuring the relationship between dark matter halo mass and galaxy luminosity or stellar mass is essential for understanding how the galaxies are characterized by their host halos. The stellar-to-halo mass relation (SHMR) probes the integrated efficiency of the past stellar mass assembly. Growing evidence indicates that the stellar-to-halo mass ratio ($M_*/M_{\rm halo}$) reaches a maximum at $M_{\rm halo} \sim 10^{12}$ (see Figure 1.12; e.g., Mandelbaum et al. 2006; Conroy & Wechsler 2009; Moster et al. 2010; Behroozi et al. 2010; Leauthaud et al. 2012). That mass scale, called the *pivot mass*, marks the mass at which the accumulated stellar mass growth has been the most efficient (Leauthaud et al. 2011). Recent advantage of deep galaxy surveys have enabled us to study the SHMR beyond $z > 1$ up to $z \sim 8$ (e.g., Behroozi et al. 2013a; McCracken et al. 2015; Harikane et al. 2015).

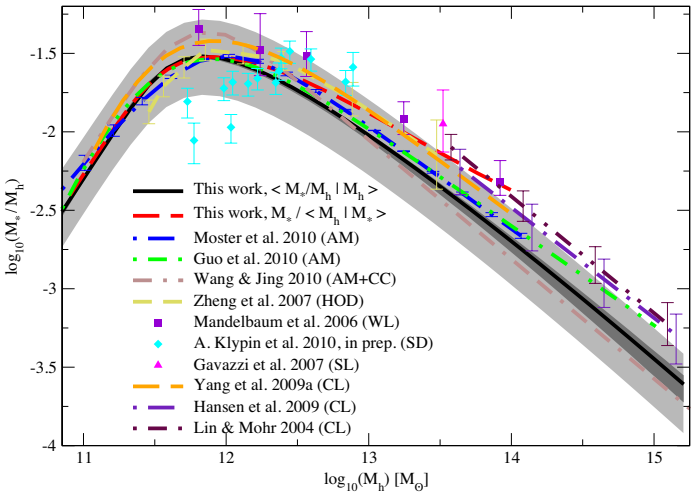

Figure 1.12: Stellar-to-halo mass relation, based on various measurements. This figure is taken from (Behroozi et al. 2010).

1.10 Outline of this thesis

In this thesis, we explore the galaxy evolution at redshift $z \sim 1.6$ using a galaxy sample constructed from a near-infrared spectroscopic campaign, the FMOS-COSMOS survey, carried out using the Fiber Multi-Object Spectrograph (FMOS) on the Subaru telescope. Our global aims are to investigate the intrinsic properties of star-forming galaxies and the environmental effects on the galaxy evolution at the peak epoch of the cosmic star formation history. In particular, we investigate the star formation and physical conditions of ionized gas in star-forming regions based on multiple nebular emission lines in the rest-frame optical window. Our survey has also mapped the three-dimensional spatial distribution of star-forming galaxies at $1.43 \leq z \leq 1.74$ in the COSMOS field, which enabled us to study the connection between our galaxy sample and and the host dark halos.

First, we measure star formation rates (SFRs) of galaxies based on the Hα flux observed by FMOS, then determine the evolution of the so-called star-forming main sequence, a tight correlation between SFR and stellar mass. Our sample galaxies show SFRs that are roughly 20 times larger than those seen in local galaxies. To obtain the intrinsic SFRs, we determine the amount of dust extinction based on the Balmer decrement (observed Hβ/Hα flux ratios) implementing stacking analysis.

Second, we extensively investigate the excitation state and chemical enrichment of ionized gas using empirical diagnostic diagrams based on the flux ratios of emission lines, including Hα, [*N ii*], [S II], Hβ, and [O III]. Comparing with local galaxies from the SDSS, we discusse how the ISM properties have evolved and what is the primary origin of the offset seen in the BPT diagram at high redshifts. We also study the redshift evolution of mass–metallicity relation using multiple metallicity indicators, and examine the so-called fundamental metallicity relation at high redshift with a simple theoretical model.

Finally, we measure the two-point correlation function of our galaxy sample based on their spectroscopic redshifts, then we found a significant clustering over the range of the projected distance $0.05 \lesssim r_{\rm p} \lesssim 20$ Mpc. Based on a halo occupation distribution model, we study the properties of dark halos that host our sample galaxies.

This thesis is organized as follows. We provide an overview of our FMOS-COSMOS survey project in Chapter 2. We report on the results from the above three main studies in Chapters 3, 4, and 5, respectively. Finally, we summarize the conclusions and future prospects in Chapter 6. In Appendices, we review the basic theoretical framework of the relevant matters: chemical evolution, photoionization equilibrium, ΛCDM cosmology, structure formation. We also note some details in our clustering measurement, presented in Chapter 5.

Chapter 2

The FMOS-COSMOS Survey

We explore the formation and evolution of galaxies based on the FMOS-COSMOS survey, a data set constructed with the Fiber Multi-Object Spectrograph (FMOS) mounted on the Subaru telescope. This is a joint effort based on three 'intensive' programs approved by National Astronomical Observatory of Japan (NAOJ) and programs awarded through the University of Hawaii, Institute for Astronomy (PI D. Sanders). Our observations were carried out between 2012 March and 2016 April, with the latter date indicting the completion of the project due to the decommissioning of FMOS. The survey is designed to detect rest-frame optical emission lines for galaxies at $1.4 \lesssim z \lesssim 1.7$ in the near-infrared spectral window.

2.1 Background and goals

Over the last decade, the history of galaxy mass assembly through cosmic time has been made clearer with numerous efforts based on multi-wavelength imaging and spectroscopic surveys using 8–10 meter class telescopes (e.g., VVDS, VUDS, zCOSMOS surveys) and deep surveys with space telescopes (e.g., *HST* and *Herschel*). Such large galaxy surveys have accumulated data, which have enabled us to explore their intrinsic properties such as their stellar mass, star formation rate (SFR), stellar population, morphology and chemical enrichment of the interstellar medium (ISM), as well as the galaxy distribution. As a consequence, it has been shown that most galaxies had higher SFRs at higher redshifts, at least up to $z \sim 3$, than those seen now. Local galaxies either have declined or had been quenched while subsequently passively evolving until today. Such evolutionary processes of individual galaxies comprise the global star formation history of the universe, which measures the mean amount of star formation per unit cosmic volume, that peaks at $z \sim 2$–3 and shows a declination until $z = 0$ (see Figure 1.2; Hopkins & Beacom 2006; Madau & Dickinson 2014, and references therein).

In particular, recent rest-frame optical spectroscopic campaigns (e.g., SDSS, DEEP2, VVDS, VIPERS surveys) have constructed extensive galaxy samples with quality spectra, which are essential to identify their redshift and to evaluate the physical properties of individual galaxies. However, there has been a wide gap at $1 \lesssim z \lesssim 2$, which came to be called the *redshift desert*, because it had been difficult to penetrate with an optical spectrograph due to the fact that strong rest-frame optical spectral features, such as the Hα, [O III] lines, and 4000Å break, are redshifted to near-infrared. However, this redshift range is particularly important because it marks the epoch where galaxies transition from the peak of cosmic star formation history to the regime of more passive evolution.

Around 2010–2012, long-awaited multi-object near-infrared spectrographs mounted on the world's largest telescopes, i.e., VLT/KMOS, Keck/MOSFIRE, and Subaru/FMOS, have provided the means for surveys to fill out such a gap in redshift space. In particular, Fiber Multi-Object Spectrograph (FMOS; Kimura et al. 2010) on the Subaru telescope is unique with having a high-multiplicity and a wide field-of-view. Our broad aim is to construct a large galaxy sample at a redshift range $1.4 \lesssim z \lesssim 1.7$ by taking advantage of Subaru/FMOS, and to advance our understanding of galaxy evolution at this most active epoch by obtaining accurate measurements

of galactic properties, such as SFR, dust extinction, gas-phase metallicity, and other emission line characteristics, as well as the environmental properties base on the three-dimensional galaxy distribution.

2.2 Fiber Multi-Object Spectrograph

Fiber Multi-Object Spectrograph (FMOS; Kimura et al. 2010) is a near-infrared spectrograph mounted on the prime focus of the Subaru telescope. FMOS consists of two spectrographs (IRS1 and IRS2) that cover a near-IR spectral window from 0.9 μm to 1.8 μm (see Figure 2.1). In total, 400 fibers ($1''.2$ in diameter; Murray et al. 2008; Akiyama et al. 2008a) are embedded in the circular field-of-view of $30'$ in diameter, belonging to each of the spectrographs (see Figure 2.3). In the cross-beam switching (CBS) mode, two fibers belonging to the same spectrograph are allocated for one science object. Following the ABAB nodding pattern of the telescope, each of the paired fibers observes a target and the other measures the sky background spatially close to the object in turn. Therefore, about 200 science targets can observed simultaneously in the CBS mode. Fibers are assigned for objects using the FMOS-Echidna Spine-to-Object Allocation software.

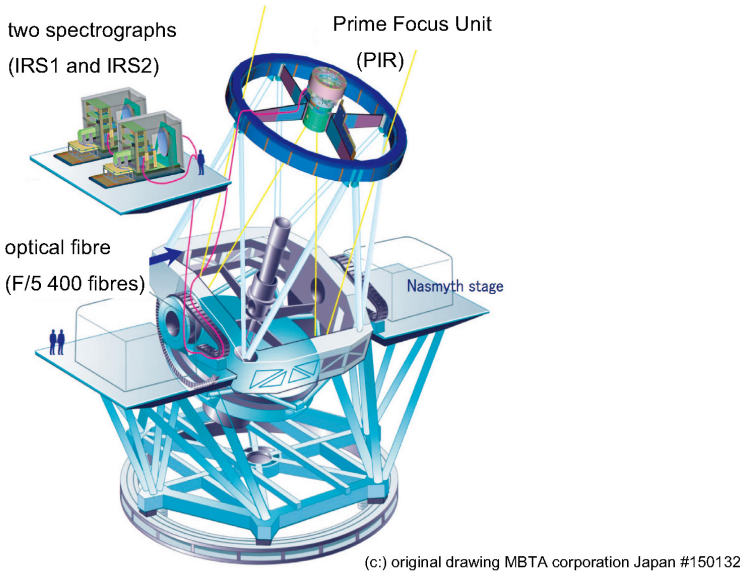

Figure 2.1: Illustration of the mechanical layout of FMOS on the Subaru telescope. The optical unit is put at the prime focus. This figure is taken from Kimura et al. 2010.

In the high-resolution (HR) mode, the spectral window is divided into multiple wavelength ranges with a spectral resolution from $R = \lambda/\Delta\lambda \sim 1600$ to $R \sim 2600$, as summarized in Table 2.1[1]. Note that we find the actual spectral resolution achieved approximately $R \approx 3000$ in the H-long band, which is higher than the nominal value ($R \sim 2600$), by measuring widths of artificial Th–Ar lines in calibration frames. The data used in this Thesis was taken with the HR mode.

FMOS is equipped with an OH airglow suppression system that masks out strong atmospheric emission lines (see Figure 2.4). The OH mask blocks out approximately 30% of the whole spectral window of the H-long and J-long gratings. The HR mode well resolves the pixels that are masked out by OH masks, and hence the effect of convolution among signals on good pixels and pixels being masked out is small.

[1] http://www.subarutelescope.org/Observing/Instruments/FMOS/performance.html

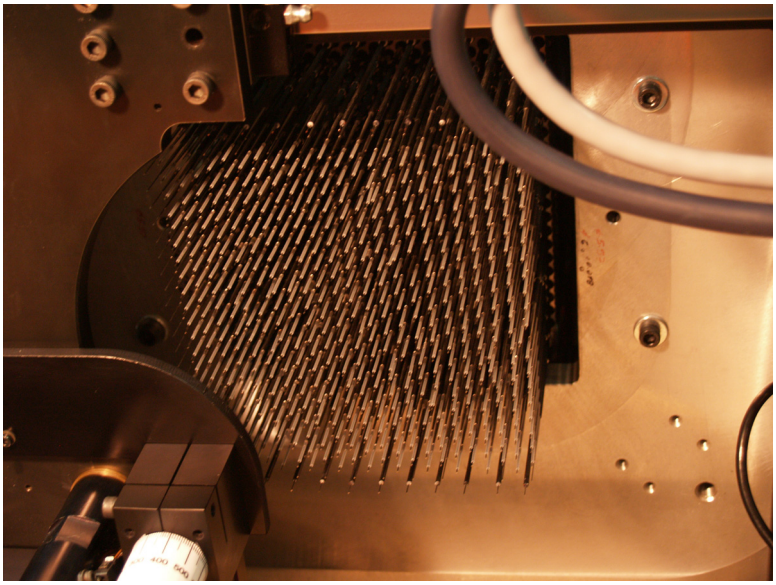

Figure 2.2: Close up view of the Echidna fibers at the focal plane. 400 science-fibers cover the 30′-diameter FoV, which are connected to the spectrographs. The spacing between neighboring spines is 7 mm. This figure is taken from Akiyama et al. 2008a.

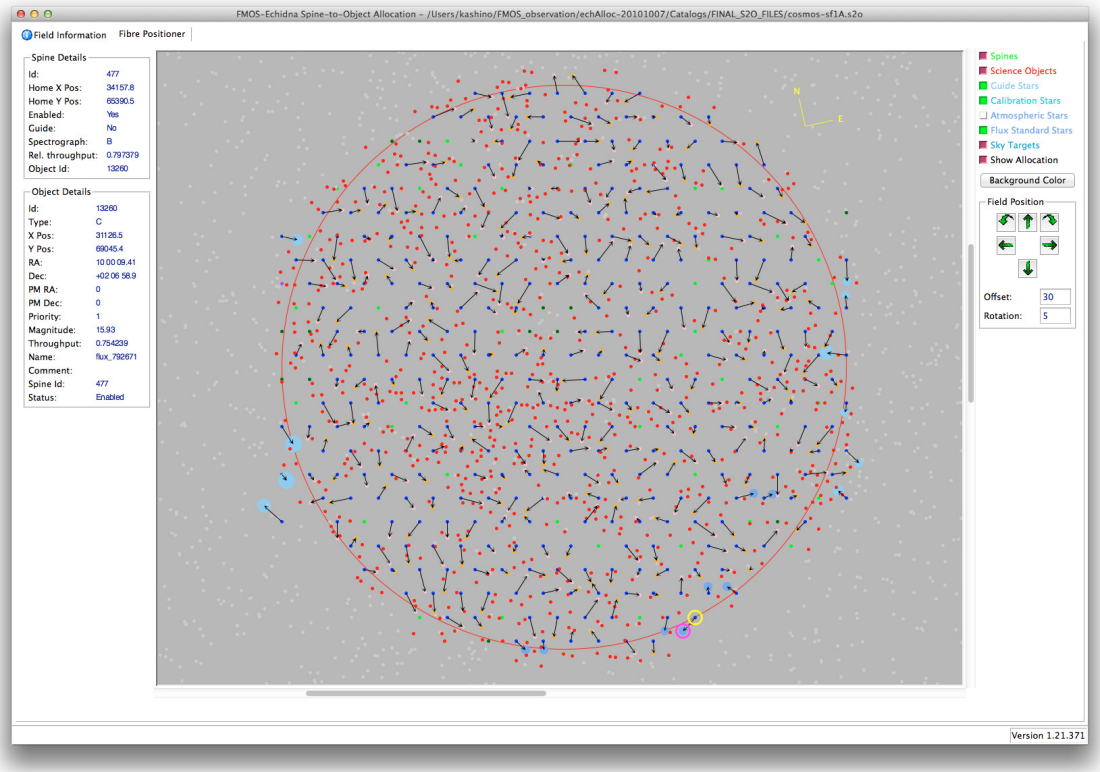

Figure 2.3: GUI of the FMOS-Echidna Spine-to-Object Allocation software. A red circle indicates the FMOS field-of-view of 30′-diameter. Small dots are as follows. Red: objects within the observable area. Orange: objects for which fibers are allocated. Light pink: dummy positions of objects for the B-position exposure. Blue: home positions of allocated fibers with their movement shown by arrows. Green: home position of un-allocated fibers. Blue circles: positions of flux standard stars. Light blue circles: guide stars.

Table 2.1: Spectral coverage, resolution, and sensitivity in the High Resolution mode.

Band name	**Coverage** μm	**Resolution** $R = \lambda/\Delta\lambda$ (FWHM)	**Sensitivity** erg sm^{-2} s^{-1}
J-short	0.92–1.12	1600	1.7×10^{-16}
J-long	1.11–1.35	1900	0.4×10^{-16}
H-short	1.40–1.60	2400	0.5×10^{-16}
H-short prime	1.45–1.67	2400	0.5×10^{-16}
H-long	1.60–1.80	2600	0.5×10^{-16}

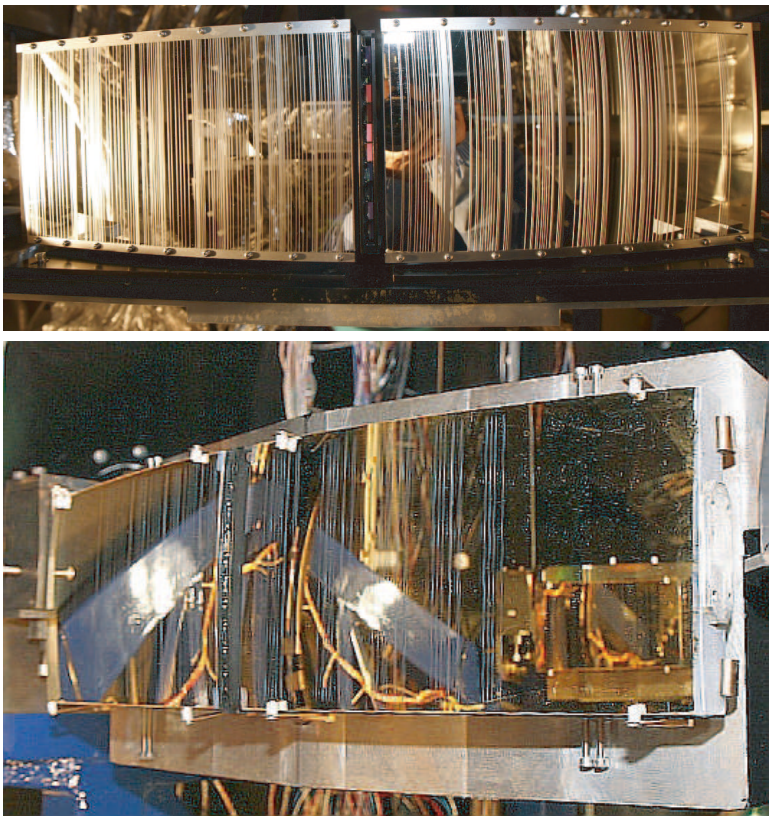

Figure 2.4: OH mask mirror on IRS1 (top) and IRS2 (bottom). This figure is taken from Kimura et al. (2010).

2.3 Survey strategy

The FMOS-COSMOS survey is specially designed to detect the Hα emission line that falls within the H-long band (1.6–1.8 μm; $R \approx 3000$) from star-forming galaxies at $1.43 < z < 1.74$. Following an early program with the low-resolution mode (PI: J. Silverman), our current project makes use of the HR mode, which is suitable to cleanly separate the Hα and [N II] lines. We operate FMOS in the CBS mode, targeting about 200 objects in each pointing.

Our observations cover four footprints each with a FoV of 0.20 square degrees in the Cosmological Evolution Survey (COSMOS) field, marked by blue circles in Figure 2.5. Through the contribution from the University of Hawaii, we also cover three additional outer footprints (red circles). The coordinates, R.A. and Declination, are summarized in Table 2.2. Through the program as a whole, we covered the entire COSMOS field with 12 footprints, including black circles in Figure 2.5. The survey area of the central four footprints is 0.81 deg^2 (1.1 deg^2 including the outer three footprints). We observe each FMOS footprint for the maximal amount of time possible in one night with on-source exposure times from 3 to 5 hr. The 5 hr integration permits us to detect an emission line with a flux down to 2×10^{-17} erg cm^{-2} s^{-1} with $S/N = 5$ (see Figure 2.6).

Table 2.2: FMOS footprints

Name	R.A.	Decl.
HR1	09:59:56.0	+02:22:14
HR2	10:01:35.0	+02:24:53
HR3	10:01:19.7	+02:00:30
HR4	09:59:38.7	+01:58:08
HR1E	10:00:28.7	+02:37:45
HR2E	10:02:01.4	+02:10:43
HR3E	09:58:47.5	+02:10:09

Follow-up observations were carried out for a subset of targets using the J-long grating (1.11–1.35 μm), mainly through the collaboration with the University of Hawaii (PI D. Sanders) to supplement our observations acquired through the Subaru intensive program. These observations are intended to cover the Hβ and [O III]λ5007 lines for galaxies with a positive Hα detection. Those lines are essential to measure the dust extinction based on the Hα to Hβ ratio (i.e., Balmer decrement), an indication of the photoionization state of the ISM, and to confirm redshift measurements based on a single emission line.

2.4 Target selection

Our main target objects are composed of massive star-forming galaxies identified in the COSMOS photometric catalog (Capak et al. 2007; McCracken et al. 2010, 2012) that includes the Ultra-VISTA/VIRCAM photometry and the higher-level physical properties of individual galaxies (Ilbert et al. 2009, 2013). For each galaxy, the multi-wavelength photometry is fit using the LePhare photometric analysis code (Arnouts & Ilbert 2011) to derive photometric redshift, stellar mass, SFR, color excess, galaxy age, and so on. To achieve our scientific goals, the target selection is intended to maximize the efficiency of detecting Hα in the FMOS H-band window by imposing selection limits on K-band magnitude ($K < 23$–23.5), stellar mass ($M_* \gtrsim 10^{10}\ M_\odot$), photometric redshift ($1.4 \lesssim z_{\rm phot} \lesssim 1.7$), and predicted H$\alpha$ flux ($f^{\rm pre}$(Hα) $\geq$ 4–10 $\times 10^{-17}$ erg sm^{-2} s^{-1}). Details of our sample selection for each study are described later in each Chapter.

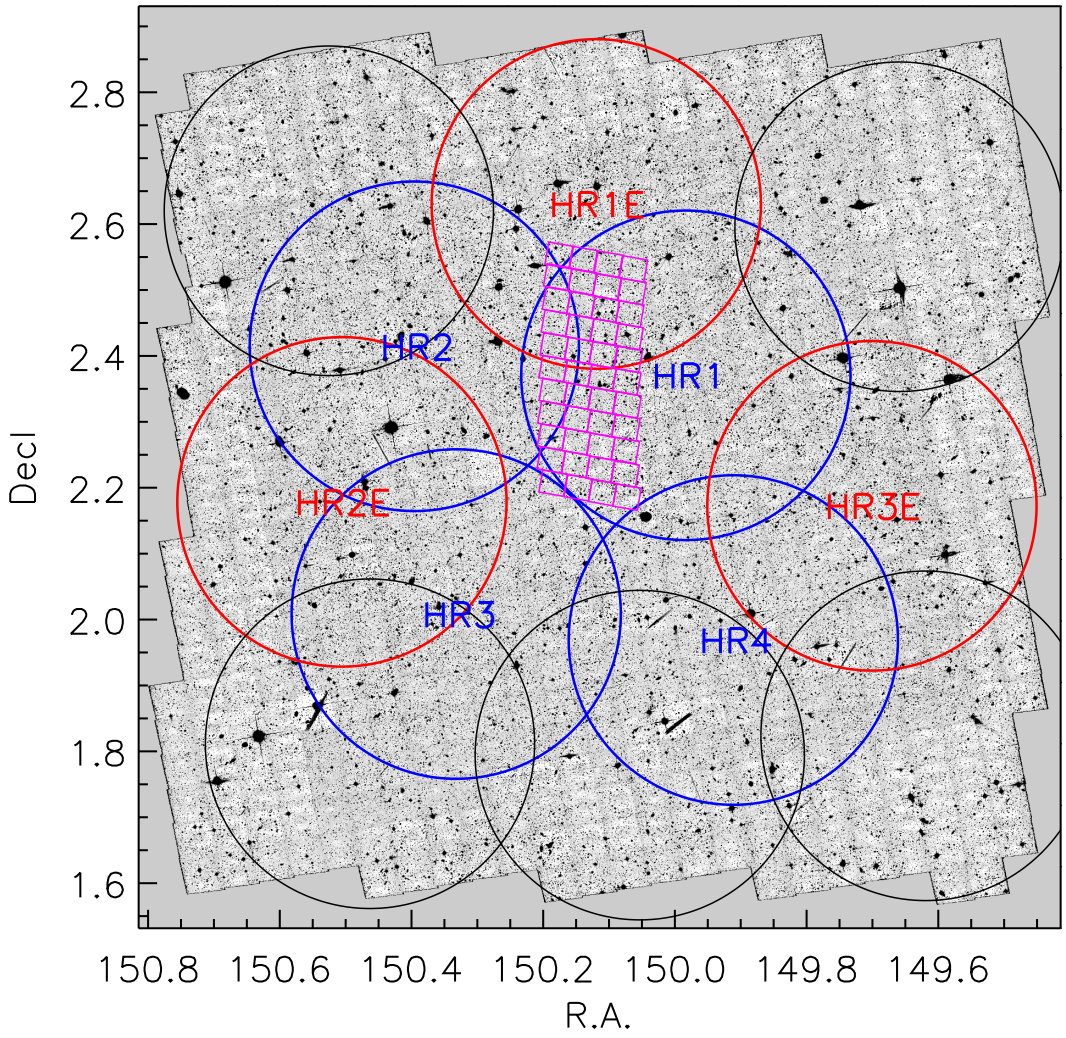

Figure 2.5: FMOS footprints overlaid on the *HST*/ACS mosaic image of the COSMOS field. The area with WFC3 NIR imaging from CANDELS is shown in magenta. This Thesis reports on observations of the central four (HR1, HR2, HR3, HR4) and additional three outer (HR1E, HR2E, HR3E) footprints.

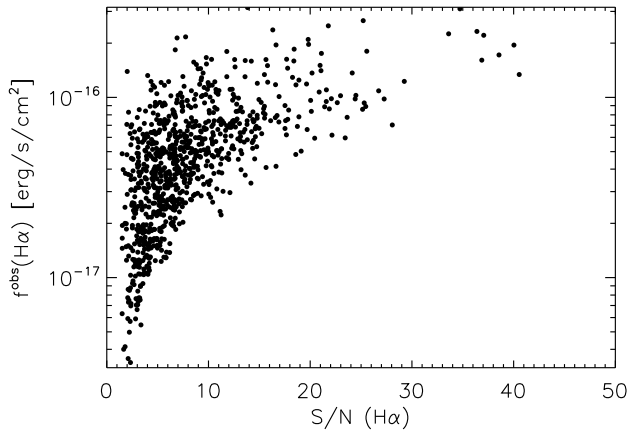

Figure 2.6: Observed Hα flux as a function of signal-to-noise ratio.

Our program uses different subsamples of the main FMOS catalog to tune the selection of targets to best address specific science topics. Some fraction of fibers are used for 1) far-IR sources from the *Herschel* PACS Evolutionary Prove Surveys (Lutz et al. 2011) and 2) X-ray-selected AGNs identified in the *Chandra*-COSMOS survey (Elvis et al. 2009) and the Legacy survey (Civano et al. 2016). The COSMOS field has been covered with *Herschel*-PACS imaging at 100 μm and 160 μm bands. The flux limits correspond to a SFR of $\sim 100\ M_{\odot}\mathrm{yr}^{-1}$ at $z = 1.6$. Those include objects have a SFR elevated well above (more than three times) the main sequence of normal star-forming galaxies (Rodighiero et al. 2014). X-ray sources identified in the *Chandra* catalogs are included to study the evolution of high-z AGNs and super massive black holes. These objects are generally rarer than normal star-forming galaxies, thus the wide FOV of FMOS is very suitable to capture them. The FMOS fibers are allocated preferentially for those objects, so that we don't miss them.

2.5 Data analysis

2.5.1 Data reduction

All raw data are reduced using the public software FIBRE-pac (FMOS Image-Based REduction Package; Iwamuro et al. 2012). The base reduction platform is IRAF. The data is processed separately for each spectrograph (IRS1 and IRS2) in the same manner. The reduction process uses the detector-flat images that are taken through the engineering observations. These are homogeneous thermal images that give the quantum efficiency of the detectors of the spectrographs. A bad pixel mask is constructed based on the detector-flat image, which is also included in the package. Through the reduction process, science frames are divided by the detector-flat image to remove the pixel-to-pixel fluctuation of the quantum efficiency, and corrected for bad pixels by replacing with an interpolated value from the surrounding pixels. For each pointing, observers take the calibration data just before or after (i.e., evening or dawn) all science exposures. The calibration data include the *dome-flat* frames and the *comparison* (Th–Ar) frames. The data reduction is separated into two processes, for the calibration data and for the science data. Here, we provide an outline of the reduction procedure.

Prior to the reduction of the science frames, the dome-flat and comparison images are processed to correct for the image distortion and to determine the wavelength calibration. The dome-flat images are processed to determine transformation to correct for distortion in the spatial direction (y-axis). Through this process, the image is reformed to straighten the spectra

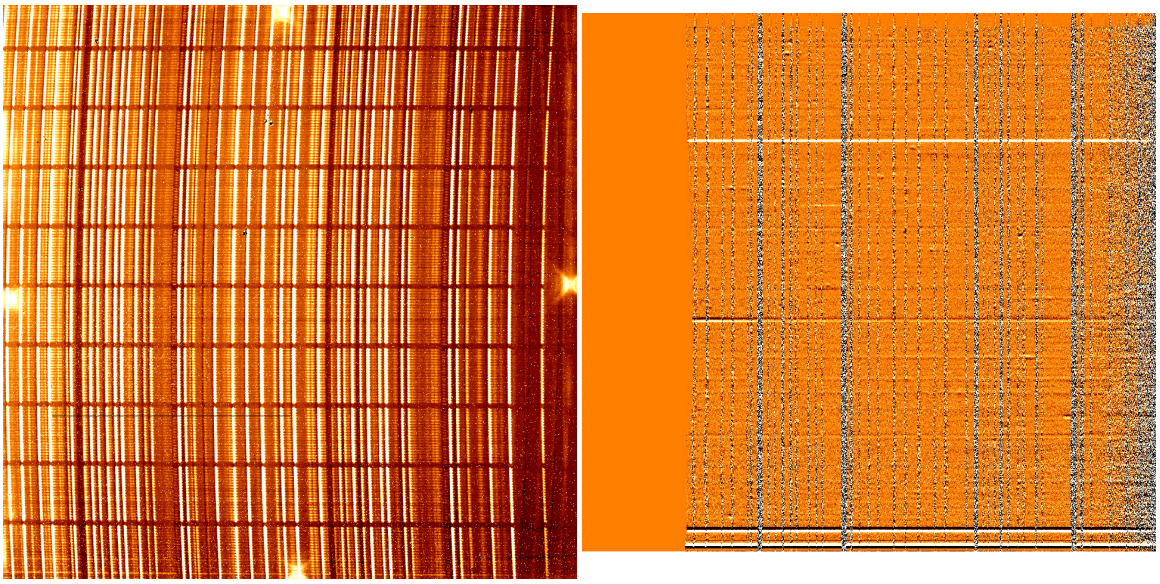

Figure 2.7: A single raw frame and the reduced frame from an observation on 14/03/2012 (UT).

from each fiber with a width of 9 pixels, then converted into a combined 1D spectral image. Then the frame is corrected for the spectral distortion (x-axis). Consequently, the slit pattern of the OH masks is straightened in the corrected image. The two-dimensional transformation, determined here, is applied for other frames as well. Figure 2.7 shows a raw science frame (left panel) where individual spectra from fibers are distorted.

The wavelength calibration is determined based on a set of known emission lines of the Th-Ar lamp. Using the distortion parameters obtained from the dome-flat image, the Th-Ar spectral images are converted to a combined 1D image. The relation between the observed wavelength and the pixels of each spectrum are determined with a cubic function. The typical calibration error of the spectra is less than 1 pixel, corresponding to $\simeq 1.2$ Å in the high-resolution mode.

Following the aforementioned preparatory process, the science frames are processed. In the cross-beam switching mode, the exposures are carried out following the ABAB nodding pattern of the telescope. Initially the sky background is removed in the $A - B$ subtraction. The $A - B$ sky subtraction is performed using two different sky images taken before and after the science exposure, i.e., $A_n - B_{n-1}$ and $A_n - B_n$ with a optimized weight to minimize the residual sky errors. For these sky-subtracted frames, the detector cross talk and bias difference between the quadrants are corrected. Then, the pixel-to-pixel variation is calibrated by using the detector-flat image. After the bad pixels are removed, the obtained image is corrected for the distortion by using parameters obtained from the dome-frat images. Then, the residual OH airglow emission lines are subtracted.

All frames from the entire exposure time are combined into a single averaged image, and a fine subtraction of the residual background and the bad pixel corrections are performed finally. Since each target is observed by two fibers in the CBS mode, the corresponding spectra of the positions A and B are combined.

Finally, we correct spectra for the atmospheric absorption features by using a flux calibration star, whose spectral type is known, observed in the science exposure. The wavelength is calibrated based on the pixel–wavelength relation obtained from the Th-Ar lamp image. In the HR mode, the pixel resolution is 1.25 Å/pix. The photon counts recorded by the imaging sensor is converted to the physical quantity (Jy) by using a conversion factor determined by the engineering observations.

After these processes have finished, we assessed the quality of observations by comparing

the photometric magnitudes and the observed flux densities of the targets. We select the flux calibration stars, which are need to be $J(\mathrm{AB}), H(\mathrm{AB}) = 15$–$18$, from those in the two Micron All Sky Survey and Sloan Digital Sky Survey Data Release 9. Some stars were observed optical-spectroscopically and their spectral types were determined. We use those preferentially. Some stars that we used, however, are not observed spectroscopically, hence we determined their spectral type based on published correlations between the optical–near-IR colors and the spectral types (Covey et al. 2007). The spectral types determined by this way are not accurate, but we confirmed that it is not critical for the finally reduced data.

Figure 2.7 (right panel) displays a reduced 2D frame, which combines all the frames from a 5 hr on-source integration. The final image is set to have 1920 pixels × 1800 pixels including 200 spectra with a width of 9 pixels for each. Examples of the flux calibrated 1D spectra of eight galaxies are displayed in Figure 2.8 with their 2D spectra. We overlay regions impacted by OH lines and indicate emission lines with positive detections.

2.5.2 Emission line measurement

We measure spectroscopic redshifts based on the presence of emission lines. In H-long spectra, we assume the strongest emission line is typically Hα due to the agreement with the photometric redshift. Prior to the emission line fitting, we inspect all the FMOS spectra using the graphical interface SpecPro (see Figure 2.9; Masters & Capak 2011). For each galaxy, a spectroscopic redshift is assigned manually by identifying emission lines based on both the one- and two-dimensional spectra. In the J-long spectra, the [O III]λ5007 is usually assumed to be the strongest in the case that there is no redshift information from the H-long spectrum. By using SpecPro, we mark positions of emission lines, and then the corresponding redshifts are used as a initial value for the fitting procedure described below.

We determine the strength of emission lines in the FMOS spectra by modeling the emission line profile with a Gaussian function. Prior to the line fitting, individual FMOS spectra are converted to a flux unit of erg cm^{-2} s^{-1} Å^{-1} from μJ. We run a fitting algorithm that utilizes the MPFIT package for IDL (Markwardt 2009) to measure the centroid, amplitude and full-width at half maximum (FWHM) and associated errors of each emission line (Hα and [NII]$\lambda\lambda$6583, 6548, Hβ and [OIII]$\lambda\lambda$5007, 4959). For individual spectra, the value of each pixel is weighted using the noise spectra, which are based on the pixel variance among frames. We define a weight function as follows,

$$W(\lambda) = \begin{cases} 1/N_\lambda^2(\lambda) & \text{(clean window)} \\ 0 & \text{(pixels impacted by OH)} \end{cases} \tag{2.1}$$

where $N_\lambda(\lambda)$ is an error spectra. To mitigate the impact of residual OH lines, pixels that are affected by the residual sky lines or the OH airglow masks are excluded from the fit. The removed pixels are identified in the noise spectra as regions with relatively higher noise as compared with the typical level of $\sim 5 \times 10^{-19}$ erg cm^{-2} s^{-1} A^{-1}. For each error spectrum, the threshold of the noise level is defined by tracing the typical noise level, in which the systematic enhancement of the noise level at the edges of the spectral window is taken into account (see Figure 2.10).

Each emission line is modeled by a Gaussian with the lower bound on the FWHM set to the spectral resolution of the instrument ($\sim$ 120 and 90 km s^{-1} for J-long and H-long, respectively). We fix the width of the [N II] lines to be equivalent to that of Hα, and the flux ratios [N II] λ6584/[N II] λ6548 to the theoretical value of 2.96 (Storey & Zeippen 2000). In the J-long spectra, the line widths of Hβ and [O III] are fixed to the same, and the ratio [O III]λ5007/[O III]λ4959 is 2.98. In Figures 2.10 and 2.11, we show an example spectrum with a best-fit model.

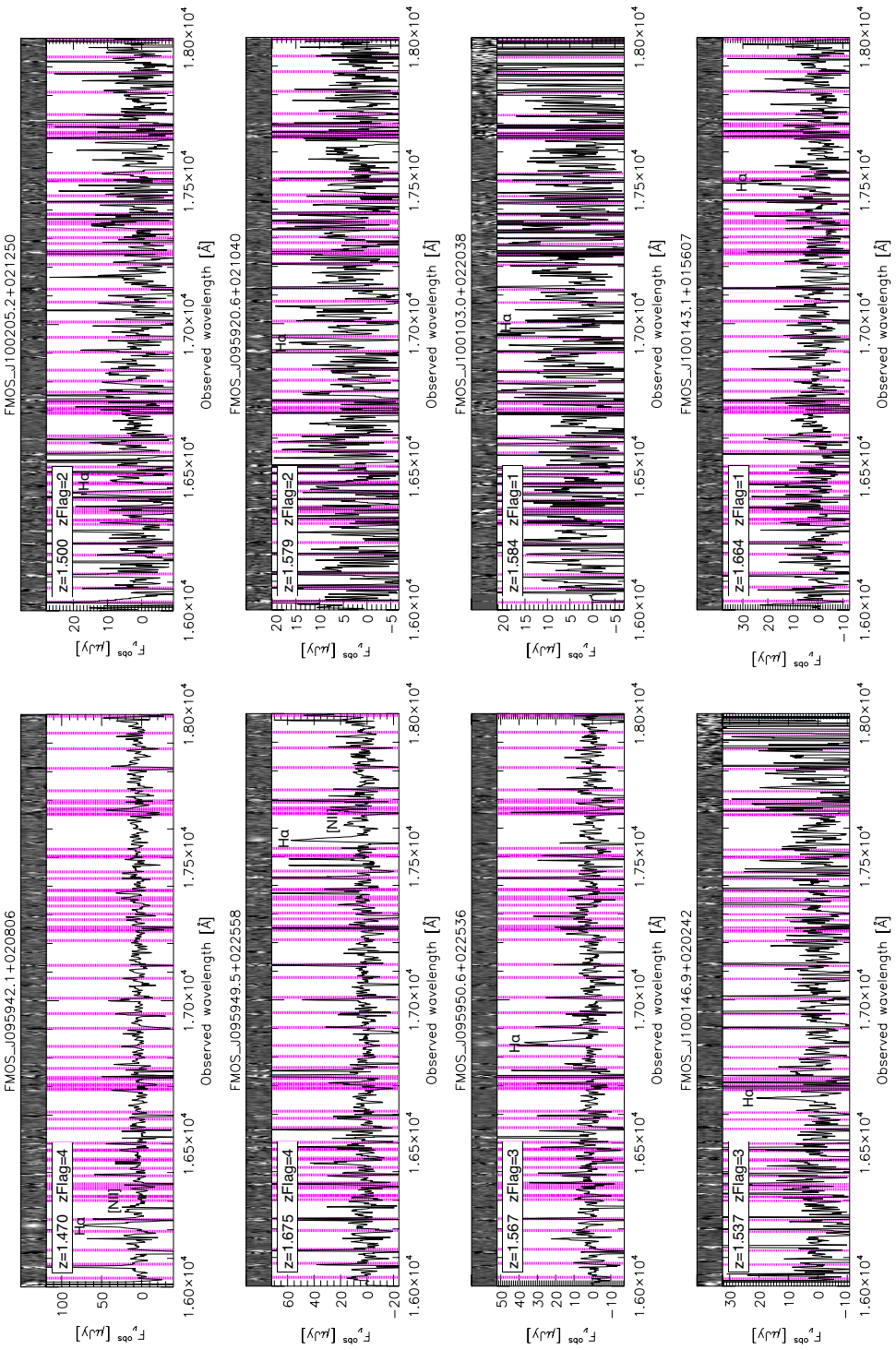

Figure 2.8: Examples of FMOS H-long spectra (1D and 2D). The Hα emission line used to measure the spectroscopic redshift is indicated. vertical bands mark the spectral regions impacted by OH lines. This figure appears in Silverman et al. (2015).

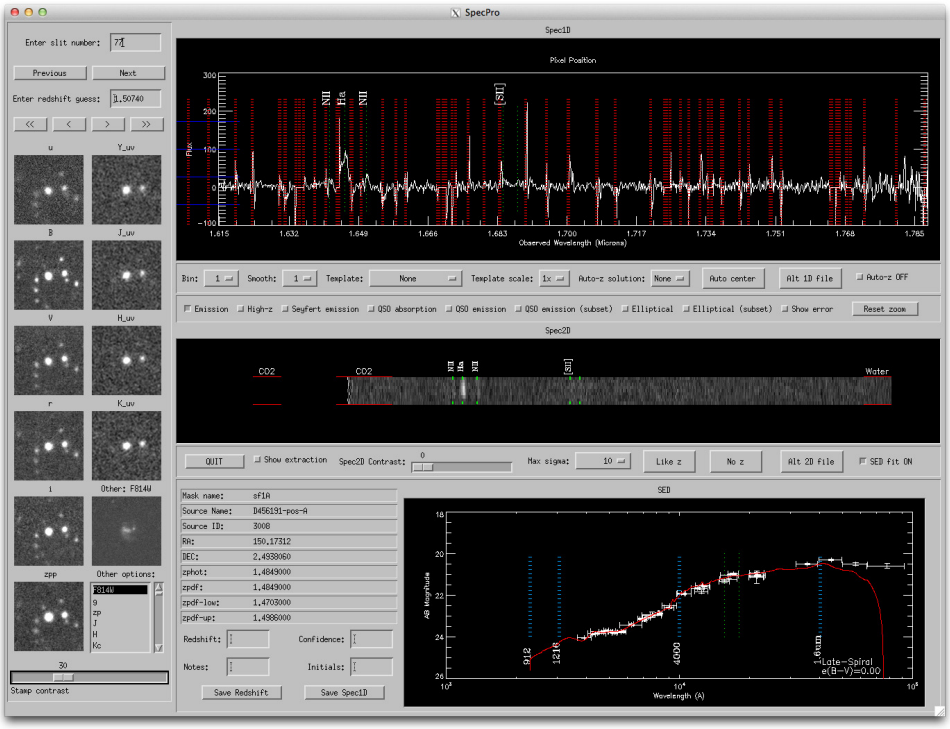

Figure 2.9: GUI of the SpecPro software, showing 1D (top panel) and 2D (middle panel) spectra of a single galaxy. Positions of the Hα, [N II], and [S II] lines are marked. The bottom frame displays the photometry data and predicted SED of the galaxy. Stamp images of the galaxy in multi-wavelength bands are shown on the left side.

2.5.3 Aperture correction

The emission line flux, measured on the observed spectra, arises from only the amount of photons falling within the aperture of the FMOS fiber of 1$''$.2-diameter. Therefore, it is necessary to correct for flux falling outside the fiber aperture to obtain the total intrinsic flux, thus to derive physical quantities such as SFR. The amount of aperture loss depends on the extended nature of the galaxy, and some observational factors that include variable seeing conditions and fiber positioning errors ($\sigma \sim 0''.2$; Kimura et al. 2010). With a typical size ($\sim 0''.5$) of our science sources and seeing condition of $\sim 1''$, the amount of flux falling outside the FMOS fiber is considerable ($\sim 50\%$ or more).

For each galaxy, the aperture correction is determined by estimating the fraction of the flux falling within the aperture towards the total flux. We use the *Hubble Space Telescope*/Advanced Camera for Surveys (ACS) $I_{\rm F814W}$-band images (Koekemoer et al. 2007) under the assumption that the rest-frame UV and Hα emission (i.e., HII regions) have the same spatial distribution (Mancini et al. 2011).

We smooth the ACS I-band image of galaxies in our sample by convolving with a Gaussian point-spread function of an effective seeing size as determined below. We then perform aperture photometry using SExtractor (Bertin & Arnouts 1996) to measure the total flux (FLUX_AUTO) and the aperture flux (within 1$''$.2 diameters; FLUX_APER) based on the original ACS images and smoothed images, respectively. Then, the correction factor is defined as $c_{\rm aper}$ = FLUX_AUTO/FLUX_APER. Figure 2.12 shows examples of the original and smoothed ACS images for ten galaxies in our sample. We see that some fraction of the total flux falls outside the FMOS fiber aperture under the typical seeing condition even if the intrinsic size of a galaxy is smaller than the size of the fiber aperture. For the majority of observed galaxies, the aperture correction can be determined, although not for some of them mainly due to blending with

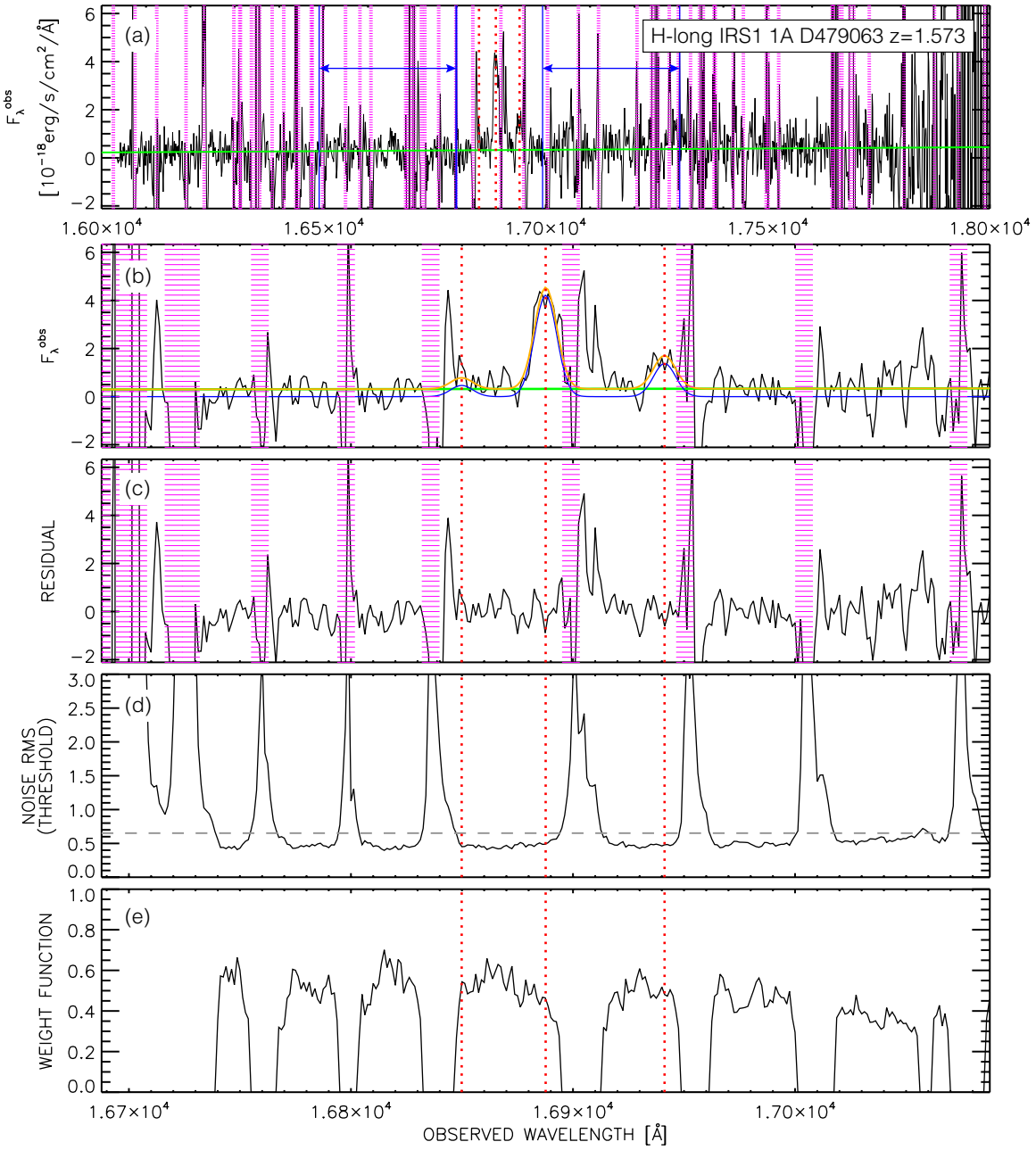

Figure 2.10: An H-long spectrum of a galaxy at $z = 1.573$ with a significant detection of Hα and [N II]λ6584 as indicated by vertical dotted lines (red). Individual panels are as follows: (a) entire observed spectrum with regions impacted by OH lines shown in magenta. Two blue arrows indicate the regions used to determine the continuum level by fitting a linear function shown in green. (b) Zoom-in of the observed spectrum centered on Hα. The overall fit to the spectrum is indicated in yellow with the components marked in green (continuum) and blue (emission lines). (c) Residual after subtracting the best-fit model of the spectrum. (d) Expected noise level and threshold (horizontal dashed line) for avoiding the wavelength range impacted by OH lines. (e) Weight function applied to each pixel for the spectral fitting. This figure is presented in Silverman et al. (2015).

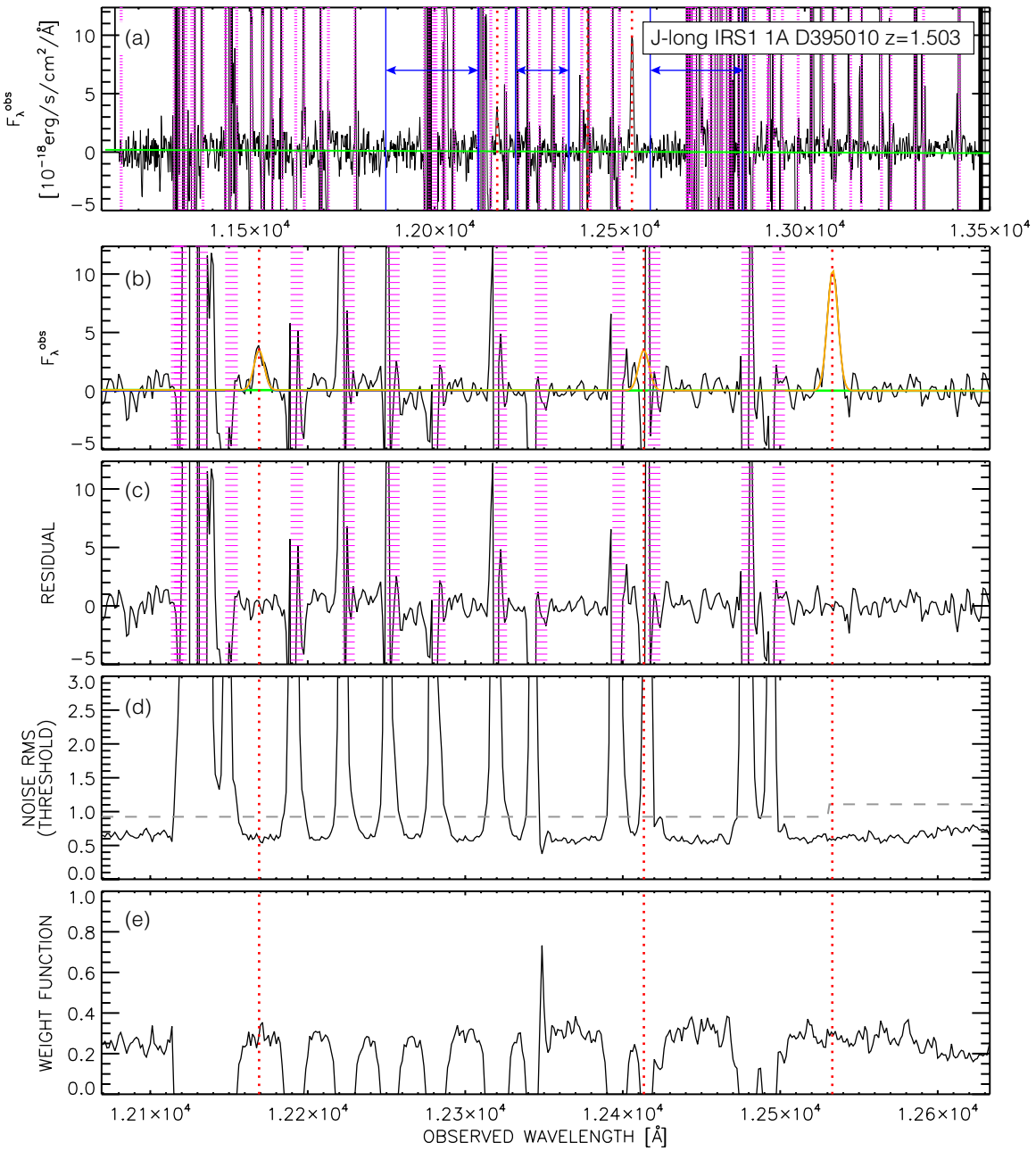

Figure 2.11: Fitting the Hβ and [O III]λ5007 emission lines in a J-long band spectrum of a galaxy at $z = 1.503$. Panels are equivalent to those shown in Figure 2.10. This figure is presented in Silverman et al. (2015).

foreground or background sources, locating close to the target object.

To determine the smoothing scale, i.e., the effective seeing, we use bright galaxies that have the continuum detected in the FMOS spectra. We compare the observed continuum flux and the Ultra-VISTA H and J-band photometry (McCracken et al. 2012) of each object. For this purpose, we use only galaxies for which the continuum is detected with FMOS at a $> 5\sigma$ significance and the magnitude of $H < 23$ (or $J < 23$ for the J-long observations). The continuum flux measured on the FMOS H-long (J-long) spectrum is converted to the broad band H (J)-band magnitude by using response curves for the Ultra-VISTA filters[2]. In practice, we construct sets of the ACS images convolved with different smoothing scales, then perform photometry to measure FLUX_APER to obtain a set of the correction factors for each seeing sizes. Next, we determine the best smoothing scale such that the corresponding set of $c_{\rm aper}$ minimize the systematic difference between the FMOS magnitude corrected by $c_{\rm aper}$ and the UVISTA magnitude. In Figure 2.13, we present the distribution of FMOS and UVISTA magnitudes for five different observations. It is apparent that there is considerable flux loss for all objects in each observation, and that the FMOS magnitudes are offset towards fainter magnitudes as compared to the UVISTA magnitude. In contrast, the FMOS magnitude corrected for the aperture loss is in good agreement with the UVISTA magnitude on average. We note that an effective seeing determined in this way is essentially an average of the seeing conditions over the duration of a full exposure, and also includes the effects of random fluctuation of the fiber positions during exposure.

We find the dispersion of the relation between the FMOS and UVISTA magnitudes to be $\sigma = 0.42$ (based on a Gaussian fit to the distribution of magnitude offsets), which corresponds to an uncertainty on the flux for an individual galaxy to be within a factor of 1.5. Once the effective seeing size is determined for a pointing, we derive the correction factors for all galaxies including faint ones, where the continuum is not detected in the FMOS spectrum. The resulting aperture correction factors are distributed in the $\sim$ 1.2–5 range, with a typical value of $\sim$ 2.2. The aperture corrections derived by this method are suitable for application to an entire sample that includes faint objects for studying the properties of the sample statistically. Meanwhile, it may be more accurate to correct the flux based on the direct comparison between the continuum magnitude from the FMOS spectrum and other photometry if one measures the properties of a single bright galaxy that have a significant detection of the continuum.

[2]http://www.eso.org/sci/facilities/paranal/instruments/vircam/inst.html

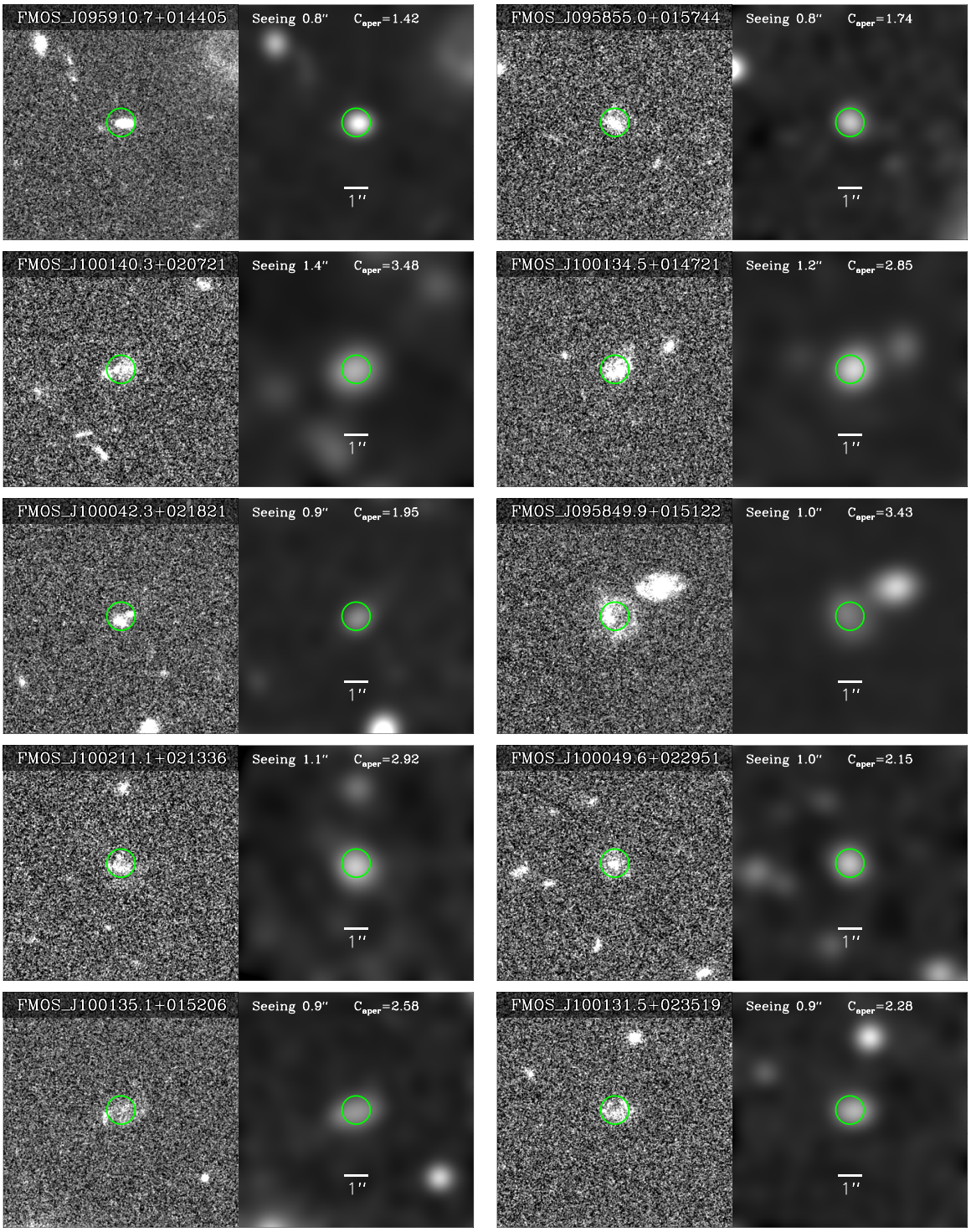

Figure 2.12: Examples of the *HST*/ACS images (left) and their smoothed images (right) for 10 galaxies in our sample. In each panel, the unique index of the galaxy, effective seeing of that observation (i.e., the smoothing kernel), and the aperture correction factor ($c_{\rm aper}$) is indicated. Green circles show the aperture of the FMOS fiber.

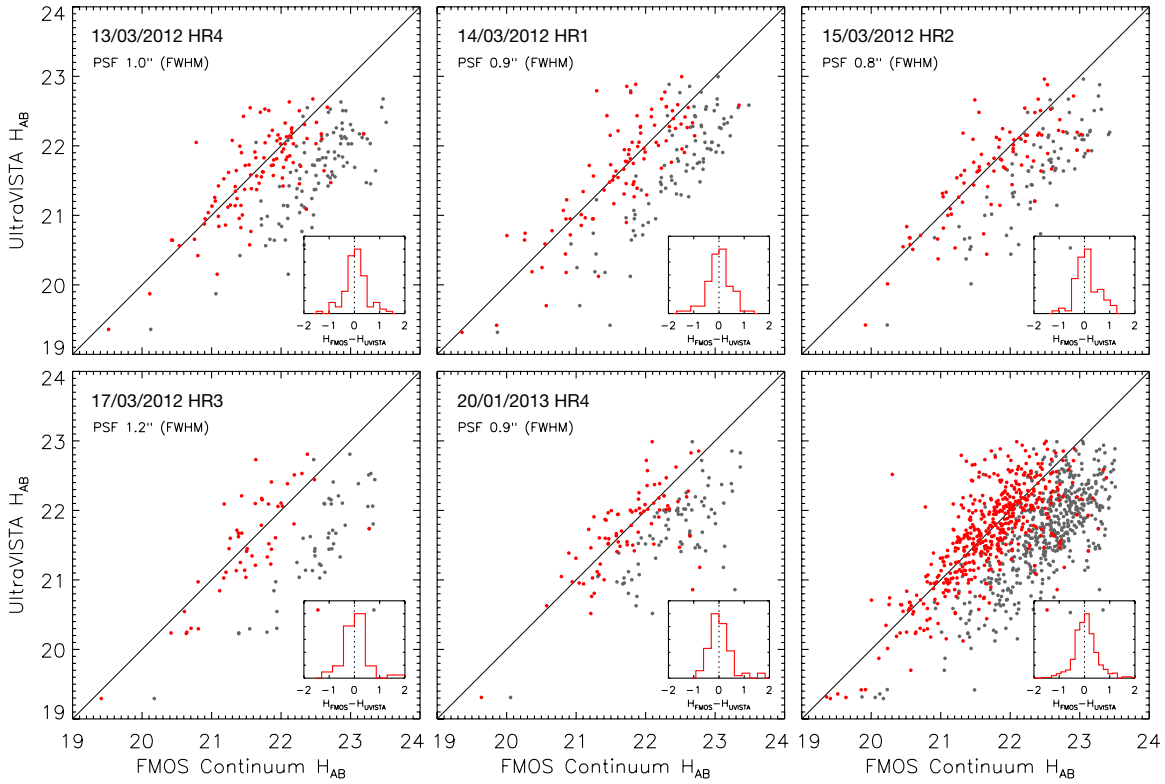

Figure 2.13: Comparison of continuum flux observed by FMOS with ground-based photometry (UltraVISTA) for five different H-long observations with varying effective seeing sizes. Circles indicate the comparison with (red) and without (gray) an aperture correction applied. In each panel, a histogram of the difference is shown. The bottom right panel shows the combined sample of seven observations. This figure is presented in Silverman et al. (2015).

Chapter 3

Hα-based star formation rates and dust extinction

3.1 Introduction

Direct measurements of stellar mass (M_*) and star formation rate (SFR) of galaxies at all redshifts provide essential information for our understanding of galaxy formation and evolution. A wide variety of SFR indicators are currently accessible through the exploitation of a broad range of the electromagnetic spectrum (see Kennicutt & Evans 2012, for a review). This has enabled us to establish, up to $z \sim 3$, that a tight correlation exists between these two quantities, with the bulk of star-forming galaxies clustering around a "main sequence" (MS) in the SFR$-M_*$ plane (e.g., Elbaz et al. 2007; Daddi et al. 2007; Noeske et al. 2007; Salim et al. 2007; Pannella et al. 2009; Karim et al. 2011; Whitaker et al. 2011; Zahid et al. 2012, and references therein). However, the MS slope and dispersion differ appreciably from one study to another, likely due to sample selection, adopted SFR indicator, extinction law, and the method used to measure stellar masses.

It is clear that evolutionary studies of the MS require consistency with redshift and, in particular, the use of a well-calibrated SFR indicator. In the Local Universe, the most accurate and extensively implemented SFR estimator is based on the Hα emission line luminosity as applied to large spectroscopic surveys such as the Sloan Digital Sky Survey (SDSS; Brinchmann et al. 2004). However, beyond a redshift of $z \sim 0.5$, Hα is redshifted to the near infrared and one has to rely on other SFR indicators, such as [O II]λ3727, mid-IR, UV luminosities or 1.4 GHz radio flux. The "bolometric" infrared luminosity (8$-$1000 μm) is another very powerful SFR indicator, but current Herschel data are not deep enough to fully map the MS, instead identifying and characterizing outlying *starburst* galaxies (Rodighiero et al. 2011).

Efforts have been made to detect Hα in the near-IR with narrow-band imaging or grism spectroscopy (e.g., Villar et al. 2008; Shim et al. 2009; Ly et al. 2011; Sobral et al. 2013). Recently, new ground-based near-IR instruments (Subaru/Fiber Multi-Object Spectrograph (FMOS), Keck/MOSFIRE, the Very Large Telescope (VLT) /KMOS) have acquired spectra for large samples of galaxies at $z > 0.5$, and detect the emission lines Hβ, [O III]λ4959, 5007, Hα, [N II]λ6548, 6583. In particular, Subaru/FMOS (Kimura et al. 2010), with its high multiplex and wide field-of-view, enables us to utilize the "local" SFR indicator, Hα, for galaxies at $0.5 \lesssim z \lesssim 1.8$. Previous studies with FMOS have been implemented in the low-resolution mode ($R \sim 600$; e.g., Yabe et al. 2012; Roseboom et al. 2012).

In this study, we have exploited the first opportunity to use FMOS in high-resolution mode ($R \sim 2600$) to detect Hα from galaxies in the COSMOS field at $1.4 \lesssim z \lesssim 1.7$ as offered by our "Intensive Program" (S12B-045, PI: J. Silverman). Throughout this work, we assume $H_0 = 70$ km s^{-1}, $\Omega_\Lambda = 0.75$, $\Omega_\mathrm{M} = 0.25$, AB magnitudes, and a Salpeter (1955) initial mass function (IMF).

3.2 Target selection, observations and analysis

Our sample is chosen to represent the star-forming galaxy population in the COSMOS field for which we can detect Hα. This is achieved by a selection based on stellar mass ($M_* > 10^{10}\ M_\odot$), photometric redshift ($1.4 \lesssim z_{\rm phot} \lesssim 1.7$), color ($B-z$, $z-K$) and predicted Hα flux (see below). These are sBzK-selected (Daddi et al. 2004) galaxies, from the catalog of McCracken et al. (2010), based on deep near-IR imaging from the Canada-France-Hawaii Telescope with $K_{\rm s} < 23$, and optical imaging (B_J, z^+) from the Subaru Suprime-Cam (Taniguchi et al. 2005) . Photometric redshift estimates are from Ilbert et al. (2009) based on photometry as described in Capak et al. (2007).

A critical component of our selection further depends on the SFRs and extinction properties that likely result in the detection of Hα with a flux greater than 4×10^{-17} erg cm^{-2} s^{-1}, the limit corresponding to a line detection with a significance greater than 3σ for integration times of 5 hr. SFRs are estimated from the rest-frame UV luminosity as derived from B_J photometry and corrected for reddening using the $B_J - z$ color (following Daddi et al. 2004, 2007). To estimate the expected Hα flux, following Calzetti et al. (2000) we use a multiplicative factor to compensate for the differential reddening between stars and line-emitting regions ($E_{\rm neb}\ (B-V) = E_{\rm star}\ (B-V)/0.44$). This relative reddening of stars and nebular regions is further addressed in §3.4.1 and §3.4.2. For this study, we isolate those galaxies with an error on $E_{\rm star}\ (B-V)$ less than 0.03 mag. We highlight that the imposition of a limit on the expected Hα flux, at the level given above, results in a sample of target galaxies having moderately higher SFRs and lower levels of extinction ($E_{\rm star}\ (B-V) \lesssim 0.5$).

In this study, we use a sample of 755 galaxies satisfying the above criteria observed during six nights in 2012 March and two nights in 2013 January. This sample is a subset of the full data set used later in the thesis. Spectroscopic redshifts are measured with a quality flag which describes the significance of the emission line as judged by eye in two-dimensional spectra. A flag of 2 is indicative of a strong line covering a number of contiguous pixels with both Hα and [N II]λ6583 seen is some cases. Emission lines with low signal-to-noise (S/N), whose reliability is questionable, are assigned a flag of 1. Of the 271 galaxies with spectroscopic redshifts, there are 168 with robust (flag = 2) line detections. We note that our failures (flag = 0) are likely due to either an Hα line being masked out by the OH suppression system, the true redshift being outside the observed wavelength interval, or Hα being extremely weak, possibly due to high extinction.

We acquired additional spectroscopy using the J-long grating to detect the Hβ (and [O III]λ5007) required to measure the Balmer decrement and correct for extinction. These observations were carried out in 2012 March, 2012 December and 2013 February through a cooperative effort with the University of Hawaii (PI: D. Sanders). In our sample, 182 galaxies have both H- and J-long coverage and 89 of them have a quality detection of Hα. While most individual spectra do not show a clear detection of Hβ, the emission line is highly significant in the mean spectra (see below).

3.3 Spectral analysis

3.3.1 Emission line fitting

We run a fitting algorithm to measure the flux and associated error of emission lines observed in the H (Hα and [N II]$\lambda\lambda$6583, 6548) and J (Hβ and [O III]$\lambda\lambda$5007, 4959) bands. See Chapter 2 for full details of the flux measurements and the corrections for the aperture effects.

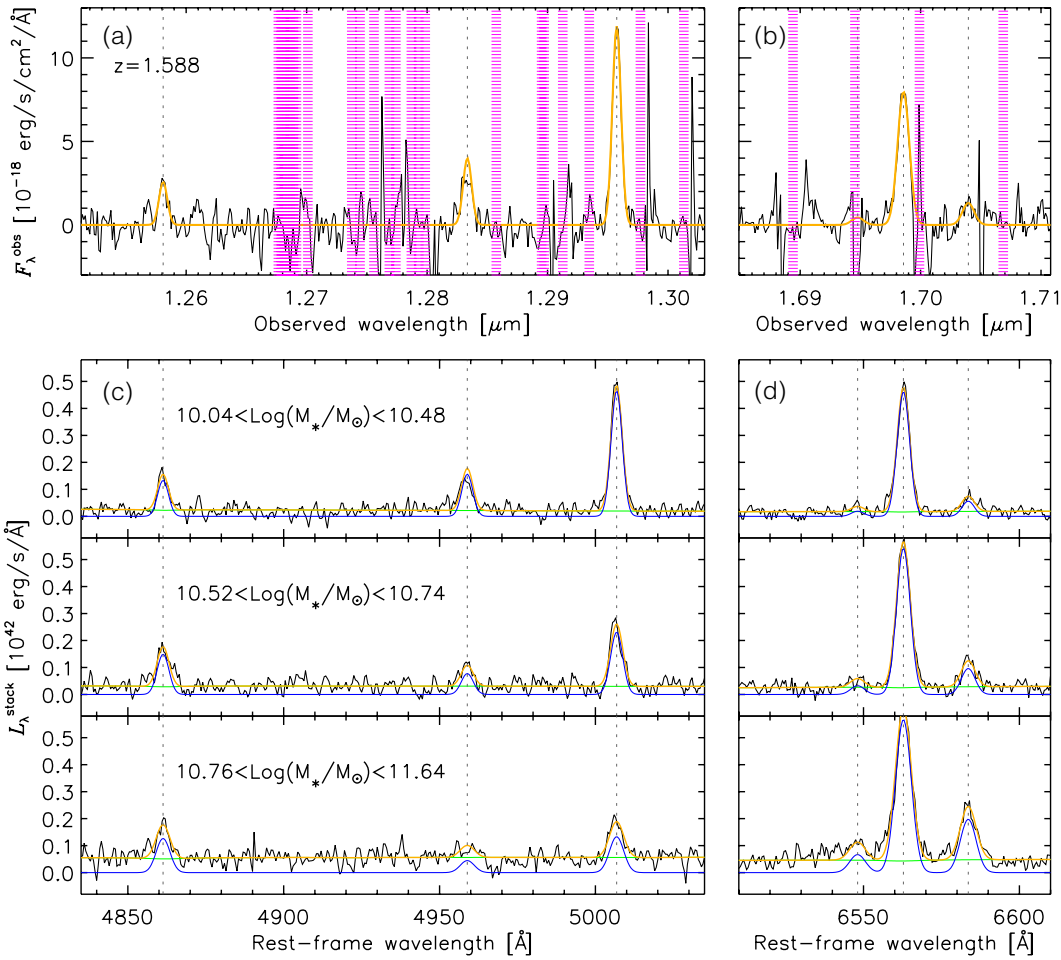

Figure 3.1: Top panels: example spectrum of a galaxy at $z = 1.588$ with strong emission lines detected using both the J-long ((a); Hβ, [O III]$\lambda\lambda$4959, 5007) and H-long ((b); Hα, [N II]$\lambda\lambda$6548, 6583) gratings. Spectral intervals effected by OH emission are shown (hatched regions). The emission line model is shown in yellow. Bottom panels: mean spectrum in three mass bins. Fits to the mean spectrum are indicated by the green (continuum), blue (emission lines), and yellow (total) curves.

3.3.2 Co-added spectra

Since our data do not permit an evaluation of the Balmer decrement for most individual galaxies, we measure the average ratio of Hα/Hβ as a function of both stellar mass and reddening $E_{\rm star}$ $(B-V)$. With 89 galaxies having both a quality Hα detection and a J-band spectrum, we split galaxies into three bins of mass or reddening and average their de-redshifted spectra. We perform a simple average using only pixels free of OH emission, without error weighting spectra to avoid biasing the stack toward lower extinction, typical of galaxies with high S/N line detections. In Figures 3.1 (c)–(d), we show the mean spectra binned by stellar mass.

3.4 Results

3.4.1 Balmer decrement as a dust extinction probe

To achieve an intrinsic Hα luminosity used for determining an extinction-free SFR, we must assess the level of attenuation. Throughout our analysis, we assume the applicability of the Calzetti et al. (2000) extinction law ($R_V \equiv A_V/E(B-V) = 4.05$, $k_{\rm H\alpha} = 3.325$, $k_{\rm H\beta} = 4.598$, $k_{1500} = 10.33$). The Balmer decrements Hα/Hβ have been widely used to quantify the reddening in not

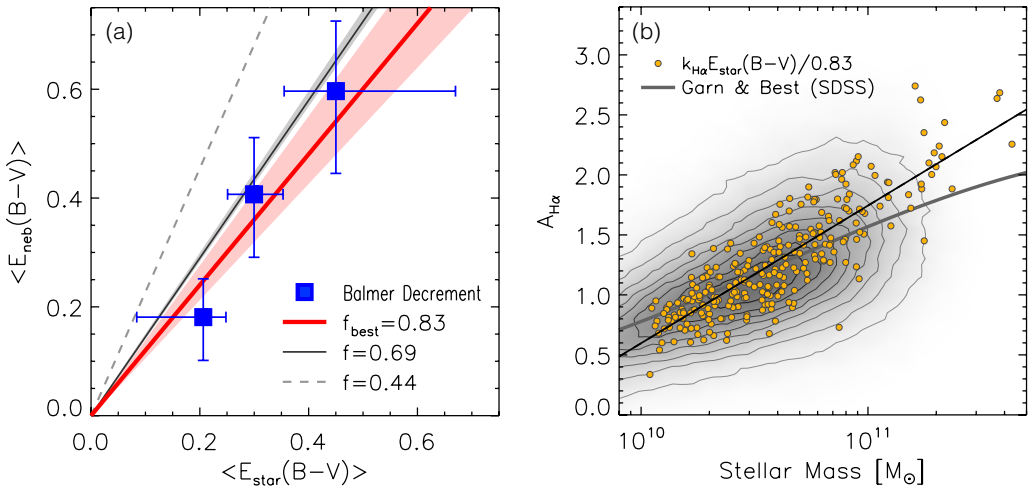

Figure 3.2: (a) $\langle E_{\rm neb}\ (B-V)\rangle$ vs. $\langle E_{\rm star}\ (B-V)\rangle$. Filled squares indicate the results from our co-added spectra with a best-fit relation (thick red line). The vertical bars show the 1σ errors while the horizontal bars indicate the bin size in $E_{\rm star}\ (B-V)$. The shaded area shows the errors on the fit. (b) $A_{\rm H\alpha}$ vs. M_*: yellow circles represent the values of $k_{\rm H\alpha}E_{\rm star}\ (B-V)/0.83$ for FMOS galaxies with a best-fit line (thin solid line). The contours in gray scale show the distribution of $\sim 191,600$ SDSS galaxies with the best-fit (thick gray line).

only local but higher (up to $z \sim 1.5$) redshift galaxies (e.g., Ly et al. 2012; Domínguez et al. 2013; Momcheva et al. 2013):

$$E_{\rm neb}\,(B-V) = \frac{2.5}{k_{\rm H\beta} - k_{\rm H\alpha}} \log\left[\frac{\rm H\alpha/H\beta}{2.86}\right], \tag{3.1}$$

which is applicable for the interstellar medium under the assumption of case B recombination with a gas temperature $T = 10^4$ K and an electron density $n_{\rm e} = 10^2$ cm^{-3}. While we have a measure of the color excess $E_{\rm star}\ (B-V)$ based on the observed $B_J - z$ color for each galaxy (see Daddi et al. 2007), we need to establish whether this information can be used to accurately assess the extinction affecting the nebular emission. Our aim is to establish a method to apply an extinction correction for individual Hα-detected galaxies lacking the detection of Hβ.

Calzetti et al. (2000) formulated the empirical relation $E_{\rm neb}\ (B-V) = E_{\rm star}\ (B-V)/f$ with $f = 0.44$ by studying a sample of low-redshift starburst galaxies (see also Moustakas & Kennicutt 2006). However, it is not established whether this conversion factor is applicable for star-forming galaxies at higher redshifts. While some studies at high-z support the validity of this relation (Förster Schreiber et al. 2009; Wuyts et al. 2011; Mancini et al. 2011), Reddy et al. (2010) argue that such excess reddening for nebular emission may not be needed for UV-selected galaxies at $z \sim 2$ (see also Onodera et al. 2010; Price et al. 2014; Koyama et al. 2015, for a similar conclusion). Values of the f factor larger than 0.44 are also favored in a recent *Herschel* study (Pannella et al. 2015). Rather than being dependent on redshift, this factor may be related to specific SFR (see Equations (15) and (16) of Wild et al. 2011).

For this exercise, we resort to using stacked spectra, as described in §3.3.2. We specifically measure $\langle E_{\rm neb}\ (B-V)\rangle$ in three bins of $E_{\rm star}\ (B-V)$. The measured Balmer line fluxes require a correction for the underlying stellar absorption, which we assume to be $\mathrm{EW}_{\rm abs}^{\rm H\beta} = 2.0$, $\mathrm{EW}_{\rm abs}^{\rm H\alpha} = 1.8$ (Nakamura et al. 2004). The stellar absorption impacts the Hβ luminosity at the $\lesssim 10\%$ level while this is less for Hα ($\lesssim 2\%$). As shown in Figure 3.2 (a), the nebular extinction $\langle E_{\rm neb}\ (B-V)\rangle$ ranges from 0.1 to 0.7 that corresponds to $0.7 \lesssim A_{\rm H\alpha} \lesssim 2$. Furthermore, there is a clear correspondence between the nebular and stellar extinction that can be fit with a linear relation characterized by $f = 0.83 \pm 0.10$, a factor that is dissimilar to the canonical value of 0.44

and is consistent within the errors with an extrapolation of the relation from Wild et al. (2011) .

In Figure 2 (b), we compare the levels of extinction of FMOS and low-redshift galaxies, i.e., $A_{\mathrm{H}\alpha}$ (at a given stellar mass) as derived from the individual values of E_{star} $(B-V)$ for each galaxy and modified by our new factor $f = 0.83$. Star-forming galaxies at $z \sim 0.1$ from SDSS DR9 are indicated with stellar masses provided by MPA-JHU and the best-fit relation of Garn & Best (2010). While showing very good agreement between the two samples at the low-mass end ($M_* \lesssim 6 \times 10^{10}\ M_\odot$), the FMOS sample is elevated from the best-fit relation of SDSS galaxies at higher masses. This is in slight disagreement with results from Sobral et al. (2012) at $z = 1.47$, who implemented a hybrid approach using [O II]/Hα calibrated against the Balmer decrement of low-redshift galaxies. This inconsistency may not be surprising since the use of the [O II]/Hα ratio as an indicator of dust attenuation is questionable, given that the gas-phase metallicity and the ionization parameter can also affect this ratio. However, we cannot definitely rule out agreement with both of these studies due to the uncertainties of our extinction corrections. A best-fit relation to the FMOS data (small yellow circles in Figure 3.2 (b)) can be expressed as follows:

$$A_{\mathrm{H}\alpha} = (0.60\pm0.03) + (1.15\pm0.04)\log\left[\frac{M_*}{10^{10}M_\odot}\right]. \tag{3.2}$$

In Table 3.1, we list our measurements based on our line-fitting routine and provide the derived measure of extinction in bins of E_{star} $(B-V)$ and stellar mass.

Table 3.1: Measurements Based on Co-added Spectra.

No. of	Color Excess Bin			$L_{\mathrm{obs}}^{\mathrm{stack}}$ (10^{42} erg s^{-1})		EW (Å)		Color Excess
Spectra	Min	$\langle E_{\mathrm{star}}\ (B-V)\rangle$	Max	Hα	Hβ	Hα	Hβ	$E_{\mathrm{neb}}\ (B-V)$
30	0.084	0.2063	0.248	2.891 ± 0.085	0.818 ± 0.059	124 ± 4	28 ± 2	0.18 ± 0.08
29	0.251	0.2997	0.353	2.651 ± 0.087	0.576 ± 0.068	100 ± 4	18 ± 2	0.41 ± 0.11
30	0.355	0.4501	0.670	3.341 ± 0.120	0.581 ± 0.090	77 ± 3	11 ± 2	0.60 ± 0.14
No. of	Stellar Mass Bin			$L_{\mathrm{obs}}^{\mathrm{stack}}$ (10^{42} erg s^{-1})		EW (Å)		Attenuation
Spectra	M_*^{min}	$\langle M_*\rangle$	M_*^{max}	Hα	Hβ	Hα	Hβ	$A_{\mathrm{H}\alpha}$
30	10.039	10.281	10.477	2.312 ± 0.067	0.583 ± 0.051	127 ± 5	23 ± 2	0.93 ± 0.28
29	10.521	10.611	10.739	2.999 ± 0.090	0.709 ± 0.080	107 ± 4	22 ± 3	1.11 ± 0.34
30	10.761	11.025	11.635	3.604 ± 0.122	0.701 ± 0.095	76 ± 3	13 ± 2	1.66 ± 0.41

3.4.2 Comparing Hα- and UV-based SFR indicators

We now compare the SFRs derived from Hα and from UV, assuming that both intrinsic SFRs are the same and then determine what level of extinction (as parameterized by our factor f) is needed to match the observed values. In Figure 3.3, we plot the ratio $\mathrm{SFR}_{\mathrm{H}\alpha}^{\mathrm{uncorr}}/\mathrm{SFR}_{\mathrm{UV}}^{\mathrm{uncorr}}$ for our quality (flag = 2) sample as a function of E_{star} $(B-V)$. SFRs are derived from the Hα luminosity using Equation (2) of Kennicutt (1998) or from the UV luminosity using Equation (7) of Daddi et al. (2007);

$$\mathrm{SFR}_{\mathrm{H}\alpha}(\mathrm{M}_\odot\ \mathrm{yr}^{-1}) = 7.9\times10^{-42}\times L_{\mathrm{H}\alpha}\ (\mathrm{erg\ s}^{-1}), \tag{3.3}$$

$$\mathrm{SFR}_{\mathrm{UV}}(\mathrm{M}_\odot\ \mathrm{yr}^{-1}) = L_{1500}\ (\mathrm{erg\ s}^{-1}\ \mathrm{Hz}^{-1})/8.85\times10^{-27}. \tag{3.4}$$

We see a clear correlation between this ratio and the reddening thus we can express the ratio of the observed SFRs in terms of both E_{star} $(B-V)$ and a specific value of f as follows,

$$\mathrm{SFR}_{\mathrm{H}\alpha}^{\mathrm{uncorr}}/\mathrm{SFR}_{\mathrm{UV}}^{\mathrm{uncorr}} = \ 10^{-0.4E_{\mathrm{star}}\ (B-V)(3.33/f-10.3)}. \tag{3.5}$$

It is apparent that our data clearly falls well above the line representing the case where $f = 0.44$. While the $f = 0.83$ case as determined from the Balmer decrement is more closely aligned with

the observed data than the canonical value, we find that a best-fit of Equation (3.5) to the data yields a value of $f = 0.69 \pm 0.02$. This best-fit value of f is specific to the present sample, the procedures adopted to estimate the SFRs and assumed extinction law. Based on the limitations of the current data set, we conclude that the value of f likely lies between 0.69 and 0.83. For subsequent analysis, we average the results of the two approaches to arrive at a factor $f = 0.76$.

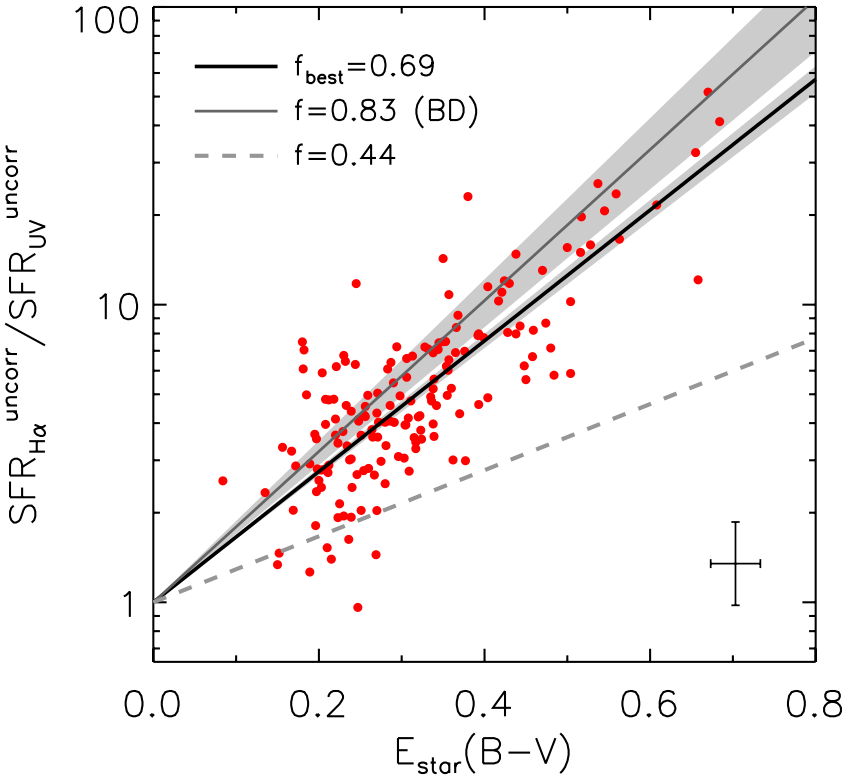

Figure 3.3: Ratio of observed (not corrected for extinction) Hα- to UV-based SFRs as a function of $E_{\rm star}\,(B-V)$. The typical errors are shown in the lower right corner. Lines show the relations with different values of f as labeled.

3.4.3 Star-forming main sequence at $z \sim 1.6$

We derive SFRs from extinction-corrected Hα luminosities based on the color excess for each galaxy modified for nebular emission using $f = 0.76$. In Figure 3.4, SFRs are shown to cover a range of $\sim 10{-}500\ M_\odot\ {\rm yr}^{-1}$ typical for star-forming galaxies at these redshifts, and exhibit a close relation with stellar mass as described in the literature as the "main sequence". A fit to all Hα detections (flag = 1 and 2) yields the following relation:

$$\log {\rm SFR} = (1.25 \pm 0.03) + (0.81 \pm 0.04) \log \left[\frac{M_*}{10^{10} M_\odot}\right]. \tag{3.6}$$

This relation has a very similar normalization and slope as compared to related studies at high redshifts (e.g., Daddi et al. 2007; Wuyts et al. 2011). We recognize that the slope may be biased low due to the sensitivity limit of our survey (SFR $\simeq 10\ M_\odot\ {\rm yr}^{-1}$; see § 3.2); such a bias is typical of spectroscopic samples that are more likely to measure a redshift if the SFR is above the average near the low-mass limit of the survey. The slope is also dependent on the adopted extinction law.

We measure the width of the MS to be $\sigma_{\rm MS} \sim 0.22$ dex, somewhat lower than typically reported values ($\sim$ 0.25–0.3 dex). Such comparisons are not trivial since the observed width

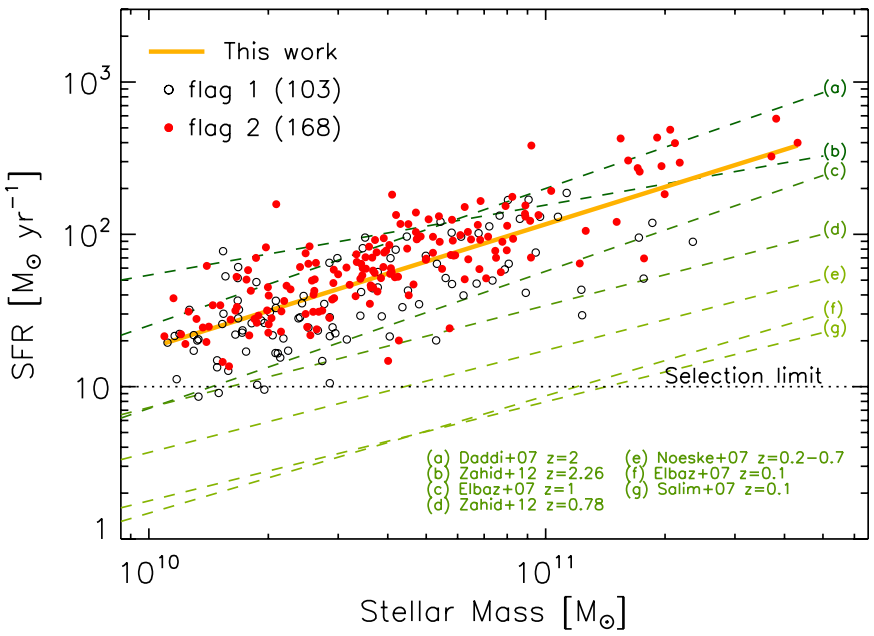

Figure 3.4: SFR vs. M_*. FMOS galaxies with flag 2 (1) are indicated by the filled (open) circles with a best-fit (yellow solid line). Our selection limit is shown by the dotted line. Additional lines show the MS from other published studies.

is dependent on various factors such as the redshift range considered, the imposed selection on expected Hα flux, the impact of redshift failures, and variations in dust extinction not properly accounted for. Indeed, Silverman et al. (2015) report that the dispersion in the SED-based SFRs is reduced by a factor of 1.4 due to a limit on the expected Hα flux (4×10^{-17} erg s^{-1} cm^{-2}). On the other hand, it may be that a tighter sequence is realized when employing a more accurate SFR indicator, namely, Hα in our case.

3.5 Conclusions

In this Chapter, we present the first results based on the early data from the FMOS-COSMOS survey to measure the SFRs based on the Hα emission line and establish the relation between the SFR and the stellar mass. This has entailed a detailed study of the extinction properties of our sample, based both on measurements of the Balmer decrement in bins of color excess (stellar) and stellar mass, and a comparison of Hα and UV-based SFR indicators. Due to the complex selection of our sample and success rate of emission line detection, our results pertain to a specific subset of the overall high-redshift galaxy population, and are as follows:

1. The extinction $A_{\mathrm{H}\alpha}$ ranges between ~ 0.6 and ~ 2.5, as measured from the Balmer decrement, and appears to exceed the corresponding values for low-redshift galaxies in SDSS at $M_* \gtrsim 6 \times 10^{10}\ M_\odot$.

2. The relation between the nebular and stellar extinction is determined to be $E_{\mathrm{neb}}\ (B-V) = E_{\mathrm{star}}\ (B-V)/f$ where f is between 0.69 and 0.83. This differs from the canonical factor ($f = 0.44$) and may indicate a more uniform dust distribution in high-z galaxies as compared to local galaxies. This also suggests that hot, massive stars and H II regions are spatially correlated more tightly in high redshift galaxies.

3. A SFR$-M_*$ relation based on Hα luminosity, corrected for extinction, shows a clear correspondence between these two parameters with a slope of 0.81, a width of 0.22 dex, and a

normalization 10–20 times elevated from the local relation that is in close agreement with related high-z studies.

The higher levels of extinction seen in our sample may be a consequence of both gas masses and SFRs being typically $\sim 10\times$ higher (e.g., Daddi et al. 2010), in galaxies at $z \sim 1.6$ as compared to local counterparts. Nonetheless, we may expect some modulation of the extinction due to the lower metallicities typically seen in high-redshift galaxies, which was first noted by Hayashi et al. (2009) for a sBzK-selected sample (see also Erb et al. 2006; Yabe et al. 2012). To conclude, we highlight that a larger sample with spectroscopic coverage of Hβ will improve the signal-to-noise ratio of stacked spectra and average Balmer decrements, while detections of individual galaxies will give the dispersion in extinction at a given mass, thus lessening biases inherent in the current sample.

Chapter 4

Excitation state and chemical enrichment

4.1 Introduction

The physical conditions of the interstellar medium (ISM) provide clues to understanding the current state and past activity of star formation and gas reprocessing in galaxies. Numerous efforts to study the ISM in low-redshift galaxies ($z \lesssim 0.3$) are based on large spectroscopic data such as the Sloan Digital Sky Survey (e.g., Kauffmann et al. 2003b; Tremonti et al. 2004; Brinchmann et al. 2004). A wide variety of empirical diagnostics of the gas properties have been established, especially based on spectral emission lines in the rest-frame optical window.

The Baldwin-Philips-Terlevich (BPT; Baldwin et al. 1981; Veilleux & Osterbrock 1987) diagnostic diagram has been used to distinguish star-forming galaxies from those hosting and/or dominated by an AGN (see §1.5). A large data set from SDSS has shown that local star-forming galaxies cluster around a relative tight relation between the line ratios [N II]/Hα and [O III]/Hβ (e.g., Kauffmann et al. 2003b), which is referred to as the *abundance sequence*, and established a clean classification of these populations (e.g., Kauffmann et al. 2003b; Kewley et al. 2006; Stasińska et al. 2006; Lara-López et al. 2010a). Over the last decade, the universality of the abundance sequence of high-redshift galaxies has been examined through near-infrared spectroscopic campaigns. Early studies have reported an offset of the distribution of star-forming galaxies at high redshifts ($z \sim 1$–3) from the local abundance sequence based on relatively small samples (e.g., Shapley et al. 2005; Erb et al. 2006; Liu et al. 2008). More recent, the offset has been reproduced using larger samples (e.g., Steidel et al. 2014; Shapley et al. 2015; Hayashi et al. 2015) observed with multi-object near-infrared spectrographs. This offset likely reflects more extreme conditions of H II gas in high-z galaxies. Various mechanisms have been suggested to explain the offset in the BPT diagram, with some relating to the properties of the ionizing radiation field such as having a larger ionization parameter (Kewley et al. 2015) or a harder radiation field inferred by their high star formation and/or presence of metal-poor stars (Steidel et al. 2014). Alternative explanations are an enhancement of the nitrogen-to-oxygen abundance ratio and high gas pressure (e.g., Masters et al. 2014). However, such an offset for high redshift galaxies on the BPT diagram has not firmly been established across the general star-forming population since their location can be significantly affected by sample selection (see Juneau et al. 2014; Shapley et al. 2015). Recently, the luminosity dependence of the location of the BPT sequence has been studied (e.g., Cowie et al. 2016).

The gas-phase metallicity (hereafter metallicity) is one of the most important probes of galaxy evolution to trace past star formation history. The abundance of heavy elements is further influenced by both inflowing gas that dilutes the metal fraction of the ISM, and outflows that transpose metals into the circumgalactic environment (e.g., Köppen & Edmunds 1999; Dalcanton 2007; Ellison et al. 2008; Erb 2008; Finlator & Davé 2008; Mannucci et al. 2010; Cresci et al. 2010; Peeples & Shankar 2011; Bouché et al. 2012; Lilly et al. 2013). In the Local Universe, a correlation between stellar mass and metallicity has been robustly established based on large

data (e.g., Tremonti et al. 2004; Andrews & Martini 2013; Zahid et al. 2011). The existence of a mass–metallicity (MZ) relation has been extended up to $z \sim 3$ or more (e.g., Erb et al. 2006; Maiolino et al. 2008; Yabe et al. 2012, 2014, 2015; Zahid et al. 2014a,b; Wuyts et al. 2014; Maier et al. 2014, 2015; Sanders et al. 2015) with an evolution where the metallicity decreases with redshift at a fixed stellar mass. However there still remains some discrepancies between various studies that implement different sample selection methods and/or metallicity determinations.

An anti-correlation between metallicity and SFR at a fixed stellar mass has been seen in local galaxies (e.g., Ellison et al. 2008). In particular, Mannucci et al. (2010) introduced SFR into the MZ relation as the third parameter, and proposed a relation between those three quantities, referred to as the *Fundamental Metallicity Relation* (FMR). Although its actual shape has not been completely established yet due to the difference in sample selection or in adopted metallicity indicators from one study to another, a number of studies have found that introducing SFR reduces the scatter in the MZ relation (Lara-López et al. 2010b, 2013; Mannucci et al. 2011; Yates et al. 2012; Andrews & Martini 2013; Zahid et al. 2014b). This trend indicates that upward fluctuations of the infall rate of pristine/metal-poor gas would boost new star formation, while diluting the oxygen abundance of the ISM (Ellison et al. 2008; Mannucci et al. 2010), as supported by several analytic works and numerical simulations (e.g., Davé et al. 2012; Dayal et al. 2013; Lilly et al. 2013). Measuring the M_*-Z-SFR relation at all redshifts is essential to constrain the model of galactic star formation and chemical evolution. Beyond the Local Universe, however, the dependence of SFR of the MZ relation has not been established yet (see e.g., Wuyts et al. 2014; Zahid et al. 2014b; Yabe et al. 2014; Steidel et al. 2014; Salim et al. 2015; Guo et al. 2016b).

To further understand the typical characteristics of high-z H II regions, it is highly desirable to construct a well-controlled sample that represents typical star-forming galaxies at each epoch. With the availability of multi-object near-infrared spectrographs (i.e., MOSFIRE, FMOS, KMOS) on large telescopes, we can access key rest-frame optical emission lines such as Hβ, [O III]λ5007, Hα, [N II]λ6584, and [S II]$\lambda\lambda$6717, 6731 for samples consisting of up to 10^3 galaxies at $z \gtrsim 1$ (e.g., Rudie et al. 2012; Tonegawa et al. 2015; Kriek et al. 2015). We construct a large sample of Hα-detected galaxies that trace the star-forming main sequence over a stellar mass range $10^{9.6} \lesssim M_*/M_\odot \lesssim 10^{11.6}$ from the FMOS-COSMOS survey to study the typical properties of H II regions of galaxies at $1.43 \leq z \leq 1.74$. We use the rest-frame optical key emission lines to evaluate the excitation state, gaseous metallicity, and electron density of H II gas while minimizing the impact of AGNs.

This Chapter is organized as follows. In §4.2, we describe our samples and spectral analysis. We present our results in §4.3, and discuss the physical origins of high excitation seen in high-z star-forming galaxies in §4.4. In §4.5, we provide an assessment of the effect of AGNs based on our stacking analysis of *Chandra* X-ray images. We present a reanalysis of the metallicity measurements of our sample in §4.6. In §4.7, we study the relation between mass, metallicity, and SFR. We finally summarize our results and implications in §4.8. Throughout this Chapter, we use a cosmology with $(h, \Omega_M, \Omega_\Lambda) = (0.7, 0.3, 0.7)$ and assume the Salpeter (1955) initial mass function (IMF; 0.1–100 $M_\odot$). All magnitudes are given in the AB magnitude system.

4.2 Data

4.2.1 Target selection

In this Chapter, we utilize a larger catalog of galaxies with spectroscopic redshifts from the FMOS-COSMOS survey than presented in Chapter 3. The larger sample is the result of additional FMOS observations carried out with the same setup described Silverman et al. (2015) in between December 2013 and February 2014. The characteristics of this sample are statistically

equivalent to those used in our previous studies (Kashino et al. 2013; Zahid et al. 2014b; Silverman et al. 2015). The survey area is 0.81 deg^2, covered by four FMOS footprints (HR1–HR4) listed in Table 2.2. The observing runs, reported in this study, are listed in Table 4.1. Note that we include observations of outer footprints (HR1E–HR3E, Table 2.2), but only galaxies within the overlap regions with the central four footprints are used in this study.

Table 4.1: Summary of the observations

Data (UT)	Proposal ID	Pointing	Grating
2012 Mar 13	UH-B3	HR4	H-long
2012 Mar 14	S12A-096	HR1	H-long
2012 Mar 15	S12A-096	HR2	H-long
2012 Mar 16	S12A-096	HR1	H-long
2012 Mar 17	S12A-096	HR3	H-long
2012 Mar 19	S12A-096	HR1	J-long
2012 Dec 29	UH-B5	HR2	J-long
2013 Jan 19	UH-18A	HR3	H-long
2013 Jan 20	S12B-045I	HR4	H-long
2013 Jan 21	S12B-045I	HR3	J-long
2013 Jan 22	S12B-045I	HR4	J-long
2013 Jan 20	S12B-045I	HR4	H-long
2013 Jan 21	S12B-045I	HR3	J-long
2013 Dec 29	S12B-045I	HR2	H-long
2014 Jan 22	UH-11A	HR1E	H-long
2014 Jan 24	UH-11A	HR2E	H-long
2014 Jan 25	UH-11A	HR3	H-long
2014 Jan 26	S12B-045I	HR1	H-long
2014 Jan 27	S12B-045I	HR4	H-long
2014 Feb 08	S12B-045I	HR1	J-long
2014 Feb 09	S12B-045I	HR4	J-long
2014 Feb 10	S12B-045I	HR4	J-long
2014 Feb 11	UH-38A	HR3E	H-long

Our sample of galaxies is based on the COSMOS photometric catalog (McCracken et al. 2012; Ilbert et al. 2013) that includes the Ultra-VISTA/VIRCAM photometry, and an imposed magnitude limit of $K_S < 23.5$. This K_S-band limit provides a high stellar mass completeness ($\sim 85\%$) of galaxies with 10^{10} $10^{10} M_\odot$ (Ilbert et al. 2013). The majority of our sample is selected to have a stellar mass above $10^{9.8}$ $M_\odot$ and a photometric redshift between 1.46 and 1.72. These values are derived for each object by fitting spectral energy distribution (SED) using the LePhare code (Arnouts & Ilbert 2011) with population synthesis models (Bruzual & Charlot 2003) and a Chabrier (2003) IMF. Hereafter, we convert all stellar masses to a Salpeter (1955) IMF by applying a multiplicative factor of 1.7 (Ilbert et al. 2010).

To achieve a high success rate of detecting the Hα emission line, we calculate the expected Hα flux for each galaxy in the photometric catalog and use these values in our target selection. The prediction of Hα flux represents a total flux from each galaxy (without considering flux loss due to the fiber aperture) calculated with Equation 2 of Kennicutt (1998),

$$L_{\mathrm{H}\alpha}\ (\mathrm{erg\ s^{-2}}) = \mathrm{SFR}\ (\mathrm{M_\odot yr^{-1}})/7.9 \times 10^{42}. \quad (4.1)$$

Here, the SFRs are derived from the SED fitting, assuming a constant star formation history

(see Silverman et al. 2015 for details). Dust extinction is taken into account based on the color excess $E_{\rm star}\ (B-V)$, estimated from the SED, and a Calzetti et al. (2000) extinction curve. Extinction for the nebular component is related to the stellar extinction via $A({\rm H}\alpha) = 3.325E_{\rm star}\ (B-V)/f$, where $f = 0.66$ is assumed[1]. In early observations, a predicted Hα flux threshold of 4×10^{-17} erg cm^{-2} s^{-1} is set without taking into account the $\sim 50\%$ aperture loss. In the subsequent intensive program, the limit of the predicted Hα flux was raised to 1×10^{-16} erg cm^{-2} s^{-1}. The majority (89%) of our sample have a predicted Hα flux higher than 1×10^{-16} erg cm^{-2} s^{-1}. This flux limit is equivalent to SFR $\sim 20\ M_\odot$ yr^{-1} for galaxies at $z \sim 1.6$ with typical values of dust attenuation.

4.2.2 Spectral fitting

We perform a fitting procedure that utilizes the MPFIT package for IDL (Markwardt 2009) to measure a flux and an associated error of an emission line on individual and composite spectra. The fitting of key emission lines (Hα, [N II]$\lambda\lambda$6548, 6584, Hβ, [O III]$\lambda\lambda$4959, 5007) present in individual spectra are described in detail in Chapter 2 and published papers (Kashino et al. 2013; Silverman et al. 2015). Here, we further perform a fit to the [S II]$\lambda\lambda$6717, 6731 lines based on redshift determined from the Hα line. For individual spectra, the value of each pixel is weighted using the noise spectra and the pixels that are impacted by the OH airglow masks are excluded from the fit. For composite spectra, we use weights based on the variance estimated by jackknife resampling (see §4.2.7).

In our emission line fitting procedure, first, the continuum is fit with a linear function to pixels near the emission lines and subtracted from the data. Each emission line is modeled with a Gaussian profile. The [N II]$\lambda\lambda$6584, 6548 and Hα lines are simultaneously fit with a fixed line width. We further fix the ratio [N II]λ6584/[N II]λ6548 to the laboratory value of 2.86, and the line widths of [S II]$\lambda\lambda$6717, 6731 are fixed to the same as the Hα line. The Hβ and [O III] lines are modeled independently from Hα–[N II] with the of the [O III] doublet fixed to 2.98. This avoids any systematic effects potentially due to uncertainties of the wavelength calibration and provides an independent evaluation of key lines (e.g., Hα, [O III]). The observed line widths of Hα and [O III]–Hβ system agree with each other on average.

4.2.3 Correction for Balmer absorption

It is known that the stellar atmospheric absorption is considerable in lowering significantly the observed flux of the Hβ emission line (e.g., Nakamura et al. 2004; Groves et al. 2012). Therefore, we correct the observed Hβ flux for this underlying absorption as a function of stellar mass as given in Zahid et al. (2014b):

$$f_{\rm corr} = \max\left[1,\ 1.02 + 0.30\log\left(M_*/10^{10}M_\odot\right)\right]. \tag{4.2}$$

This relation has been converted to be used with a Salpeter IMF. We apply the absorption correction to the measured Hβ flux of individual galaxies in our FMOS sample, and the measurements based on the composite spectra. The Hα flux is not corrected for the stellar absorption since the flux loss is expected to be negligible ($<$ a few percent; see Kashino et al. 2013).

The Balmer absorption correction reduces the line ratio [O III]/Hβ by 11% on average and maximally 50% at the high mass end. The typical amount of correction is consistent with

[1]Large uncertainties remain in the conversion between the amount of extinction towards stellar emission and that toward nebular emission, which likely depends on the geometrical properties of stars, dust, and star-forming regions. While $f = 0.44$ is canonically applied locally (Calzetti et al. 2000), some studies report on a larger value between 0.44 and 1 for high-z galaxies based on the Balmer decrement measurement or the comparison between SED- (or UV-) based SFRs and Hα-SFRs (e.g., Kashino et al. 2013; Price et al. 2014; Koyama et al. 2015; Valentino et al. 2015)

Shapley et al. (2015) and Steidel et al. (2014). The application of such a correction does not affect our scientific conclusions. We note that the Balmer absorption correction is applied for only the FMOS sample, and not for the local galaxies from the MPA/JHU catalog, in which the correction is already taken into account by measuring the emission line intensities after the stellar continuum subtraction based on a population synthesis model (see Tremonti et al. 2004 for details).

4.2.4 Sample selection for analysis

In this study, we use 701 galaxies (approximately 40% of observed galaxies) having a detection of the Hα emission line with a signal-to-noise ratio (S/N) greater than 3 in the H-long spectrum. The range of spectroscopic redshift is $1.43 \leq z \leq 1.74$. Figure 4.1 shows a comparison between spectroscopic and photometric redshifts and a histogram of $(z_{\rm phot} - z_{\rm spec})/(1 + z_{\rm spec})$. We find that the two redshifts are in agreement with $\sigma(\Delta z/(1+z)) = 0.027$ (0.022 with 3-σ clipping), and a small systematic offset of $(\Delta z/(1+z)) = -0.01$.

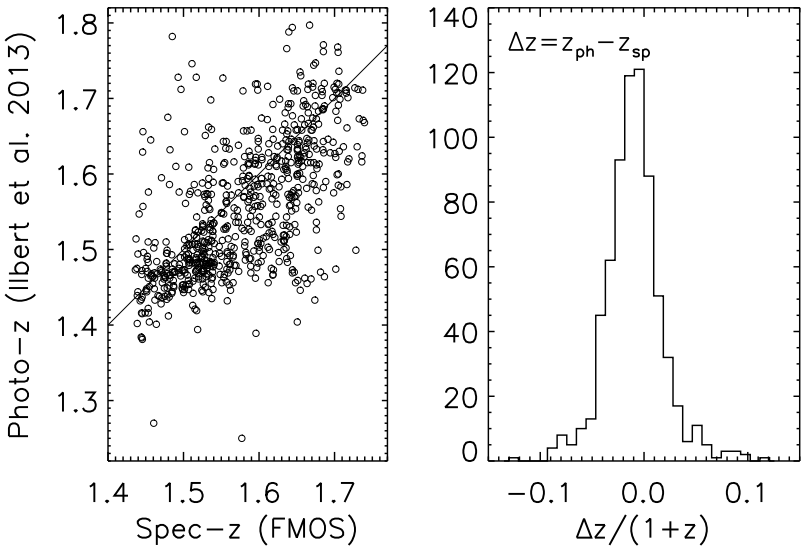

Figure 4.1: Comparison of spectroscopic and photometric redshifts for 701 galaxies with an Hα detection, and a histogram of $(z_{\rm phot} - z_{\rm spec})/(1 + z_{\rm spec})$.

We define two subsamples based on the spectral coverage. *Sample-1* consists of all 701 galaxies with a positive Hα detection in the H-long band, regardless of the presence or absence of the J-long coverage. *Sample-2* consists of 310 galaxies (a subset of Sample-1) having the additional J-long spectrum. The numbers of detections of each emission line are summarized in Table 4.2. For the [S II] doublet lines, we count the number of objects with both [S II]$\lambda\lambda$6717, 6731 lines detected at either S/N > 1.5 or > 3. The numbers of galaxies with simultaneous detections of multiple emission lines are provided as well. We further group galaxies by the S/N of their emission line measurements: high-quality (HQ) if S/N > 5 for Hα and S/N > 3 for other lines, or low-quality (LQ) if S/N > 3 for Hα and S/N > 1.5 for others.

We make use of co-added spectra by stacking in bins of galactic properties (see §4.2.7 for details) to account for galaxies with faint emission lines and avoid a bias induced by galaxies with the strongest lines (i.e., largest SFR and least extinction). For stacking analysis, galaxies are restricted to those having a redshift measurement between $1.43 \leq z \leq 1.67$ to cover all the key emission lines including [S II]$\lambda\lambda 6717, 6731$. The numbers of galaxies used for the stacking analysis is given in the bottom row in Table 4.2. To check the potential impact of residual OH

emission and the suppression mask, we construct a sample that consists of only galaxies for which the redshifted wavelength of [N II]λ6584 is more than 9Å from an OH line[2] ($\sim$ 50% of the full sample) to ensure that the [N II] line is free from OH contamination (see also Stott et al. 2013). We repeat all analyses throughout this work with this restricted sample and confirm that the results do not change.

Table 4.2: Summary of emission line detections of the FMOS sample

Coverage	*H*-long		*H* & *J*-long	
Name	**Sample-1**[b]	**w/o AGNs**	**Sample-2**	**w/o AGNs**
Hα	701 (500)[a]	642 (469)	310 (241)	283 (224)
[N II]	436 (278)	383 (233)	216 (133)	190 (110)
[S II]	77 (17)	73 (17)	32 (5)	31 (5)
Hβ	-	-	138 (99)	127 (94)
[O III]	-	-	171 (160)	158 (147)
[N II] + Hα [e]	436 (246)	383 (217)	216 (115)	190 (99)
[S II] + Hα	77 (17)	73 (17)	32 (5)	31 (5)
[N II] + [S II] + Hα	61 (13)	57 (13)	28 (2)	27 (2)
[O III] + Hβ	-	-	121 (70)	110 (67)
[N II] + Hα + [O III] + Hβ	-	-	87 (40)	76 (37)
[S II] + Hα + [O III] + Hβ	-	-	19 (5)	18 (5)
$N_{\rm stack}$[f]	-	554	-	246

[a] The threshold S/N is 3 for Hα and 1.5 for other lines. In parentheses, the numbers of detections with a higher S/N (>5 for Hα and >3 for other lines) are listed.
[b] Sample-1 consists of 701 galaxies with a positive Hα detection.
[c] The numbers of galaxies after the AGN exclusion. See §4.2.5.
[d] Sample-2 consists of 310 galaxies with both an positive Hα detection and an additional *J*-long spectrum.
[e] The numbers of galaxies with multiple emission line detections are listed in the 6th-11th rows. See §4.2.4.
[f] The numbers of objects that are used for stacking ($1.43 \leq z \leq 1.67$). See §4.2.7.

4.2.5 Identification of AGN

AGNs are excluded for a clean investigation of the conditions of H II regions of star-forming galaxies. We identify possible AGN candidates based on either their X-ray emission, rest-frame optical emission-line width (i.e., Hα), or emission-line ratios. From the sample shown in Figure 4.2, we identify 22 objects (3%) associated with an X-ray point source in the catalog provided by the *Chandra* COSMOS Legacy survey (Elvis et al. 2009; Civano et al. 2016), which covers the entire FMOS survey area. These X-ray detected galaxies are likely to host AGNs because such luminous X-ray emission ($L_{\rm X-ray} \gtrsim 4 \times 10^{42}$ erg s^{-1} at 0.5–7 keV) is expected to arise from a hot accretion disk around an AGN. In addition, four objects have an emission line width (full width at half maximum) greater than 1000 km s^{-1}, which are taken to be unobscured (type-I) AGNs; one of these is included in the X-ray point source catalog. We also identify 39 objects (5.5%) based on their rest-frame optical emission-line properties that are located above the BPT classification boundary at $z \sim 1.6$ (Kewley et al. 2013b) (see §4.3.1) or have either a line ratio

[2]The list of the OH lines in the FMOS coverage are available at http://www.subarutelescope.org/Observing/Instruments/FMOS/index.html

of $\log [\mathrm{N\,II}]/\mathrm{H}\alpha > -0.1$ or $\log [\mathrm{O\,III}]/\mathrm{H}\beta > 0.9$. Of these, four galaxies are detected in the X-ray band and a single object has a broad (> 1000 km/s) Hα line. The majority of AGNs identified based on narrow line ratios are likely obscured (type-II) AGNs.

The fraction of the objects with an X-ray detection (3%) is roughly similar to that reported by Silverman et al. (2009, 2% at $z \sim 1$), who utilized a galaxy sample from the 10k catalog of the zCOSMOS-bright survey (Lilly et al. 2007). The X-ray source fraction of our sample achieves 10% at $M_* > 10^{11}$ M_*. Such an X-ray AGN fraction at the high-mass end is lower than those at the equivalent redshift range from the literature (~ 30%; e.g., Bundy et al. 2008; Brusa et al. 2009; Yamada et al. 2009). This is likely due to the prior selection on the predicted Hα flux applied for galaxies in our sample.

In total, 59 (8%) objects are taken as potential AGN candidates, which are marked in Figure 4.2 (magenta circles). The total AGN fraction is roughly consistent with that of Yabe et al. (2014, 6%) that uses a sample of star-forming galaxies at $z \sim 1.4$, while Yabe et al. (2014) do not use any X-ray observations, thus they probably miss some AGNs. The AGN fraction increases with stellar mass and achieves 25% at $M_* > 10^{11}$ M_*. Such a trend is consistent with previous studies (e.g., Reddy et al. 2005). Table 4.2 lists the number of galaxies in each sample before and after the exclusion of those hosting AGNs. For stacking analysis, we only use galaxies with the AGN candidates having been removed. In §4.5, we address the additional contribution of AGN photoionization to the stacked emission line measurements.

4.2.6 Stellar masses, SFRs, and the main sequence

Stellar masses and SFRs are derived from SED fitting based on a spectroscopic redshift (measured from FMOS) using LePhare (Arnouts & Ilbert 2011) with a constant star formation history assumed. Although a Chabrier IMF is assumed in the stellar population synthesis calculations, the physical values are converted to a Salpeter IMF. The statistical errors of derived stellar masses and SFRs are typically 0.05 dex and 0.2 dex, respectively. While the errors on the quantities are improved due to the use of spectroscopic redshifts, the statistical characteristics of the recalculated stellar masses do not differ from the original sample used for target selection. The sample spans a range of stellar mass $9.6 \lesssim \log\ M_*/M_\odot \lesssim 11.6$ with a median mass of $\log M_*^{\mathrm{med}}/M_\odot = 10.4$. We highlight that our sample includes a large number of very massive galaxies ($M_* \geq 10^{11}$ $M_\odot$; 120 in total, 92 after removing AGN: see §4.2.5).

Figure 4.2 (top panel) shows the SFR as a function of M_* for our full sample, compared with the complete distribution of K_S-selected ($K_\mathrm{S} < 23.5$) galaxies in the equivalent redshift range ($1.46 \leq z_{\mathrm{photo}} \leq 1.72$, gray dots). The K_S-selected galaxies (7987) show a clear correlation between stellar mass and SFR (i.e., star-forming main sequence) with a standard deviation around the relation of 0.37 dex. Of these, those with $M_* \geq 10^{9.8}$ and f_{pre} (Hα) $\geq 10^{-16}$ erg s^{-1} cm^{-2} (2324) are marked as small yellow circles. Our sample galaxies with an Hα detection (Sample-1) are shown as small cyan circles and follow the distribution of the parent sample. To quantify a potential bias in our sample, we fit a power-law relation (SFR $\propto M_*^\alpha$) to the K_S-selected and Hα-detected samples separately for galaxies with $M_* \geq 10^{9.8}$ $M_\odot$. While the slope is consistent between the two samples ($\alpha = 0.66 \pm 0.01$ for the former and 0.68 ± 0.02 for the latter), the Hα-detected sample is slightly biased towards higher SFRs by ~ 0.15 dex over the entire stellar mass range due to the self-imposed limit on the predicted Hα flux. However, such a bias is less than half of the scatter of the main sequence. The inset panel shows the normalized distribution of the difference in SFR from the fit to the main sequence for both the K_S-selected (filled gray histogram) and Hα-detected (blue solid histogram) galaxies. As clearly evident, our final sample well traces the star-forming main sequence at $z \sim 1.6$.

We also measure SFRs from the Hα flux detected by FMOS following Equation 2 of Kennicutt (1998). As described in Kashino et al. (2013), the observed Hα flux is corrected for the flux falling outside the FMOS 1″.2-diameter fiber aperture. This aperture correction factor is evaluated for

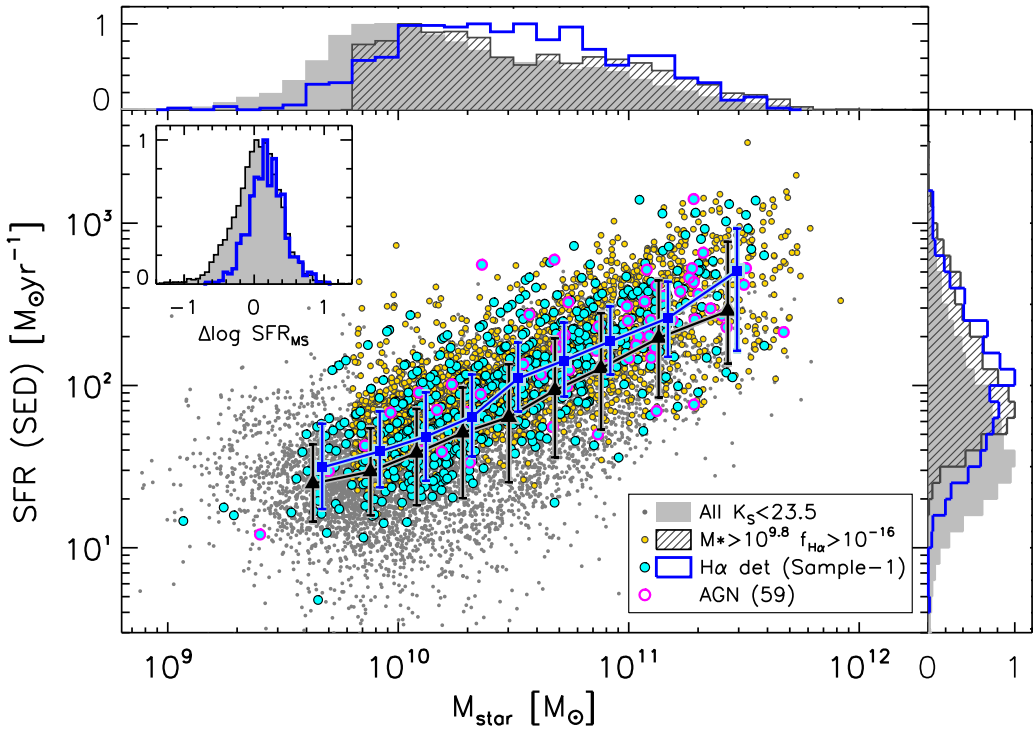

Figure 4.2: SFR (SED) versus M_* for galaxies at $1.43 \leq z \leq 1.74$: all galaxies with $K_{\rm S} < 23.5$ and $1.46 \leq z_{\rm photo} \leq 1.72$ in the FMOS survey area (gray dots, filled histogram normalized to their peak value), galaxies with $M_* \geq 10^{9.8}\ M_\odot$ and a predicted Hα flux $f(\mathrm{H}\alpha) \geq 1 \times 10^{-16}$ erg s^{-1} cm^{-2} (yellow circles, hatched histograms), galaxies with an Hα detection (cyan circles, blue thick-line histograms), AGN candidates (magenta circles). The median SFRs in eight stellar mass bins for both the $K_{\rm S}$-selected and Hα-detected samples are indicated by large symbols (triangles and squares respectively) with error bars indicating the 68th percentiles. An inset panel shows histograms of the difference in SFR from fit to the main sequence for $K_{\rm S}$-selected (filled gray histogram) and Hα-detected (thick blue line) galaxies. The Hα-detected sample well traces, while being less biased, the star-forming main sequence that the all $K_{\rm s}$-selected galaxies form at this redshift (see §4.2.6).

each object from a comparison between the observed continuum flux from FMOS spectra and the Ultra-VISTA H and J-band photometry (McCracken et al. 2012), as described in §2.5.3. The observed Hα flux is corrected for dust extinction. The amount of extinction (i.e., color excess $E_{\rm star}(B-V)$) is estimated from SED fitting, then it is converted to the extinction towards nebular emission by assuming $f = E_{\rm neb}(B-V)/E_{\rm star}(B-V) = 0.59$, which is adjusted to bring observed Hα-based SFRs into agreement with the SED-based SFRs. While we assumed $f = 0.66$ in our target selection (§4.2.1), the application of a different f-factor does not change any of our conclusions.

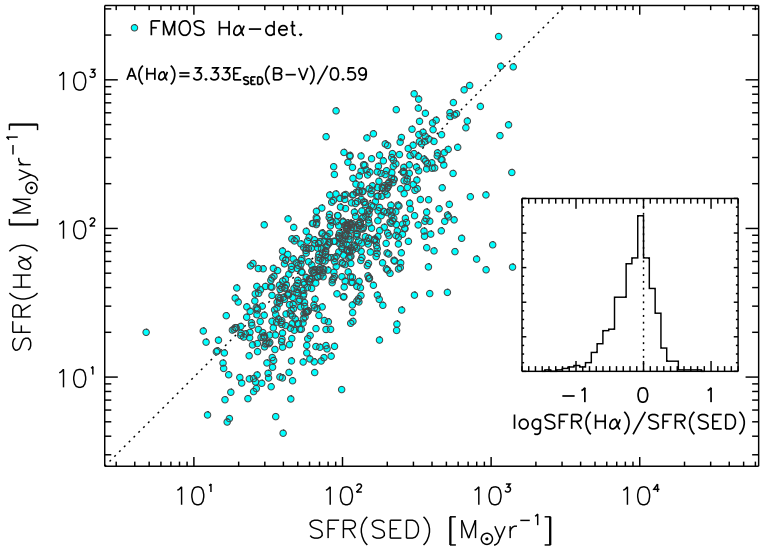

Figure 4.3: Comparison between SFRs based on either the SED-fitting or observed Hα luminosities. An inset shows the distribution of the difference log [SFR(Hα)/SFR(SED)]. The two SFRs are in agreement with a standard deviation of 0.27 dex.

4.2.7 Spectral stacking

We construct average spectra to determine the typical strengths of weak lines such as Hβ, [N II] and [S II]. Individual spectra of galaxies at $1.43 \leq z \leq 1.67$ are stacked in bins of stellar mass. This redshift range ensures that all the emission lines used in this study fall in the spectral coverage of FMOS. A fair fraction (30%) of the pixels in individual spectra that are strongly impacted by the OH mask and residual sky lines are removed by identifying them in the noise spectra as regions with relatively large errors as compared with the typical noise level of $\sim 5 \times 10^{-19}$ erg cm^{-2} s^{-1} A^{-1} (see Figure 11 in Silverman et al. 2015). We transform all individual spectra to the rest-frame wavelength based on their spectroscopic redshifts with a pixel resolution of 0.5 Å/pix. For a galaxy at $z = 1.5$, the pixel resolution of the de-redshifted spectrum is equivalent to that of the observed spectrum (1.25 Å/pix).

After subtracting the continuum, the individual de-redshifted spectra are averaged by using the *resistant_mean.pro*, an IDL routine available in the Astronomy User's Library. We apply a 5σ clipping, which removes data that deviates from the median by more than five times the median absolute deviation at each pixel. We do not apply any weighting scheme to avoid possible biases. The associated noise spectra are computed using a jackknife resampling method. The

variance at each pixel is given by

$$\sigma^2_{\rm jack} = \frac{N-1}{N}\sum_{i=1}^{N}\left(F_i - \frac{1}{N}\sum_{i=1}^{N}F_i\right)^2 \tag{4.3}$$

where N is the sample size used for stacking (after a 5 σ clip) and F_i is the stacked spectra composed of $N-1$ spectra by removing the i-th spectrum. Figure 4.4 shows the composite spectra of Sample-1 and Sample-2 in five bins of stellar mass. We ensure that the reduced χ^2 of the fit to each composite spectrum is approximately unity (0.8–1.2). Therefore, we conclude that our model fits to the observed composite spectra are accurate. The errors on the flux measurements and flux ratios for the stacked spectra are calculated from Equation 4.3 with F_i replaced by an arbitrary quantity (i.e., flux or line ratio) measured on the i-th-removed stacked spectrum.

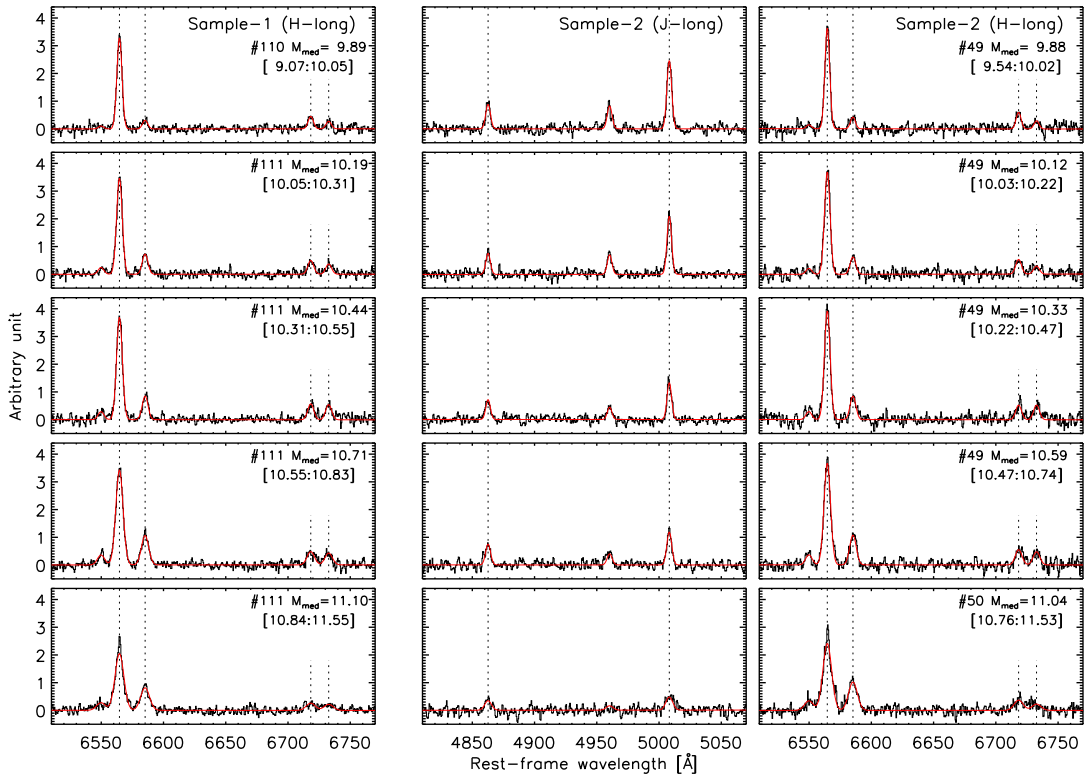

Figure 4.4: Composite spectra in five bins of stellar mass of Sample-1 (left column) and Sample-2 (middle and right column). The number of individual spectra is indicated for each bin (e.g., #110). The stellar mass increases from top to bottom, as their median value ($\log M_*/M_\odot$) and interval are shown in each panel. Observed spectra and the best-fit model are shown by black thin solid lines and red thick curves. Vertical dotted lines show the positions of Hα, [N II]λ6584, [S II]$\lambda\lambda$6717, 6731, Hβ, and [O III]λ5007.

We note that individual spectra are averaged without any renormalization; this may result in a flux-weighted co-added spectrum that is not representative of galaxies with the faintest emission lines. To examine such effects, we normalize each spectrum by the amplitude of the Hα emission line before co-adding. We then find that the results presented in this study do not depend on whether such a scaling is applied or not. All results presented hereafter are based on a stacking analysis without any such renormalization of the individual spectra. Throughout, we measure average emission line ratios using co-added spectra of Sample-1 and Sample-2 split into

eight and five bins of stellar mass, respectively. In Table 4.3, we list the emission line ratios and their associated jackknife errors.

Table 4.3: Emission line ratios from co-added spectra in M_* bins.

Median M_*[a]	$N2$[b]	$S2$[c]	$N2S2$[d]	$O3$[e]
Sample-1, 8 bins				
9.84	-1.09 ± 0.12	-0.61 ± 0.07	-0.48 ± 0.13	–
10.04	-0.87 ± 0.07	-0.61 ± 0.07	-0.25 ± 0.09	–
10.21	-0.64 ± 0.04	-0.60 ± 0.06	-0.04 ± 0.07	–
10.35	-0.70 ± 0.05	-0.55 ± 0.05	-0.15 ± 0.07	–
10.51	-0.55 ± 0.04	-0.52 ± 0.06	-0.03 ± 0.06	–
10.69	-0.52 ± 0.04	-0.62 ± 0.07	0.10 ± 0.08	–
10.85	-0.46 ± 0.04	-0.57 ± 0.06	0.12 ± 0.07	–
11.16	-0.37 ± 0.05	-0.61 ± 0.09	0.24 ± 0.10	–
Sample-2				
9.88	-0.93 ± 0.08	-0.60 ± 0.09	-0.34 ± 0.11	0.46 ± 0.06
10.12	-0.77 ± 0.06	-0.64 ± 0.06	-0.13 ± 0.07	0.43 ± 0.06
10.33	-0.67 ± 0.04	-0.56 ± 0.07	-0.11 ± 0.07	0.23 ± 0.07
10.59	-0.53 ± 0.04	-0.54 ± 0.05	0.01 ± 0.05	0.14 ± 0.08
11.04	-0.37 ± 0.04	-0.60 ± 0.07	0.22 ± 0.08	0.03 ± 0.16

[a] Median $\log M_*/M_\odot$ of each mass bin.
[b] $N2 = \log([\mathrm{N\,II}]\lambda 6584/\mathrm{H}\alpha)$.
[c] $N2 = \log([\mathrm{S\,II}]\lambda\lambda 6717, 6731/\mathrm{H}\alpha)$.
[d] $N2S2 = \log([\mathrm{N\,II}]\lambda 6584/[\mathrm{S\,II}]\lambda\lambda 6717, 6731)$.
[e] $O3 = \log([\mathrm{O\,III}]\lambda 5007/\mathrm{H}\beta)$, corrected for Balmer absorption (see §4.2.3).

4.2.8 Local comparison sample

We extract a sample of local galaxies from the Sloan Digital Sky Survey (SDSS) Data Release 7 (Abazajian et al. 2009) to compare with the ISM properties of our high-z galaxies. The emission-line flux measurements are from the MPA/JHU catalog (Kauffmann et al. 2003a; Brinchmann et al. 2004; Tremonti et al. 2004) based on Data Release 12 (Alam et al. 2015) for which the stellar absorption is taken into account by subtracting a stellar component as determined from a population synthesis model. We use *total* SFRs from the MPA/JHU catalog, in which SFRs within and outside the SDSS fiber aperture are combined. The *in-fiber* SFRs are based on the extinction-corrected Hα luminosities falling within the fiber (Brinchmann et al. 2004), and SFRs outside the fiber are estimated from the SDSS photometry outside the fiber, following the method described in Salim et al. (2007). We convert SFRs to a Salpeter IMF from a Kroupa (2001) IMF by multiplying by a factor of 1.5 (Brinchmann et al. 2004).

Stellar masses are derived using the LePhare code (see Zahid et al. 2011 for details) instead of using the JHU/MPA values. Stellar masses from LePhare are based on a Chabrier IMF, and are smaller than those provided by MPA/JHU by approximately 0.2 dex on average with a dispersion between the two estimates of 0.14 dex. For this study, the stellar masses are converted to a Salpeter IMF.

The SDSS galaxies are selected over a redshift range of $0.04 < z < 0.1$ to reduce the effects of redshift evolution. Kewley et al. (2005) reported that line measurements are highly biased towards the central area that may be more quenched when a covering fraction is less than 20%. To avoid such aperture effects, we impose a lower redshift limit of 0.04. Furthermore, we require 5σ

detections for Hα and 3σ for all other emission lines used in this study ([N II]λ6584, [S II]$\lambda\lambda$ 6717, 6731, Hβ, and [O III]λ5007). We classify galaxies as either star-forming or AGN as those below or above the classification line of Kauffmann et al. (2003b) on the BPT diagram (see §4.3.1). The final sample of local sources consists of 80,003 star-forming galaxies and 31,899 AGNs. In Figure 4.5, we show the distribution of M_* and SFR for the SDSS star-forming galaxies. For AGNs, the stellar mass distribution is shown by the filled histogram. The central 99 percentiles of the star-forming galaxies and AGNs include objects with $8.7 < \log M_*/M_\odot < 11.1$ and $9.7 < \log M_*/M_\odot < 11.6$, respectively.

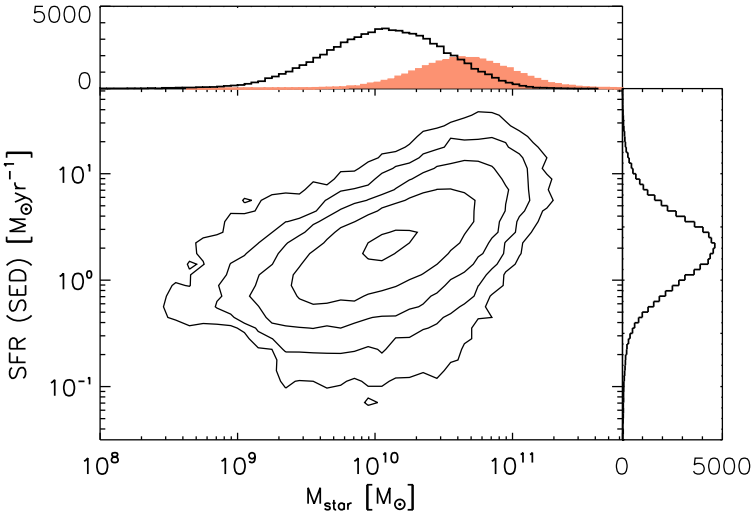

Figure 4.5: M_* vs. SFR for local star-forming galaxies from the SDSS survey. Their distributions of stellar mass and SFR are shown by empty histograms. Filled histogram indicates the stellar mass distribution of local AGNs.

4.3 Emission line properties

4.3.1 BPT diagnostic diagram

We present in Figure 4.6 the BPT diagram for high-redshift galaxies from our FMOS sample. The line ratios for 87 individual galaxies that have detections of all four lines (Sample-2) are indicated by the data points. We further illustrate the quality of the measurements by splitting the sample into two groups: high-quality (HQ, S/N > 5 for Hα and S/N > 3 for [N II]λ6584, Hβ, and [O III]λ5007), or low-quality (LQ, S/N > 3 for Hα and S/N > 1.5 for others). As previously mentioned, an absorption correction is applied to the observed Hβ fluxes (see §4.2.3). To aid in our interpretation of the high-redshift data, we plot the distribution of line ratios of local SDSS galaxies (gray contours in Figure 4.6). We further highlight the local sequence of star-forming galaxies by a commonly used functional form (Kewley et al. 2013a):

$$\log([\mathrm{OIII}]/\mathrm{H}\beta) = \frac{0.61}{\log([\mathrm{NII}]/\mathrm{H}\alpha) + 0.08} + 1.10. \quad (4.4)$$

More than half of our FMOS galaxies deviates from the above local abundance sequence towards higher [O III]/Hβ and/or higher [N II]/Hα ratios, and a large number of objects are beyond the local boundary of Kauffmann et al. (2003b), a local demarcation between star-forming galaxies and AGNs. Kewley et al. (2013b) derive a redshift evolution of the boundary to distinguish star-forming galaxies and AGNs. We show this prediction at $z = 1.6$ (thin dotted

line) that is consistent with the location of the majority of the FMOS sources. With the same functional form as Equation 4.4, we perform a fit to our sample and find the following relation at $z \sim 1.6$ (Cyan thick curve in Figure 4.6):

$$\log([\mathrm{O\,III}]/\mathrm{H}\beta) = \frac{0.61}{\log([\mathrm{N\,II}]/\mathrm{H}\alpha) + 0.1336} + 1.081. \quad (4.5)$$

Here, the coefficient is fixed to be the same value (0.61) as the local relation (Equation 4.4). We remove AGN candidates (see §4.2.5), by using only galaxies with line ratios located in the star-forming region as defined by the redshift-dependent boundary at $z = 1.6$. The mean locus of the FMOS sample seems to be well expressed by this formula. The average measurements, based on the stacked spectra of Sample-2 in five bins of stellar mass (see Table 4.3), are also representative of the entire trend and in good agreement with the best-fit relation thus confirming a clear offset from the local mean sequence (Kewley et al. 2013a). Here it is important to highlight that our sample maps the distribution on the BPT diagram below $\log([\mathrm{O\,III}]/\mathrm{H}\beta) = 0$ down to ~ -0.4 by individual measurement as a result of the considerable sampling rate of the massive galaxy population.

To further examine the robustness of the high-z abundance sequence, we apply a more strict limit on the $[\mathrm{N\,II}]/\mathrm{H}\alpha$ ratio to remove potential AGNs. Following Valentino et al. (2015), we decrease the N2 limit from -0.1 (see §4.2.5) to -0.4 (Cid Fernandes et al. 2010). With this restricted sample ($N_{\mathrm{stack}} = 225$), we obtain stacked measurements that also show a significant offset from the local mean sequence thus reaffirming our results. We conclude that the offset of the high-z star-forming population cannot be explained by the effects of AGNs.

This offset on the BPT diagram has been previously reported in our FMOS studies (Zahid et al. 2014b; Kartaltepe et al. 2015) and other studies (e.g., Shapley et al. 2005; Erb et al. 2006; Liu et al. 2008; Newman et al. 2014; Cowie et al. 2016) based on stacking analyses and individual measurements. We show in Figure 4.6 the fits to the samples at $z \sim 2.3$ from Steidel et al. (2014) (orange dashed line) and Shapley et al. (2015) (magenta long-dashed line). Steidel et al. (2014) derived the relation to rest-frame UV-selected galaxies from the KBSS-MOSFIRE survey, which lies above our relation as a whole. Shapley et al. (2015) also confirmed the offset using a galaxy sample from the MOSDEF survey, although more similar to our FMOS sample than the KBSS results. The difference between these samples at $z \sim 2.3$ is likely due to the difference in the adopted sample selection that results in varying typical ionization states: the larger offset in the Steidel et al. (2014) sample may be caused by the selection based on the rest-frame UV emission, especially which likely leads to higher $[\mathrm{O\,III}]/\mathrm{H}\beta$ ratios (see §4.3.2). Masters et al. (2014) measured the line ratios for highly active galaxies at $z \sim 2$, whose average measurement is significantly different from the local sequence while consistent with the Steidel et al. (2014) sample, as shown in Figure 4.7.

At $z \sim 1.5$, three groups provide BPT measurements using Subaru/FMOS, including our FMOS-COSMOS program (see Figure 4.7). Yabe et al. (2014) measured line ratios using the stacked spectra of star-forming galaxies at $z \sim 1.4$. The Yabe et al. sample is selected based on stellar mass and Hα flux, and can be considered to be representative of star-forming galaxies at this epoch, whose characteristics are similar to our sample. Their results are well consistent with our stacking measurements in the BPT diagram. Hayashi et al. (2015) constructed a sample of $[\mathrm{O\,II}]\lambda\lambda$3727, 3729 emitters at $z \sim 1.5$ with an Hα detection with FMOS. Their sample shows larger offset compared to Yabe et al., Shapley et al., and our samples, while it is consistent with the Steidel et al. sample. The Hayashi et al. sample follows a M_*–SFR relation with a slope of 0.38, which is shallower than other studies ($\sim$ 0.7–0.9, e.g., Kashino et al. 2013; Whitaker et al. 2014). Consequently, the sample is biased towards a population having high specific SFR (sSFR) at $\log(M_*/M_\odot) \sim 9$, and it might be responsible to the observed high $[\mathrm{O\,III}]/\mathrm{H}\beta$ ratios (a large BPT offset) in their sample. The authors also mention the possibility that their $[\mathrm{O\,II}]$

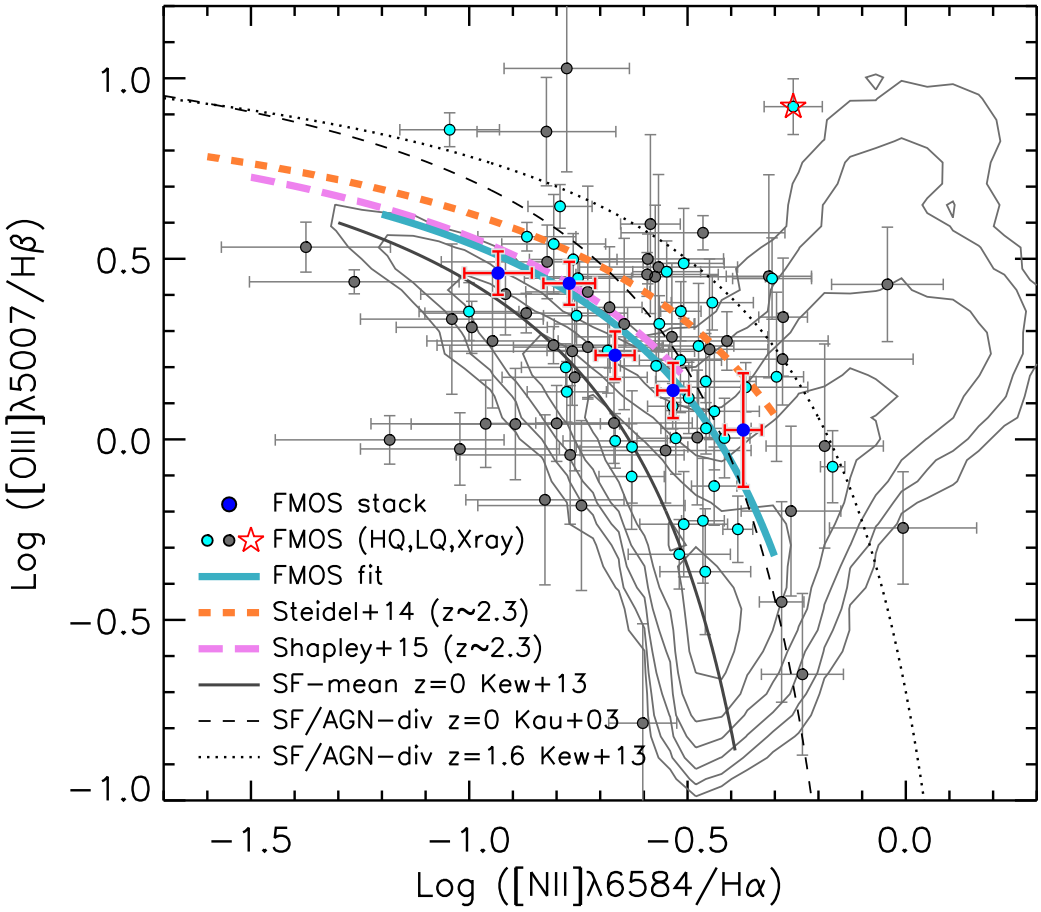

Figure 4.6: The BPT diagnostic diagram: log([OIII]/Hβ) versus log([NII]/Hα). Individual FMOS galaxies (87) are shown with circles for two groups: high- (HQ, cyan) or low-quality (LQ, dark gray). A single object detected in the X-ray band is indicated by a star. Large blue circles are average measurements (Sample-2) in five mass bin with associated errors. The median stellar mass increases from left to right. Thin curves indicate the empirical mean abundance sequence of local galaxies given by Equation 4.4 (solid line: Kewley et al. 2013a), the empirical classification of star-forming galaxies and AGNs for the local SDSS sample (dashed line: Kauffmann et al. 2003b), and the empirical prediction of the classification at $z = 1.6$ (dotted line: Kewley et al. 2013b). Thick cyan solid curve is the best fit to our individual measurements (Equation 4.5). Fits to samples at $z \sim 2.3$ are shown by thick short-dashed (Steidel et al. 2014) and thick long-dashed (Shapley et al. 2015) curves. Contours show the distribution of the local sample in log scale. Our sample shows a clear offset of the mean location from the local sequence.

emitter selection causes such a bias.

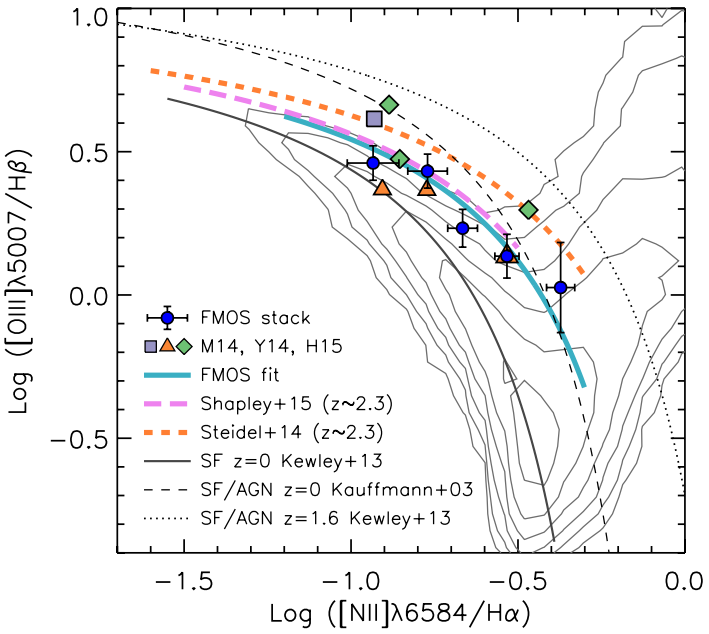

Figure 4.7: Comparison of the mean locations of high-z galaxies on the BPT diagram. Blue circles with error bars show our stacking results, as in Figure 4.6. A cyan thick solid curve indicates our best-fit relation for the individual galaxies expressed by Equation 4.5. Square, triangle, and diamond symbols indicate the stacking measurements at $z \sim 2$ (Masters et al. 2014, M14), z$\sim$ 1.4 (Yabe et al. 2014, Y14), and $z \sim 1.5$ (Hayashi et al. 2015, M15), respectively. Orange thick short- and pink long-dashed lines indicate the best-fit to samples at $z \sim 2.3$ from Steidel et al. (2014) and Shapley et al. (2015), respectively. Thin solid, dotted, and dashed curves and contours are the same as in Figure 4.6.

Based on these independent studies, it is likely that the BPT offset continuously increases with redshift, at least, up to $z \sim 2$. However, it is essential to understand the selection biases to accurately establish the redshift evolution of the location of star-forming galaxies on the BPT diagram. Obviously, the presence of an offset indicates that high-z star-forming galaxies occupy a region in the H II gas parameter space differing from the locus of local galaxies on average. As discussed in §4.4, several possible origins of the offset for high-z galaxies has been suggested and discussed, including ionization parameter, the shape of the UV radiation from the ionizing sources, and gas density (e.g., Masters et al. 2014; Shapley et al. 2015; Hayashi et al. 2015; Kewley et al. 2015; Cowie et al. 2016).

4.3.2 Mass–Excitation (MEx) diagram

To further illustrate the magnitude of the [O III]/Hβ offset, we show in Figure 4.8 the mass-excitation (MEx) diagram (M_* vs. [O III]/Hβ). This diagram was introduced by Juneau et al. (2011) to identify galaxies hosting an AGN at intermediate redshifts. Local star-forming galaxies show a decline of the [O III]/Hβ ratio with increasing stellar mass because more massive galaxies are more metal-rich and metal-line cooling becomes more efficient in such systems. In contrast, AGNs present much higher ratios as compared to star-forming population, especially at $M_* \gtrsim 10^{10}\ M_\odot$.

Figure 4.8 shows the line ratios [O III]/Hβ as a function of M_* for 121 galaxies in our sample at $z \sim 1.6$ (filled circles), split into two groups: high-quality (S/N (Hα) > 5 and S/N ([O III], Hβ) $>$

3) or low-quality (S/N (Hα) > 3 and S/N ([O III], Hβ) > 1.5). The distribution of local star-forming galaxies (gray contours) and AGNs (red contours) are indicated for comparison. We highlight the demarcations between star-forming, composite objects, and AGNs, derived by Juneau et al. (2014) for local galaxies (dashed line). It is clear that galaxies in our sample show higher [O III]/Hβ ratios on average as compared to local galaxies at a fixed stellar mass, and that many individual measurements fall within regions classified as composites (between the curves) or AGNs (above upper line) while the error bars are typically too large to constrain the true category for which each one belongs. The average measurements, based on the stacked spectra of Sample-2 in five M_* bins (see Table 4.3), confirm a substantial offset towards higher [O III]/Hβ ratios by ~ 0.5 dex. Despite the offset, we note that the global trend is similar to local star-forming galaxies, showing a clear negative correlation between stellar mass and line ratio.

Juneau et al. (2014) also derive the offset of the boundary as a function of luminosity threshold of Hα or [O III]λ5007 emission line (Equation B1 of Juneau et al. 2014) to maximize the fraction of objects successfully classified as star-forming or AGN population. We shift the boundaries by $\Delta \log M_* = 0.54$ dex (solid lines), assuming an Hα luminosity limit of $L_{\rm H\alpha} = 10^{42}$ erg s^{-1}, which is corresponding to SFR ~ 10 M_* yr^{-1}, for our sample. While the amount of the offset is less constrained at high luminosities ($L_{\rm H\alpha} > 10^{40.7}$ erg s^{-1}; Juneau et al. 2014), the boundary, derived here, shows a good agreement with galaxies in our FMOS sample. The majority of the FMOS sources falls below the demarcation line thus classified as star-forming galaxies with most of the rest classified as composites. At the same time, half of potential AGNs (star and squares in Figure 4.8) falls within the AGN-dominant region. While our sample is not purely luminosity-limited, it is likely that the luminosity-dependent boundary derived based on local galaxies provides a good classification even for high redshift galaxies, as originally reported by Juneau et al. (2014).

We also plot the measurements for $z \sim 2.3$ galaxies from Steidel et al. (2014). They show significantly higher line ratios compared to the local galaxies and even to our FMOS sample over the entire stellar mass range probed. These higher [O III]/Hβ ratios are essentially responsible for the large offset on the BPT diagram of the Steidel et al. sample (see Figure 4.6). These elevated ratios may be due to a combination of sample selection (UV-bright subsample of the population) and the redshift evolution of typical conditions (e.g., an enhanced amount of hotter stars; see Steidel et al. 2014).

4.3.3 The [S II]-BPT diagram

In this section, we present additional comparisons of the line ratios between high-z and local galaxies by incorporating the [S II]$\lambda\lambda$6717,6731 emission lines detected in the FMOS H-long band. All results in this section are based on average measurements on the stacked spectra to achieve reasonable measurements of faint [S II] doublet lines. While we do not detect individual [S II] lines in most cases, co-added spectra permit an average flux measurement of the lines.

An alternative BPT diagram compares the line ratios [S II]$\lambda\lambda$6717,6731/Hα and [O III]λ5007/Hβ to segregate the star-forming population and AGN (hereafter "[S II]-BPT" diagram; Veilleux & Osterbrock 1987), although it does not provide as clear a separation as that based on [N II]/Hα (Kewley et al. 2006; Pérez-Montero & Contini 2009). Contrary to offsets seen in the standard BPT diagram at high redshifts (Figure 4.6), no systematic offset in the [S II]-BPT diagram has been reported (e.g., Domínguez et al. 2013; Masters et al. 2014).

In Figure 4.9, we compare the line ratios [S II]/Hα and [O III]/Hβ for 19 individual galaxies of Sample-2 (high-quality — S/N (Hα) > 5 and S/N (others) > 3; low-quality — S/N (Hα) > 3 and S/N (others) > 1.5) and the average line ratios based on stacked spectra in five bins of stellar mass (Table 4.3). Four objects fall within the AGN region, above the classification line derived by Kewley et al. (2006, thin solid line in Figure 4.9). One of them is identified as an AGN based on the [N II]/Hα and [O III]/Hβ ratios (open square). From the individual measurements,

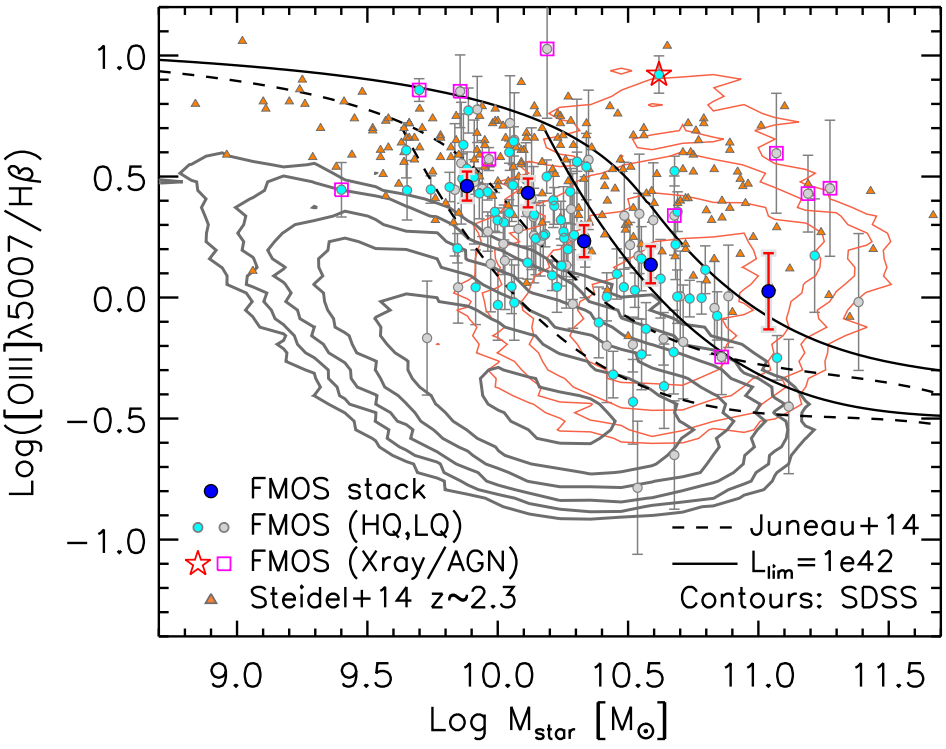

Figure 4.8: The mass–excitation (MEx) diagram: M_* vs. [O III]λ5007/Hβ. Individual FMOS galaxies are shown with filled circles for two groups: high-quality (HQ, cyan) and low-quality (LQ, gray). AGN candidates are indicated by a star (X-ray detected source) and magenta squares (others). Large blue circles are average measurements of Sample-2 based on the stacked spectra in five mass bins. Contours show the distribution of the local star-forming galaxies (gray) and AGNs (red). Dashed curves indicate the demarcation between star-forming, composite objects, and AGNs, derived by Juneau et al. (2014). The boundary for an Hα luminosity limit of 10^{42} erg s^{-1} are indicated by solid curves. Our individual and stacked points show much higher [O III]/Hβ ratios than those of local star-forming galaxies, as well as the Steidel et al. (2014) sample at $z \sim 2.3$ (orange triangles).

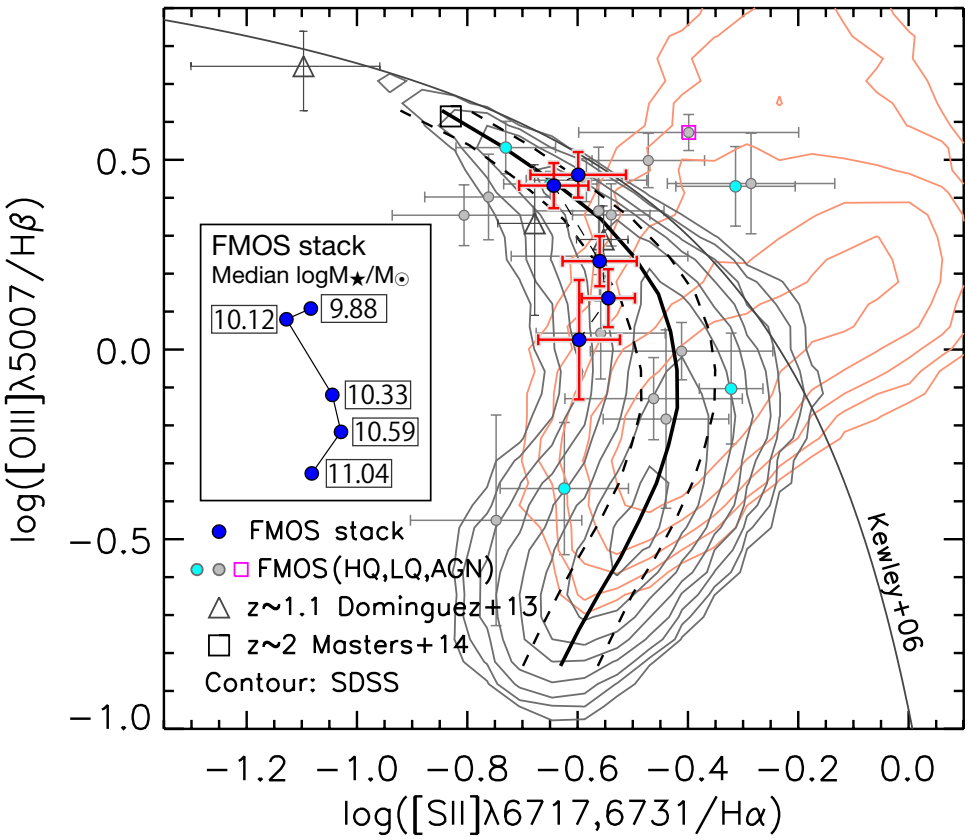

Figure 4.9: [S II]-BPT diagram: [O III]λ5007/Hβ vs. [S II]$\lambda\lambda$6717, 6731/Hα. Individual FMOS galaxies are shown with filled circles for two groups: high-quality (HQ, cyan) and low-quality (LQ, gray). A single AGN candidate is indicated by a magenta square. Large blue circles are average measurements in five mass bin (Sample-2) with the median masses of each bin given in the inset box. Data from Domínguez et al. (2013) (triangles) and Masters et al. (2014) (squares) are presented. Contours show the distributions of the local star-forming galaxies (gray) and AGNs (red). Thick solid and dashed curves indicate the median and central 68 percentiles of log [S II]/Hα in bins of log [O III]/Hβ for local star-forming galaxies. A thin solid curve is a demarcation between star-forming galaxies and AGN for local galaxies (Kewley et al. 2006). Our FMOS sample shows an offset towards lower [S II]/Hα ratios at a fixed [O III]/Hβ from the mean local relation at $M_* \gtrsim 10^{10.5}$ $M_\odot$, which suggests an enhancement of the ionization parameter in high-z galaxies (see §4.9).

the distribution appears to follow that of local star-forming galaxies; although, we are hampered by the limited sample size and errors on individual measurements. On the other hand, our average measurements clearly indicate a similarity to local galaxies (indicated by the solid curve to represent the median [S II]/Hα in bins of [O III]/Hβ) at the lower masses, while there is a departure towards lower [S II]/Hα ratios with increasing stellar mass. We note that Shapley et al. (2015) find similar [S II]/Hα and [O III]/Hβ ratios to our measurement, showing a sign of a shift towards lower [S II]/Hα values at high stellar masses, though the authors do not comment on the offset in the [S II]-BPT diagram. We further discuss the reasons for such an offset in § 4.4.

An additional diagnostic relation for emission-line galaxies is based on the line ratios [S II]$\lambda\lambda$6717, 6731/Hα and [N II]/Hα. This S2N2 diagram was first introduced by Sabbadin et al. (1977) to distinguish planetary nebulae, H II regions, and supernova remnants. In past years, this diagram has been applied to galaxies. Lamareille et al. (2009) used the S2N2 diagram to separate star-forming galaxies and Seyfert-2 galaxies. Lara-López et al. (2010a) corroborated that the S2N2 diagram is a reliable tool for segregation of star-forming and AGNs.

In Figure 4.10, we show the S2N2 diagram for 61 individual galaxies (high-quality — S/N (Hα) >

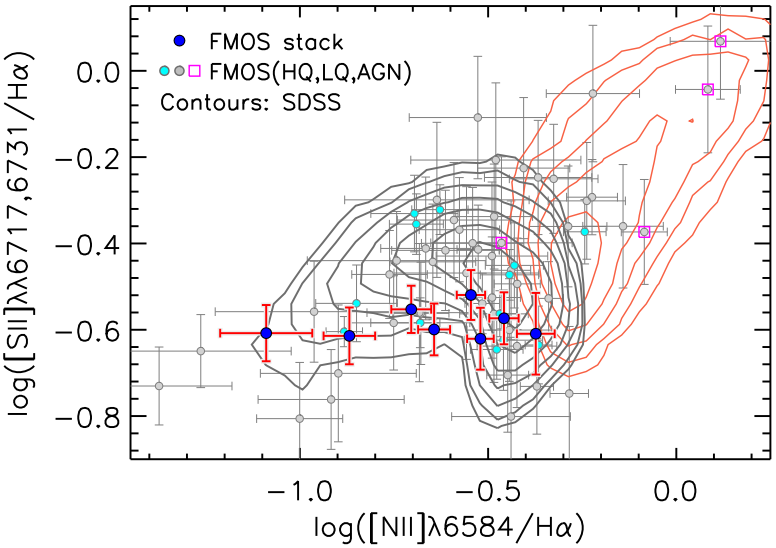

Figure 4.10: Comparison of [N II]λ6584/Hα and [S II]$\lambda\lambda$6717, 6731/Hα. Individual FMOS galaxies are shown with filled circles for two groups: high-quality (HQ, cyan) and low-quality (LQ, gray). Magenta squares indicate AGN candidates. The average measurements are based on the stacked spectra of Sample-1 in eight stellar mass bins (large blue circles). Contours show the distribution of the SDSS star-forming galaxies (gray) and AGNs (red). Our sample shows no specific trend between these line ratios, unlike the local sample (see §4.3.3).

5 and S/N ([N II],[S II]) > 3; low-quality — S/N (Hα) > 3 and S/N ([N II],[S II]) > 1.5) and average measurements based on stacked spectra (Sample-1; Table 4.3). Individual galaxies are in general in agreement with the distribution of local star-forming galaxies (gray contours). On the other hand, the average measurements have lower [S II]/Hα ratios at a given [N II]/Hα as compared with local galaxies with the exception of those at the highest masses. These average measurements occupy a narrow range of log[S II]/Hα ~ -0.6 having no specific trend with [N II]/Hα or stellar mass, as seen with local galaxies, even though our high redshift sample spans a similar range in [N II]/Hα as local galaxies. Finally, we see that there is minimal contribution of AGNs (see §4.5 for a full assessment on AGNs within our star-forming populations) to our stacked signal while a few individual sources are possibly present.

The S2N2 diagram also provides an assessment of the impact of AGNs on our analysis, independently of other assessments such as the BPT diagram and X-ray emission (see §4.5). Figure 4.10 indicates that the majority of the stacked measurements are far from the local AGNs while the most massive bin approaches the edge of the AGN distribution (red contours in Figure 4.10). Therefore, it is likely that contamination from AGNs is negligible in our stacking analysis with respect to studying the properties of H II regions in our sample. Meanwhile, some individual measurements show high line ratios and fall within the AGN region on the upper-right side of the figure while the error bars are large. Those objects are plausibly AGNs. However, we do not remove such objects based on the [S II]/Hα ratio because only a small fraction of our sample have the detection of sulphur lines and to keep our selection as homogeneous as possible.

4.3.4 Electron density

The electron density n_e can be measured from the intensity ratio [S II]λ6717/[S II]λ6731. Here, we convert the [S II] doublet ratio into n_e using the TEMDEN routine from the NEBULAR package of the STSDAS/IRAF, assuming a fixed electron temperature of $T_e = 10^4$ K. While this

temperature is commonly assumed for typical H II regions, the electron temperature is sensitive to the gas-phase metallicity with a variation of $\sim$ 5000–20000 K (e.g., Wink et al. 1983; Andrews & Martini 2013). We note that the dependence of the electron density, derived from [S II] lines, on the temperature is weak around this choice (maximally $\lesssim 0.2$ dex; Copetti et al. 2000). The line ratio is sensitive to the electron density over the range $10 \lesssim n_{\rm e}/{\rm cm}^3 \lesssim 5 \times 10^3$, while it saturates at upper ([S II]λ6717/[S II]λ6731~ 1.45) and lower (~ 0.45) limits for lower and higher electron densities, respectively. The doublet lines are well resolved with the high resolution of FMOS (see Figure 4.4). Due to the close spacing of the lines in wavelength, the measurements are free from uncertainties in the absolute flux calibration and not impacted by dust extinction. However, no single galaxy has a significant measurement of the line ratio to constrain the electron density. Therefore, we rely on stacking analysis.

In Figure 4.11, we present the average ratio [S II]λ6717/[S II]λ6731 based on stacked spectra (Sample-1). The average electron density of the full sample is $n_{\rm e} = 222^{+172}_{-128}$ cm^{-3} with errors based on jackknife resampling. This value is higher than the average electron density in local galaxies ($n_{\rm e}$ = 10–100 cm^{-3}; Brinchmann et al. 2008). We split the sample into mass bins, but do not find any significant trend with mass due to large uncertainties on our measurements.

Our results are consistent with findings reported in the literature. For example, Shirazi et al. (2014) find that the electron density of ionized gas in high-z star-forming galaxies ($z \approx 2.4$–3.7) is enhanced as compared to matched local galaxies, selected to have the same stellar mass and sSFR. Shimakawa et al. (2015) estimated the electron densities of 14 Hα emitters at $z = 2.5$ by the line ratio [O II]λ3729/λ3726, and find a median electron density of 291 cm^{-3}. Sanders et al. (2016) found a median $n_{\rm e} = 225^{+119}_{-4}$ cm^{-3} from the [O II] doublet and $n_{\rm e} = 290^{+88}_{-169}$ cm^{-3} from the [S II] doublet for a sample at $z \sim 2.3$ from the MOSDEF survey. Onodera et al. (2016) found $\sim 10^{2–3}$ cm^{-3} for star-forming galaxies at $z \approx 3.3$. Therefore, we can safely conclude that H II regions in high-z galaxies do have an electron density a few to several times larger than that of local galaxies on average.

Moreover, we compare our measurement with local galaxies having high SFRs that match those of our FMOS sample. We select local star-forming galaxies with $\Delta \log {\rm SFR} > 0.7$ dex, where $\Delta \log {\rm SFR}$ is defined as the difference between the observed SFR and the typical value of main-sequence galaxies at a given stellar mass (Elbaz et al. 2007). Figure 4.11 shows that such high-SFR local galaxies are biased towards a smaller [S II] doublet ratio (i.e., a higher electron density) that is more similar to that of our high-z sample, as compared to the entire local sample.

4.3.5 The line ratio [N II]/[S II]

Kewley & Dopita (2002) investigated the usability of the line ratio [N II]λ6584/[S II]$\lambda\lambda$6717,6731 as an abundance diagnostic. Sulphur is one of α-capture elements, including e.g., O, Ne, Si, produced through *primary* nucleosynthesis in massive stars and supplied to the ISM through type-II supernovae. In contrast, nitrogen is generated through the primary origin and the *secondary* process that uses heavy elements initially stored in stars, such as the CNO cycle, in which ^{12}C and ^{16}O are converted into ^{14}N. The production of the secondary nitrogen increases with the increasing amount of initially-contained metals in stars. Therefore, the [N II]/[S II] ratio is sensitive to the total chemical abundance at a regime where the secondary nitrogen production is predominant, while it is almost constant when most of nitrogen has the primary origin (see e.g., Figure 4 of Kewley & Dopita 2002). The advantage of the use of [N II]/[S II] is that their wavelengths are separated by only $\sim$ 140 Å, hence, they are able to be observed simultaneously and the line ratio is nearly free from the effect of dust extinction (typically < 0.03 dex). Here, we do not take account for the dust extinction, and define

$$N2S2 = \log\left([{\rm N\,II}]\lambda6584/[{\rm S\,II}]\lambda\lambda6717,6731\right). \quad (4.6)$$

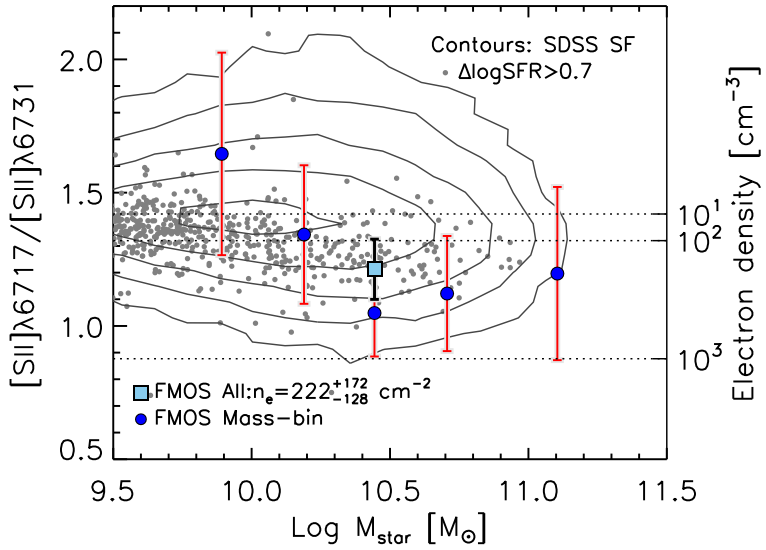

Figure 4.11: The line ratio of [S II]λ6717/[S II]λ6731 as a function of stellar mass. The corresponding electron densities are given on the right vertical axis and by the horizontal dashed lines ($n_{\rm e} = 10, 10^2$ and 10^3 cm^{-3}). Blue filled circles indicate the average measurements based on the stacked spectra in five bins of stellar mass (Sample-1), and the cyan square shows the measurement based on the stacked spectrum of the entire sample ($n_{\rm e} = 222^{+172}_{-128}$ cm^{-3}). Contours show the distribution of the local star-forming galaxies. Gray dots indicate local sources with an offset from the local star-forming main sequence $\Delta \log({\rm SFR}) \geq 0.7$ (see §4.3.4).

In Figure 4.12 (a), we shows the [N II]/[S II] ratio as a function of stellar mass for local star-forming galaxies (contours) and our FMOS sample (filled circles). The local sample shows a clear correlation between the line ratio and stellar mass above $M_* \sim 10^{9.5} M_\odot$ and reaches $N2S2 \sim 0.3$ at the massive end ($\gtrsim 10^{11}\ M_\odot$), as demonstrated by the median values in stellar mass bins. This strongly-correlated trend corresponds to the regime where the secondary nitrogen production is dominant.

We find that 61 individual galaxies with a $N2S2$ measurement show a significant correlation with stellar mass at $> 99\%$ confidence level. The trend of these individual measurements are well represented by the average measurements based on the composite spectra of Sample-1 in eight bins of stellar mass (see Table 4.3). The average $N2S2$ ratio of our sample spans ~ -0.5–0.3 with a strong correlation with stellar mass. This indicates that, on average, the secondary nitrogen production is more predominant in more massive galaxies, and also, for the majority of our sample, the ISM is sufficiently enriched enough that nitrogen is predominantly produced by the secondary process. In contrast, it is interesting to highlight that the primary nitrogen production is still likely predominant in the lowest massive galaxies in our sample ($M_* \lesssim 10^{10}\ M_\odot$). The $N2S2$ reaches to the same level as local galaxies at the massive end ($\gtrsim 10^{11} M_\odot$) while, on average, galaxies with $M_* < 10^{11} M_\odot$ have lower $N2S2$ values than found in local galaxies at the same stellar mass. That is to say, in such galaxies, the intrinsic nucleosynthesis has not proceeded as much as local galaxies. Obviously, this trend is related to the mass–metallicity relation as discussed in §4.6.

We here note that that the $N2S2$ value is less sensitive to the change of the ionization parameter $q_{\rm ion}$. While the values of [N II]/Hα and [S II]/Hα depend on $q$ion, the behavior of [N II] and [S II] track each other. According to the photoionization calculation by Dopita et al. (2013, see Figure 20), the [N II]/[S II] ratio is nearly invariance of $q_{\rm ion}$ over $\log q/({\rm cm\ s^{-1}}) \sim 7.0$–$8.5$ at lower ratios ($N2S2 \sim -0.5$; i.e., at lower masses), while it increases maximally by $\lesssim 0.1$ dex at at higher

ratios ($N2S2 \sim 0$; i.e., at high masses) as $q_{\rm ion}$ increases by 0.5 dex (from $\log q_{\rm ion}/({\rm cm\ s^{-1}}) = 7.0$ to 7.5). While an enhancement of $q_{\rm ion}$ of $\lesssim 0.5$ dex is expected to arise in high-z galaxies (see §4.4), such a dependence of $N2S2$ on q little change the trend seen in Figure 4.12.

It is also important to note that the [N II]/[S II] ratio begins to flatten below $\sim 10^{9.5} M_{\odot}$, as seen both with the contours and in the median points. This flattening likely indicates that, in such lower mass galaxies, the secondary nitrogen production does not overcome completely the primary one. The [N II]/[S II] ratio can be considered as a proxy of the nitrogen-to-oxygen (N/O) abundance ratio. The primary nitrogen-to-oxygen ratio is known to be $\log({\rm N/O}) \approx -1.5$ (e.g., van Zee et al. 1998; Pilyugin et al. 2012; Andrews & Martini 2013; Vincenzo et al. 2016). According to the relation between N/O and [N II]/[S II] from Pérez-Montero & Contini (2009), the value of $N2S2 = -0.51$ corresponds to this level of N/O, which agrees with the lowest level seen in the local galaxies at $M_* \lesssim 10^9\ M_{\odot}$ (horizontal dotted line in Figure 4.12 (a)). We also highlight that the stacked point of our FMOS sample reaches to the pedestal level at the lowest mass, which likely means that the primary nitrogen production is still likely comparable to the secondary part in galaxies at $M_* \lesssim 10^{10}\ M_{\odot}$ at higher redshift. Lastly, however, we caution that the selection effects in the local sample concerning the detection of emission lines affect the shape of the flattening of the M_*–[N II]/[S II] relation at lower masses, while the similar flattening can be reproduced when local galaxies are selected by imposing $S/N > 20$ only for the Hα line but no S/N cut for other lines.

Figure 4.12 (b) compares the line ratios [O III]/Hβ and [N II]/[S II]. The average measurements, based on the Sample-2 composite spectra in five mass bins, clearly show higher [O III]/Hβ ratios at a given [N II]/[S II] (and *vice versa*) as compared to local galaxies. The majority of individual measurements (17 objects; high-quality — S/N (Hα) > 5 and S/N (others) > 3; low-quality — S/N (Hα) > 3 and S/N (others) > 1.5) are also above the local relation, in agreement with the stacks. This characteristic of high-z star-forming galaxies is very similar to that found in the Shapley et al. 2015 sample at $z \sim 2.3$ using the individual measurements. This fact qualitatively indicates that high-z star-forming galaxies tend to maintain higher excitation state relative to their evolutionary stage of chemical enrichment, than local galaxies at a similar level of chemical enrichment.

4.4 Physical explanation for changes in emission line properties

An explanation of the changes in emission line properties of high-z galaxies is essential to understand the characteristics of their ionized gas in star-forming regions. In particular, it is important to specify the primary cause of the offset seen in the BPT diagram, which has been reported by many studies (e.g., Shapley et al. 2005; Erb et al. 2006; Liu et al. 2008; Newman et al. 2014; Masters et al. 2014; Zahid et al. 2014b; Yabe et al. 2014; Steidel et al. 2014; Kartaltepe et al. 2015; Hayashi et al. 2015; Cowie et al. 2016). Several possible factors have been suggested and discussed, including the ionization parameter, hardness of the EUV radiation field, and gas density (pressure). A higher ionization parameter, $q_{\rm ion}$, facilitates the excitation of singly-ionized elements to a double-ionized state, thus increasing [O III]/Hβ, especially at lower metallicities, while decreasing [N II]/Hα and [S II]/Hα (Kewley & Dopita 2002). Alternatively, a harder ionizing radiation field has also been considered as an origin of the BPT offset that increases all three of the line ratios given above (Levesque et al. 2010; Kewley et al. 2015). Recently, Steidel et al. (2016) suggest the presence of harder stellar spectra due to existence of metal-poor and massive binary systems. In addition, a higher H II gas density will increase the three line ratios due to the higher rate of collisional excitation of metal ions. As a result, the entire abundance sequence will be shifted towards the upper right on the BPT diagram (e.g., Brinchmann et al. 2008; Kewley et al. 2013a). Kewley et al. (2013a) summarize the effects of varying ISM properties on the star-forming locus in the BPT diagram.

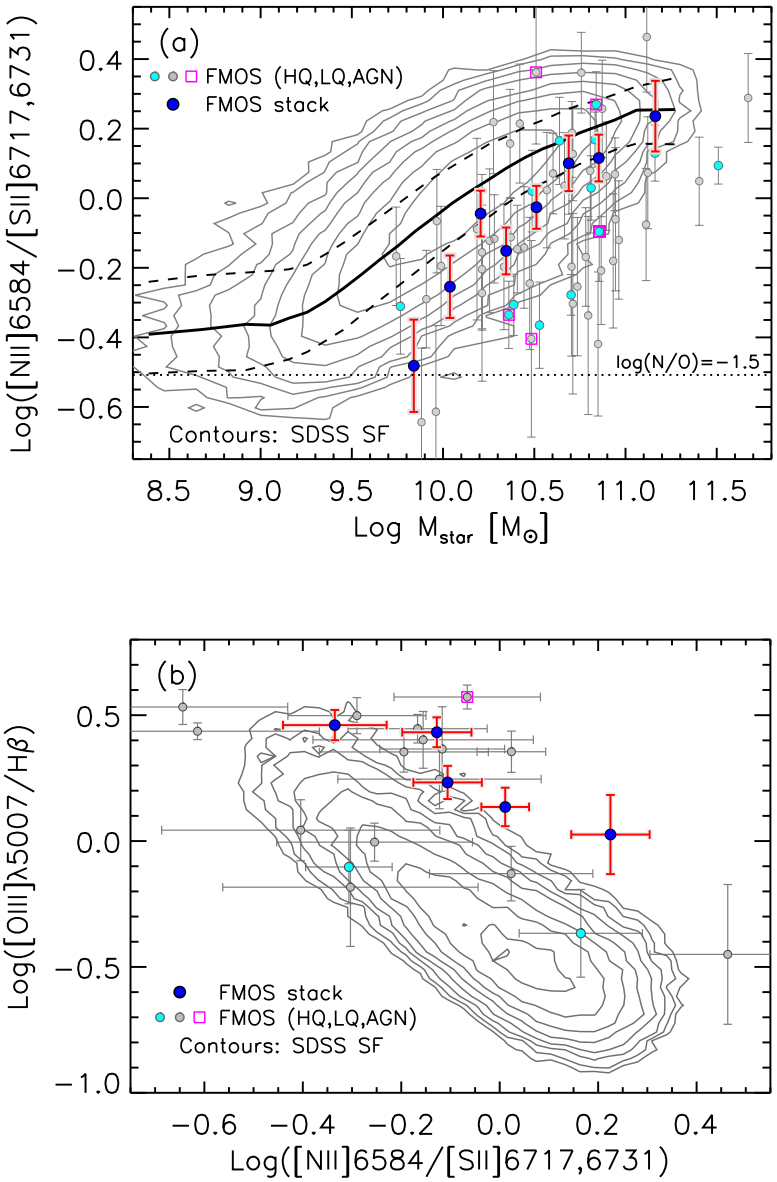

Figure 4.12: (a) The line ratio of [N II]λ6584/[S II]$\lambda\lambda$6717, 6731, a proxy of the N/O ratio (thus the chemical enrichment; see §4.3.5), as a function of stellar mass. Symbols are the same as Figure 4.10. A solid line represents the median $N2$ values in small bins of stellar mass and dashed lines indicate the interval containing the central 68% of the local galaxies (contours). A horizontal dotted line indicates the $N2S2$ value that corresponds to log(N/O) = −1.5 (see §4.3.5). (b) [N II]λ6584/[S II]$\lambda\lambda$6717, 6731 vs. [O III]λ5007/Hα. Individual FMOS galaxies are shown with filled circles for two groups: high-quality (HQ, cyan) and low-quality (LQ, gray). A magenta square indicates an AGN candidate. The average measurements are based on the stacked spectra of Sample-2 in five stellar mass bins (large blue circles). The stellar mass increases from the left to right.

4.4.1 Comparison with theoretical models

To consider the impact of these physical effects, we aim to determine how much each factor, i.e., metallicity Z, ionization parameter $q_{\rm ion}$, and gas pressure and hardness of stellar spectra, contributes to changes in the location of high-z galaxies in emission line diagnostic diagrams. We use the photoionization code `MAPPINGS V` (Dopita et al. 2016) to compare theoretically-calculated emission line ratios with our observational data (Figure 4.13). While the model grids do not exactly reproduce the observed emission ratios, they do provide qualitative insight into changes in the emission line ratios for high-z galaxies.

In Figure 4.13, we present comparisons between the observations and theoretical model. In panel (a), we make use of a new diagnostic tool, recently proposed by Dopita et al. (2016), using combinations of the line ratios [N II]λ6584/Hα, [N II]λ6584/[S II]$\lambda\lambda$6717,6731, and [O III]λ5007/Hβ to clearly separate the dependence on metallicity from the effects of changes in $q_{\rm ion}$ and gas pressure (see Figure 2 of Dopita et al. 2016). The model values of line ratios are computed as as function of $U = q_{\rm ion}/c$ and Z $(12 + \log({\rm O/H}))$, at different gas pressures ($\log P/k = 5.2$ or 6.2 cm^{-3} K). Here, the ionization parameter is defined as the ratio of ionizing photon number density to the hydrogen atom density at the inner surface of an ionized cloud. In Figure 4.13, we present additional comparisons of the line ratios [N II]/[S II] vs. [O III]/Hβ (panel b), [S II]-BPT (c), and the BPT diagram (d). In each panel of Figure 4.13, we consider changes in Z and $q_{\rm ion}$, and individual physical effects that can be responsible for the differences in line ratios between low-z and high-z galaxies at a given stellar mass. For local galaxies, we show the stacked line ratios in forty bins of stellar mass at $M_* > 10^{8.5}$ $M_\odot$ and the same five mass bins as the FMOS sample, calculated from the mean emission line fluxes of individual galaxies in each bin. In the following subsections, we describe the effects of each physical factor in detail.

Metallicity

First, we consider the changes in line ratios, as expected from the models, due to changes in metallicity. In Figure 4.13 (a), it is shown that galaxies in our FMOS sample have the same metallicity as the local sample at the massive end ($M_* > 10^{10.8}$ $M_\odot$), while metallicities of lower mass galaxies are lower than those of local galaxies at the same stellar masses[3]. Such a decline in Z for high-z galaxies with $M_* \lesssim 10^{10.8}$ $M_\odot$ (binned data labelled as #1–4 in the panel) contribute significantly to changes in line ratios. The shift, corresponding to a decline in metallicity, is shown by a black thin arrow in panels (b–d). The magnitude of the shift increases with decreasing stellar mass. As a result, the metallicity of our FMOS galaxies in the lowest mass bin is equivalent to the lowest level seen in local galaxies with $M_* \sim 10^{8.5\text{–}9}$ $M_\odot$. We note that no shift based on ΔZ arises for the most massive bin (Fig 4.13; data labelled as #5).

Ionization parameter

Next, we investigate the effects of varying ionization parameter on the emission line ratios. As plainly shown in the MEx diagram (Figure 4.8), high-z galaxies have elevated [O III]/Hβ ratios compared with local galaxies over the full range of stellar mass ($10^{9.6} \lesssim M_*/M_\odot \lesssim 10^{11.6}$). Higher [O III]/H$\beta$ ratios are also seen at a given stage of chemical enrichment, as indicated by [N II]/[S II] (Figure 4.12 (b)). These higher [O III]/Hβ ratios are easily produced by a higher ionization parameter. Further evidence of an enhancement in $q_{\rm ion}$ comes from a shift towards lower [S II]/Hα. Therefore, an increase in $q_{\rm ion}$ likely plays an important role in causing the offset in the BPT diagram, while a harder ionizing radiation field is less likely to be the only reason of the offset, and the ionization due to AGNs is likely negligible, at least not enough to fully explain the offset, as further assessed in §4.5.

[3]We further investigate the mass–metallicity relation of our sample based on the [N II]/Hα ratio and the theoretical calibration from Dopita et al. (2016) in §4.6.

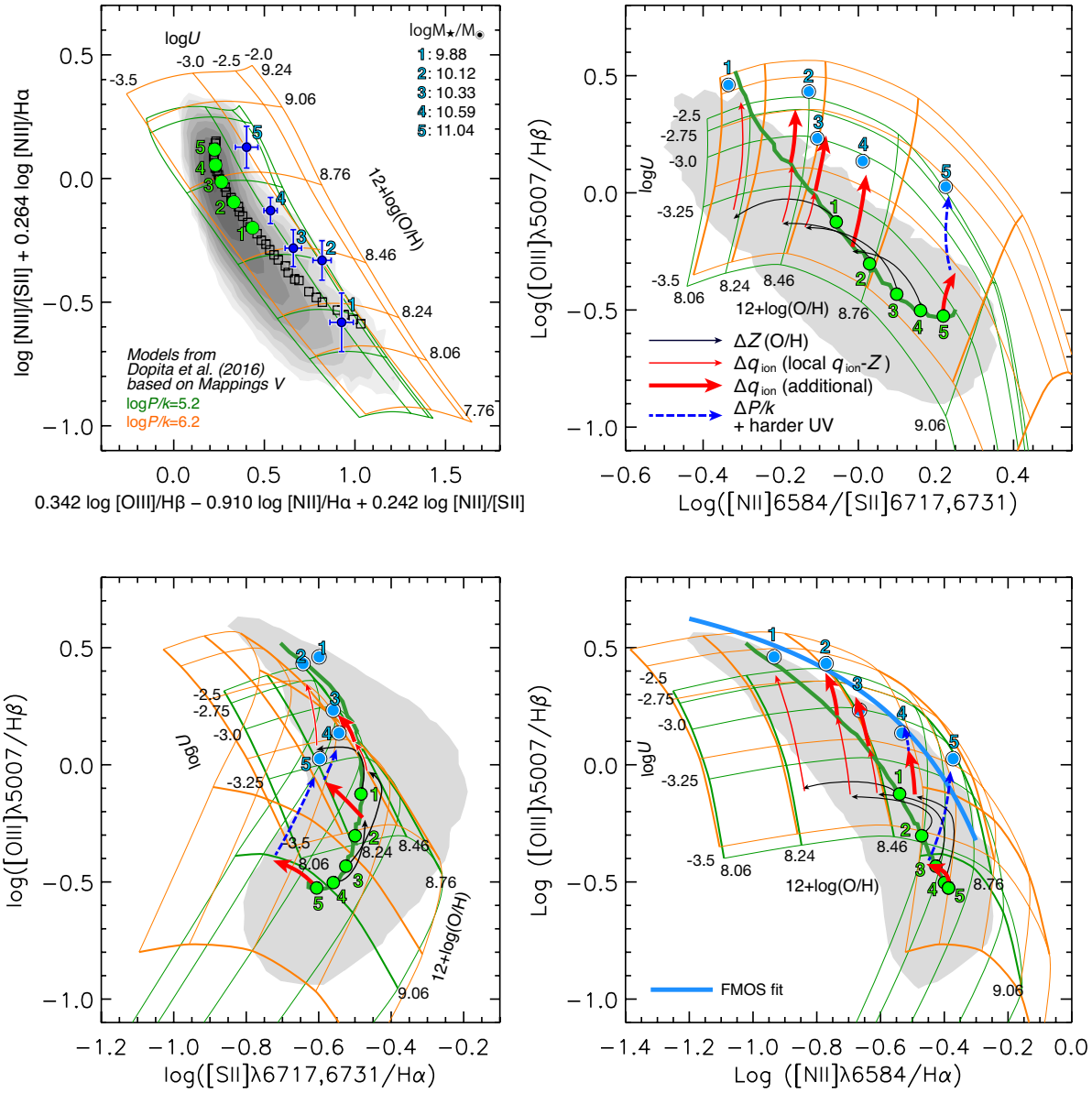

Figure 4.13: Emission line ratios of low-z and high-z (FMOS) samples in comparison with theoretical model grids for varying metallicity (12 + log(O/H)), ionization parameter ($U = q_{\rm ion}/c$), and gas pressure (P). (a) Comparison of combinations of line ratios, as presented in Figure 2 of Dopita et al. (2016), indicating a ~ 0.3 dex enhancement of the ionization parameter (U) in high-z galaxies relative to local galaxies. Average measurements are based on stacked spectra in five stellar mass bins (large blue circles), increasing from the bottom (no. 1) to top (no. 5). The median M_* are given in the upper right corner. Shaded contours show local star-forming galaxies, with their stacks in forty mass bins (squares) or the same bins as the FMOS sample (green circles, labelled as #1–5). Panels (b–d) Line-ratio diagrams comparing high-z and local galaxies at the same stellar masses, on the [N II]/[S II] vs. [O III]/Hβ (b), the [S II]-BPT (c), and the BPT (d) diagrams. The average values of our FMOS and local samples are the same in all panels. Average values for low-z galaxies split into 40 M_* bins are indicated by a thick green line. Arrows indicate changes in the emission line properties for the each factor separately (black thin arrows – decrease in metallicity; red thin arrows – enhancement of ionization parameter expected from the local $q_{\rm ion}$–Z anti-correlation; red thick arrows – excessive enhancement of ionization parameter; dashed arrows – remaining effects possibly due to high gas pressure and harder radiation field) A shaded region indicates an outline of distribution of local star-forming galaxies.

By comparing with the models shown in Figure 4.13 (a), it is clearly evident that galaxies in our sample, except for the lowest mass galaxies ($M_* < 10^{10}\ M_\odot$), have ionization parameters $\log U \sim -3$, approximately 0.2–0.3 dex higher, on average, than that of local star-forming galaxies, even if a higher gas pressure is considered. Our results are consistent with previous studies showing that typical high-z ($0.5 \lesssim z \lesssim 3$) galaxies have $q_{\rm ion}$ elevated by a factor of $\sim$ 2–10 compared with local galaxies (e.g., Shirazi et al. 2014; Nakajima & Ouchi 2014; Hayashi et al. 2015; Onodera et al. 2016). Here, it is important to consider an anti-correlation between $q_{\rm ion}$ and Z seen in local galaxies at $12+\log({\rm O/H}) \lesssim 8.6$ (see e.g., Kojima et al. 2016), which is evident in panels (b) and (d). Therefore, we consider an enhancement in $q_{\rm ion}$ to have two different contributions: 1) one expected from the decrease in Z based on the local $q_{\rm ion}$–Z anti-correlation and 2) an additional excess for high-z galaxies. From panel (a), it is likely that our FMOS sample shows an excessive enhancement in $q_{\rm ion}$, i.e., higher $q_{\rm ion}$ *at fixed* Z, except for the lowest mass bin.

In panels (b–d), a shift of line ratios corresponding to $\Delta q_{\rm ion}$ is shown , following a shift due to a change in metallicity, separately for the two effects (i.e., due to local $q_{\rm ion}$–Z relation and an additional contribution). There is no shift due to the local $q_{\rm ion}$–Z relation for the two highest mass bins (blue circles labelled as #4–5) since the changes in Z is enough small as compared to those of local galaxies (green circles). In panel (c), the shift towards both lower [S II]/Hα and higher [O III]/Hβ due to higher $q_{\rm ion}$ is clearly shown, especially, in the most massive bin; it is clear that the only factor that can produce a shift towards left is an enhancement in $q_{\rm ion}$. For the two intermediate mass bins (green circles labelled as #2–3), the enhancement in $q_{\rm ion}$ is clearly evident and not fully accounted by that expected from the $q_{\rm ion}$–Z relation. Thus, it is evident that an enhancement, independent of $q_{\rm ion}$–Z relation, is required to fully produce the offset of high-z galaxies in the emission line diagrams. We note that, for the lowest mass bin (green circle #1), the entire enhancement in $q_{\rm ion}$ is expected from the local $q_{\rm ion}$–Z relation anti-correlation.

Additional effects (ISM gas density and hardness of the radiation field

While a higher [O III]/Hβ ratio likely indicates an an enhancement of ionization parameter, we do not rule out that additional factors may be contribute these higher ratios since [O III]/Hβ increases with a higher gas density and a harder ionizing radiation field. In particular, the significance of additional effects is clearly sown in the [S II]–BPT diagram (panel c), in which a higher $q_{\rm ion}$ will shift the line ratios towards upper left (thick red arrow), an additional shift towards upper right is also needed (blue dotted arrow). We attribute the latter effect to a higher gas pressure, supported by the observed high electron density (see §4.3.4), as demonstrated by the theoretical grids of different P/k. The remaining shift is, however, unlikely to be fully explained by a higher gas pressure. Therefore, we surmise that a harder ionizing radiation field probably plays a significant role as well, especially in the most massive high-z galaxies ($M_* \gtrsim 10^{10.8}\ M_\odot$), while it is unachievable to confirm the hardening of the radiation field with our current data.

To conclude, we find that it is likely that all three factors contribute to changes in line ratios at high redshift. Based on our observations and comparison with the models, we argue the following: (1) High-z galaxies have a higher $q_{\rm ion}$ as compared to local galaxies at the same stellar mass. (2) The enhancement in $q_{\rm ion}$ is larger at $M_* \gtrsim 10^{10}\ M_\odot$ than that expected from the $q_{\rm ion}$–Z anti-correlation seen in local galaxies. (3) High gas density (pressure) and hardening of the ionizing radiation field are required to fully explain the high-z emission line properties, especially at the most massive end. Based on these points, we advocate an elevation of the ionization parameter *at fixed metallicity* s a primary origin of the BPT offset of high-z galaxies.

4.4.2 What causes an enhancement of ionization parameter?

Following the above discussions, we consider how the characteristics of H II regions in high-z star-forming galaxies re different from those in local galaxies. If a fixed inner radius of an ionized gas sphere is assumed, the ionization parameter is inversely proportional to the gas density (see Appendix B). Therefore, with the higher gas density of our sample (§4.3.4), a higher $q_{\rm ion}$ requires an increase in the production rate of ionizing photons. An enhancement of the ionizing photon flux in individual H II regions could be simply expected to occur when a large number of stars form in each gas cloud as compared to local galaxies (Kewley et al. 2015). Further, it could also arise due to harder stellar spectra, which induces additional changes in line ratios, as discussed above. A hardening of the overall stellar radiation field is probably caused by a top-heavy IMF that increases the relative amount of hot massive stars, a metal-poor stellar population that will have a harder spectrum (see e.g., Levesque et al. 2010), or existence of massive binaries (Steidel et al. 2016), while it is difficult to estimate the intrinsic shape of the spectrum of the ionizing radiation field in high-z galaxies.

Alternatively, we could consider the effects from low density (~ 0.1 cm^{-3}) diffuse ionized gas in galaxies, which is ionized by radiation from hot massive stars as well as (bright) H II regions (e.g., Reynolds 1984, 1992; Domgorgen & Mathis 1994). In a galaxy-wide spectrum, the nebular emission consists of the combination of emission from individual H II regions and a more diffuse ionized gas, which is known to have a very low ionization parameter, as compared to dense H II regions, as indicated by weak [O III] lines (Domgorgen & Mathis 1994). Therefore, the contribution from diffuse ionized gas may decrease an effective value of $q_{\rm ion}$ estimated from a galaxy-wide spectrum, although such effects have not been well understood yet. To further investigate the effects from diffuse ionized gas, we use observational data of individual H II regions in local spiral galaxies from van Zee et al. (1998) for comparison with our observational data. In Figure 4.14, we present the BPT and [S II]-BPT diagrams with these measurements. The data of individual H II regions cover a wide range of each emission line ratio, as spanned by local galaxies, and well traces the abundance sequence of local galaxies in the BPT diagram. Therefore, the offset of high-z galaxies remains in comparison with local individual H II regions. In contrast, individual H II regions are shifted towards lower [S II]/Hα ratios (Figure 4.14 (b)) at $\log$[O III]/H$\beta > -0.5$. Such smaller [S II] ratios are likely to be observed as a result of the fact that [S ii] line fluxes from photodissociation regions, which extend around H II regions, are missed in the observations. Therefore, we conclude that, although the diffuse gas ionized gas may play a role in part, the changes in the contribution from diffuse ionized gas do not fully explain the changes in the observed emission line ratios in high-z galaxies.

4.4.3 Enhancement of N/O

Previous studies have reported a lack of any significant offset between local and high-z galaxies in the [S II]-BPT diagram, as an indication that the offset in the BPT diagram is caused by another effect than a higher ionization parameter or a harder ionizing radiation field (Masters et al. 2014; Shapley et al. 2015). An elevated nitrogen-to-oxygen (N/O) abundance ratio at a given O/H has been suggested as such a possible cause of the BPT offset towards large [N II]/Hα at a fixed [O III]/Hβ (e.g., Masters et al. 2014; Steidel et al. 2014; Shapley et al. 2015; Yabe et al. 2015; Sanders et al. 2016; Cowie et al. 2016; Masters et al. 2016). However, the quantitative constraint of N/O–O/H calibration absolutely requires a metallicity determination that is independent of N abundance (e.g., direct $T_{\rm e}$ or R_{23} index) and a reliable measurement of N/O of high-z galaxies. While our existing data cannot solve these problems, future [O II]$\lambda\lambda$3726, 3729 follow-up observations will permit to further study these issues.

We highlight that a recent study by Steidel et al. (2016) found by using a composite spectrum of $z \sim 2.4$ galaxies that their average N/O and $T_{\rm e}$-based O/H are in excellent agreement with the local N/O-O/H relation. Thus, it is conceivable that an enhanced N/O is not the main

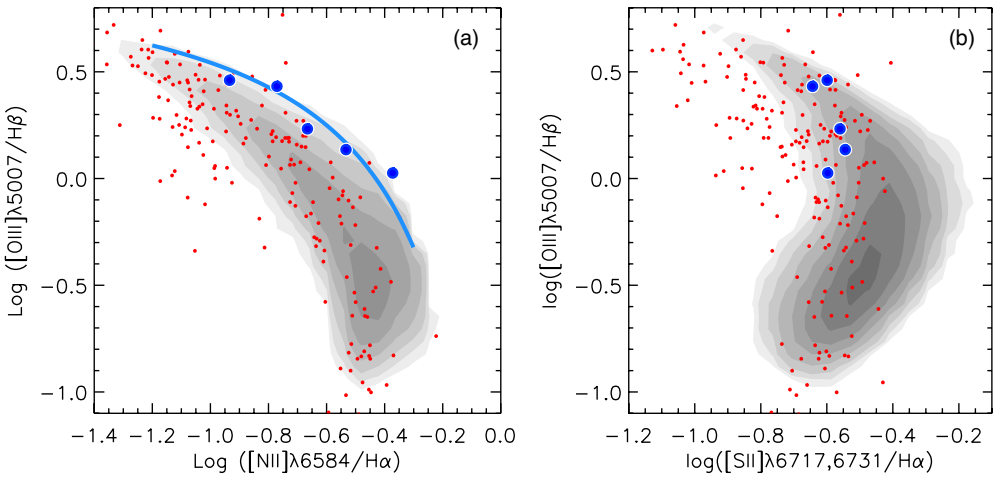

Figure 4.14: The BPT diagram (panel a) and the [S II]-BPT diagram (b). Blue circles indicate the stacks of our FMOS sample in five mass bins. Local star-forming galaxies are shown by gray contours. For comparison, the measurements of individual H II regions in local spiral galaxies by van Zee et al. (1998) are shown with red circles.

factor of the BPT offset at high redshifts. Lastly, we also note that Masters et al. (2016) recently concluded that a higher N/O ratio at fixed ionization parameter results in an offset of the locus of the local sequence in the BPT diagram to the right in [N II]/Hα. Since the N/O ratio is a proxy of the chemical evolution (see §4.3.5 and §4.6.2), their argument is almost equivalent, but from an opposite point of view, to our conclusion.

4.5 Assessment of AGN contamination

As described in §4.2.5, we remove AGNs from our star-forming galaxy samples for all analyses in this Chapter. Our data, as presented on line-ratio diagrams (Figures 4.6, 4.9 and 4.10), shows no strong signature of ionizing radiation from AGN. However, the possibility that weak and/or obscured AGNs affect the results cannot be completely ruled out. Here, we assess the contribution of such hidden AGNs on the results based on the co-added spectra.

X-ray emission is an effective indicator of the existence of an AGN. We measure the average X-ray luminosities by stacking the *Chandra X-ray Observatory*/Advanced CCD Imaging Spectrometer (ACIS) *I* images from the *Chandra*-COSMOS Legacy survey (Elvis et al. 2009; Civano et al. 2016) by using the CSTACK tool[4] (v4.3; Miyaji et al. 2008). To examine how the X-ray luminosity depends on the exclusion of individually-detected AGN, we compare three samples with different criteria of the removal of possible AGNs; 1) no AGN cut is applied, 2) excluding individual X-ray detected sources, and 3) excluding all possible AGN candidates (X-ray sources, FWHM(Hα) $>$ 1000 km s^{-1}, or identified with the BPT diagram; see §4.2.5). The last case is implemented for the results based on stacking analysis throughout the Chapter. Figure 4.15 shows the stacked X-ray images, separately in two bandpasses (soft: 0.5–2 keV, hard: 2–8 keV), from the two samples without (case 1) and with (case 3) AGN removal. We combine the images in five bins of stellar mass. Therefore, we have no X-ray image for the $\sim$ 10% of objects in our sample, which are not considered for the X-ray stacking analysis.

The average count rate is converted into flux assuming a spectrum with $\Gamma = 1.7$ and a Galactic column density $N_{\rm H} = 2.7 \times 10^{20}$ cm^{-2} (Elvis et al. 2009; Dickey & Lockman 1990). The average rest-frame X-ray luminosity is calculated as Equation 4 in Lehmer et al. (2008), with a

[4] http://cstack.ucsd.edu/cstack/

median redshift. Table 4.4 lists the X-ray luminosities and associated errors in each bin. When no AGN cut is applied (case 1), the X-ray emission is significantly detected in the two most massive bins at $S/N > 5$ in both the soft and hard bandpasses. When the AGN cut is applied (case 2 and 3), only the most massive bin ($\log M_*/M_\odot > 11.1$) presents a significant detection ($S/N > 3$) in the X-ray band. In the third and forth bins ($10.4 < \log M_*/M_\odot < 11.1$), the X-ray emission is detected at a significance of $S/N \sim 2$–3. There are cases with no detection ($S/N < 1$) in the lowest two mass bins, in which there is no or a few objects that are individually detected in the X-ray band (see Table 4.4).

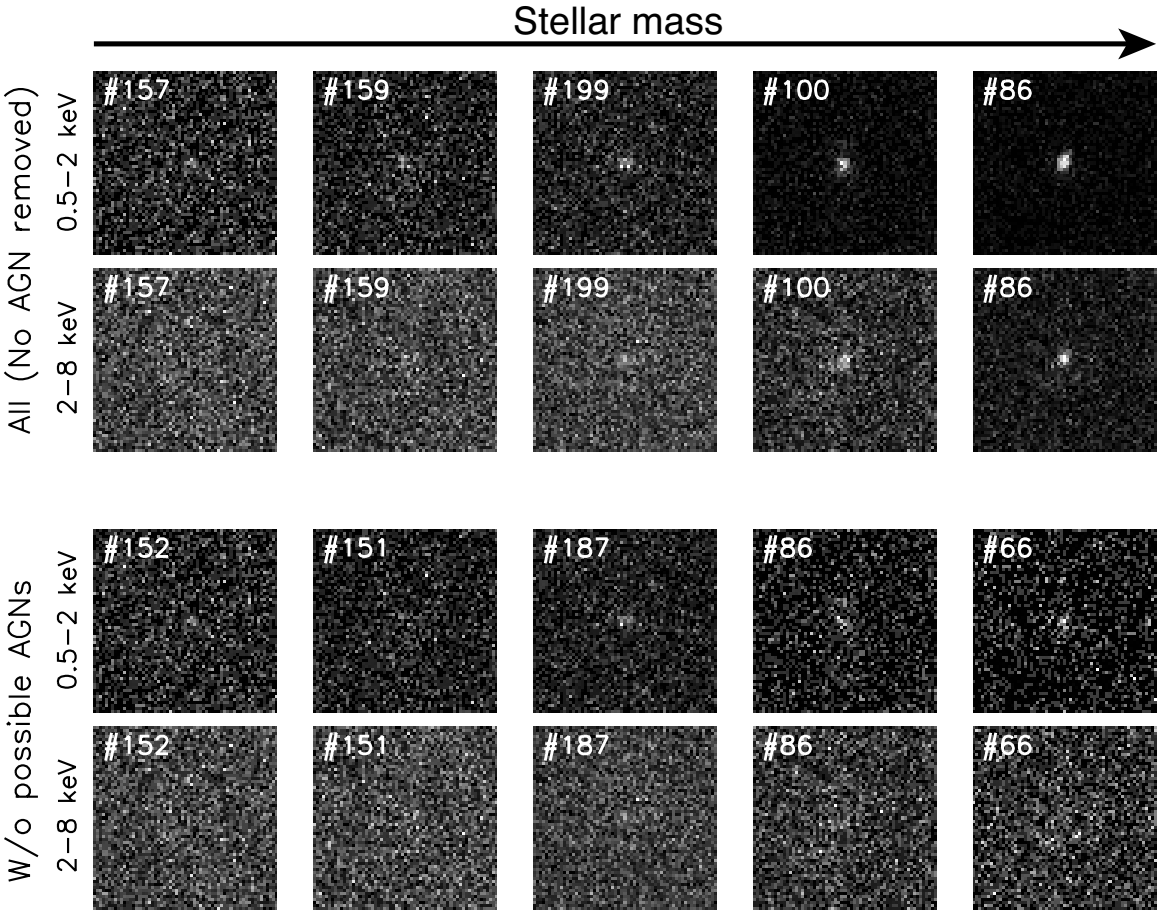

Figure 4.15: Chandra stacked images (30 arcsec on each side) in two bandpasses (soft: 0.5–2 keV, hard: 2–8 keV) of our sample in five bins of stellar mass. The number of individual images for stacking is indicated in each panel. The upper group shows the stacked images for the sample including all SED-selected galaxies without any removal of possible AGNs (case 1) in each stellar mass bin. The lower group shows for the sample in which all AGN candidates are removed (case 3) for the same stellar mass ranges as above. The stellar mass increases from left to right (see Table 4.4).

To further investigate the presence of AGN, we compare the mean SFR and mean X-ray luminosity of the full *Chandra* bandpass ($L_{0.5-8\ \mathrm{keV}}$) in each bin in Figure 4.16. The mean SFRs are derived from dust-corrected Hα luminosity (see §4.2.6). Following Lehmer et al. (2008), we compare our data with an SFR–$L_{\mathrm{X-ray}}$ relation for star-forming galaxies derived by Persic & Rephaeli (2007) and a relation with three times large X-ray luminosity, which corresponds to ~ 2.5 times the rms scatter of the mean L_X–SFR relation, to distinguish AGNs from non-AGN. We compare the measurements for the samples with the different X-ray exclusion criteria (cases 1, 2, and 3). We see that $L_{0.5-8\ \mathrm{keV}}$ is correlated with SFR at SFR $\gtrsim 100\ M_\odot \mathrm{yr}^{-1}$ ($M_* \gtrsim 10^{10.4} M_\odot$) in all the cases and that the removal of individual X-ray detected sources primarily affects the

Table 4.4: X-rat luminosity measurements

Median $\log M_*/M_\odot$ [a]	9.93	10.26	10.60	10.96	11.25
Range	[9.1:10.1]	[10.1:10.4]	[10.4:10.8	[10.8:11.1]	[11.1:11.7]
Case 1: No AGN exclusion applied					
No. of images[b]	157	159	199	100	86
Soft[c]	0.114 ± 0.079	0.321 ± 0.086	0.281 ± 0.077	1.199 ± 0.132	2.462 ± 0.180
Hard[d]	< 0.748[f]	0.582 ± 0.504	0.825 ± 0.443	3.261 ± 0.664	7.252 ± 0.803
Full[e]	< 0.758	0.902 ± 0.511	1.106 ± 0.450	4.460 ± 0.677	9.714 ± 0.823
Case 2: X-ray luminous objects removed					
No. of images	157	156	195	93	78
Soft	0.114 ± 0.079	0.236 ± 0.086	0.230 ± 0.076	0.424 ± 0.115	0.484 ± 0.134
Hard	< 0.748	< 0.759	0.740 ± 0.443	1.572 ± 0.657	3.431 ± 0.776
Full	< 0.758	0.613 ± 0.513	0.970 ± 0.449	1.997 ± 0.667	3.916 ± 0.788
Case 3: All possible AGNs removed					
No. of images	152	151	187	86	66
Soft	< 0.121	0.214 ± 0.086	0.201 ± 0.078	0.452 ± 0.122	0.497 ± 0.145
Hard	< 0.767	< 0.774	0.832 ± 0.453	1.480 ± 0.681	2.872 ± 0.840
Full	< 0.776	< 0.785	1.034 ± 0.459	1.932 ± 0.692	3.369 ± 0.852

[a] Median stellar mass each mass bin.
[b] Number of stacked images in each bin of the soft band.
[c] Soft band (0.2–2 keV) luminosity in units of 10^{42} erg s^{-1}.
[d] Hard band (2–5 keV) luminosity in units of 10^{42} erg s^{-1}.
[e] Full band (0.5–8 keV) luminosity in units of 10^{42} erg s^{-1}.
[f] Upper limits are given as 1.5 times of noise levels if $S/N < 1$.

average X-ray luminosity of the more massive bins. As a result of the AGN exclusion, the X-ray luminosities are reduced down to the level where the residual contribution from AGNs likely to be negligible in three larger stellar mass bins. For two lower mass bins, upper limits on $L_{0.5-8\ \mathrm{keV}}$ are calculated as 1.5 times the noise level shown by the downward arrows.

Figure 4.16 indicates that, once the individually detected AGNs are removed, the contribution to the X-ray luminosities in the stack from unidentified AGNs is small, and that levels of the residual X-ray luminosity are comparable to the levels that are normally expected for star-forming galaxies (solid line in Figure 4.16). While the limit of the lowest mass bin does not reject a probability that a contribution from AGNs exists, the AGN contribution can be expected to be negligible in such a range of stellar mass. Therefore, we conclude that the impact from AGN are small in our stacking analysis enough to appropriately assess the properties of star-forming H II regions over the entire stellar mass range spanned by our sample.

4.6 Chemical enrichment of interstellar medium

We previously reported the metallicity measurements of individual galaxies and the average mass–metallicity (MZ) relation based on our FMOS program (Zahid et al. 2014b) using a smaller subset (162 galaxies) of the current data set with an sBzK selection (Daddi et al. 2004). Our MZ relation indicated that the most massive galaxies at $z \sim 1.6$ are fully mature similar to local massive galaxies while the lower mass galaxies are less enriched as compared to local galaxies at a fixed stellar mass. The difference in average metallicity increases with decreasing mass, and reaches approximately 0.5 dex at $M_* = 10^{10}\ M_\odot$. Here, we revisit the MZ relation using a sample four times larger than presented in Zahid et al. (2014b). In particular, the number of massive ($M_* > 10^{11}\ M_\odot$) galaxies in the sample is larger by an order-of-magnitude.

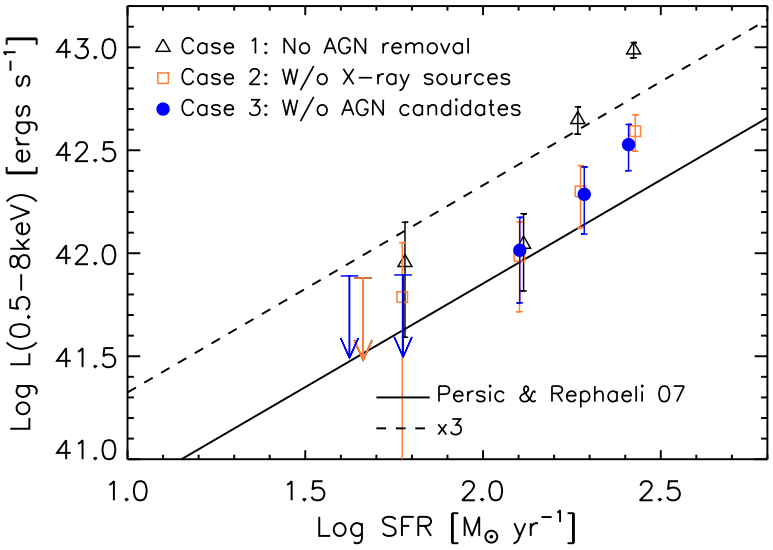

Figure 4.16: Comparison between the mean SFR (from dust-corrected Hα luminosity) and the 0.5–8 keV luminosity $L_{0.5-8\ \mathrm{keV}}$ in each bin of stellar mass. The X-ray luminosities $L_{0.5-8\ \mathrm{keV}}$ are measured by stacking the Chandra ACIS-I images. Different symbols shows the measurements for different cases of the AGN removal (triangles; no AGN removed, squares: without Chandra X-ray detected sources, filled circles: without all potential AGN candidates; see the text). An SFR–L_{X} relation for star-forming galaxies from Persic & Rephaeli (2007) and a relation with three times larger $L_{0.5-8\ \mathrm{keV}}$ are shown by the solid and dashed lines, respectively.

4.6.1 Empirical metallicity determination using [N II]/Hα

We use the line ratio [N II]/Hα to evaluate the gas-phase metallicity, i.e., the oxygen abundance normalized by 10^{12} hydrogen atoms, $12 + \log(\mathrm{O/H})$. The advantage of using this ratio is the close spectral proximity of the lines thus not requiring any correction for extinction. The high-resolution mode of FMOS cleanly separates the two lines. However, [N II]/Hα is sensitive to the ionization parameter and hardness of the ionizing radiation field. At fixed metallicity ($12 + \log(\mathrm{O/H}) = 8.5$), a 0.5 dex increase in q_{ion} produces a decrease in [N II]/Hα, leading to a ~ 0.4 dex underestimate of metallicity (Kewley & Dopita 2002).

Furthermore, metallicities based on the [N II] line depends on the relation between the N/O and O/H ratios. Any locally-calibrated empirical metallicity indicators implicitly rest on the assumption of a universal (locally-calibrated) N/O vs. O/H relation, as well as theoretical calibrations, while it is not ensured for high-z galaxies. Dopita et al. (2016) argue that changes in the emission line properties of high-z galaxies can be explained by changes in the ionization parameter and gas pressure, without resorting to an explanation based on differences in the N/O vs. O/H relation (see also §4.6.2). However, the chemical evolutionary stage of high redshift galaxies, specifically concerning nitrogen enrichment, is unlikely to be the same as in local galaxies. Indeed, an enhancement of N/O at a fixed O/H has been advocated to explain the offset in the BPT diagrams of high-z galaxies (see §4.4.3). Moreover, fluctuations in the gas content of galaxies in response to high accretion rates, would affect O/H but not the N/O ratios (see Kashino et al. 2016; Masters et al. 2016). It is clear that a direct calibration of the relation between N/O and O/H is required to improve upon metallicity determinations of high-z galaxies.

With this caveat in mind, we estimate the metallicities of both local galaxies and the FMOS sample based on a locally-calibrated relation. The line ratio is converted to metallicity as given

in Maiolino et al. (2008):

$$N2 = -0.7732 + 1.2357x - 0.2811x^2 - 0.7201x^3 - 0.3330x^4 \quad (4.7)$$

where $N2 = \log([\mathrm{N\,II}]\lambda6584/\mathrm{H}\alpha)$ and $x = 12 + \log(\mathrm{O/H}) - 8.69$. This relation is nearly linear over the metallicity range of interest ($8 < \log(\mathrm{O/H} < 9$), while at higher metallicity (above $N2 \sim -0.3$) the line ratio begins to saturate (Maiolino et al. 2008). This saturation is the result of metal cooling, which leads to a decrease in the collisional excitation rate of N^+ (Osterbrock & Ferland 2006).

Figure 4.17 (a) shows the $[\mathrm{N\,II}]\lambda6584/\mathrm{H}\alpha$ ratio as a function of stellar mass. We plot 436 galaxies with Hα and [N II] detections in Sample-1. The FMOS sample has a broad distribution of $[\mathrm{N\,II}]/\mathrm{H}\alpha$ that spans much of the SDSS locus (see also Zahid et al. 2014b). Many galaxies with less secure measurements ($1.5 < S/N([\mathrm{N\,II}]) < 3$) have a low $[\mathrm{N\,II}]/\mathrm{H}\alpha$ ratio. This is expected because the intensity of the [N II] line is generally much weaker than Hα and difficult to detect with FMOS for a reasonable amount (∼a few hours) of integration time. It is also shown that 54 galaxies have a high [NII]/Hα ratio ($N2 > -0.2$, 12% of sources with the $[\mathrm{N\,II}]/\mathrm{H}\alpha$ measurement) The locus of such a population shows good agreement with the distribution of the local AGN population. In contrast, however, roughly half of the X-ray-detected sources are located at lower $[\mathrm{N\,II}]/\mathrm{H}\alpha$, consistent with local star-forming galaxies, while the others show higher $N2$ values, especially at high masses. This possibly suggests that AGNs are presented in our sample if there is no prior exclusion, especially, at high stellar masses (Mancini et al. 2015), and that the presence of the X-ray observations is important to construct a sample of pure star-forming galaxies.

To overcome the low S/N of individual detections of the [N II] line, we plot, in Figure 4.17 (b), the metallicities based on the average $[\mathrm{N\,II}]/\mathrm{H}\alpha$ ratios measured from the stacked spectra for Sample-1 split into eight bins of stellar mass (see Table 4.3). Average spectra reduce the bias with respect to detecting [N II] since galaxies are only identified by the presence of an Hα detection. As described in §4.2.5, we remove galaxies identified as AGN based on the BPT diagram (or $N2 > -0.1$ if no $[\mathrm{O\,III}]/\mathrm{H}\beta$ measurement is available), X-ray detection, or FWHM> 1000 km/s. For the local galaxies, we take the median $[\mathrm{N\,II}]/\mathrm{H}\alpha$ ratios in 50 bins of stellar mass, shown by squares with the 16 and 84 percentiles of the metallicity. Both the local and the FMOS samples are well fit with a model from Zahid et al. (2014a). The model fit and the interpretations are fully described in §4.6.3.

Our data show a level of metallicity similar to local galaxies at the massive end ($M_* > 10^{11}\ M_\odot$), while the average measurements in less massive galaxies are lower than those in local galaxies. The difference in metallicity with the local sample extends down to our lower mass limit ($\sim 10^{9.6}\ M_\odot$). The average $[\mathrm{N\,II}]/\mathrm{H}\alpha$ measurements are consistent with the previous measurements from Zahid et al. (2014b, gray triangles in Figure 4.17 (b)). We further assess the effects of excluding potential AGN by their $[\mathrm{N\,II}]/\mathrm{H}\alpha$, particularly at the massive end. With an upper limit of −0.3 on individual values of $\log([\mathrm{N\,II}]/\mathrm{H}\alpha)$, the stacked measurements are still consistent with local massive galaxies, although the values are lower by $\Delta \log(\mathrm{O/H}) \sim 0.15$.

In Figure 4.17 (b), we also show MZ relations based on $[\mathrm{N\,II}]/\mathrm{H}\alpha$ from the literature at $z \sim 1.4$–2.3 (Erb et al. 2006; Yabe et al. 2014, 2015; Steidel et al. 2014), which are converted here to Salpeter IMF and the Maiolino et al. (2008) metallicity calibration. Our measurements are nearly in agreement with the measurements by Yabe et al. (2014) also based on FMOS observations.

Here, we note that that the $[\mathrm{N\,II}]/\mathrm{H}\alpha$ ratios are expected to weakly depend on the Hβ luminosity, $L(\mathrm{H}\beta)$. Given the typical $\log L(\mathrm{H}\beta)/(\mathrm{erg\ s^{-1}}) \sim 41.5$–42 in our sample (see Silverman et al. 2015), the luminosity-adjusted O/H vs. $N2$ relation derived by Cowie et al. 2016, which encloses the systematic effects due to the change in the ionization parameter as well, reduces the difference between the derived MZ relations at $z \sim 0$ and $z \sim 1.6$ by ~ 0.15–0.2 dex. In this case, however, it is still seen that the metallicities of high-z galaxies with $M_* \sim 10^{10}\ M_\odot$

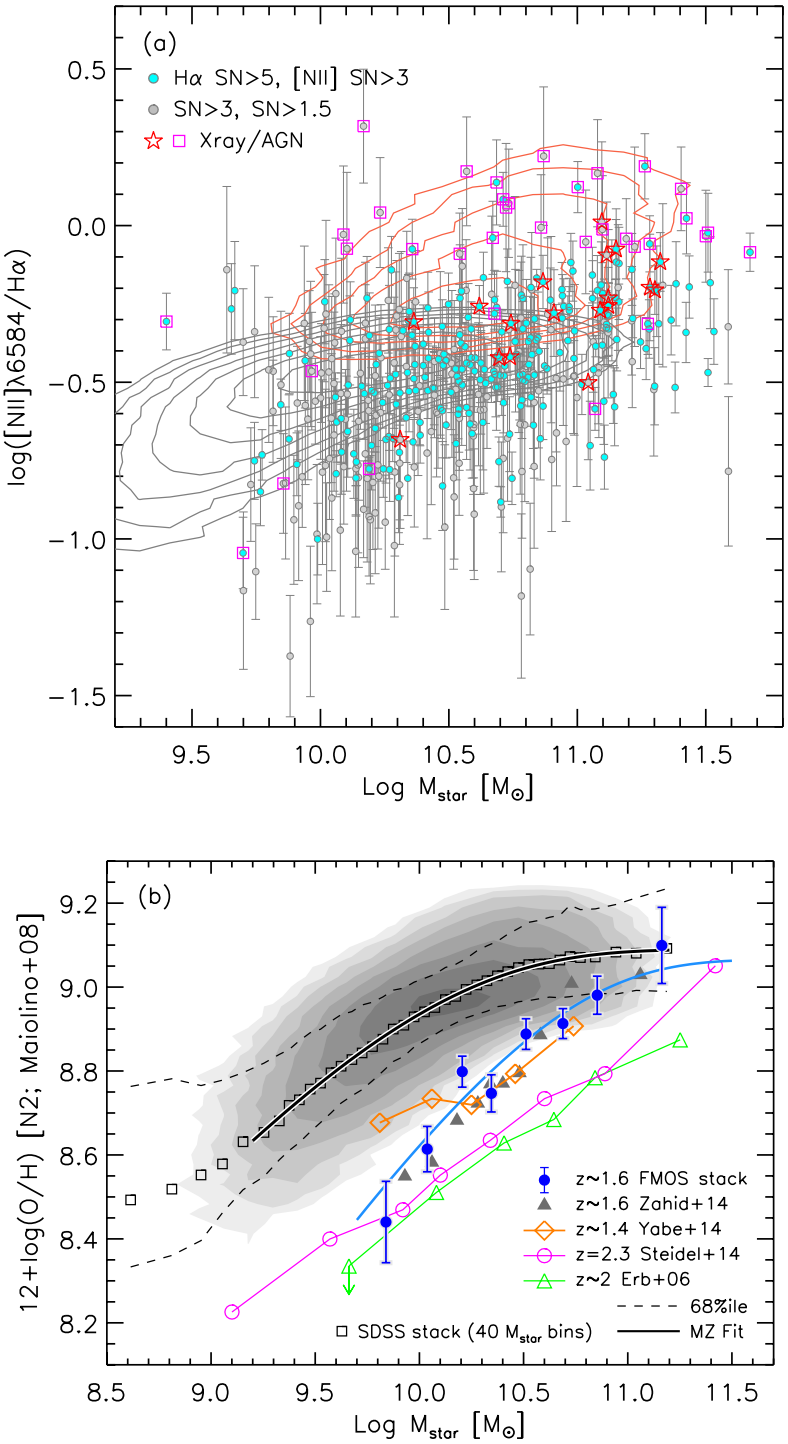

Figure 4.17: Mass–metallicity relation. (a) [N II]/Hα as a function of stellar mass. Individual FMOS galaxies are shown with the quality of measurement as labelled (cyan, $S/N > 3$ for Hα and [N II] lines; gray, $S/N(\mathrm{H}\alpha) > 3$ and $1.5 < S/N([\mathrm{N\,II}]) < 3$). AGN candidates are highlighted by stars (X-ray detected sources) and magenta squares (others). Contours show the distribution of the local star-forming galaxies (gray) and AGNs (red). (b) Mass–metallicity relation. The oxygen abundance is calculated from the average [N II]/Hα ratio with Equation 4.7. The [N II]/Hα ratios of Sample-1 are measured based on the stacked spectra in eight mass bins (filled circles). Filled triangles indicate our previous measurement from Zahid et al. (2014b). Empty symbols show the measurements in the literature as labelled. Shaded contours show local star-forming galaxies, with the mean line ratios of the local galaxies divided in 40 stellar mass bins (squares) and the 68th percentile (dashed lines). Solid curves show the best-fit relations parametrized in Equation 4.9, for the FMOS (blue) and the local (black) samples.

are smaller than those seen in local galaxies at the same stellar mass. While we recognize that there are some systematic biases between the metallicity determination at different samples at two epochs, the later part of the paper basically uses the MZ relation from the locally-calibrated metallicity indicators without any specific correction.

4.6.2 New calibration with [N II]/[S II]

Recently, Dopita et al. (2016) have introduced a new metallicity calibration using both the line ratios [N II]/Hα and [N II]/[S II]. This calibration is almost independent of the ionization parameter and gas pressure, effective over the metallicity range of $8 < 12 + \log(\mathrm{O/H}) < 9$, expressed as follows:

$$12 + \log(\mathrm{O/H}) = 8.77 + N2S2 + 0.264N2 \tag{4.8}$$

where $N2S2$ is defined as Equation 4.6. The inclusion of the [N II]/[S II] term in the determination of the metallicity provides an assessment of how nucleosynthesis has proceeded through the ratio of secondary-to-primary elements. This calibration assumes a relation between the N/O ($\approx$N/S) ratio and the O/H ratio, as illustrated in Figure 1 of Dopita et al. (2016). Although the authors argue that it is not necessary to urge upon the changes in the N/O ratio at a fixed O/H to explain the emission line properties of high-z galaxies, it still remains unclear whether the assumption of a single N/O vs. O/H relation is proper at higher redshifts (and even for local galaxies). Moreover, this relation assumes a one-to-one relation between N/S and N/O, i.e., a constant S/O. We note that variation of the S/O ratio is expected to be small ($\sim$ 0.1 dex), and indeed the S/O ratio is almost independent of metallicity (Izotov et al. 2006), which support the use of the [N II]/[S II] ratio as a proxy of the N/O ratio (Pérez-Montero & Contini 2009).

With these considerations and caveats in mind, we present in Figure 4.18 the MZ relation with metallicity determined from Equation 4.8 for both local and our high-z galaxies. Similar to the [N II]/[S II] ratio shown in Figure 4.12 (a), the metallicity in local star-forming galaxies begins to flatten at low masses ($M_* \lesssim 10^{9.2}\ M_\odot$), where primary component becomes comparable to the secondary one as the metallicity decreases. Except for the lo metallicity tail, the mean line ratios of local galaxies are well fit with the Zahid et al. (2014a) model, as well as the FMOS sample, similarly to the [N II]/Hα-based MZ relation (see §4.6.3). The MZ relation for the FMOS sample is qualitatively equivalent to the results based on the [N II]/Hα ratios (shown in Figure 4.17 (b)) in indicating that the metallicities of high-z galaxies are, on average, smaller than those in local galaxies at low masses, then increase with increasing stellar mass, reaching a level ($12 + \log(\mathrm{O/H}) \approx 8.9$) similar to local galaxies at $M_* \gtrsim 10^{11}\ M_\odot$. However, we note that the metallicity range spanned by our sample ($8 \lesssim 12 + \log(\mathrm{O/H}) \lesssim 8.9$) is slightly different from that in the case of the $N2$-based metallicity with the Maiolino et al. (2008) calibration ($8.4 \lesssim 12 + \log(\mathrm{O/H}) \lesssim 9.1$). We remind readers that there are likely systematic uncertainties in the absolute metallicity calibrations based on different techniques and/or indicators (e.g., Kewley & Ellison 2008).

In this analysis, we remove those with $N2 > -0.1$ to exclude strong AGNs (see §4.2.5). However, there still remain the possibility that the average [N II]/Hα measurements are enhanced by weak AGNs. Therefore, we examine if the metallicity measurements are affected by the changes in selecting which galaxies to stack. We lower the threshold to $N2 = -0.3$ thus excluding all galaxies with values above this limit. We find that galaxies at the high mass end still have metallicities in agreement with local massive galaxies. Therefore, we conclude that the most massive galaxies are fully matured, as reported when using the [N II]/Hα-based metallicity.

It is worth noting that the FMOS sample is more offset from the local relation in the $N2$-based metallicity (Figure 4.17 (b)), than that based on the Dopita et al. (2016) calibration. Here, the offset is measured by the width of the local relation (i.e., central 68th percentiles) of each case, instead of by the value of $\Delta \log(\mathrm{O/H})$. This is most likely explained by different sensitivity of the [N II]/Hα ratios and the Dopita et al. (2016) indicator on the ionization parameter. As

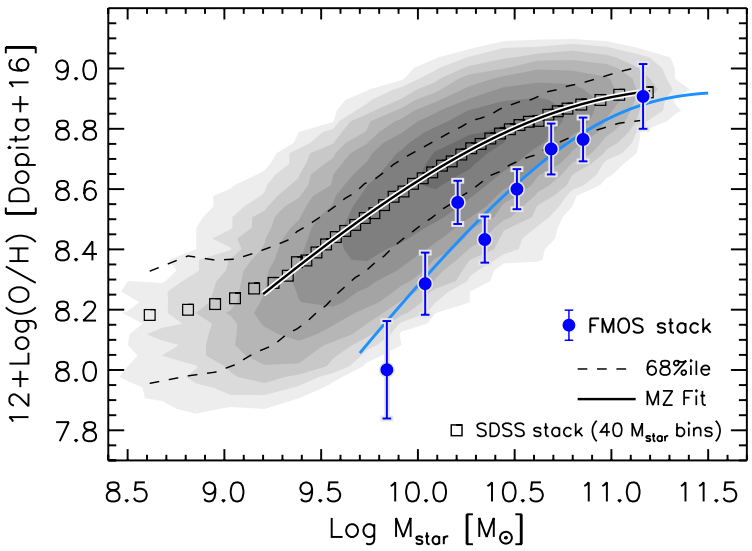

Figure 4.18: Mass–metallicity relation based on a calibration introduced by Dopita et al. (2016, Equation 4.8). Symbols are the same as those in Figure 4.17. Local galaxies are shown by shaded contours with mean values in 40 M_* bins (squares) and the 68th percentiles (dashed lines) in mass bins.

described above, the former is more sensitive, and decrease with increasing ionization parameter, while the latter is almost insensitive to it.

4.6.3 Evolution of the MZ relation

Zahid et al. (2014a) introduced the concept of a universal relation between metallicity and the stellar-to-gas mass ratio ($M_*/M_{\rm gas}$) as the underlying origin of the MZ relation. In this framework, an observed MZ relation can be parametrized as

$$12 + \log({\rm O/H}) = Z_0 + \log\left[1 - \exp\left(-\left[\frac{M_*}{M_0}\right]^{\gamma}\right)\right]. \tag{4.9}$$

Here, Z_0 is the asymptotic metallicity at the massive end. M_0 is the characteristic stellar mass where the relation begins to flatten, and γ is the power-law slope of the relation at $M_* \ll M_0$. Given the assumption of a power-law relation between stellar and gas mass, $M_{\rm gas} \propto M_*^{\delta}$ (Peeples et al. 2014), the term $(M_*/M_0)^{\gamma}$ approximately equals $(M_*/M_{\rm gas})$ and the slope γ is prescribed by the slope δ as $\gamma = 1 - \delta$.

We model the observed MZ relations based on both the two metallicity indicators described in §4.6.1 and §4.6.2 with Equation 4.9. This fitting function differs from the function used in our previous study (Zahid et al. 2014b) and has a more physically motivated form. We note that fitting the current measurements with the model given in Zahid et al. (2014b) yields results consistent with those found in our past study. The best-fit parameters in Equations 4.9 are listed in Table 4.5. For our sample, the stacked measurements in eight M_* bins are use for the fit. To derive the local MZ relation, we fit the same formulation to the median values in 35 stellar mass bins at $M_* > 10^{9.2}$ $M_\odot$. Our derivation at $z \sim 1.6$ is in agreement with an earlier version by Zahid et al. (2014a) accounting for the different methods to measure stellar mass and metallicity between the two studies.

In Figure 4.17 (b), the model well represents the observed MZ relations at $z \sim 0$ and $z \sim 1.6$. Z_0 and γ are statistically consistent between the two samples. Therefore, the evolution of the

Table 4.5: Best-fit parameters of the mass–metallicity relation (Equation 4.9)

Sample	Redshift[a]	Z_0[b]	$\log(M_0/M_\odot)$[c]	γ[d]
Indicator: Maiolino et al. (2008; Eq. 4.7)				
SDSS	0.069	9.089 ± 0.002	9.85 ± 0.01	0.559 ± 0.007
FMOS	1.55	9.07 ± 0.13	10.5 ± 0.4	0.71 ± 0.45
FMOS	1.55	[9.089][e]	10.60 ± 0.05	[0.559]
Indicator: Dopita et al. (2016; Eq. 4.8)				
SDSS	0.069	8.942 ± 0.004	10.30 ± 0.02	0.578 ± 0.005
FMOS	1.55	8.92 ± 0.26	10.7 ± 0.6	0.83 ± 0.47
FMOS	1.55	[8.942]	10.89 ± 0.08	[0.578]

[a] Median redshift of each sample.
[b] Asymptotic metallicity parameter in Equation 4.9.
[c] Characteristic mass.
[d] Power-law slope at $M_* \ll M_0$.
[e] Values given in square brackets have been fixed to the SDSS values.

MZ relation is quantified by the evolution of the turnover mass M_0, at which the metallicity begins to saturate. Motivated by this fact, we fit a model to our data with Z_0 and γ fixed to the local values ($Z_0 = 9.089$ and $\gamma = 0.559$; see Table 4.5). In this case, we find M_0 to be consistent with the case where Z_0 and γ are free parameters. Likewise, the model also well fit the local and high-z MZ relations based on the Dopita et al. (2016) metallicity indicator as shown in Figure 4.18. While the parameter constraints, especially M_0, are different from those based on the $N2$-based metallicity, both the consistency in Z_0 and γ between the two epochs and the decrease of M_0 with redshift are . Exactly speaking, the change in M_0 is not statistically significant in the case with three free parameters, while being confirmed when Z_0 and γ are fixed to the local values.

Figure 4.19 shows the relation between metallicity (from the [N II]/Hα ratio) and $\gamma \log(M_*/M_0)$ for the local sample ($\gamma = 0.56$) and the FMOS sample ($\gamma = 0.71$, filled circles; $\gamma = 0.56$, open circles). The measurements from our FMOS sample agree well with the local relation. Thus, our results strongly support the existence of the universal relation since $z \sim 1.6$ to the present day. In the context of the model underlying Equation 4.9, $(M_*/M_0)^\gamma \sim (M_*/M_{\rm gas})$, thus the observed decline of M_0 with cosmic time is simply interpreted as a result of gas consumption and stellar mass assembly through star formation. We also note that our results are consistent with a time-invariant slope of the M_*–$M_{\rm gas}$, while the errors on γ are too large to constrain its evolution (if any).

Moreover, selection effects may be present at low masses that impact our determination of γ. Our sample is potentially biased towards a population having high SFRs and being less obscured by dust. This bias may be induced by the observational limit of detecting Hα and the self-imposed selection on the predicted Hα flux. Metallicity is expected to be anti-correlated with SFR (see §4.7) and the amount of metal is commonly known to be correlated with the amount of dust (e.g., Issa et al. 1990; Schmidt & Boller 1993; Lisenfeld & Ferrara 1998). Therefore, such a selection may impact the shape of the MZ relation. In particular, the effects may be considerable at low masses because low mass dusty galaxies, which are expected to have a low Hα flux and to be more metal rich, tend to fall below our selection limit. In such cases, the measurements at the lower mass end may be biased towards lower metallicities, leading to a MZ relation with a steeper slope. Indeed, such biases arise in the local relation as well when a high S/N or luminosity threshold of the Hα line is applied for the selection. Selecting local galaxies

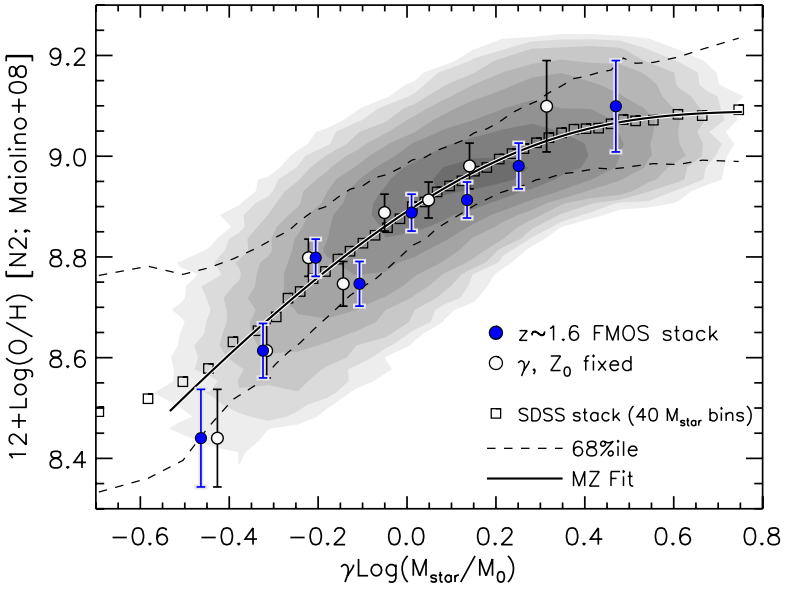

Figure 4.19: Metallicity vs. $\gamma \log(M_*/M_0)$, a proxy of stellar-to-gas mass ratio (see §4.6.3), for the local and FMOS samples. Filled circles indicate the average metallicity based on the Sample-1 co-added spectra in eight mass bins (same as in Figure 4.17 (b)). Open circles show our measurements with Z_0 and γ fixed to the local values. A solid curve is given by Equation 4.9 with the parameters that are determined from the SDSS sample. Dashed lines indicate the 68 percentiles. Excellent agreement between the two measurements at $z \sim 0$ and $z \sim 1.6$ suggests the existence of a universal relation between metallicity and stellar-to-gas mass ratio.

with $L(\mathrm{H}\alpha) \geq 10^{41}$ erg s^{-1} (with no corrections for aperture and dust) yields $\gamma = 0.62 \pm 0.02$ for the $N2$-based MZ relation. In contrast, however, we find that the slope of the local MZ relation based on the Dopita et al. (2016) indicator is almost insensitive to such luminosity threshold.

In Figure 4.17 (b), the MZ relations derived at higher redshifts ($z \gtrsim 2$, Erb et al. 2006; Steidel et al. 2014) show a clear correlation between stellar mass and metallicity. At the lowest mass ($M_* \sim 10^{9.8} M_\odot$), our sample is in agreement with the relations at $z \gtrsim 2$. In contrast, our sample galaxies are more enriched as compared to $z \gtrsim 2$ galaxies at $M_* \gtrsim 10^{10}$ $M_\odot$. The slope of the Steidel et al. MZ relation is found to be approximately 0.34, which is significantly shallower than those found in the relations at lower redshifts. However, the origin of the difference in the shape of the MZ relation is not clear. In contrast to Erb et al. (2006) and Steidel et al. (2014), Wuyts et al. (2014) reported that the shape of the MZ relation does not change up to $z \sim 2.3$ using a compilation of samples. As mentioned above, selection effects probably impact the shape of the MZ relation. In particular, there is the possibility that the $z \gtrsim 2$ samples that are shown in Figure 4.17 miss some of the dusty galaxies, which tend to be metal rich, because of their UV-based selection (Erb et al. 2006; Steidel et al. 2014).

4.7 Stellar mass–metallicity–SFR relation

Observations of an anti-correlation between metallicity and SFR at a fixed stellar mass have advocated a simple picture, in which inflows of metal-poor gas fuel star formation, while diluting gas-phase metal abundance (e.g., Ellison et al. 2008; Mannucci et al. 2010). Mannucci et al. (2010) proposed the so-called *fundamental metallicity relation* (FMR) and demonstrated that local star-forming galaxies, and also high-z ($\lesssim 2.5$) sources as well, follow such a single redshift-invariant relation. The actual shape of the FMR, however, is known to depend on the methodology

(see e.g., Andrews & Martini 2013; Kashino et al. 2016), while the existence of the SFR–Z anti-correlation has been accepted, at least for local lower mass galaxies ($M_* \lesssim 10^{10}$ $M_\odot$; see e.g., Yates et al. 2012). Beyond $z > 1$, however, it remains unclear both whether the Z-SFR anti-correlation exits and whether the FMR does evolve or not.

4.7.1 Metallicity–SFR anti-correlation

Most recent studies at $z \sim 2$ find no significant Z-SFR anti-correlation (Wuyts et al. 2014; Steidel et al. 2014; Sanders et al. 2015). In contrast, we previously reported on an Z-SFR anti-correlation, by using an sBzK-selected subset of the current data (Zahid et al. 2014b). Salim et al. (2015) also detected a weak Z–SFR anti-correlation at $z \sim 2$ based on individual measurements, as well as Guo et al. (2016b) do at $z \sim 0.6$. Salim et al. (2015) argue that binning by SFR (or sSFR) obscures such a weak SFR dependence of metallicity in noisy high-z data. With the current data, we examine again if the metallicity depends on SFR at a given stellar mass. Here, we use the [N II]/Hα ratios to determine the metallicities since the Dopita et al. (2016) indicator is known to be less sensitive to instantaneous fluctuations of the metallicity due to infalling gas (Kashino et al. 2016).

In Figure 4.20, we show the [N II]/Hα ratios as a function of specific SFR (sSFR = SFR/M_*). We use sSFR instead of SFR to avoid the effects from the underlying mass–metallicity strong correlation in broad mass bins. We find an anti-correlation between sSFR and Z at all masses, which is statistically significant, by fitting a log-liner function to the individual galaxies with a [N II]/Hα measurement. The anti-correlation is stronger for less massive galaxies. However, the bias concerning the detection of the faint [N II] line certainly exists in the individual measurement. In particular, the [N II] line in low metallicity galaxies, thus which tends to be much fainter than Hα, can be detected only when their sSFRs are high. Therefore, an sSFR–Z anti-correlation in individual measurements is expected to be caused, at least in part, by such a bias. Indeed, the stacked measurements from two subsamples binned by sSFR in each mass bin do not show any significant dependence of Z on sSFR, i.e., we do not confirm our previous results. While this contradiction is possibly due to the effects of sample selection, it is still desirable to further study this issue with a larger sample and accurate SFR estimation to constrain (possibly weak if any) correlation between metallicity and SFR.

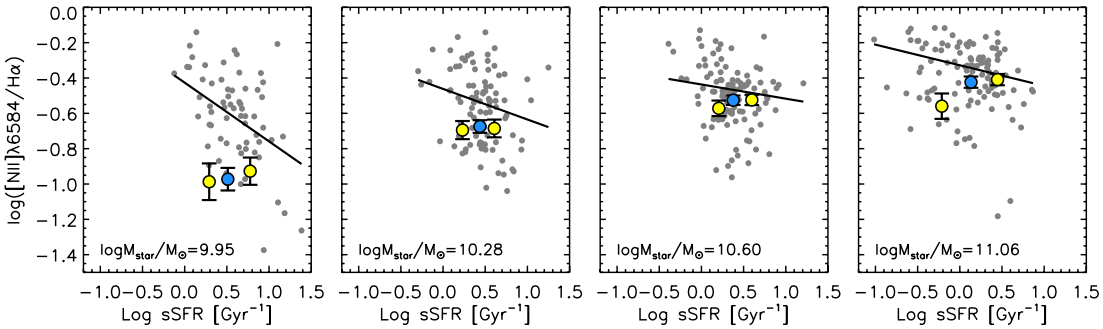

Figure 4.20: Specific SFR vs. [N II]/Hα in four bins of stellar mass (median M_* is shown in each panel). In each bin, stacked points of the full sample and two subsets separated by sSFR are shown by blue and two yellow circles, respectively. Individual FMOS galaxies with a [N II]/Hα measurement are shown as gray circles. Solid lines are linear fit to individual points in each bin. Individual points show significant sSFR–Z anti-correlation, while the stacks do not.

4.7.2 Fundamental metallicity relation

We examine the cosmic evolution of the relation between metallicity, stellar mass, and SFR. It is worth noting that a lack of a significant SFR–Z correlation at a given single redshift (i.e.,

within a narrower SFR range) does not mean that there is a lack of the correlation over a wider SFR range with consideration of the redshift evolution of the main sequence. In the context of the FMR, the redshift evolution of the MZ relation is expressed as a shift on the surface of the M_*–SFR–Z space while these parameters varying with cosmic time. Mannucci et al. (2010) defined a quantity combining M_* and SFR as $\mu_\alpha = \log M_* - \alpha \log \mathrm{SFR}$ that minimizes the dispersion in metallicity over small intervals on a grid of the M_*–SFR plane. Here, the parameter α refers to the projection parameter. We choose $\alpha = 0.32$ for comparison with the original FMR by Mannucci et al. (2010), although $\alpha = 0.30$ is derived for the [N II]/Hα-based metallicity by Andrews & Martini (2013) and Zahid et al. (2014b) using the SDSS sample. The use of $\alpha = 0.30$ does not change our conclusions. We note that Mannucci et al. (2010) use the metallicity calibration of Maiolino et al. (2008), the same as implemented here, thus there is no need for an additional conversion factor.

Figure 4.21 shows the metallicity derived from the [N II]/Hα ratios as a function of the projected axis (μ) with the FMR from Mannucci et al. (2010) (thin solid curve) overlaid. The line ratios are measured on the composite spectra of the Sample-1 in eight bins of either the μ value or stellar mass. In the latter case, the values of μ are calculated by median stellar mass and SFR in each bin. Here, we show the results obtained using Hα-based SFRs (see §4.2.6); our conclusion does not change when using SED-based SFRs. The measurements in the two binning cases (μ_α-bin or M_*-bin) are consistent within the uncertainties.

Our FMOS sample shows good agreement with the Mannucci et al. FMR (thin solid curve in Figure 4.21) while there is a small offset towards higher metallicities at $\mu \sim 10$. However, we note that Mannucci et al. (2010) derived the FMR using *in-fiber* SFR, which is not corrected for the fiber aperture loss, while we derive the *total* SFRs for our FMOS sample accounting for the fiber loss (see Zahid et al. 2014b). The use of a mixture of total and in-fiber SFRs may be misleading and results in an inaccurate physical understanding. Therefore, we derive a new relation between μ and metallicity for the local galaxies, using total SFRs based on Hα luminosities, for which the aperture effect and dust extinction are corrected (see §4.2.8). We note that, however, the metallicity is based on in-fiber emission line fluxes, i.e., not global values, and this possibly causes a bias towards higher O/H. To avoid such a bias preferably, we select local galaxies with $z \geq 0.04$ following Kewley et al. (2005).

Figure 4.21 shows the distribution and the average relation, based on mean metallicity in 40 bins of μ, of the local sample. Our high-redshift measurements are in good agreement with the local galaxies at $\mu > 9.8$. In contrast, the difference in metallicity with the local relation extends at $\mu < 9.8$ down to the lower limit, although the discrepancy becomes smaller as compared with the offset in the MZ relation. At the low mass end, the offset is approximately $\Delta \log(\mathrm{O/H}) \sim 0.2$ dex in the FMR while about 0.3 dex in the MZ relation. Here, we stress that there still remain a significant offset in the metallicity between the relations at two epochs in spite of the fact that the bias towards high SFRs in our sample is mitigated by computing the projection axis μ. Thus, as first reported in Zahid et al. (2014b), our data do not support the extrapolation from the local galaxies, particularly at low M_* and high SFR, as proposed by Mannucci et al. (2010).

Maier et al. (2014) have studied the FMR at $z > 2$ and found that high-z galaxies in their sample are consistent with a universal FMR that is based on the physically motivated formulation from Lilly et al. (2013) (see also Onodera et al. 2016), but not with the Mannucci et al. FMR. In the framework of Lilly et al. (2013), the equilibrium gas-phase metallicity, Z_{eq}, is given as a function of M_* and SFR (see Appendix A.2 for details). We follow the parametrization of Equation 3 in Maier et al. (2014):

$$Z_{\mathrm{eq}} = Z_{\mathrm{in}} + \frac{y}{1 + \lambda(1-R)^{-1} + \varepsilon^{-1}\ ((1+\beta-b)\mathrm{SFR}/M_* - 0.15)} \tag{4.10}$$

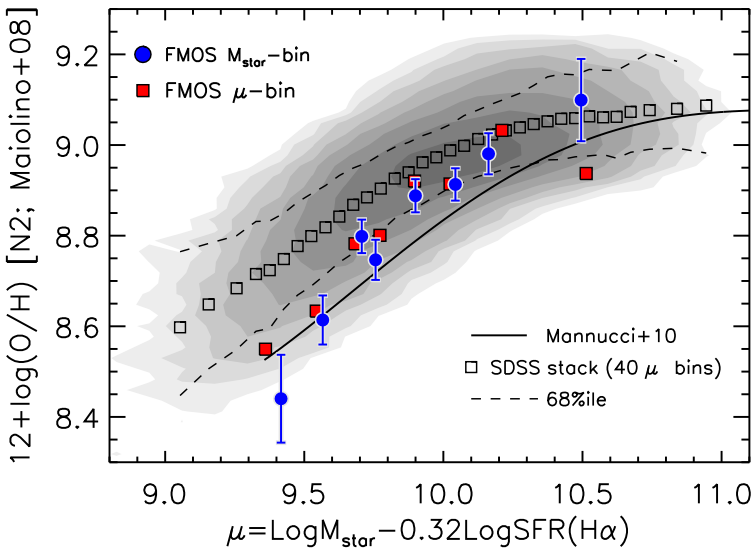

Figure 4.21: Projected M_*-Z-SFR relation: metallicity versus $\mu_{\alpha=0.32}(M_*, \mathrm{SFR})$. The metallicities are determined from the [N II]/Hα ratio and μ is calculated using Hα-based SFRs for our sample. Symbols indicate the measurements on the stacked spectra in eight bins of either stellar mass (blue circles) or μ value (red squares). Shaded contours show local star-forming galaxies, with the mean metallicities in forty bins of μ and the central 68th percentiles (dashed lines). The thin solid line indicates the original FMR derived by Mannucci et al. (2010) (based on in-fiber SFRs).

where $Z_{\rm in}$ is the metallicity of the infalling gas, y is the yield, $R = 0.27$ (for a Salpeter IMF) is the fraction of mass returned into ISM, λ is the mass-loading factor, given as $\lambda \propto M_*^a$, and $\varepsilon = \mathrm{SFR}/M_{\rm gas} \propto M_*^b$ is the star formation efficiency. $\beta = -0.25$ is the slope of the relation between stellar mass and specific SFR (sSFR = SFR/M_*), i.e., sSFR $\propto M_*^\beta$. Although Lilly et al. (2013) assumed $R = 0.4$ and $\beta = -0.1$, the use of such different values does not change our conclusions. We note that Equation 4.10 is a form for $z = 0$ and that the form for high redshifts will depends on the time variation of parameters, as discussed in Lilly et al. (2013). In particular, the star formation efficiency is likely to increase with redshift by a factor $\sim (1 + z)$ (e.g., Genzel et al. 2010; Sargent et al. 2014). Here, we compare our measurements at $z \sim 1.6$ to this model without considering the time dependence to examine whether our measurement at $z \sim 1.6$ follow a non-evolving M_*–Z–SFR relation.

We determine the parameters from a model fit to the SDSS sample using total SFRs, as listed in Table 4.6. We use galaxies with $9.2 \leq \log M_*/M_\odot \leq 10.6$ and $-1 \leq \log \mathrm{SFR}/(M_\odot\ \mathrm{yr}^{-1}) \leq 1$, which are binned by $\Delta \log M_* = 0.1$ dex and $\Delta \log \mathrm{SFR} = 0.1$ dex. The average metallicity is calculated from mean fluxes of the Hα and [N II] lines of individual galaxies in each bin. Errors are derived from the jackknife resampling. To fit the model as a function of both M_* and SFR, we utilize the MPFIT2DFUN IDL procedure (Markwardt 2009). The derived values are nearly equivalent to those given in Lilly et al. (2013) except for the star formation efficiency ε that is two or three times higher here. This is most likely because we use the total SFRs to derive the FMR of the SDSS sample whereas Lilly et al. (2013) use in-fiber SFRs, as in Mannucci et al. (2010). In the fitting, $Z_{\rm in}$ is fixed to zero while the use of a different value within $0 < Z_{\rm in}/y < 0.1$ does not change our conclusions.

Based on this physically-motivated model, we find that our sample at $z \sim 1.6$ is consistent with a non-evolving FMR relation. Figure 4.22 shows average metallicities for galaxies in our sample and for local objects, as a function of SFR (panel a) and sSFR (panel b) for galaxies

Table 4.6: Fits of Lilly et al. (2013) FMR model to the SDSS sample

$\log y$[a]	λ_{10}[b]	a	ε_{10}^{-1} [Gyr][c]	b
9.11 ± 0.01	0.38 ± 0.04	-0.60 ± 0.03	1.4 ± 0.2	0.40 ± 0.05

[a] Given in units of $12 + \log(\mathrm{O/H})$
[b] Mass-loading factor at $M_* = 10^{10}\ M_\odot$.
[c] Star formation efficiency at $M_* = 10^{10}\ M_\odot$.

of different M_*. We first separate the local sources into 0.2 dex-wide M_* bins, then divide into 50 SFR bins within each M_* bin. The average metallicities are shown separately for each M_* bin, as color-coded in the plot. The functional form of the FMR (Lilly et al. 2013) reproduces the behavior of local galaxies in each mass bin (dashed curves). Filled circles show the average metallicities of the FMOS galaxies (Sample-1) based on the composite spectra in eight mass bins. Figure 4.22 shows good agreement between our $z \sim 1.6$ measurements and the model prediction extrapolated from the local sample within ~ 0.1 dex at each M_*. This is more clearly seen in the lower panels (d) and (e), in which we show the deviations of observed metallicity from the model values at corresponding M_* and SFR.

The agreement between our observations and the model is also seen in panels (c) and (f) of Figure 4.22, where we present the MZ relation and the metallicity deviation from the model for the local (squares) and FMOS galaxies (filled circles), respectively. We separate the local sample into 0.3 dex-wide SFR bins, then divide into 40 M_* bins. The average metallicities are presented as a function of M_* separately for each SFR bin as color-coded. We overlaid the predictions from the best-fit FMR at median SFR of each bin for the local (dashed lines) and our FMOS (solid lines) samples. The expected metallicities at the median M_* and SFR of each bin of the FMOS sample (open diamonds) show good agreement with the data points.

Our measurements at low masses require a rapid decline of metallicity at higher SFRs (see Figure 4.22 (a, b)). This trend is naturally induced by considering galaxy evolution regulated by gas inflow and mass loss in the model of Lilly et al. (2013). Our finding is consistent with the conclusion in Maier et al. (2014), claiming that whether a FMR is truly fundamental (i.e., independent of redshift) depends on the formulation of the model and its extrapolation to regions of the M_*–SFR parameter space different from that occupied by local galaxies.

Lastly, we note that the deviation from the model at $z \sim 1.6$ likely to be correlated with stellar mass (or SFR) and, in particular, the deviation at high masses ($M_* \gtrsim 10^{10.5}\ M_\odot$) is statistically significant. In this study, we do not take account for the time evolution of model parameters. However, in reality, the parameters are possibly dependent on the epoch, although their time dependence has not been established yet. We find that it is difficult to reproduce the observed $z \sim 1.6$ MZ relation unless assuming a much higher mass loading factor (twice or more locally). However, we need a larger sample that spans wide range of the parameter space with redshift, stellar mass, and SFR, to obtain further physical insights over cosmic time.

4.8 Conclusions

We investigate the physical conditions of ionized gas in star-forming galaxies on the main sequence at $1.43 < z < 1.74$ using, in total, 701 galaxies with an Hα detection from the FMOS-COSMOS survey. This is the first time using such a large sample over a wide stellar mass range of $10^{9.6} \lesssim M_*/M_\odot \lesssim 10^{11.6}$ at these redshifts. Our main results are as follows:

1. We confirm a clear offset from the mean locus of the local star-forming galaxies on the BPT diagram using both individual measurements and stacking measurements for our FMOS

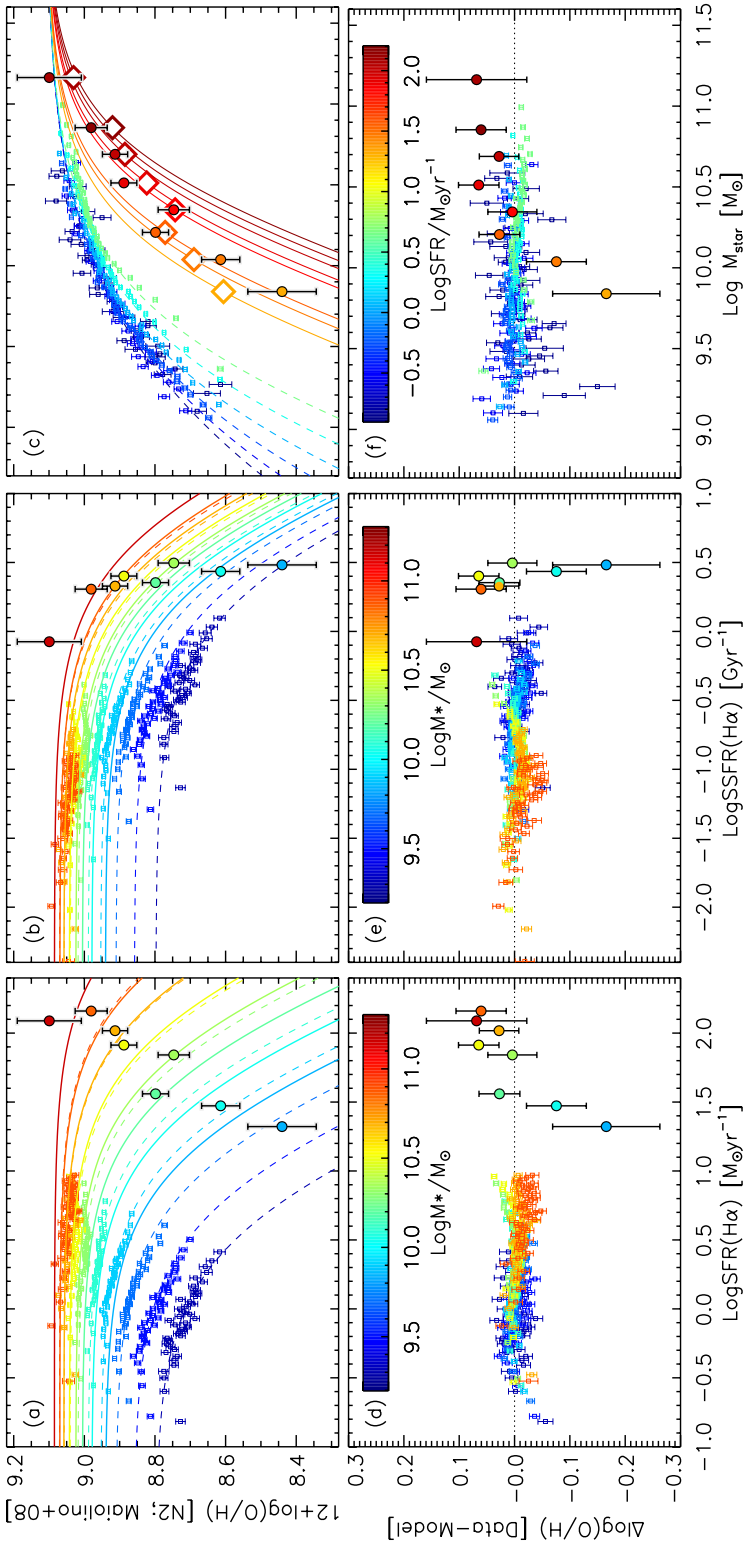

Figure 4.22: Metallicity as a function of SFR (a), sSFR (b) and stellar mass (c) as compared to the model of Lilly et al. (2013). The FMOS measurements (Sample-1) based on composite spectra in eight mass bins are indicated by filled circles, color-coded by M_* (a, b) or SFR (c). Colored open squares show average metallicities of the SDSS galaxies (see text). Dashed lines show the model metallicity computed for the SDSS sample from Equation 4.10 at median M_* (a, b) or SFR (c) in each bin. Solid lines indicate the same FMR at median M_* (a, b) or SFR (c) in each bin for our FMOS sample. In panel (c), diamonds indicates the metallicities predicted by the best-fit FMR at the median M_* and SFR for each bin of our FMOS sample. (d, e, f) Differences between observed metallicities and theoretical predictions at the corresponding M_* and SFR from the model fit to the local sample (related to panels (a), (b), and (c), respectively.)

sources. This offset amounts to an increase by a factor of ~ 0.5 dex in the mass–excitation (MEx) diagram (M_* vs. [O III]/Hβ) between our FMOS sample and local SDSS galaxies.

2. We assess the effects of AGNs on our stacking analysis by using the X-ray imaging data set from the *Chandra*-COSMOS Legacy survey. Stacking the images permit us to evaluate the average X-ray luminosity and the contribution from AGNs in subsamples separated into stellar mass bins. We make sure that the AGN contamination is well removed, by excluding objects that are included in the X-ray point source catalog and those identified based on their rest-frame optical emission line properties, thus not responsible for the offsets seen in the emission line diagrams.

3. We measure the emission line ratio [S II]$\lambda\lambda$6717, 6731/Hα with average spectra and find lower values of [S II]/Hα at the highest two mass bins ($M_* \gtrsim 10^6\ M_\odot$) as compared with local star-forming galaxies at a fixed [O III]/Hβ (see Figure 4.9 in §4.3.2). These smaller [S II]/Hα ratios suggest that a higher ionization parameter of the ISM is evident, while rule out significant ionization due to AGNs.

4. The average electron density is measured based on the emission line ratio [SII]λ6717/[SII]λ6731 using stacked spectra that gives a value of $n_\mathrm{e} = 222^{+172}_{-128}$ cm^{-3} for the full sample, which is higher than the average value of local star-forming galaxies ($n_\mathrm{e} \sim 10$–10^2 cm^{-3}). This enhancement in electron density is consistent with those shown in a selected local sample with high star formation rates: such an enhancement may contribute to offsets seen in the BPT diagram.

5. We use the line ratio [N II]/[S II] as a proxy of the chemical evolutionary phase of galaxies. The measurements of the this ratio based on the stacked spectra indicate that the secondary production of nitrogen is predominant in star-forming galaxies above $M_* \gtrsim 10^{10}\ M_*$ at $z \sim 1.6$. In contrast, it is likely that in lower mass galaxies ($M_* \lesssim 10^{10}\ M_*$), the primary process is not negligible in the entire nitrogen production. Furthermore, we find that our sample show higher [O III]/Hβ ratios relative to the level of [N II]/[S II], as compared to local galaxies. This may indicate that galaxies in our sample have higher excitation state relative to their evolutionary stage of the chemical enrichment.

6. A relatively high ionization parameter in galaxies at $z \sim 1.6$ is confirmed by comparing with the theoretical model grid (see Figure 4.13), which indicates that galaxies in our FMOS sample have an average ionization parameter $\log U \sim -3$, approximately 0.2–0.3 dex higher than the average of local star-forming galaxies at a fixed stellar mass. We found that the enhancement in the ionization parameter *at fixed metallicity*, i.e., a larger q_ion than expected from the local q_ion–Z anti-correlation, is essential to produce the offset of high-z galaxies from the locus of local galaxies in the emission line diagnostic diagrams. In addition, it turns out that additional effects from higher electron density and/or harder ionizing radiation are likely important, especially at the massive end.

7. With a relatively high electron density, we would attribute the changes in the ionization parameter to an enhancement of the production rate of ionizing photons in individual H II regions in high-z galaxies that may be caused by a scaling up of the radiation field and also by a hardening of its spectrum. In addition, we found, by comparing our data with the measurements of pure H II regions (Figure 4.14), that the effects from the changes in the contribution of diffuse ionized gas, which is larger in local galaxies, do not fully explain the changes in observed emission line ratios.

8. We derive the mass–metallicity relation from the [N II]/Hα ratio for our $z \sim 1.6$ sample, while keep in mind that the line ratio may be systematically off due to changes in ionization

parameter, hardness of stellar spectra, and in the N/O vs. O/H relation (if any): in particular, a higher $q_{\rm ion}$ leads to an underestimate of metallicity, thus make the difference between the local and high-z MZ relations larger. Our results are fully consistent with the previous derivation for a sBzK-selected subsample in the FMOS-COSMOS survey (Zahid et al. 2014b). The current data strengthens our previous result that the most massive galaxies ($M_* \gtrsim 10^{11}\ M_\odot$) are fully matured at a level similar to local galaxies. In contrast, at the lowest masses ($M_* \sim 10^{9.8}\ M_\odot$), the metallicity is on average ~ 0.4 dex smaller than local galaxies. Our sample at $z \sim 1.6$ is in good agreement with a universal metallicity relation proposed by Zahid et al. (2014a), which is founded on the fundamental relation between metallicity and stellar-to-gas mass ratio.

9. We evaluate metallicity adopting a new calibration by Dopita et al. (2016), which uses the line ratios [N II]/[S II] and [N II]/Hα. The novelty of this indicator is that it is less sensitive to changes in the ionization parameter, but also does not react to the instantaneous fluctuations of O/H that are expected to caused by the varying amount of infalling gas. The derived mass–metallicity relation shows a trend that is qualitatively equivalent to that seen in the relation based on the [N II]/Hα ratio, while the absolute values of metallicity is slightly different. In addition, the relative difference between the local and high-z MZ relation is smaller than that from the [N II]/Hα-based MZ relation, which is likely because of the independency of the indicator from the ionization parameter.

10. The mass–metallicity–SFR relation for our FMOS sample shows a discrepancy from the FMR derived by Mannucci et al. (2010), with metallicities smaller than values expected by the extrapolation from local galaxies. In contrast, our measurements are consistent with a physically-motivated model from Lilly et al. (2013), in which the star formation is instantaneously regulated by the gas mass, gas inflow, and mass loss by outflow. This model well reproduces a rapid decline in metallicity at high SFRs as shown in our data.

We comprehensively explain the changes in observed emission line properties of high-z galaxies, and specify the origin of the offset from the local sequence in the BPT diagram. Near future multi-object spectrographs (e.g., Subaru/PFS, VLT/MOONS) will allow us to establish the evolution of the ISM properties, especially based on accurate individual measurements instead of stacks, with less biased large samples and high-quality spectral data.

Chapter 5

Connection between galaxies and dark matter halos

5.1 Introduction

Large-scale galaxy surveys have found that the Universe contains various structures made by galaxies, including clusters, which are connected by filamentary structures, and voids (e.g., de Lapparent et al. 1986; Colless et al. 2001). In the standard ΛCDM framework, the formation of cosmic large-scale structures is dominated by the evolution of cold dark matter (CDM), as verified by a series of cosmological N-body simulations (e.g., Kravtsov et al. 2004; Springel et al. 2005). While CDM cannot be observed directly through electromagnetic waves, galaxies form from the baryonic gas cooling in the potential wells of dark matter halos. Thus, galaxies trace the distribution of underlying invisible dark matter.

In the bottom-up structure formation scenario, more massive halos are more clustered, and located in denser environments. As mentioned in §1.9, we see in recent large galaxy surveys that different galaxy populations trace the dark matter distribution in different ways. This fact means that the formation and evolution of galaxies are essentially connected to the assembly history of dark matter halos. There have been many efforts to interpret such trends by linking visible galaxies to halos.

To relate the observed galaxy distribution to the underlying dark halos, the halo occupation distribution (HOD) framework has been developed, which describes the average number of galaxies hosted by a halo as a function of halo mass (see e.g., Cooray & Sheth 2002, for a review). The observed galaxy clustering is well reproduced by an HOD model, providing key physical quantities such as minimum halo mass hosting at least a single galaxy in a population of interest.

To clarify early stages of galaxy formation, accurate measurements of galaxy clustering and its interpretation at higher redshifts are required. The HOD models have been applied to interpret the galaxy clustering in the Local Universe, and also at high redshifts up to $z \sim 7$ (e.g., Wake et al. 2011; Geach et al. 2012; Durkalec et al. 2015; Harikane et al. 2016). In most high redshift ($z \gtrsim 1$) surveys, however, the galaxy clustering has been investigated by measuring the angular correlation function $\omega(\theta)$ based on the photometric redshifts. While imaging surveys provide large and deep samples with much lower cost as compared to spectroscopy, it is challenging to resolve the redshift evolution due to the contamination of back/foreground luminous objects and a wide range of redshift with large uncertainties. Spectroscopic surveys at higher redshifts generally tend to be restricted to target relatively bright objects, which are, for example, quasars, starbusrts, or even if not such extreme objects, having relatively high SFRs. Therefore such samples are definitely not representative of the general galaxy population and may not a good tracer of relatively small scale structures.

The history of galaxy evolution is the history of transformation of gas into stars, which has been most activated at a redshift range $1 \lesssim z \lesssim 3$, the peak epoch of the star formation history

of the Universe. What environment do such intense activities occurs in? Measuring the clustering of galaxies and interpreting them in the CDM framework provide essential information for constraining the environmental dependence of star formation. For such purposes, it is important to sample a representative galaxy population at each epoch.

In this work, we present measurements of projected galaxy clustering and an HOD constraint using a sample constructed from the FMOS-COSMOS survey. FMOS provides an advantage to construct a representative sample of the general galaxy population by its wide field-of-view (~ 0.5 deg^2) and high multiplicity. Furthermore, we successfully map the small scale structures down to $< 0.1\ h^{-1}$ Mpc, where the contribution from galaxies that reside in the same halo (i.e., one-halo term) become important, as a result of our target sampling rate.

This Chapter is organized as follows. In §5.2, we describe our data and sample. Our clustering analysis is described in §5.3. We present our clustering measurements in §5.4. In §5.5 and §5.6, we interpret the galaxy clustering with an HOD modeling and discuss the physical meanings of the derived quantities, respectively. We finally summarize our results and conclusion in §5.7.

Throughout the Chapter, a flat ΛCDM cosmology with $(h, \Omega_m, \Omega_\Lambda) = (0.7, 0.3, 0.7)$ is assumed. We use a Chabrier (2003) initial mass function (IMF) for comparison with other studies referred to in this Chapter. Conversion factor to a Chabrier IMF is 1/1.7 for both stellar masses and SFRs given in Chapters 3 and 4 that use a Salpeter IMF (Silverman et al. 2015). we use "log" to denote a logarithm with a base 10 ($\log_{10}$).

5.2 Data

5.2.1 Sample selection

In this study, we use a catalog from observations between March 2012 and February 2014, as listed in Table 5.1. The survey area is covered by the four FMOS footprints (HR1–HR4) listed in Table 2.2.

Our sample of galaxies is based on the COSMOS photometric catalog (Ilbert et al. 2013) that includes the Ultra-VISTA/VIRCAM photometry (McCracken et al. 2012). Photometric redshifts and stellar masses are derived by Ilbert et al. (2013) with the SED fitting using the Le Phare software (Arnouts & Ilbert 2011), assuming Bruzual & Charlot (2003) population synthesis models. We derive star formation rates (SFRs) assuming a constant star formation history and compute the predicted Hα flux ($f_{\mathrm{H}\alpha}^{\mathrm{pre}}$) for each galaxy, as described in §4.2.1 (see also Silverman et al. 2015). The dust extinction is taken into account based on the color excess $E_{\mathrm{star}}(B-V)$, estimated from the SED fitting, and a Calzetti et al. (2000) extinction curve, with a relation of extinction for nebular ($A_{\mathrm{H}\alpha}$) and stellar component assumed (see Chapter 4):

$$A_{\mathrm{H}\alpha} = 3.325 E_{\mathrm{star}}(B-V)/0.66. \tag{5.1}$$

From the COSMOS catalog, we find 7006 galaxies that have a stellar mass (M_*) above $M_*^{\mathrm{lim}} \equiv 10^{9.57}\ M_\odot$, photometric redshift $1.46 \leq z_{\mathrm{phot}} \leq 1.72$, in the FMOS survey area shown in Figure 5.1. Here, we remove regions that are impacted by bright stars (shaded areas). The faint limit of the catalog ($K_{\mathrm{S}} \sim 24$) is appropriate to achieve a high completeness enough for our purpose ($> 90\%$ at the least mass end and more for larger stellar masses; Ilbert et al. 2013). We refer to this sample as the *M_*-selected* sample throughout this Chapter.

Our targets for the FMOS observations are restricted to those with the Ultra-VISTA/VIRCAM photometry $K_{\mathrm{S}} < 23.5$. Additionally, a limit on the predicted Hα flux is applied to achieve an acceptable success rate of detecting Hα emission line. While such a flux limit has been varied through the observing program, we select galaxies that have $f_{\mathrm{H}\alpha}^{\mathrm{pre}} \geq f_{\mathrm{H}\alpha}^{\mathrm{lim}} \equiv 1{\times}10^{-16}$ erg cm^{-2} s^{-1}, which is the highest limit, for this study, so that all galaxies have been included in the input catalog for the past pointing. This flux limit is equivalent to SFR $\sim 20\ M_\odot$ yr^{-1} for galaxies at

Table 5.1: Summary of the observations

Data (UT)	Proposal ID	Pointing	Grating
2012 Mar 13	UH-B3	HR4	H-long
2012 Mar 14	S12A-096	HR1	H-long
2012 Mar 15	S12A-096	HR2	H-long
2012 Mar 16	S12A-096	HR1	H-long
2012 Mar 17	S12A-096	HR3	H-long
2012 Mar 19	S12A-096	HR1	J-long
2012 Dec 29	UH-B5	HR2	J-long
2013 Jan 19	UH-18A	HR3	H-long
2013 Jan 20	S12B-045I	HR4	H-long
2013 Jan 21	S12B-045I	HR3	J-long
2013 Jan 22	S12B-045I	HR4	J-long
2013 Jan 20	S12B-045I	HR4	H-long
2013 Jan 21	S12B-045I	HR3	J-long
2013 Dec 29	S12B-045I	HR2	H-long
2014 Jan 25	UH-11A	HR3	H-long
2014 Jan 26	S12B-045I	HR1	H-long
2014 Jan 27	S12B-045I	HR4	H-long
2014 Feb 08	S12B-045I	HR1	J-long
2014 Feb 09	S12B-045I	HR4	J-long
2014 Feb 10	S12B-045I	HR4	J-long

$z \sim 1.6$. With in the effective survey area, we find 6453 galaxies with $M_* \geq M_*^{\rm lim}$ and $K_{\rm S} \leq 23.5$, and 2139 galaxies of these have $f_{\rm H\alpha}^{\rm pre} \geq f_{\rm H\alpha}^{\rm lim}$. Throughout this Chapter, the former and the latter samples are refereed to as the $M_* + K_{\rm S}$-*selected* and *FMOS-parent* sample, respectively.

From the FMOS-parent sample, we observed 1182 galaxies in the H-long grating, which are referred to as the *FMOS-target* sample. In this sample, there are biases in the on-sky distribution of the observed galaxies due to the fiber allocation scheme, which is carefully taken into account in the analysis (see §5.3.3). To measure the galaxy clustering, we make use of 516 galaxies, included in the FMOS-target catalog, with a positive Hα detection in the H-long window ($1.43 \leq z \leq 1.74$). This *FMOS-spec-z* sample sample is restricted to those having one or more emission lines with S/N ≥ 3 (mostly Hα). The sample size and the selection criteria are summarized in Table 5.2. In Figure 5.1, we show the positions of the galaxies within the FMOS-parent sample, target sample, and the spec-z sample, respectively. The survey area covered by the four FMOS footprints is 0.810 deg^2. The shaded regions are masked areas removed due to the presence of a bright star or a ghost light. Taken together, 4.9% of the survey area is masked. The total survey volume is 8.98×10^5 (Mpc/h)^3 ($1.43 \leq z \leq 1.74$). The effective volume over $1.46 \leq z \leq 1.72$, which is the selection range of the FMOS-parent sample, is 7.54×10^5 (Mpc/h)^3. The number densities of the FMOS photometric samples are calculated with the latter volume, as listed in Table 5.2.

5.2.2 Sample characteristics

Figure 5.2 shows SFRs as a function of stellar mass for galaxies in our sample. Galaxies with $K_{\rm S} \leq 23.5$ ($1.46 \leq z_{\rm phot} \leq 1.72$; gray dots) show a strong correlation between SFR and M_* (i.e., the star-forming main sequence; e.g., Daddi et al. 2007; Whitaker et al. 2012) with a standard deviation around the relation of 0.37 dex and a power-law slope of 0.66 ± 0.01. While the

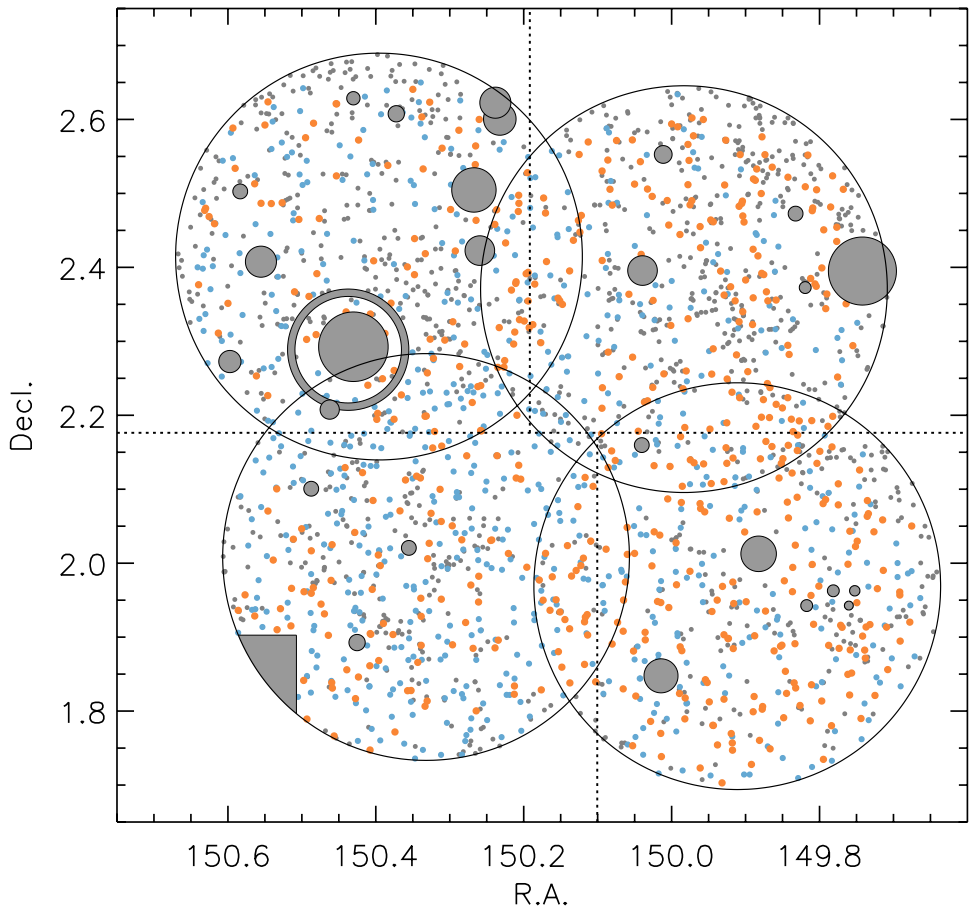

Figure 5.1: Four FMOS footprints (large circles) and masked-out regions (shaded areas) shown with the sample galaxies. Gray small dots indicates the FMOS-parent sample. The FMOS-target and spec-z samples are shown by blue and orange circles, respectively. The blue dots are a subset of the orange dots, and the orange dots are a subset of the blue dots. Dotted lines indicates partitions for jackknife resampling (see §5.3.4).

Table 5.2: Galaxy samples within the FMOS survey area

Sample name	N[a]	n[b]	**Selection**	**Mean** M_*[c]	**Median** M_*[c]
Photo-z M_*-selected	7006	9.29	$1.46 < z_{\rm phot} < 1.72$, $M_* \geq 10^{9.57}\ M_\odot$	10.42	10.04
Photo-z $M_*, K_{\rm S}$-selected	6453	8.55	+ $K_{\rm S} < 23.5$	10.45	10.10
FMOS-parent	2319	3.07	+ Predicted $f({\rm H}\alpha) > 10^{-16}$ erg s^{-1} cm^{-2}	10.58	10.20
FMOS-target	1182		+ Observed	10.59	10.23
FMOS-spec-z	516		+ Hα-detected at $1.43 < z < 1.74$	10.54	10.22

[a] Number of galaxies in each sample.
[b] Number density of photometrically-selected samples in units of $(10^{-3}h^3{\rm Mpc}^{-3})$, computed in the volume over $1.46 < z < 1.72$ ($7.54 \times 10^5\ h^{-3}{\rm Mpc}^3$).
[c] Mean and median stellar mass of each sample, expressed in $\log M_*/M_\odot$.

FMOS-parent sample ($K_S \leq 23.5$, $M_* \geq M_*^{\rm lim}$, $f_{H\alpha}^{\rm pre} \geq f_{H\alpha}^{\rm lim}$) traces the underlying sequence, it is obvious that many galaxies having relatively small SFRs are missed in the selection due to the self-imposed limitation on predicted Hα flux. The FMOS-spec-z sample that is used for the clustering analysis has such a bias as well. The median SFRs and the 68th percentiles are shown in eight stellar mass bins for both the $M_* + K_S$-selected sample (triangles) and FMOS-spec-z sample (blue squares). The FMOS-spec-z sample is on average biased toward higher SFRs by ~ 0.2 dex at the stellar mass range of $M_* \lesssim 10^{10.8}\ M_\odot$. Such a bias, however, is approximately only half of the scatter of the underlying sample. Therefore, we stress that the FMOS spec-z sample well traces a general star-forming population lying on the main sequence over the entire stellar mass range probed in this study ($10^{9.57} \leq M_*/M_\odot \lesssim 10^{10.4}$) and the SFR range of $15 \lesssim$ SFR $\lesssim 600 M_\odot {\rm yr}^{-1}$. The mean and median stellar masses of each sample are listed in Table 5.2.

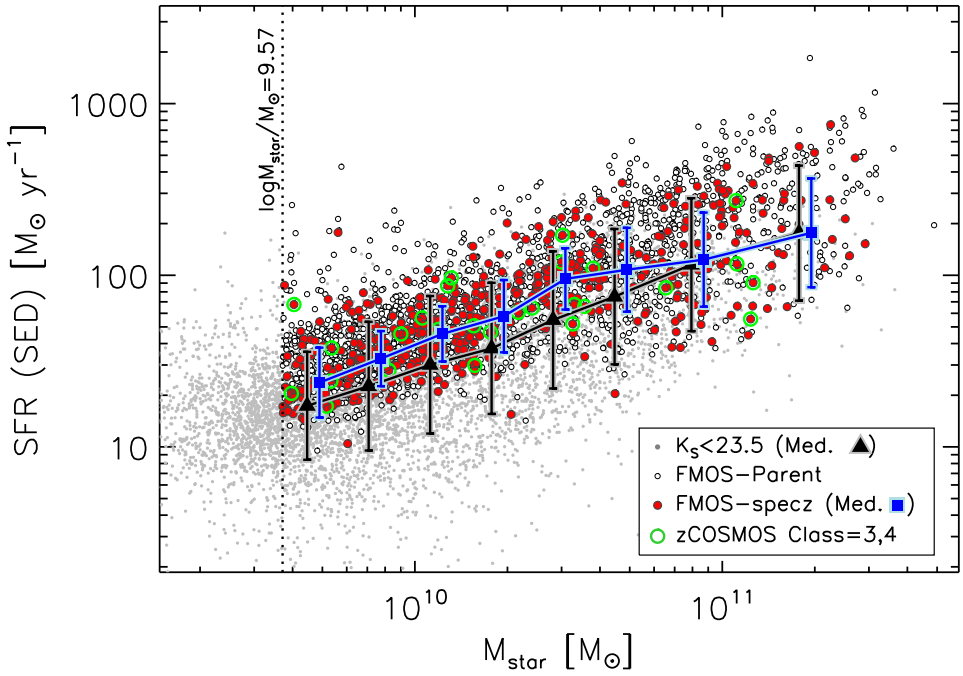

Figure 5.2: SFR (SED) versus M_* for galaxies in our sample ($1.43 \leq z \leq 1.74$). Gray dots show all galaxies with $K_S < 23.5$ and $1.46 \leq z_{\rm phot} \leq 1.72$ in the FMOS survey area. The FMOS-parent and FMOS-spec-z samples are shown by open and red filled circles, respectively. The median SFRs in eight M_* bins are indicated for the $K_S < 23.5$ galaxies and FMOS-spec-z samples. The error bars indicate the central 68th percentiles in SFR in each bin. A vertical dotted line indicates the threshold stellar mass for our sample selection ($M_*^{\rm lim} = 10^{9.57}\ M_\odot$).

In Figure 5.3, we show the distribution of spectroscopic redshifts of the FMOS-spec-z sample with positions of OH lines shown. Those wavelengths are converted into redshift based on the wavelength of the Hα emission line. It is seen that the number of successful detections is suppressed near the OH masks. In addition, the detection rate smoothly decreases towards both sides of the spectral coverage due to the relatively higher noise level at the edges of the image sensor and the uncertainties on the photometric redshift used for the sample selection. We take into account these effects on the radial distribution of the sample galaxies, as described in §5.3.2. Figure 5.4 compares the spectroscopic and photometric redshifts for 516 galaxies in the FMOS-spec-z sample, and shows the histogram of $(z_{\rm phot} - z_{\rm spec})/(1 + z_{\rm spec})$. We find that these two redshifts are in agreement within the root-mean-square of $\sigma(\Delta z/(1+z)) = 0.024$ and an offset

of $\langle \Delta z/(1+z) \rangle = -0.009$. This is consistent with our report based on the subset of our sample in Silverman et al. (2015).

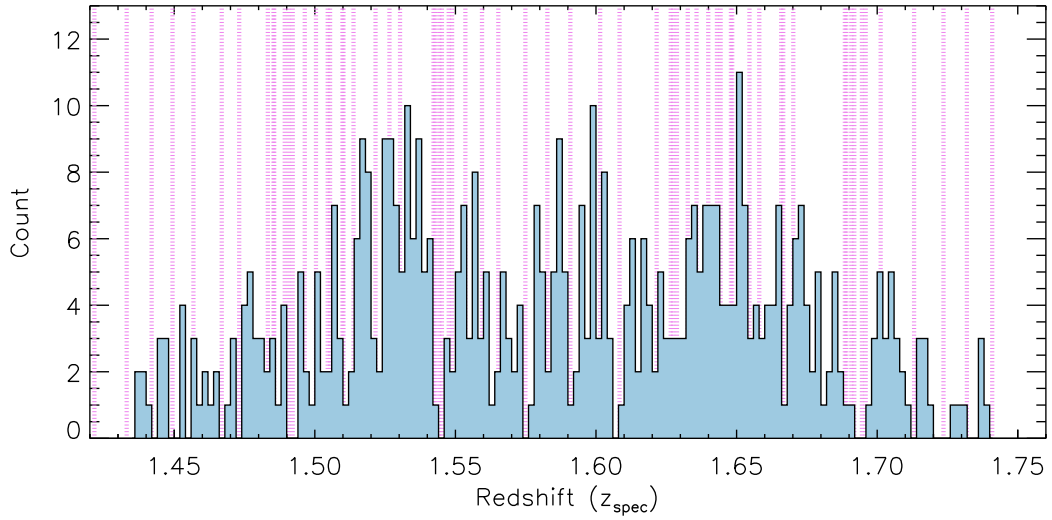

Figure 5.3: Distribution of spectroscopic redshifts of the FMOS-spec-z sample. Magenta stripes indicate positions of OH lines, which are converted into the redshift using the wavelength of the Hα emission line.

We evaluate the effects of the observational sampling bias. Figure 5.5 shows the distribution of the stellar mass, photometric redshift, and the predicted Hα flux of our samples (FMOS-parent, -target, and -spec-z samples). The ratios of the number of galaxies in the FMOS-target sample or in the FMOS-spec-z sample to the number of galaxies in the FMOS-parent sample are shown in the upper panels. We highlight here that the sampling rate is almost uniform as a function of stellar mass and photometric redshift. Consequently, the median stellar mass and median redshift of the FMOS-spec-z sample are in good agreement with those of the FMOS-parent sample (see Table 5.2). In contrast, the right panel of Figure 5.5 indicates that the FMOS-spec-z sample is slightly biased towards a population having higher $f^{\rm pre}_{\rm H\alpha}$. Such a bias is expected from the fact that strong Hα emission is easier to detect even at noisy pixels (near the OH mask or the edge of the spectral window). However, the median $\log f^{\rm pre}_{\rm H\alpha}$ ($= -15.79$) of the FMOS-spec-z sample is still close to the median $\log f^{\rm pre}_{\rm H\alpha}$ ($= -15.83$) of the FMOS-parent sample. Therefore, we conclude that the observational sampling bias is small enough not to significantly affect the characteristics of the FMOS-parent sample.

Further we assess the stellar mass completeness of our sample. Figure 5.6 compares the stellar mass distributions of our photometric samples (M_*-selected, $M_* + K_{\rm S}$-selected and FMOS-parent samples). The ratios of the number of galaxies in the $M_* + K_{\rm S}$-selected or FMOS-parent samples to the number of galaxies in the M_*-selected sample are shown as a function of stellar mass in the upper panel. The M_*-selected and $M_* + K_{\rm S}$-selected samples show a distribution that monotonically decreases with increasing M_*. In the latter sample, however, approximately 20% of galaxies close to the lower mass limit ($M_* \lesssim 10^{10}\ M_\odot$) are missed due to the $K_{\rm S} < 23.5$ selection, while the stellar mass completeness reaches almost unity at $M_* > 10^{10.1}\ M_\odot$. In the FMOS-parent sample, a large fraction of galaxies in the M_*-selected catalog are missed due to the limit on the predicted Hα flux. The sampling rate increases almost linearly with increasing $\log M_*$. Consequently, the FMOS-parent sample shows a M_* distribution with a gentle decline and has slightly higher mean and median stellar masses, as listed in Table 5.2, as compared to the M_*-selected or $M_* + K_{\rm S}$-selected samples. Given an expected dependence of the clustering amplitude on stellar mass, such a selection bias potentially affects an observed galaxy correlation

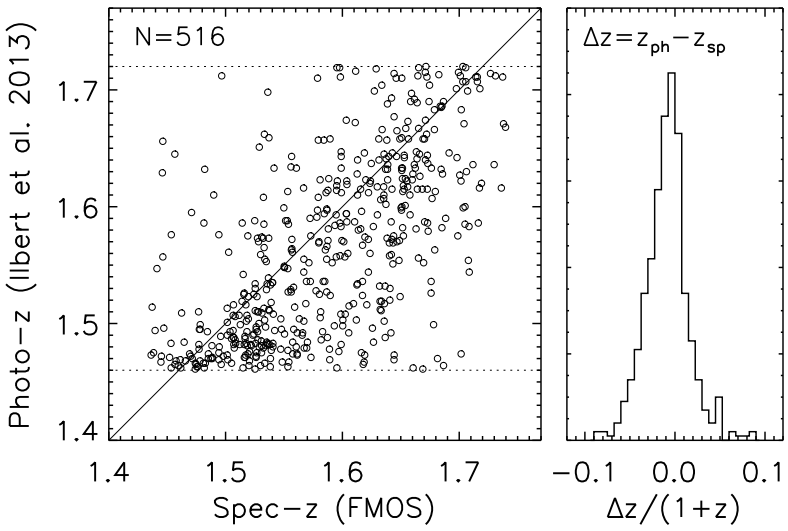

Figure 5.4: Comparison of the spectroscopic and photometric redshifts for 516 galaxies in the FMOS-spec-z sample, and a histogram of $(z_{\rm phot} - z_{\rm spec})/(1 + z_{\rm spec})$. Horizontal dotted lines indicates the lower and upper limits of our selection on the photometric redshift ($1.46 < z_{\rm phot} < 1.72$).

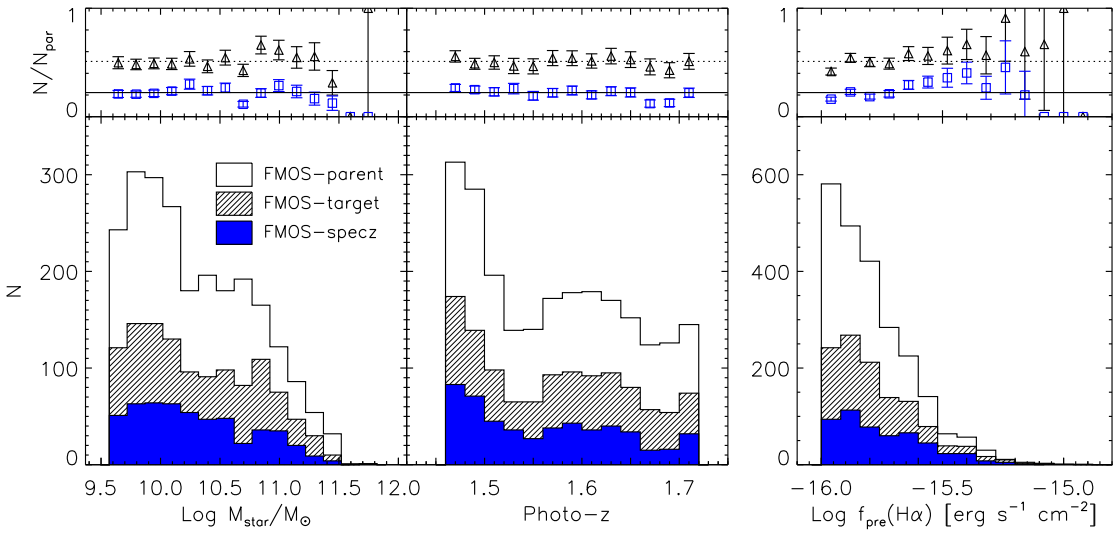

Figure 5.5: Distributions of stellar mass (left), photometric redshifts (middle), and predicted Hα flux (right) of our samples (FMOS-parent sample: empty histograms, FMOS-target sample: hatched histograms, FMOS-spec-z sample: blue filled histograms). Upper panels show the ratios of the number of galaxies in the FMOS-target sample (triangles) or FMOS-spec-z sample (squares) to the number of galaxies in the FMOS-parent sample in each bin, with error bars indicating the Poisson noise.

function. These effects of the stellar mass incompleteness of our sample will be further discussed using mock samples in Appendix E.2. We finally make sure that such effects do not significantly impact our results and conclusions.

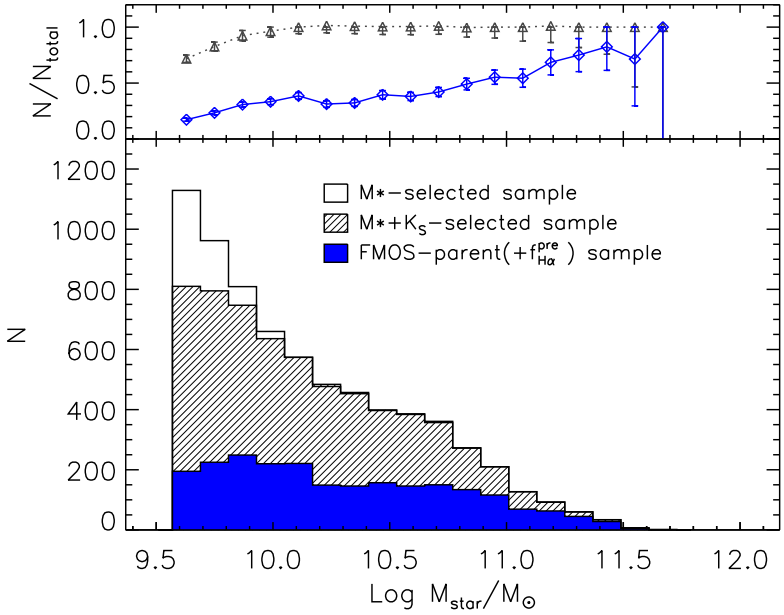

Figure 5.6: Stellar mass distributions of our photo-z samples. Histograms show the numbers of galaxies in each 0.12 dex bin (M_*-selected: empty, $M_* + K_S$-selected: hatched, FMOS-parent: filled histogram). The upper panel shows the ratios of the number of galaxies in the $M_* + K_S$-selected sample (triangle) and FMOS-parent sample (diamond) to the number of galaxies in the M_*-selected sample in each bin, with error bars indicating the Poisson noise.

5.2.3 Mock samples

Observational biases specific to the FMOS observation can impact clustering measurements and inferred physical quantities. We validate our correction schemes for such artificial biases by using a set of mock samples constructed from cosmological N-body simulations. We utilize the new numerical galaxy catalog (ν^2GC, Ishiyama et al. 2015) to take advantage of its large simulation volume. The medium-volume simulation (ν^2GC-M) that we use follows 4096^3 particles with a mass resolution of $2.2 \times 10^8\ h^{-1}\ M_\odot$ in a comoving box with a side length of 560 h^{-1} Mpc. We employ the halo catalog at a scale factor $a = 0.384871$ ($z = 1.598$), close to our median redshift, in which halos and subhalos are identified with the Rockstar algorithm (Behroozi et al. 2013b). The full simulation box is divided into 64 sub-volumes of $70 \times 70 \times 560\ h^{-3}\mathrm{Mpc}^{-3}$, each of which encloses the entire FMOS survey volume. In each sub-box, we mimic our observations while considering the FMOS fiber allocation scheme and the shape of the bright star mask to construct realistic target mock samples. We use them to examine the correction scheme for the bias on the on-sky distribution of the spec-z galaxies due to the fiber allocation. Details of the mock construction and the correction scheme are described in Appendix E.1.1.

We assess the effects of the stellar mass incompleteness in our sample by using the Bolshoi simulation (Klypin et al. 2011). The Bolshoi simulation traces 2048^3 particles with a mass resolution of $1.35 \times 10^8\ h^{-1} M_\odot$ in a cubic box with a side length of 250 h^{-1} Mpc. The Bolshoi simulation team made the halo/subhalo catalogs at all epochs public, thus one can trace the merger histories of individual halos. We use the public Rockstar catalog at $a = 0.38435$

($z = 1.602$), and construct mock samples. We describe the mock sample construction and the assessment of the bias effects in Appendix E.2.

5.3 Clustering measurement and model fit

5.3.1 Two-point correlation function

The two-point auto-correlation function is a powerful and commonly used tool to quantify the inhomogeneity of a three-dimensional distribution of galaxies. The correlation function $\xi(r)$ measures the excess of the probability of finding pairs of two galaxies as a function of separation r. We use the Landy & Szalay (1993) estimator to calculate the correlation function:

$$\xi(r) = \frac{N_R(N_R-1)}{N_D(N_D-1)}\frac{DD(r)}{RR(r)} - 2\frac{N_R-1}{N_D}\frac{DR(r)}{RR(r)} + 1, \tag{5.2}$$

where N_D and N_R are the number of galaxies and random objects, respectively. $DD(r)$, $DR(r)$, $RR(r)$ are the number of data–data, data–random, random–random pairs with a comoving separation within the interval $[r, r+dr]$, respectively. For the use of the estimator, it is necessary to construct a random sample which follows the geometrical properties of the real galaxy sample. We describe the construction of the random sample in §5.3.2.

In redshift surveys, the radial distance computed from redshift departs from the actual distance due to the peculiar motion of a galaxy, which distorts the shape of the correlation function. To minimize these effects, we measure the correlation function on a two-dimensional grid of galaxy-galaxy separations, parallel and perpendicular to the line of sight, and integrate it along the line of sight. We define the separations following Fisher et al. (1994). Given a pair of galaxies at positions $\boldsymbol{r}_1$ and $\boldsymbol{r}_2$ in the redshift comoving space, the separation $\boldsymbol{s}$ and the line-of-sight vector $\boldsymbol{l}$ are defined as $\boldsymbol{s} = \boldsymbol{r}_1 - \boldsymbol{r}_2$ and $\boldsymbol{l} = (\boldsymbol{r}_1 + \boldsymbol{r}_2)/2$, respectively. The parallel and perpendicular separations are then

$$\pi \equiv |\boldsymbol{s}\cdot\boldsymbol{l}|/|\boldsymbol{l}|, \qquad r_\mathrm{p} \equiv \sqrt{|\boldsymbol{s}|^2 - \pi^2}. \tag{5.3}$$

The *projected* correlation function $w_\mathrm{p}(r_\mathrm{p})$ is related to the real-space correlation function as follows:

$$w_\mathrm{p}(r_\mathrm{p}) = \int_0^{\pi_\mathrm{max}} \xi(r_\mathrm{p}, \pi)\, d\pi. \tag{5.4}$$

where r_p and π are perpendicular and parallel projections of the separation of two galaxies, respectively. While the upper limit π_max should be infinity in the ideal survey, in practice it has to be finite for real data to avoid adding noise to the measurements. We adopt $\pi_\mathrm{max} = 30h^{-1}$ Mpc, which is large enough to eliminate the effect of peculiar motions. We count pairs of galaxies and random objects on the two-dimensional mesh which is binned logarithmically in the r_p direction and linearly in π. Considering the small number of galaxy pairs with a small separation ($r_\mathrm{p} \lesssim 1\ h^{-1}$ Mpc), we employ a set of size-variable bins that have larger widths at small scales.

5.3.2 Construction of random samples

In order to measure the galaxy clustering by using the estimator (Equation 5.2), it is necessary to create a reference random sample that follows the same geometrical properties as the real data (see Figure 5.1). To avoid introducing shot noise, the random sample needs to contain a lot of objects that are randomly distributed in the survey volume. The random sample that we use contains $N_R = 45000$ objects, which is about 90 times larger than that of the data.

In the random sample, we consider the radial selection function, i.e., the realistic distribution of galaxies along the line of sight. It is commonly challenging to determine the radial distribution of random objects, in which the intrinsic galaxy distribution, sample selection, and the observational limit are merged. The most simple way is to use the distribution of the real data. However, such a way is useful only for large surveys since the real distribution reflects specific clustered structures for a survey with a small survey volume. To define the underlying distribution of galaxies, we employ the COSMOS photometric catalog (Ilbert et al. 2013). Figure 5.7 shows the distribution of the radial distance calculated from the photometric redshift for $\sim 10^4$ galaxies with $K_{\rm S} < 23.5$ and $M_* > M_*^{\rm lim}$. We smooth the binned distribution with a Gaussian kernels with a standard deviation of 150, 250, or 450 h^{-1} Mpc. The distribution smoothed with the shortest kernel (150 h^{-1} Mpc) still traces specific structures in the histogram. In contrast, smoothing with the longest kernel (450 h^{-1} Mpc) produces an artificial enhancement at both edges of the redshift range. Therefore, we decided to use the distribution that is smoothed with the 250 h^{-1} Mpc Gaussian kernel, which seems to well trace the global radial distribution of galaxies in the catalog.

To estimate the underlying distribution of true redshifts of the FMOS-parent sample, we take into account the uncertainties on each photometric redshift estimate. Figure 5.7 (lower panel) illustrates the method to define the radial distribution of our sample. We extract the smoothed distribution between $1.46 < z_{\rm phot} < 1.72$, and then convolve it with a Gaussian with a standard deviation of $\sigma_{z_{\rm photo}} = 0.062$, which is a typical error on the photometric redshifts of our sample (Silverman et al. 2015). As a result, we obtain the realistic underlying radial distribution of our sample galaxies (dashed line).

Furthermore, we consider the effects of the OH airglow mask and the detector sensitivity, which affect the success rate of the emission line detection in response to the pixel position. At the positions of the OH mask and residual sky lines, the noise level is generally high (see Figure 2.10). As described in §2.5.2, we define the weight function based on the noise level for each spectrum, and remove the pixels at the OH masks for fitting the emission lines. Moreover, the noise level of pixels close to the edges of the wavelength coverage is generally high, so that the success rate of the line detection declines. As a consequence, the detection count decreases at the positions around the OH lines and towards the edges of the redshift window in the observed distribution of our sample galaxies as shown in Figure 5.3.

We assess the detection rate of the Hα emission line with variable amplitudes and line widths as a function of redshift over the FMOS H-long coverage by performing a set of Monte-Carlo simulations. The simulations are conducted based on the observed emission line properties and the noise spectra of all 516 galaxies in the FMOS-spec-z sample. For each galaxy, we define a multi-Gaussian profile that has the same amplitude and line width for the Hα and [N II] emission lines as those of the galaxy, then add random Gaussian noise on them at each pixel. The standard deviation of the random noise is based on the noise spectrum of each galaxy, which is multiplied by a factor of 1.25 to take into account the fact that the noise level is generally underestimated relative to the actual pixel variance (see Silverman et al. 2015). Then, we perform the fitting procedure for those artificial spectra in the same manner as the data, and examine if the Hα line can be detected again. We examine the detectability of this profile at all pixels in the H-long window by scanning the entire spectral coverage. Here we admit the case in which the line is detected with S/N > 3, the fraction of its flux occupied by the removed pixels is less than 70%, and the difference between the input redshift and the measured redshift ($\Delta z/(1+z)$) is less than 0.001, as the success of re-detection. Figure 5.8 shows the average detection rate as a function of redshift with positions of OH lines marked. In this weight function, there are many cracks at the positions of the OH lines, and we can see a decrease of the detection rate near both edges of the spectral coverage due to the high noise level of both ends of the image sensor. These features are expected to introduce some artificial clustering along the line-of-site direction, so that an observed correlation function is biased. We finally take into account these instrumental effect on

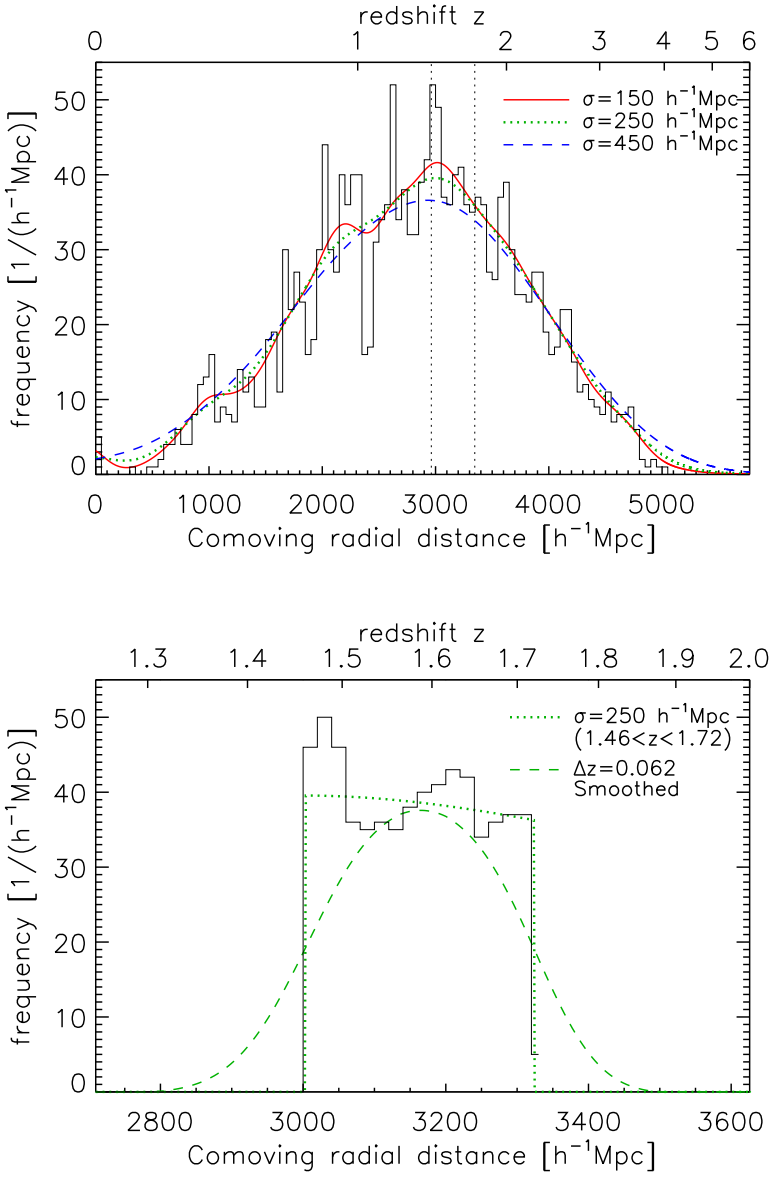

Figure 5.7: Upper panel: distribution of photometric redshifts. A solid histogram shows the distribution of galaxies with $K_S < 23.5$ and $M_* > M_*^{\rm lim}$ within the COSMOS photometric catalog (Ilbert et al. 2013). Solid, dotted, and dashed curves show the distribution that is smoothed with a Gaussian kernel of $\sigma = 150$, 250, or 450 h^{-1} Mpc, respectively. Vertical dotted lines show the photometric redshift range for the primary selection ($1.46 < z < 1.72$). Lower panel: a solid histogram and dotted curve are extracted from those in the top panel within $1.46 < z < 1.72$. Dashed curve shows the expected underlying distribution of the true redshift of our parent sample, which is defined by convolving the dotted line with a Gaussian kernel with $\sigma_z = 0.062$.

the radial selection function by multiplying the underlying distribution derived above based on the photometric catalog (Figure 5.7) by this weight function.

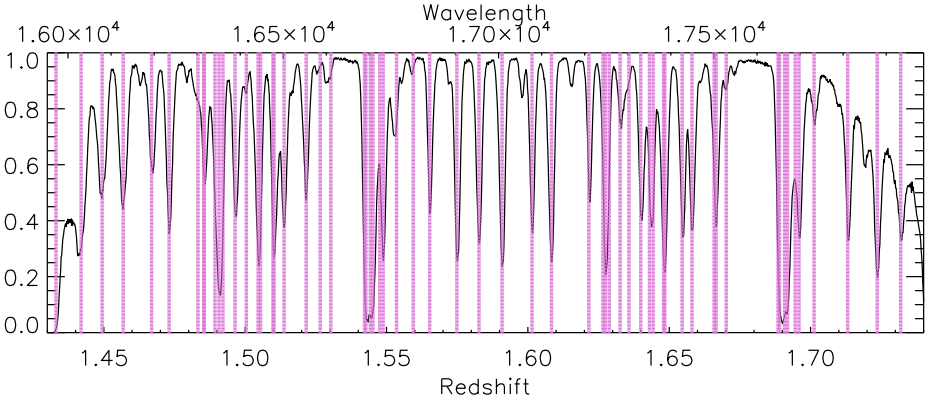

Figure 5.8: Average detection rate of the Hα emission line as a function of redshift. Corresponding observed wavelength is indicated on the top axis. Magenta stripes indicate the positions of the OH airglow masks.

For a test, we construct a random sample by assigning redshift randomly selected from the FMOS-spec-z sample allowing duplication. With this random sample, we obtain a correlation function statistically consistent with that as presented in this Chapter, although the correlation length is smaller by $\sim 1\sigma$ level than that reported in §5.4. Probably, this is because the use of redshifts resampled from the real data reflects the actual structures along the line of sight, thus make the random objects clustered. The use of such a clustered reference sample reduces an observed amplitude of galaxy clustering.

5.3.3 Corrections for critical biases

In a spectroscopic galaxy survey, a number of observational effects cause artificial biases that are complicated and not negligible in some cases. It is usually impossible to observe all galaxies from the input parent catalog in most spectroscopic surveys due to e.g., the limitations of the slit mask design or the fiber alignment. Consequently, the distribution of observed galaxies is usually biased, i.e., an observed sample is not exactly a random subset of the parent catalog.

In our FMOS observations, galaxies are selected for exposure from the input catalog by using the FMOS-Echidna Spine-to-Object allocation software (Akiyama et al. 2008b) to maximize the operational efficiency. FMOS fibers are uniformly embedded in the field-of-view, and they can move in a limited circular patrol area of each of them. Once a pair of the fibers is allocated for one galaxy, the opportunity of observing its neighborhoods decreases due to the lack of fibers and/or avoiding the fiber entanglement, although the patrol area overlaps with another one of an adjacent fiber. Consequently, the sampling rate of close galaxy pairs is suppressed, and then the clustering amplitude is reduced at scales less or similar to the minimum separation of fibers ($\sim 1'.6$). Furthermore, the numbers of multiple exposures are different among the footprints, and there were fibers which were regularly and/or irregularly out of order. Such characteristics of the fiber allocation system and our observations are expected to results in some bias in the spatial distribution of the observed galaxies in response to the galaxy separation scale.

We correct the observed correlation function for these biases by using a simple weighting scheme, in which each galaxy-galaxy pair is weighted in response to their angular separations (de la Torre et al. 2011; Durkalec et al. 2015). The weight is defined as a ratio of the probability of finding pairs in the FMOS-parent sample, which is input to the allocation software, and the probability of finding pairs in the FMOS-target sample that consists of actually observed

galaxies. We can express the weight function with the angular correlation function of each sample as follows:

$$f(\theta) = \frac{1 + \omega_{\rm par}(\theta)}{1 + \omega_{\rm tar}(\theta)} \tag{5.5}$$

where $\omega_{\rm par}(\theta)$ and $\omega_{\rm tar}(\theta)$ are the angular correlation functions of the FMOS-parent and FMOS-target samples, respectively. This correction scheme implicitly assumes that the parent sample is free from any artificial biases depending on the angular separation scale. Since the statistical uncertainties in the weight function derived from the data are large, we decided to apply the average weight function derived from a set of 64 mock samples as described in §5.2.3. In Appendix E.1, we fully describe the construction of the mock samples, the determination of the correction scheme for the fiber allocation effect, and its validation using the mock samples.

Due to the finite survey area, the observed correlation function is underestimated by an scale-independent constant C, which is known as the integral constraint;

$$w_{\rm p}(r_{\rm p}) = w_{\rm p}^{\rm obs}(r_{\rm p}) + C. \tag{5.6}$$

We calculate the integral constraint on $\xi(r_{\rm p}, \pi)$ following Roche et al. (1999) as

$$C_\xi = \frac{\sum_i \xi^{\rm mod}(r_i)\, RR(r_i)}{\sum_i RR(r_i)}, \tag{5.7}$$

where $RR(r_i)$ is the number of random-random pairs whose distance is in the linearly separated i-th bin (bin size $\Delta r = 1\ h^{-1}$ Mpc). The summation is taken over the entire survey volume. The relation between C and C_ξ is simply given by

$$C = 2\int_0^{\pi_{\rm max}} C_\xi d\pi = 2C_\xi \times 30\ h^{-1}\ {\rm Mpc}. \tag{5.8}$$

We use the scaled non-linear correlation function of dark matter as a model function, i.e, $\xi^{\rm mod} = b^2\xi_{\rm DM}$. We first evaluate b^2 by comparing the non-linear projected correlation function of dark matter with the observed $w_{\rm p}^{\rm obs}(r_{\rm p})$, and calculate the integral constant. We find $C = 0.80$ for our data by repeating this process, i.e., Equations (5.6), (5.7), and (5.8), until convergence. This value is comparable to the observed correlation amplitude at scales greater than $r_{\rm p} \sim 20\ h^{-1}$ Mpc. Therefore, we use the measurements at the scales smaller than this scale to infer physical properties.

Finally, we correct the observed correlation function for the suppression of total amplitude due to the contamination from fake sources for which a spurious signal or non-Hα emission line is misidentified as Hα. Assuming that such sources are randomly distributed in the survey space, the correlation function needs to be corrected by dividing by $(1 - f_{\rm fake})^2$ where $f_{\rm fake}$ is the fraction of fake sources in the sample. We assess the reliability of our redshift measurements using a independent spectroscopic survey including the same galaxies. In the FMOS-spec-z sample, we find 28 galaxies that have a robust redshift measurement (flag = 3 or 4) from the the zCOSMOS-deep survey (Lilly et al. 2007). Of these, 24 galaxies have the redshift measurements from the FMOS-COSMOS and zCOSMOS surveys which are mutually consistent, while four galaxies have inconsistent measurements. We assume that, for these objects, the FMOS measurement is wrong. Actually, three of these inconsistent measurements match to the zCOSMOS measurement if we suppose that the [O III]λ5007 is misidentified as Hα. Such contamination is expected to reduce the amplitude of the observed correlation function since these galaxies are uncorrelated with the galaxies with correct redshift measurements. Assuming that all 28 zCOSMOS redshifts are correct, a plausible fraction of the contamination is given by $f = 0.14 \pm 0.06$. Here we determine the error by supposing the Poisson noise. This fraction of contamination objects corresponds to an underestimate of $26 \pm 10\%$ of the amplitude of the correlation function. Figure 5.2 shows the

locus of these 28 sources in the M_*–SFR plane. Since there is no significant difference between the distribution of these sources and the entire FMOS samples, we use the above fraction to correct the underestimate of the clustering amplitude. We consider the contamination by including the $f_{\rm fake}$ as a parameter to be estimated by the Markov Chain Monte Carlo technique, with a prior given as

$$P\left(f_{\rm fake}\right) \propto \begin{cases} \exp\left[-\frac{(f_{\rm fake}-0.14)^2}{2\times 0.06^2}\right] & \text{for } f_{\rm fake} \geq 0 \\ 0 & \text{for } f_{\rm fake} < 0. \end{cases} \tag{5.9}$$

Note that any objects that are expected to be misidentified in the FMOS survey are not removed from the sample.

5.3.4 Statistical error estimates

We estimate the statistical error bars on the measurement of $\log w_{\rm p}$ of each $r_{\rm p}$ bin using the jackknife resampling method. We define 20 jackknife subsamples from the full FMOS-spec-z sample. We divide the full observed sky region into four contiguous subregions. The partitions on the sky are defined by taking the median point of numerous random points distributed in the survey field, so that all the subregions with irregular shapes have the same area (see Figure 5.1). Then we divide each into five slices along the line of sight. Each sub-volume has typically a side length of 20 h^{-1} Mpc and a depth of 80 h^{-1} Mpc, which approximately corresponds to $\pm$750 kms^{-1}. The jackknife samples are defined by omitting each subsample in turn. The random sample is also constructed for each jackknife sample in the same way. We measure the projected correlation function for each jackknife sample, and correct it for the spatial sampling bias, contamination fraction, and the integral constraint, in the same manner as applied for the data.

Since each structure of the galaxy distribution affects the pair count at different separations, the values of $w_{\rm p}(r_{\rm p})$ at different $r_{\rm p}$'s are correlated. Therefore, we need to use the full covariance matrix to fit a model to the data. The associated covariance matrix $\mathbf{C}_{ij}$ is estimated from the total dispersion among the jackknife samples as

$$\mathbf{C}_{ij} = \frac{N-1}{N}\sum_{k=1}^{N}\left[X_i^k - \langle X_i\rangle\right]\left[X_j^k - \langle X_j\rangle\right], \tag{5.10}$$

where $N = 20$ is the number of jackknife samples, X_i^k is the correlation function at the i-th separation ($r_{\rm p}$) measured for the k-th jackknife sample, and $\langle X_i\rangle$ is the average of X_i^k from $k = 1$ to $k = N$. Here, we use the logarithmic values $\log w_{\rm p}(r_{\rm p})$ rather than $w_{\rm p}(r_{\rm p})$ following the suggestion of Norberg et al. (2009). Although the parameter constraints slightly change when the linear values are used, the choice of logarithmic or linear value does not affect our main conclusions.

Each element of the covariance matrix has large uncertainties since we are able to only take a small number of jackknife samples. Therefore, we smooth the covariance matrix separately for the diagonal or off-diagonal elements following Mandelbaum et al. (2013). The diagonal elements (i.e., variance σ^2) are smoothed by a center-weighted kernel as follows,

$$\left(\sigma_i^2\right)^{\rm smooth} = (\mathbf{C}_{i-1,i-1} + 2\mathbf{C}_{ii} + \mathbf{C}_{i+1,i+1})/4. \tag{5.11}$$

Figure 5.9 (top panel) shows the jackknife covariance diagonal elements and the smoothed values. The discontinuities at $r_{\rm p} \approx 0.15$ and 6 h^{-1} Mpc are effectively suppressed while the global shape is preserved.

To smooth the off-diagonal elements, we first define the correlation matrix $\mathbf{R}_{ij} = \mathbf{C}_{ij}/\sqrt{\mathbf{C}_{ii}\mathbf{C}_{jj}}$, then we smooth it to obtain $\mathbf{R}_{ij}^{\rm smooth}$ with a 3×3 Gaussian kernel:

$$\frac{1}{16}\begin{bmatrix} 1 & 2 & 1 \\ 2 & 4 & 2 \\ 1 & 2 & 1 \end{bmatrix}. \tag{5.12}$$

The final smoothed covariance matrix $\mathbf{C}_{ij}^{\rm smooth}$ is calculated as follows,

$$\mathbf{C}_{ij}^{\rm smooth} = \begin{cases} (\sigma_i^2)^{\rm smooth} & (i=j), \\ \mathbf{R}_{ij}^{\rm smooth}\sqrt{(\sigma_i^2)^{\rm smooth}(\sigma_j^2)^{\rm smooth}} & (i \neq j). \end{cases} \tag{5.13}$$

In Figure 5.9 (middle and bottom panels), we show the original and smoothed correlation matrices. The majority of pixel-to-pixel fluctuation are well eliminated by smoothing while the overall trend is retained. We finally note that our conclusion does not depend on whether using the full covariance matrix or only the diagonal elements, or details of the smoothing method.

5.3.5 Model fit

To obtain physical insights, we fit a power-law model, scaled dark matter model, and an HOD model to the observed correlation function. Our fitting procedure employs the maximum likelihood estimation. We use 11 data points at $-1.5 < \log(r_{\rm p}/h^{-1}\ {\rm Mpc}) < 1.1$ for the model fitting since the contribution from the integral constraint becomes considerable, greater than 10% of the measured $w_{\rm p}(r_{\rm p})$, at $r_{\rm p} \gtrsim 15\ h^{-1}$ Mpc. We define the likelihood of a given model as

$$\mathcal{L} \propto \exp\left(-\frac{\chi^2_{\rm data} + \chi^2_{\rm prior}}{2}\right). \tag{5.14}$$

Here, $\chi^2_{\rm data}$ is calculated from the observed correlation function as

$$\chi^2_{\rm data} = \sum_{i=0}^{N}\sum_{j=0}^{N}\left[X_i^{\rm mod} - X_i^{\rm obs}\right]\mathbf{C}_{ij}^{-1}\left[X_j^{\rm mod} - X_j^{\rm obs}\right] \tag{5.15}$$

where $X_i^{\rm mod}$ and $X_i^{\rm obs}$ are logarithms of the model and observed correlation functions ($\log w_{\rm p}$), and $\mathbf{C}_{ij}^{-1}$ is the inverse of the smoothed covariance matrix defined in §5.3.4. $\chi^2_{\rm prior}$ is the sum of contributions from each parameter with prior information, which is given by a Gaussian function (provided in Tables 5.3 and 5.4). In the fitting, we calculate the average of the model $w_{\rm p}(r_{\rm p})$ in each $r_{\rm p}$ bin $[r_{\rm min} : r_{\rm max}]$ as follows,

$$X_i^{\rm mod} = \log_{10}\left[\int_{r_{\rm min}}^{r_{\rm max}} w_{\rm p}^{\rm mod}(r_{\rm p})dr_{\rm p}/(r_{\rm max} - r_{\rm min})\right] \tag{5.16}$$

for a fair comparison with the data.

To search the parameter space, we employ a Markov Chain Monte Carlo (MCMC) technique with the software *emcee* (Foreman-Mackey et al. 2013). We analyze a chain of 152400 steps after 25400 burn-in steps to find the best-fit parameter set that provides the maximum likelihood, and to evaluate the posterior probability distribution of each parameter. In the fitting process, we use the observed correlation function without the correction for the contamination (see §5.3.3). Instead, we include the contamination fraction $f_{\rm fake}$ as a variable parameter in the MCMC running by comparing the model multiplied by $(1 - f_{\rm fake}^2)$ to the data. The prior on $f_{\rm fake}$ is given by Equation (5.9).

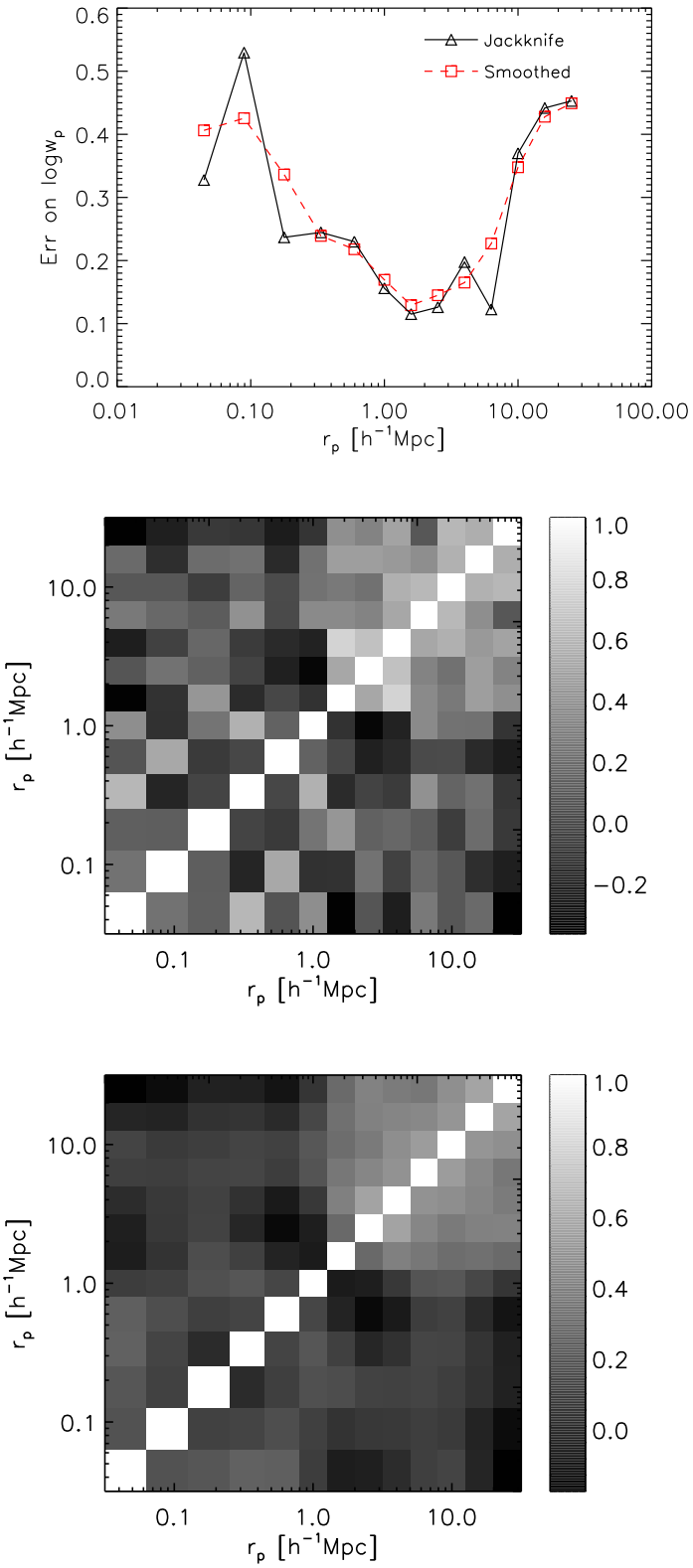

Figure 5.9: Top panel: errors on $\log w_{\rm p}(rp)$ (square root of the diagonal term of the covariance matrix $\mathbf{C}_{ij}$) derived from the jackknife resampling (triangles and solid line). The smoothed errors are indicated by squares and a dashed line. Middle panel: jackknife correlation matrix for $\log w_{\rm p}$. Bottom panel: smoothed correlation matrix.

5.4 Results

The projected correlation function $w_{\rm p}(r_{\rm p})$ is computed for the galaxy sample at $1.43 < z < 1.74$ in the central $0.8{\rm deg}^2$ of the COSMOS field. We use 516 star-forming galaxies, for which the Hα emission line is identified by the Subaru/FMOS. Figure 5.10 presents the observed $w_{\rm p}(r_{\rm p})$ with and without the corrections for the fiber allocation effect (see §5.3.3 and Appendix E.1). The error bars indicate the standard deviation of $\log w_{\rm p}(r_{\rm p})$ at each bin, which is estimated from the jackknife method (see §5.3.4). The scaled projected correlation function of dark matter and the power-law models are also shown.

Table 5.3: Parameter constraints

Model	Params.	Prior[a]	Best-fit
Power-law	$r_0/(h^{-1}$ Mpc)	–	$5.21^{+0.70}_{-0.67}$
	γ	–	$1.99^{+0.13}_{-0.17}$
	$f_{\rm fake}$	$\geq 0, G(0.14, 0.06)$	$0.14^{+0.06}_{-0.06}$
Dark Matter	$b_{\rm g}$	–	$2.59^{+0.41}_{-0.34}$
	$f_{\rm fake}$	$\geq 0, G(0.14, 0.06)$	$0.14^{+0.06}_{-0.06}$

[a] Prior probability distribution for each parameter. $G(x_0, \sigma)$ is a Gaussian function with a mean x_0 and standard deviation σ.

5.4.1 Power-law model

It is known that a real space galaxy correlation function $\xi\,(r)$ can be well described by a power-law faction $\xi\,(r) = (r/r_0)^{-\gamma}$ (e.g., Totsuji & Kihara 1969), where r_0 and γ are a correlation length and power-law slope, respectively. The correlation length describes how strongly galaxies are clustered. With this form of $\xi\,(r)$, from Equation (5.4), $w_{\rm p}\,(r_{\rm p})$ can be expressed as

$$w_{\rm p}\,(r_{\rm p}) = r_{\rm p} \left(\frac{r_{\rm p}}{r_0}\right)^{-\gamma} \frac{\Gamma\left(\frac{1}{2}\right)\Gamma\left(\frac{\gamma-1}{2}\right)}{\Gamma\left(\frac{\gamma}{2}\right)}, \tag{5.17}$$

where Γ is Euler's Gamma function. The integration limit $\pi_{\rm max}$ of Equation (5.4) is taken as infinity. We fit the form of Equation (5.17), multiplied by the contamination factor $(1 - f_{\rm fake})^2$, to the observed $w_{\rm p}\,(r_{\rm p})$, and search the parameter space (r_0, γ, $f_{\rm fake}$) with the MCMC procedure. The parameter constraints are shown in Figure 5.11, and the best-fit parameters and the associated uncertainties (68% confidence intervals) are listed in Table 5.3. We find a correlation length of $r_0 = 5.21^{+0.70}_{-0.67}\ h^{-1}$ Mpc with a slope $\gamma = 1.99^{+0.13}_{-0.17}$ for our sample. In Figure 5.10, we show the best-fit power-law model, which is in good agreement with the data.

5.4.2 Dark matter model and galaxy bias

The galaxy distribution is biases relative to the underlying matter distribution because galaxies form at peaks of the dark matter density fluctuations. A correlation function of galaxies is related to that of dark matter with the galaxy bias $b_{\rm g}$ as,

$$\xi_{\rm gg}(r) = b_{\rm g}^2 \xi_{\rm DM}(r). \tag{5.18}$$

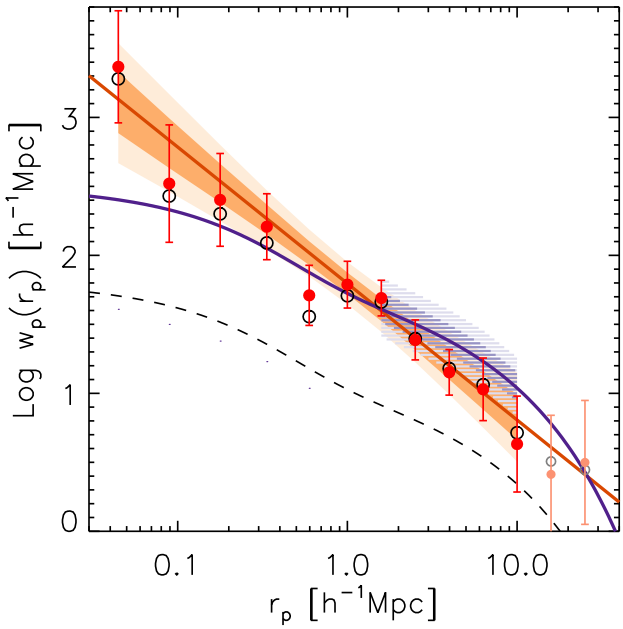

Figure 5.10: The projected two-point correlation function $w_{\rm p}(r_{\rm p})$ of 516 star-forming galaxies at $1.43 < z < 1.74$. Filled circles show $w_{\rm p}(r_{\rm p})$ corrected for the integral constraint and the scale-dependent fiber allocation effects, but the correction for the contamination is not included. The error bars indicate 1-σ uncertainties, calculated by the jackknife resampling, including the errors the weight function $f(\theta)$ (Equation 5.5). The unweighted $w_{\rm p}(r_{\rm p})$ (not corrected for the fiber allocation effect) is given by open circles. The 1–11th data points are used for the model fitting. The best-fit power-law and scaled dark matter models are shown by orange and purple lines, respectively. The 68% and 95% confidence intervals of each model are shown by dark and light shaded regions. Note that the model fits are reduced by multiplying by $(1 - f_{\rm fake})^2$. Dashed line indicates the correlation function of dark matter ($b_{\rm g} = 1$).

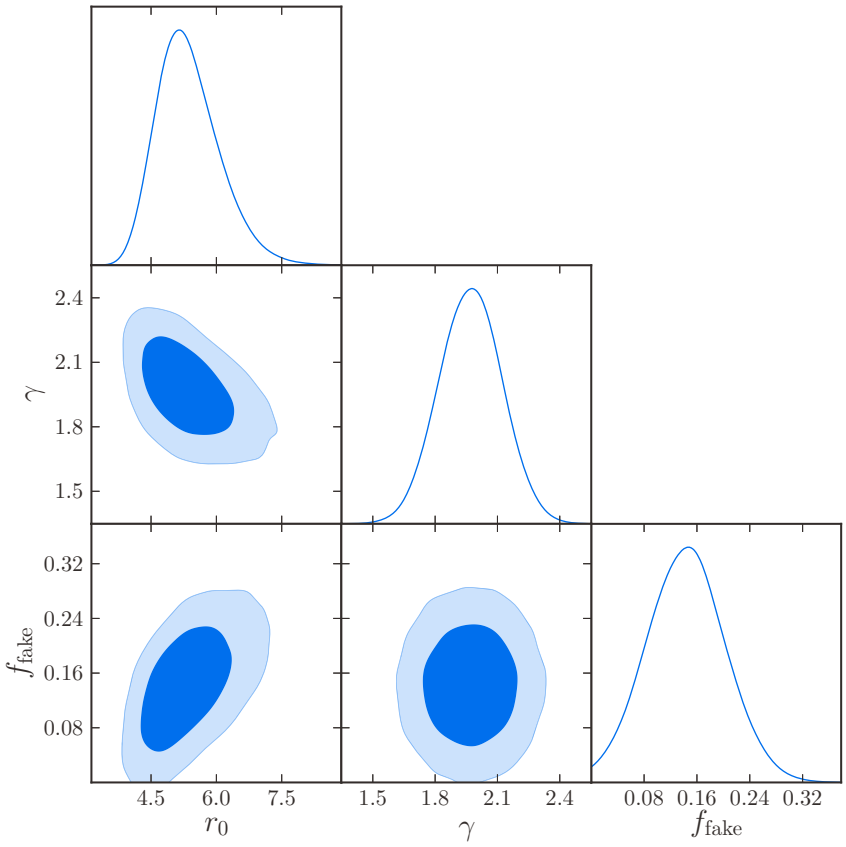

Figure 5.11: Constraints of the power-law parameters (r_0, γ) and $f_{\rm fake}$. Contours show the 68 and 95 percent confidence levels. Solid lines show the posterior probability distribution of each parameter.

While the galaxy bias can have a scale dependence, we constrain a scale-independent bias by comparing the projected dark matter correlation function $w_{\rm p}^{\rm DM}(r_{\rm p})$ with the data. Here, we fit the model of $(1-f_{\rm fake})^2 b_{\rm g}^2 w_{\rm p}^{\rm DM}(r_{\rm p})$ to the 7–11th data points at $r_{\rm p} > 1$ h^{-1}Mpc to avoid an enhancement of the resulting galaxy bias due to the significant one-halo term. We find the posterior of $b = 2.59^{+0.41}_{-0.34}$. The parameter constraints are shown in Figure 5.12 and the best-fit model is presented in Figure 5.10. We note that $b = 2.32^{+0.25}_{-0.22}$ is obtained when only the errors on each data point are used to calculate χ^2, rather than the full covariance matrix.

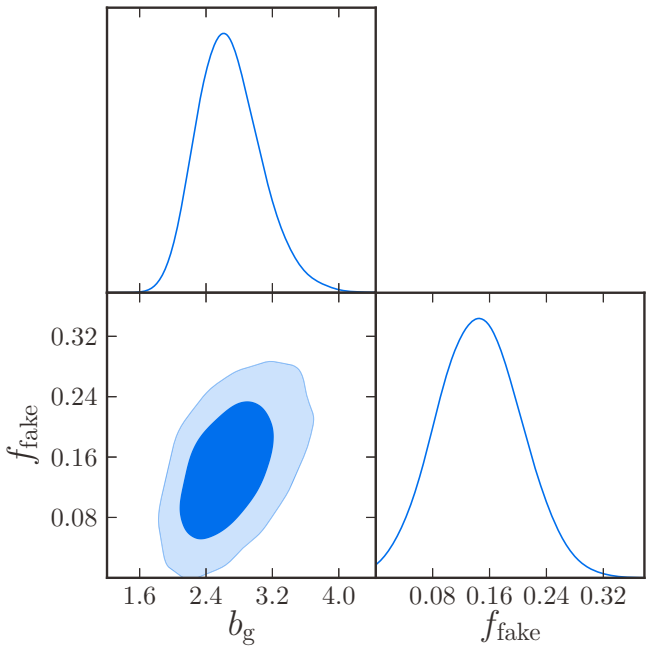

Figure 5.12: Constraints of the galaxy bias $b_{\rm g}$ and $f_{\rm fake}$. Contours show the 68 and 95 percent confidence levels. Solid lines show the posterior probability distribution of each parameter.

5.4.3 Comparison of galaxy clustering measurements

For our sample of star-forming galaxies with SFR $\gtrsim 10\ M_\odot {\rm yr}^{-1}$ at $1.43 < z < 1.74$, we observe a clustering strength of $r_0 = 5.2 \pm 0.7\ h^{-1}$ Mpc. We compare the observed correlation length with other observations up to $z \sim 5$ and predictions from the dark halo model in Figure 5.13.

At lower redshift, Shioya et al. (2008) and Nakajima et al. (2008) measured a clustering of Hα-emitters (HAEs) at $z \sim 0.24$ and $z \sim 0.4$, respectively. These samples were observed by Subaru/Suprime-Cam (Miyazaki et al. 2002) with two narrow band filters, having an Hα flux limit of typically 1–2 orders of fainter than that of our sample. The authors found a correlation length to be $r_0 = 1.6\ h^{-1}$ Mpc ($z \sim 0.24$) and $r_0 = 1.9\ h^{-1}$ Mpc ($z \sim 0.4$), which are much smaller than our results and others. Therefore, it is likely that the HAE samples in those studies are completely different from the descendant of our star-forming sample at $z \sim 1.6$.

HiZELS team conducted a wide-field near-infrared narrow-band surveys (e.g., Geach et al. 2008, 2012; Sobral et al. 2010). Sobral et al. (2010) presented a clustering analysis of HAEs at $z \sim 0.84$ and found a clustering amplitude of $r_0 \sim 2.7\ h^{-1}$ Mpc for their entire sample and $r_0 \sim 4.8 h^{-1}$ Mpc for a brighter subsample ($L_{{\rm H}\alpha} > 10^{42}$ erg s^{-1} cm^{-2}, similar to our luminosity limit). The latter measurement is similar to our results. Geach et al. (2012) measured a correlation function at $z \sim 2.23$ for HAEs with SFR $\gtrsim 7\ M_\odot$ yr^{-1}, similar to our SFR limit, and found $r_0 \sim 3.7\ h^{-1}$ Mpc.

There have been many studies that provide a clustering analysis for galaxies selected based on photometric redshift or colors. Hartley et al. (2010) presented the clustering measurement for the rest-frame color $(U-V)$ selected star-forming galaxies, and found that the correlation length of subsamples of a fixed K-band luminosity (a good proxy of stellar mass) decreases since $z \sim 3$ to the present day. Bielby et al. (2014) measured the clustering of $NUV - r$ selected star-forming galaxies at $z \sim 0.5$–1.75, showing $r_0 \sim 4$–$5\ h^{-1}$ Mpc for galaxies with $\log M_*/M_\odot = 9.6$–11. Ishikawa et al. (2015) found $r_0 = 4.12 \pm 0.07\ h^{-1}$ Mpc for gzK-selected star-forming galaxies ($K < 23$). Our measurement is roughly consistent with such past studies based on samples with stellar mass or luminosity selection similar to our sample ($K < 23.5$, $M_* > 10^{9.6}\ M_\odot$).

Using BzK colors can segregate star-forming (sBzK) galaxies at $1.4 \lesssim z \lesssim 2.5$ (Daddi et al. 2004). Hayashi et al. (2007) found $r_0 = 3.2\ h^{-1}$ Mpc for sBzK galaxies with $K < 23.3$ and $\langle z \rangle = 1.9$. Hartley et al. (2008) measured a more strong clustering with $r_0 \sim 6.8\ h^{-1}$ Mpc and argued that the contamination from those that are highly clustered at higher redshifts ($z \gtrsim 2.5$) may cause such a high amplitude. Lin et al. (2012) measured an amplitude $r_0 \sim 6.3\ h^{-1}$ Mpc for sBzK galaxies of $10 < \log(M_*/M_\odot) < 10.5$. At $z \sim 1.6$–1.7, equivalent to the median redshift of our sample, McCracken et al. (2010) measured an angular correlation function of $K_\mathrm{s} < 23$ (22) sBzK galaxies in the COSMOS field with $r_0 \sim 4.25$ (4.69) h^{-1} Mpc. While the measurements are slightly different from one study to another, our measurement is almost similar to the measurements using sBzK galaxies with a similar mass (or K-band magnitude) range.

There have been efforts that measure the clustering of Lyman break galaxies (LBGs) at $z \sim 3$–5 Bielby et al. (e.g., 2013); Kashikawa et al. (e.g., 2006); Foucaud et al. (e.g., 2003); Adelberger et al. (e.g., 2005) or more (Harikane et al. 2015), with correlation lengths similar to our measurement ($r_0 \sim 4$–$5\ h^{-1}$ Mpc). Durkalec et al. (2015) measured the projected correlation function of ~ 3000 galaxies from the VIMOS Ultra Deep Survey, including the COSMOS field, and found $r_0 \sim 4$ Mpc at $z \sim 2.5$–3.5, similar to our measurement within 1σ level.

Given these comparisons, we conclude that our result is in good agreement with the previous clustering measurements of star-forming galaxies at similar redshifts. We stress that our result is based on spectroscopically-identified galaxies with the Hα emission line, and that, for the majority (more than half) of our sample, their redshift is confirmed with the detection of one or more additional lines (i.e., [N II], Hβ, or [O III]). Although large samples from imaging surveys have enabled us to measure the galaxy clustering with much small statistical uncertainties, the broad-band selections extract galaxies from a wide range of redshift, and the effect of contamination from other redshift ranges might be considerable. Hence, it is challenging to trace the redshift evolution of the galaxy clustering. Narrow-band surveys are appropriate to extract galaxies with almost pure flux selection within a narrow redshift range, but still it is challenging to evaluate the effect of contamination from objects for which another line is misidentified.

5.5 Connecting galaxies with halos

Understanding the connection between galaxies and the underlying dark matter halos is essential for understanding how and in what environments galaxy form and evolve. In this section, we determine the properties of halos at $z \sim 1.6$ in which the general star-forming galaxies with $M_* \gtrsim 10^{9.6}\ M_\odot$ reside by modeling the observed correlation function with a halo occupation distribution (HOD) model in the standard ΛCDM framework.

5.5.1 The halo model and halo occupation distribution

In the standard CDM paradigm, dark matter halos form at over dense regions, and galaxies form in halos and subhalos. Properties of the dark matter halos have been well understood theoretically through cosmological N-body simulations because almost only gravity is important. In halo models, the global properties of halos such as the number density and halo bias are

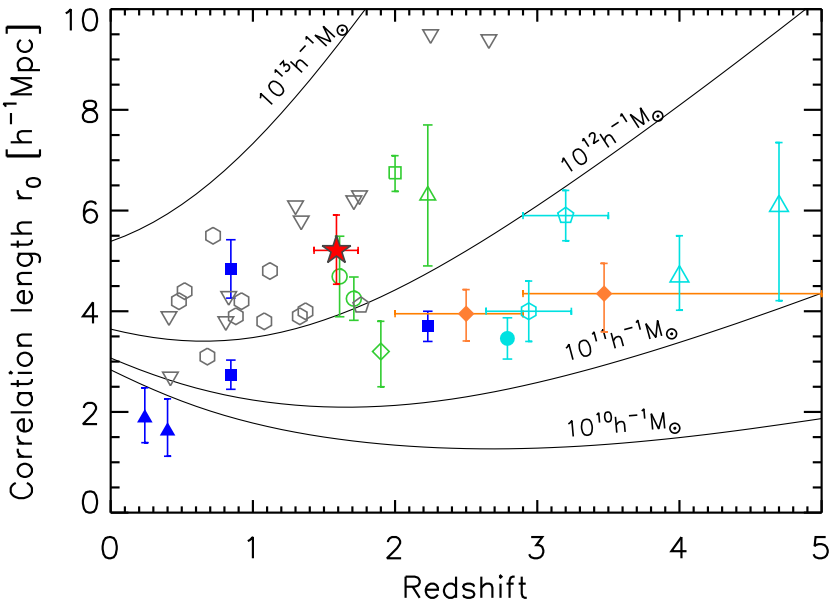

Figure 5.13: Correlation length r_0 as a function of redshift. A star symbol indicates our data. Open and filled symbols indicate measurements in the literature based on photometric and spectroscopic (or narrow-band imaging) observations, respectively; *Blue* – Hα emitters in narrow-band surveys (*Filled triangle* – Shioya et al. 2008; Nakajima et al. 2008, *Filled square* – Sobral et al. 2010; Geach et al. 2012), *Orange filled diamonds* – Durkalec et al. 2015, *Green* – sBzK galaxies (*Open circles* – McCracken et al. 2010, *Open square* – Hartley et al. 2008, *Open diamond* – Hayashi et al. 2007, *Open triangle* – Lin et al. 2012, *Gray* – other color-selected star-forming galaxies (*Open inverse triangles* – Hartley et al. 2010, *Open pentagon* – Ishikawa et al. 2015, *Open hexagons* – Bielby et al. 2014), *Cyan* – LBGs (*Filled circle* – Bielby et al. 2013, *Open triangle* – Kashikawa et al. 2006, *Open pentagon* – Foucaud et al. 2003, *Open hexagon* – Adelberger et al. 2005). Four solid curves indicate the correlation length of dark halos of different masses, as labelled.

basically determined by the halo mass while there are other dependence on e.g., the halo assembly history (e.g., Miyatake et al. 2016). The halo models provide a convenient framework to study the relation between distributions of galaxies and underlying halos. Galaxy clustering is considered as a combination of two contributions: the one-halo term arising from pairs of galaxies reside in the same halo, and the two-halo term from pairs of galaxies within distinct halos. The full correlation function is expressed as the sum of these two terms as follows:

$$1 + \xi_{\rm gg}(r) = \left[1 + \xi^{\rm 1h}_{\rm gg}(r)\right] + \left[1 + \xi^{\rm 2h}_{\rm gg}(r)\right] \Leftrightarrow \xi_{\rm gg}(r) = 1 + \xi^{\rm 1h}_{\rm gg}(r) + \xi^{\rm 2h}_{\rm gg}(r) \tag{5.19}$$

where "gg" means galaxy-galaxy auto correlation, and the "1+" is required since the pair count is proportional to $1 + \xi$.

The halo occupation distribution (HOD) framework has been developed to link the halo model and the galaxy clustering. The relation between dark halos and galaxies is described by the probability $P(N|M)$ that a halo of mass M hosts N galaxies. In a commonly-used HOD model, galaxies are divided into central or satellite galaxies (e.g., Zheng et al. 2005), and an enough massive halo is considered to contain one central and $N - 1$ satellite galaxies. In this study, we use a simple HOD framework, in which it is assumed that all galaxies reside in a halo, and that the mean number of galaxies hosted by a halo depends only on the halo mass and is independent of the formation history and the environment of halos.

The formalisms having many convolutions are simplified in the Fourier space. The galaxy correlation function is expressed in terms of the power spectrum as

$$\xi(r) = \frac{1}{2\pi^2} \int_0^\infty dk k^2 P(k) \frac{\sin kr}{kr} \tag{5.20}$$

and Equation (5.19) can be written as

$$P_{gg}(k) = P^{1h}_{\rm gg}(k) + P^{2h}_{\rm gg}(k). \tag{5.21}$$

Our calculation follows an analytical framework in van den Bosch et al. (2013). We employ the halo mass function from Tinker et al. (2010), which defines a halo as a spherically collapsed region with an average density 200 times greater than the background matter density of the Universe. We use the large-scale halo bias proposed by Tinker et al. (2010) and its empirical radial scale dependence of Tinker et al. (2012).

The one-halo term is expressed as the sum of the contribution from central–satellite and from satellite–satellite galaxy pairs hosted by the same halos as

$$P^{\rm 1h}_{\rm gg}(k, z) = \frac{1}{n^2_{\rm tot}} \int dM \frac{dn}{dM}(M, z) \left[2 \langle N_{\rm cen}|M\rangle \langle N_{\rm sat}|M\rangle u(k, M, z) + \langle N_{\rm sat}|M\rangle^2 u^2(k, M, z)\right] \tag{5.22}$$

where $n_{\rm tot}$ is the mean number density of galaxies under consideration, dn/dM is the halo mass function, $\langle N_{\rm cen}|M\rangle$ and $\langle N_{\rm sat}|M\rangle$ denote the HOD, i.e, the average numbers of central and satellite galaxies hosted by a halo of mass M, respectively. Here, we assume that the occupation numbers of centrals and satellites are independent of each other, so that $\langle N_{\rm cen} N_{\rm sat}\rangle = \langle N_{\rm cen}\rangle \langle N_{\rm sat}\rangle$, and that the satellite occupation numbers follow Poisson statistics, so that $\langle N_{\rm sat}(N_{\rm sat} - 1)\rangle = \langle N_{\rm sat}\rangle^2$, which is supported both by observations (Yang et al. 2008) and numerical simulations (Kravtsov et al. 2004). We also assume that the number density of satellite galaxies follows an NFW (Navarro et al. 1997) profile from the halo center, with the mass-concentration relation calibrated by Macciò et al. (2007), which is expressed as the Fourier transform by u in Equation (5.22). In addition, it is implicitly assumed that the central galaxies lie at the exact center of halos.

The two-halo term consists of three contributions from central–central, central–satellite, and satellite–satellite galaxy pairs hosted by distinct halos. It is expressed as

$$\begin{aligned} P_{\rm gg}^{\rm 2h}(k,z) = \frac{1}{n_{\rm tot}^2}\int dM_1 \int dM_2 \frac{dn}{dM}(M_1,z)\frac{dn}{dM}(M_2,z) \\ \left[\langle N_{\rm cen}|M_2\rangle \langle N_{\rm cen}|M_2\rangle + 2\langle N_{\rm cen}|M_1\rangle \langle N_{\rm sat}|M_2\rangle u(k,M_2,z)\right. \\ \left. + \langle N_{\rm sat}|M_1\rangle \langle N_{\rm sat}|M_2\rangle u(k,M_1,z)u(k,M_2,z)\right] P_{\rm hh}(k|M_1,M_2,z), \end{aligned} \tag{5.23}$$

where $P_{\rm hh}(k|M_1,M_2,z)$ is the cross power spectrum of halos of masses M_1 and M_2, which is calculated from the nonlinear matter power spectra (Smith et al. 2003) and the scale-dependent halo bias. The halo exclusion is also considered (see van den Bosch et al. 2013 for details).

In this study, we define the functional form of the HOD of the central galaxies as

$$\langle N_{\rm cen}|M\rangle = \frac{1}{2}\left[1+{\rm erf}\left(\frac{\log M - \log M_{\rm min}}{\sigma_{\log M}}\right)\right], \tag{5.24}$$

and the occupation number of satellite galaxies is given by

$$\langle N_{\rm sat}|M\rangle = \frac{1}{2}\left[1+{\rm erf}\left(\frac{\log(M/M_{\rm min})}{\sigma_{\log M}}\right)\right]\left(\frac{M-M_{\rm cut}}{M_1'}\right)^{\alpha}. \tag{5.25}$$

when $M > M_{\rm cut}$, otherwise $\langle N_{\rm sat}|M\rangle = 0$. $M_{\rm min}$ is a halo mass above which a halo has a single central galaxy, and this transition is smoothed by a scatter $\sigma_{\log M}$ (Zheng et al. 2005, 2007). The average number of satellite galaxies increases with increasing halo mass by a power law parametrized by a normalization M_1' and slope α. $M_1 = M_1' + M_{\rm cut}$ is a halo mass where a halo is expected to have a single satellite galaxy.

The total HOD is given by the sum of the central and satellite terms:

$$\langle N_{\rm tot}|M\rangle = \langle N_{\rm cen}|M\rangle + \langle N_{\rm sat}|M\rangle\,. \tag{5.26}$$

Once a set of HOD parameters is given, the following physical quantities are inferred:

- Average number density of galaxies

$$n_{\rm tot} = \int dM \frac{dn}{dM}(M,z)\langle N_{\rm tot}|M\rangle \tag{5.27}$$

- Effective large scale bias

$$b_{\rm g}^{\rm HOD} = \frac{1}{n_{\rm tot}}\int dM \frac{dn}{dM}(M,z)\, b_h(M)\langle N_{\rm tot}|M\rangle \tag{5.28}$$

- Satellite fraction

$$f_{\rm sat} = \frac{1}{n_{\rm tot}}\int dM \frac{dn}{dM}(M,z)\langle N_{\rm sat}|M\rangle \tag{5.29}$$

- Effective halo mass

$$M_{\rm eff} = \frac{1}{n_{\rm tot}}\int dM^2 \frac{dn}{dM}(M,z)\langle N_{\rm tot}|M\rangle \tag{5.30}$$

The effective large scale bias is the number-weighted average of the scale-dependent bias $b_h(M)$, which is given by Tinker et al. (2010). The effective halo mass is the number-weighted average mass of halos that host galaxies in our sample. The average number density of central ($n_{\rm cen}$) or satellite galaxies ($n_{\rm sat}$) are calculated by replacing $\langle N_{\rm tot}|M\rangle$ in Equation (5.27) with $\langle N_{\rm cen}|M\rangle$

or $\langle N_{\rm sat}|M\rangle$. The effective halo mass for the central galaxies can be calculated by replacing $\langle N_{\rm tot}|M\rangle$ and $n_{\rm tot}$ in Equation (5.30) with $\langle N_{\rm cen}|M\rangle$ and $n_{\rm cen}$, respectively.

5.5.2 Limitations for the HOD parameters

We search the HOD parameter space with a MCMC technique to find the best-fit parameter set and the posterior probability distribution of each parameter. While the HOD model defined above has five free parameters, our measurement based on the sample containing a relatively small number of galaxies does not permit to strongly constrain all the arameters. Therefore, we impose prior limitations on some parameters to resolve the degeneracies and to avoid overfitting.

We fix the power-law slope α to be 1, which is commonly applied even in studies using larger samples, and also impose a relation between $M_{\rm cut}$ and M_1' as

$$\log M_{\rm cut}/M_\odot = 0.76 \log M_1'/M_\odot + 2.3, \tag{5.31}$$

following Conroy et al. (2006, see also Martinez-Manso et al. 2015). We obtain $M_{\rm cut} \approx M_{\rm min}$ from our data, which is consistent with a constraint from e.g., More et al. (2015), for the best-fit parameter set.

The degeneracy between $M_{\rm min}$ and $\sigma_{\log M}$ is commonly known. Thus, we evaluate $\sigma_{\log M}$ by using a stellar-to-halo mass relation derived by Behroozi et al. (2013a), with the uncertainty on the stellar mass estimate taken into account. The prior probability distribution defined as (see Appendix E.3 for details)

$$P(\sigma_{\log M}) \propto \begin{cases} \exp\left[-\frac{(\sigma_{\log M}-0.24)^2}{2\times 0.03^2}\right] & \text{for } \sigma_{\log M} \geq 0, \\ 0 & \text{for } \sigma_{\log M} < 0. \end{cases} \tag{5.32}$$

With the HOD model parametrized by Equations (5.24) and (5.25), the total number density (Equation 5.27) indicates the abundance of all galaxies with $M_* > M_*^{\rm lim}$, rather than the number density of the sample used for the clustering analysis. Thus, we assume the our FMOS-spec-z sample is representative of the M_*-selected sample, of which the total number density in the survey volume is 9.29×10^{-3} $h^{-3}{\rm Mpc}^{-3}$ (see Table 5.2). We estimate the sample variance of the number density by using the subhalo mock catalog, and find approximately 10% fluctuation from one to another subvolume equivalent to our survey volume. Therefore, we put on the total galaxy number density a prior limitation given by $n_{\rm tot} = (9.29 \pm 0.93) \times 10^{-3}$ $h^{-3}{\rm Mpc}^{-3}$.

The prior on the contamination fraction is given by Equation (5.9), in the same matter as §5.4. Other HOD halo mass parameters $\log M_{\rm min}/M_\odot$ and $\log M_1'/M_\odot$ are limited between 9 and 15 with a uniform probability function. The prior information is summarized in Table 5.3.

5.5.3 HOD model fit

We fit the projected correlation function computed from the HOD model to the observed $w_{\rm p}(r_{\rm p})$. The variable HOD parameters are three: $\log M_{\rm min}$, $\sigma^2_{\log M}$, and $\log M_1'$. Note that the slope parameter α is fixed to 1 and $M_{\rm cut}$ is related to M_1' through Equation (5.31). We include the contamination fraction $f_{\rm fake}$ as a variable parameter by comparing the model multiplied by $(1-f_{\rm fake}^2)$ to the data. As described in §5.5.2, we put a prior on some parameters. For the fitting, we use 11 data points at $-1.5 < \log(r_{\rm p}/h^{-1}\ {\rm Mpc}) < 1.1$ and analyze 152400 MCMC steps after 25400 burn-in steps to evaluate the best-fit parameters and the posterior probability distribution of each parameter. The number of degrees of freedom in this analysis is

$$\begin{aligned} {\rm d.o.f} = 10 \quad = \quad & 11 \ [\text{data points of } w_{\rm p}(r_{\rm p})] & (5.33)\\ & +3 \ [\text{priors on } n_{\rm tot}, \sigma_{\log M}, f_{\rm fake}] & (5.34)\\ & -4 \ \left[\text{parameters: } M_{\rm min}, \sigma^2_{\log M}, M_1', f_{\rm fake}\right]. & (5.35) \end{aligned}$$

The HOD parameters are effectively constrained from our data. Figure 5.14 shows the parameter constraints with 68 and 95 percent confidence levels, and the posterior probability distribution of each parameter. The prior information and the best-fit parameters that give a minimum χ^2 are listed in Table 5.3. The constraints of the HOD is shown in Figures 5.15. We show the observed $w_{\rm p}(r_{\rm p})$ and the model in Figure 5.16. The data points are well fitted by the model and the one-halo term is significantly evident at $r_{\rm p} \lesssim 1\ h^{-1}$ Mpc. We calculate the physical quantities of the host halos given by Equations (5.27)–(5.30), and show their posterior probability distribution in Figure 5.17. The best-fit values of the inferred quantities are summarized in Table 5.3 with the 68 percent confidence intervals.

Additionally, considering the large uncertainties of the estimated contamination fraction, we perform the fitting with $f_{\rm fake}$ fixed to zero. The parameter constraints and the derived quantities are listed in the last column in Table 5.3. The results with and without the contamination fraction considered are in agreement within their 1σ uncertainties. Throughout the thesis, we discuss the galaxy–halo connection based on the main results that are corrected for the effect of the contamination sources.

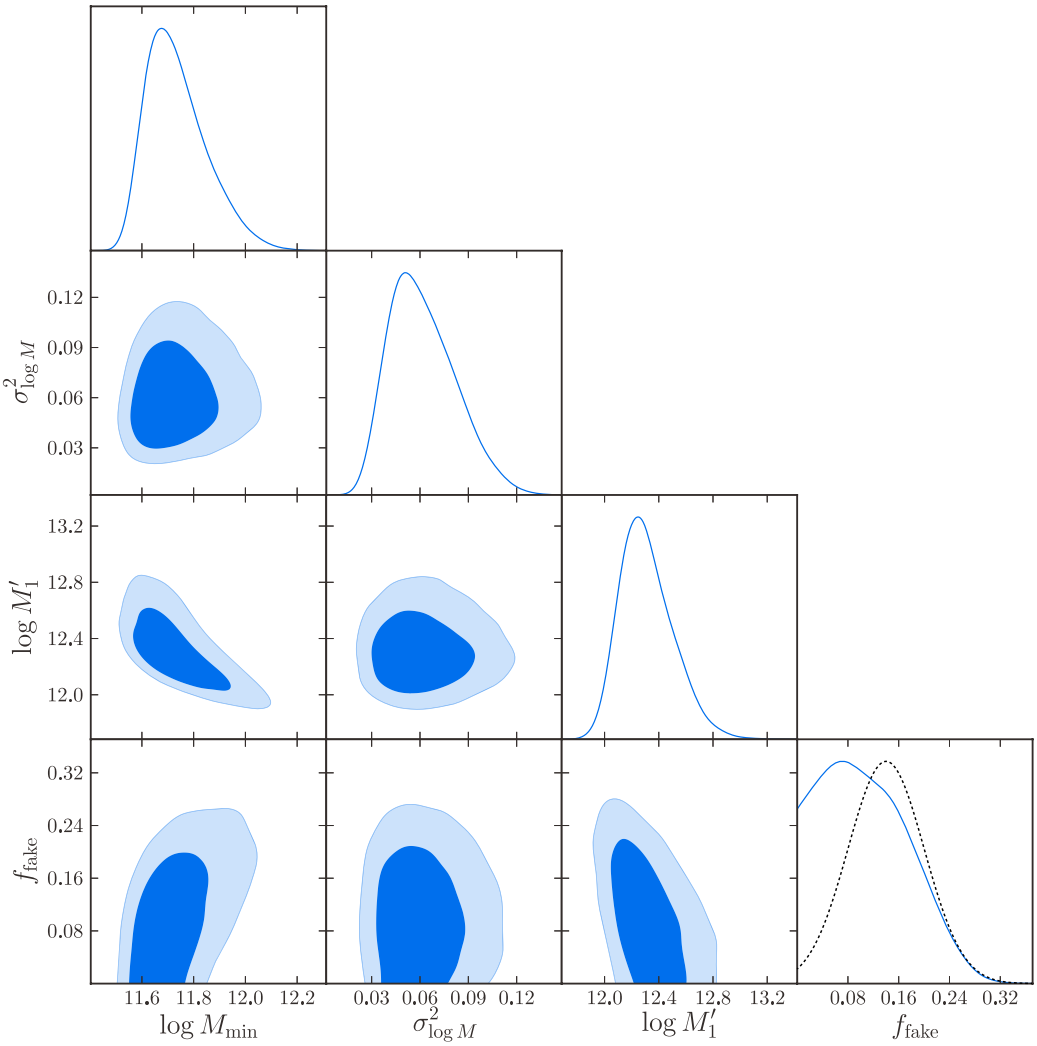

Figure 5.14: Constraints of the HOD parameters ($\log M_{\rm min}$, $\sigma^2_{\log M}$, $\log M'_1$) and $f_{\rm fake}$. Contours show the 68 and 95 percent confidence levels. Solid lines show the posterior probability distribution of each parameter. A dotted line indicates the prior probability distribution of $f_{\rm fake}$.

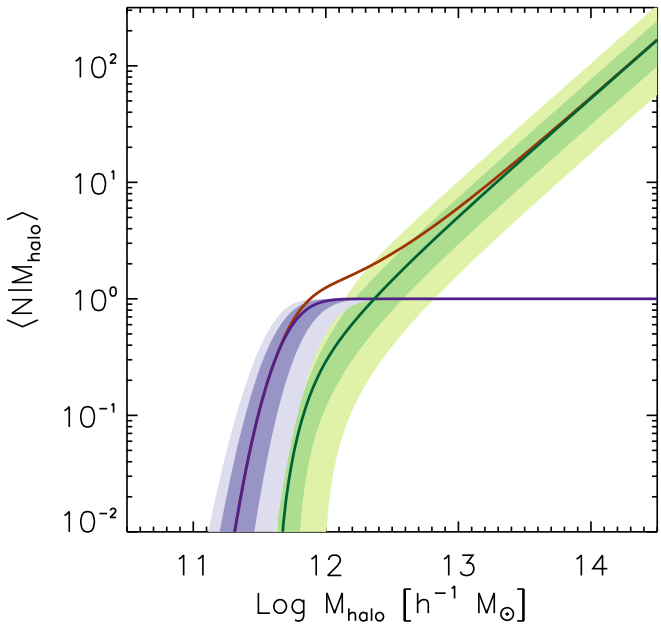

Figure 5.15: Halo occupation distribution for our sample. Purple, green and red lines show the average number of central, satellite, and total (i.e., central and satellites) galaxies in a halo as a function of halo mass, respectively. Dark and light shaded regions show the 68 and 95 percent confidence intervals of $\langle N_{\rm cen}\rangle$ or $\langle N_{\rm sat}\rangle$, respectively.

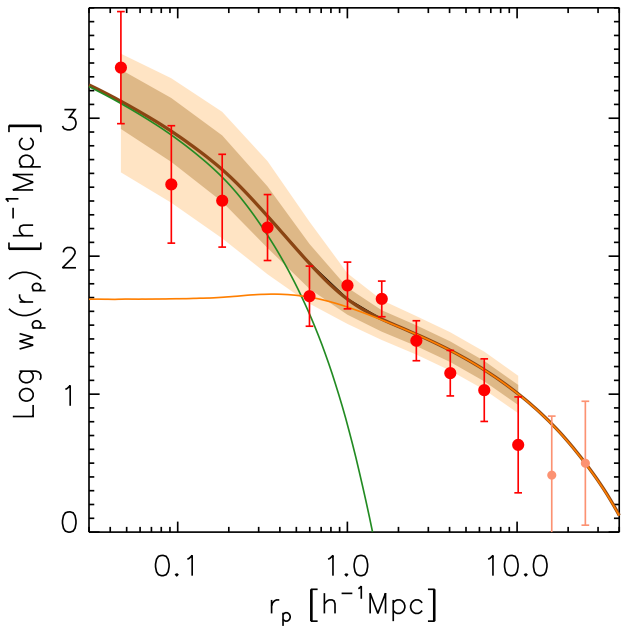

Figure 5.16: Observed projected correlation function and the prediction from the best-fit HOD model (thick solid line). Green and orange thin solid curves shows the one-halo and two-halo terms, respectively. Dark and light shaded regions show the 68 and 95 percent confidence intervals.

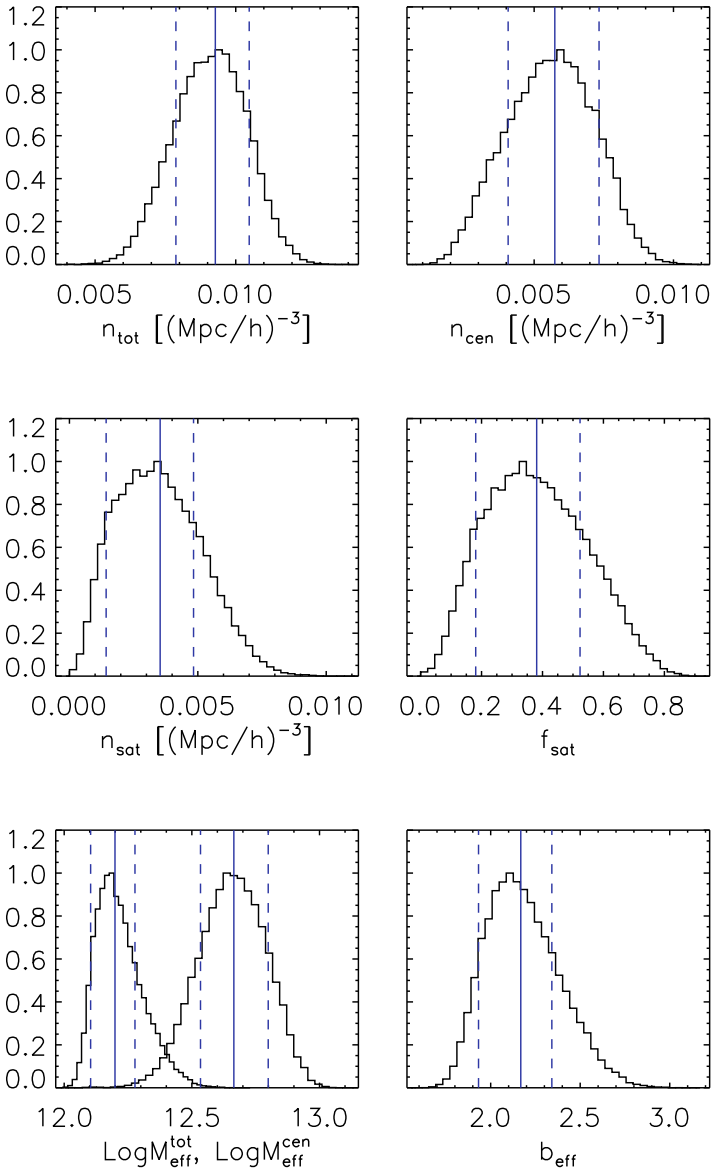

Figure 5.17: Constraints on the inferred physical quantities. Histograms show the normalized distribution of individual parameters of all 152400 MCMC steps. From the top to bottom, the average total number density ($n_{\rm tot}$), the average number density of central ($n_{\rm cen}$) and satellite galaxies ($n_{\rm sat}$), the satellite fraction ($f_{\rm sat}$), the effective halo mass ($M_{\rm eff}^{\rm tot}$), the effective central halo mass ($M_{\rm eff}^{\rm cen}$), and the effective large scale bias are shown. Vertical solid lines and dashed lines indicate the best-fit value giving a minimum χ^2 and the 68 percent confidence interval, respectively.

Table 5.4: Priors and constraints of the HOD parameters

Parameters	**Prior**[a]	**Best-fit**	**Best-fit (no $f_{\rm fake}$)**
χ^2/ν		1.23	1.01
$\log M_{\rm min}/M_\odot$	$U(9,15)$	$11.71^{+0.11}_{-0.12}$	$11.65^{+0.09}_{-0.10}$
$\sigma^2_{\log M}$	$\geq 0, G(0.24, 0.03)$ for $\sigma_{\log M}$	$0.057^{+0.020}_{-0.021}$	$0.057^{+0.022}_{-0.024}$
$\log M_1'/M_\odot$	$U(9,15)$	$12.28^{+0.18}_{-0.20}$	$12.40^{+0.22}_{-0.23}$
$f_{\rm fake}$	$\geq 0, G(0.14, 0.06)$	$0.099^{+0.053}_{-0.092}$	—
Inferred quant.	**Prior**	**Best-fit**	**Best-fit (no $f_{\rm fake}$)**
$n_{\rm tot}/({\rm Mpc}^3)$[b]	$> 0, G(9.29\,0.93)$	$9.27^{+1.21}_{-1.40} \times 10^{-3}$	$9.22^{+1.49}_{-1.56} \times 10^{-3}$
$n_{\rm cen}/({\rm Mpc}^3)$		$5.74^{+1.59}_{-1.67} \times 10^{-3}$	$6.70^{+1.61}_{-1.68} \times 10^{-3}$
$n_{\rm sat}/({\rm Mpc}^3)$		$3.53^{+1.30}_{-2.10} \times 10^{-3}$	$2.52^{+0.94}_{-1.94} \times 10^{-3}$
$f_{\rm sat}$		$0.38^{+0.14}_{-0.20}$	$0.27^{+0.10}_{-0.19}$
$M^{\rm tot}_{\rm eff}/M_\odot$		$4.62^{+1.14}_{-1.63} \times 10^{12}$	$3.78^{+0.95}_{-1.45} \times 10^{12}$
$M^{\rm cen}_{\rm eff}/M_\odot$		$1.58^{+0.29}_{-0.34} \times 10^{12}$	$1.42^{+0.20}_{-0.28} \times 10^{12}$
$b_{\rm eff}$		$2.17^{+0.17}_{-0.24}$	$2.04^{+0.14}_{-0.22}$
$\log M_1/M_{\rm min}$		$0.66^{+0.30}_{-0.27}$	$0.83^{+0.31}_{-0.26}$

[a] Prior probability distribution of each parameter. $U(x_1, x_2)$ is a top-had distribution with a interval between x_1 and x_2. $G(x_0, \sigma)$ is a Gaussian function with a mean x_0 and standard deviation σ.

[b] Observed number density of the the Photo-z M_*-selected sample. This is not a HOD parameter, but its prior is used in the MCMC running.

5.6 Discussions

5.6.1 Large scale bias and halo mass

From the HOD modeling, we find an effective large scale bias $b_{\rm eff} = 2.17^{+0.17}_{-0.24}$ and an effective halo mass $M_{\rm eff} = 4.62^{+1.14}_{-1.63} \times 10^{12}\ h^{-1}\ M_\odot$. Figure 5.18 shows the large scale bias as a function of redshift, with measurements at different redshifts based on samples with similar stellar mass limits ($M_* \gtrsim 10^{9.6} M_\odot$) in the literature. The trend seen among these measurements, including our result, is in good agreement with the prediction from the standard scenario of hierarchical structure formation, where the galaxy bias decreases with cosmic time (e.g., Mo & White 1996). In particular, with the results at higher redshifts from the VUDS survey (Durkalec et al. 2015), the decrease of the galaxy bias from the ancient eras becomes more evident. At lower redshifts, we show results from the Canada-France-Hawaii Telescope Legacy Survey (CFHTLS) by Coupon et al. (2012). Here we plot the bias measurements for three samples at $z \sim 0.3, 0.5$ and 0.7 that are selected based on the absolute g-band magnitude ($M_g - 5\log h < -19.8$). The observed galaxy number density of these samples is $n_{\rm gal} \approx 8 \times 10^{-3} h^3 {\rm Mpc}^{-3}$, similar to our M_*-selected sample. Comparing these results with our data indicates a decrease of galaxy bias from $z \sim 1.6$ to the present epoch. Our data is also similar to the measurements by Wake et al. (2011) for a samples with $M_* > 10^{10}\ M_\odot$ at $z \sim 1.5$ ($b = 2.51^{+0.04}_{-0.04}$) from the NEWFIRM Medium Band Survey.

In Figure 5.19, we show the derived halo masses ($M_{\rm min}$ and the effective halo mass $M^{\rm tot}_{\rm eff}$) for our sample, with the average growth histories of halos of different masses that are derived by Zhao et al. (2009) or Behroozi et al. (2013a). We find that our measurement of the effective halo mass is located on the mass assembly history of halos having $M_{\rm h} \approx 2 \times 10^{13}\ h^{-1} M_\odot$ at the present day (thick curve), which is comparable to the typical scale of a galaxy group. We also plot

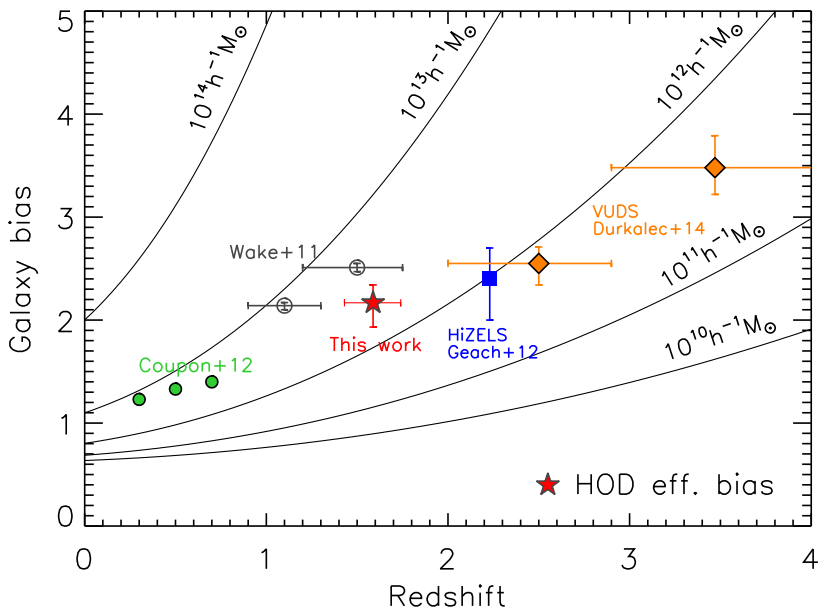

Figure 5.18: The effective galaxy bias as a function of redshift. Our result is shown by a red star. Other symbols indicate the results at several redshifts in the literature. Filled circles show the measurements for the samples at $z \sim 0.3, 0.5$ and 0.7 that are selected based on the absolute g-band magnitude ($M_g - 5\log h < -19.8$). Empty circles show the measurements by Wake et al. (2011) for sample with $M_* > 10^{10}\ M_\odot$ at $z \sim 1.1$ and $z \sim 1.5$. A blue square shows the bias of the HiZELS sample at $z = 2.23$ (Geach et al. 2012). Orange diamonds indicates the results from the VUDS survey (Durkalec et al. 2015). Solid curves show the relation among the bias, halo mass and redshift, as labelled.

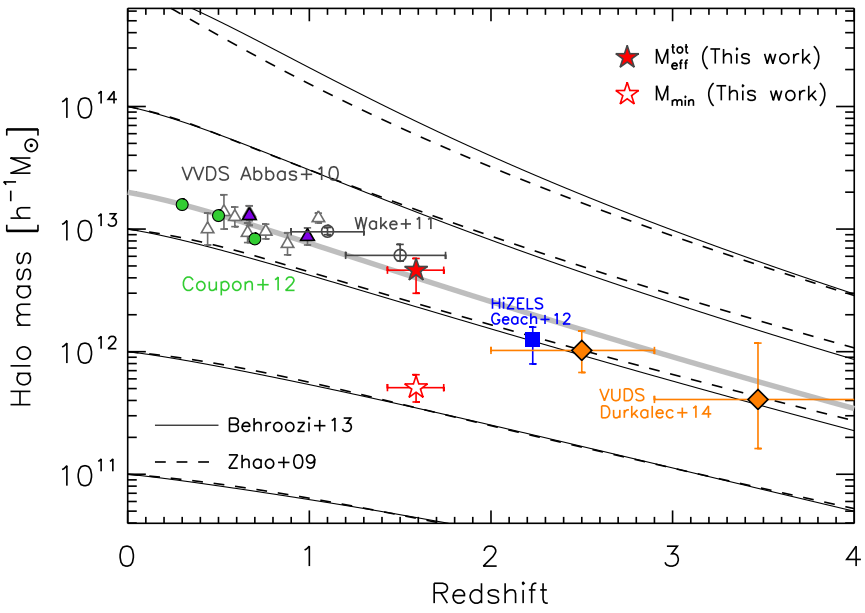

Figure 5.19: The average host halo mass as a function of redshift. Empty and filled stars indicate the $M_{\rm min}$ and the effected halo mass $M_{\rm eff}^{\rm tot}$, respectively, estimated for our sample with the HOD model. Solid and dashed curves show the mass assembly histories of host halos of different masses at $z = 0$, derived by Behroozi et al. (2013a) (solid lines) and Zhao et al. (2009) (dashed lines), respectively. A thick curve for $\log M_{\rm h} = 13.3$ at $z = 0$. Filled circles show the measurements for the samples at $z \sim 0.3, 0.5$ and 0.7 that are selected based on the absolute g-band magnitude ($M_g - 5\log h < -19.8$). The results from the VVDS survey at $0.2 \lesssim z \lesssim 1.3$ are indicated by filled triangles. Empty circles show the results at $z \sim 1.1$ and $z \sim 1.5$ from Wake et al. (2011).

effective halo masses from the literature, which are derived with an HOD modeling at different redshifts. At lower redshifts, we show the results from the CFHTLS at $z \sim 0.3, 0.5$ and 0.7 that are mentioned above (error bars are comparable to the size of the symbol; Coupon et al. 2012). Additionally, results derived by Abbas et al. (2010) at $0.2 \lesssim z \lesssim 1.3$ from the VIMOS-VLT Deep Survey (VVDS; Le Fèvre et al. 2005) are shown by triangles. We highlight that two subsamples in Abbas et al. (2010) with $M_B < -19.5$ at $z = 0.67$ and 0.99 (filled triangles) have a number density that is similar to that of our M_*-selected sample. These subsamples at lower redshifts are also located along the same halo mass assembly history as our data. The measurements at higher redshifts (Geach et al. 2012; Durkalec et al. 2015) are located along the average assembly history of halos with $\log M_{\rm h} \approx 13$ at $z = 0$ while all measurements shown here are in agreement for the host halo mass at the present day within their uncertainties. These results indicate a good agreement between the predictions of the halo mass assembly history and observations at a wide range of cosmic history since $z \sim 3$.

5.6.2 Stellar mass-to-halo mass ratio

Stellar mass-to-halo mass ($M_*/M_{\rm h}$) ratio encodes the efficiency of conversion of baryons into stars relative to the amount of the accretion of the dark matter into the host halos. Yang et al. (2003) proposed a functional form with double power-law components to express the average halo mass-to-galactic luminosity ratios, motivated by the fact that the observed luminosity function is steeper (shallower) than the halo mass function at the high (low) mass end (see also Cacciato

et al. 2013; Vale & Ostriker 2004). Later, this relation is extended to investigate the stellar-to-halo mass relation (SHMR, $M_*/M_{\rm h}$ vs. $M_{\rm h}$) based on large data sets at $z \sim 0$–1 (e.g., Zheng et al. 2007; Yang et al. 2008, 2009). As shown in many studies, it has been known that the SMHM ratio reaches a peak around a halo mass of $M_{\rm h} \sim 10^{12}\ M_\odot$ (e.g., Moster et al. 2010, 2013; Behroozi et al. 2010; Guo et al. 2010; More et al. 2011). Recently, Behroozi et al. (2013a) established an accurate SHMRs at a wide range of redshift ($0 \leq z < 8$). These studies assume a monotonic correspondence (with some scatter) between halo mass (or other indicators such as a peak maximum circular velocity) and stellar mass of galaxies, which is usually referred to as an abundance matching technique.

For our sample, we find the $\log M_*/M_{\rm h} = -2.3 \pm 0.2$ at $M_{\rm h} = M_{\rm min} = 10^{11.86}\ h^{-1}\ M_\odot$, which is measured as a ratio of the threshold stellar mass $M_*^{\rm lim}$ to $M_{\rm min}$. Here, we use a hubble parameter $h = 0.7$ to calculate halo mass, and thus the $M_*/M_{\rm h}$ ratio. In Figure 5.20, we show the observed $M_*/M_{\rm h}$ ratio with other results in the literature for comparison. We show results from Martinez-Manso et al. (2015), Wake et al. (2011), and McCracken et al. (2015) at $z \sim 1.5$–2, all of which are based on a clustering analysis with an HOD modeling. The Martinez-Manso et al. (2015) relation is determined at $12 \lesssim \log M_{\rm h} \lesssim 13.2$. The $\log M_*/M_{\rm h}$ in Wake et al. (2011) are multiply by a factor of 1.5 for a fair comparison to take into account the fact that these stellar masses are derived with a stellar population model from Maraston (2005), which provides systematically lower masses than those from the Bruzual & Charlot (2003) model (on average by $\sim 60\%$; Maraston et al. 2006). While our data provide a new constraint on the SHMR at a mass scale less than $10^{12}\ M_\odot$, it is consistent with an extrapolation of measurements from Martinez-Manso et al. (2015) and Wake et al. (2011).

We also show in Figure 5.20 the predicted SHMRs at $z = 1.6$ that are derived by Behroozi et al. (2013a) and Moster et al. (2013) with an abundance matching technique, with which our measurement is statistically consistent within the 2σ confidence level. We here recalculate the $M_*/M_{\rm h}$ ratio with the cosmology that used in Behroozi et al. (2013a) for comparison (dotted contours). The best-fit value is a slightly larger (by ~ 0.1 dex), but in agreement with the original value within the 1σ level. Although it is consistent within the 2σ (or nearly 1σ) confidence level, our best-fit measurement is likely lower than the predictions from these SHMRs. The $\log M_*/M_{\rm h}$ measurements from Martinez-Manso et al. (2015) and Wake et al. (2011) are also systematically lower than the abundance-matching-based SHMRs at the lower mass side, while the results from McCracken et al. (2015) are in good agreement. This possibly suggests that different galaxy populations obey the SHMR in different manners. For quantitative derivation and comparison of SHMRs, one needs to carefully treat the difference between adopted cosmologies (e.g., $\Omega_{\rm m}, \sigma_8$) from one study to another. We refer the reader to More (2013) for further discussions concerning such systematic effects on the galaxy clustering.

5.6.3 Baryon conversion efficiency

Given a growth history of halos and an observation of SFRs, we can calculate the fraction of baryons converted into stars to the total amount of those accreting into halos. We evaluate the instantaneous efficiency of baryon conversion by comparing the accretion rates and SFRs of galaxies. The SFRs of sample galaxies are derived from the observed Hα luminosities using a relation from Kennicutt (1998), converted to use a Chabrier (2003) IMF:

$$\mathrm{SFR}(M_\odot \mathrm{yr}^{-1}) = 4.65 \times 10^{-42} L_{\mathrm{H}\alpha}\ (\mathrm{erg\ s}^{-1}). \tag{5.36}$$

To derive the intrinsic SFRs, we correct the observed Hα flux for dust extinction, which is estimated based on the $B_z - j$ color (Daddi et al. 2007), assuming a ratio of reddening towards nebular and stellar emission to be $f = 0.66$ (see Kashino et al. 2013, and Chapter 3). Then we find an average SFR to be $\log \mathrm{SFR}/(M_\odot \mathrm{yr}^{-1}) = 1.2$ at $M_*^{\rm lim} = 10^{9.57}\ M_\odot$ with a standard

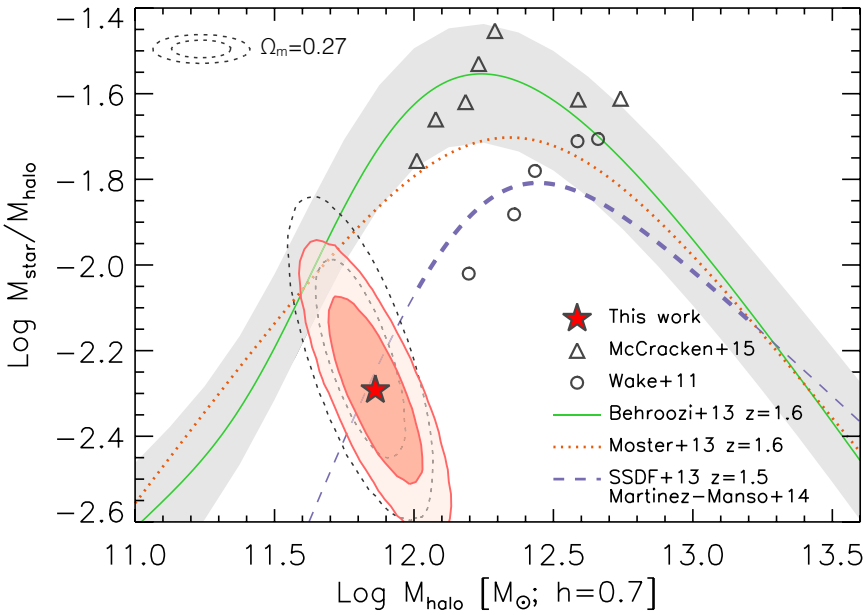

Figure 5.20: Stellar mass-to-halo mass (M_*/M_h) ratio as a function of halo mass (SHMR). A star symbols indicates the ratio $M_*^\mathrm{lim}/M_\mathrm{min}$ with the 68% and 95% confidence intervals shown by red contours. Dotted contours indicate the constraint with an alternative cosmology ($\Omega_\mathrm{m} = 0.27$, see text). A dashed line indicates the best-fit relation derived by Martinez-Manso et al. (2015) at $12 < \log M_\mathrm{h} < 13.2$ (thick dashed line) and its extrapolation (thin dashed line). Open circles show the measurements by Wake et al. (2011) for their different stellar mass threshold samples at $1.2 < z < 1.77$, whose stellar mass are multiplied by 1.5 (see text for details). Triangles indicate results for a sample at $1.5 < z < 2.0$ from McCracken et al. (2015). The SHMRs based on the abundance matching technique are shown as labelled (Behroozi et al. 2013a; Moster et al. 2013). A shaded region indicates the systematic uncertainties of the Behroozi et al. (2013a) relation.

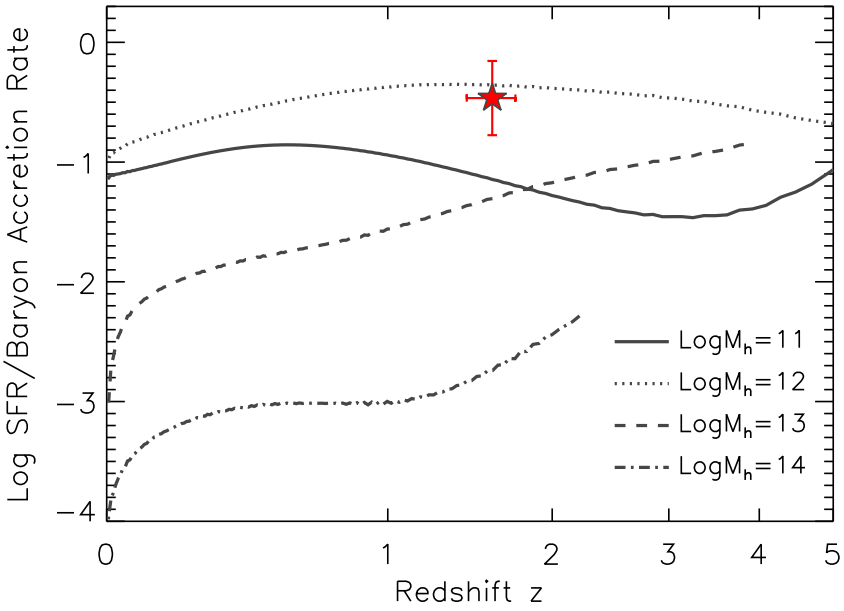

Figure 5.21: Average baryon conversion efficiency (i.e., SFR divided by baryon accretion rate) of our FMOS sample galaxies with $M_* \sim 10^{10} M_\odot$. Each curve shows the predicted efficiency as a function of redshift for each halo mass as labelled (Behroozi et al. 2013a).

deviation of 0.3 dex. For the threshold halo mass $M_{\rm min} = 7 \times 10^{11}\ M_\odot$ ($h = 0.7$), the mass accretion rates at $z = 1.588$ are calculated by using the halo mass accretion history derived by Behroozi et al. (2013a). Assuming the baryon fraction of accreting matter is equal to the cosmic baryon fraction (0.17), we calculate the baryon conversion efficiency, which is shown in Figure 5.21. We overlaid average relations for different halo masses derived by Behroozi et al. (2013a), indicating that our result is fully consistent with the average conversion efficiency expected to halos with $M_{\rm h} \sim M_{\rm min}$. Our result indicates that the main sequence galaxies with $M_* \sim 10^{9.6} M_\odot$ at $z \sim 1.6$ make use of $\sim 34\%$ (with an error of a factor 2) of baryon accreting onto halos to form new stars.

5.6.4 Satellite galaxies

In the measured projected correlation function $w_{\rm p}(r_{\rm p})$, we find a significant one-halo term, i.e., contribution from satellite galaxies. In the simple HOD model we apply, the ratio $M_1/M_{\rm min}$ indicates a gap between halo masses at which a halo acquires a central galaxy and at which a halo hosts an additional satellite galaxy respectively, corresponding the *shoulder* in the HOD (see Figure 5.15; Conroy et al. 2006).

We find the ratio of $M_1/M_{\rm min} = 4.6^{+4.5}_{-2.1}$ for our galaxy sample. This is smaller than the value of ≈ 17 that was reported as a typical ratio for local galaxies by Zehavi et al. (2011). These authors also showed that the $M_1/M_{\rm min}$ ratio decreases as the sample luminosity increases, and argued that this reduced gap for more luminous galaxies results from the fact that more massive halos form relatively late in the cosmic time, which means that there is no enough time for satellite galaxies to fall and merge onto their central galaxy. This lack of infalling time for satellites might be usually realized at higher redshifts. Conroy et al. (2006) found a decrease in $M_1/M_{\rm min}$ the ratio with increasing redshift using an abundance matching technique. They argued an elevated accretion rate of subhalos at higher redshifts, which having the mass M_1 close to $M_{\rm min}$, as the origin of the decline in the ratio. Our data supports such a picture with a prominent one-halo

term and the small value of $M_1/M_{\rm min}$. At intermediate redshifts $1 \lesssim z \lesssim 2$, Wake et al. (2011) found such a relatively small ratio ($M_1/M_{\rm min} \approx 6$), similar to our measurement, for samples with stellar mass above $\sim \times 10^{10}\ M_\odot$. Recently, Martinez-Manso et al. (2015) also found similar values $M_1/M_{\rm min} \approx 8$.

The overall satellite fraction $f_{\rm sat}$ is directly linked to the amount of the contribution from the one-halo term on the galaxy clustering. The fraction is controlled by a set of $M_{\rm min}$ and M_1, and also the shape of the halo mass function. Coupon et al. (2012) have reported an increase in the satellite fraction from $z \sim 1$ to the present day for several luminosity-limited samples. This can be straightforwardly interpreted as a result of global growth of structures.

For our sample, we find a satellite fraction $f_{\rm sat} = 0.39^{+0.14}_{-0.20}$ which is consistent with a typical value $f_{\rm sat} \approx 0.3$ for local galaxies as reported by Zehavi et al. (2011). Wake et al. (2011) found a satellite fraction of $f_{\rm sat} \approx 0.28$, which is consistent with our result, for stellar mass limit samples ($> 10^{10} M_\odot$) at $z \sim 1.5$, and also a clear dependence of the satellite fraction that shows a decrease with increasing stellar mass threshold. Martinez-Manso et al. (2015) found an similar correlation with the magnitude limit, which shows slightly smaller value ($f_{\rm sat} \sim 0.2$) at their faint-limit (corresponding to $M_* \lesssim 10^{10}\ M_\odot$). The authors also pointed out a moderate increase in the satellite fraction with cosmic time. For further understanding, a more comprehensive study beyond $z \gtrsim 1$ is necessary, especially based on spectroscopy, which is essential to determine the redshift evolution with a high time resolution.

5.7 Summary

We investigated the clustering properties of star-forming galaxies on the main sequence at $1.43 < z < 1.74$ using a data set from the FMOS-COSMOS survey. With 516 galaxies with an Hα detection, we measured the projected two-point correlation function, and studied the connections between galaxies and dark matter halos with an HOD model. Our main results are as follows:

1. The observed correlation function indicates a significant clustering at $0.03 \lesssim r_{\rm p}/(h^{-1}\,{\rm Mpc}) \lesssim 10$. By modeling it with a power-law function, we find a correlation length of $r_0 = 5.2 \pm 0.7\ h^{-1}$ Mpc, which is consistent with preceding studies at $z \sim 1.5$ using galaxies over a mass range similar to our study.

2. We model the observed correlation function using a halo occupation distribution (HOD) model with a simple parametrization given in Equations (5.24) and (5.25). The HOD parameters are effectively constrained with our current data and a significant one-halo term is confirmed with the transition scale of $r_{\rm p} \simeq 0.6\ h^{-1}$ Mpc. We derive an effective large-scale bias, $b_{\rm eff} = 2.17^{+0.17}_{-0.24}$, and average halo mass, $M_{\rm eff} = 4.62^{+1.14}_{-1.63} \times 10^{12}\ h^{-1} M_\odot$, which are consistent with other measurements from a HOD modeling. With the predictions of the mass assembly histories, we find that these halos will have grown into group-scale halos ($\sim 2 \times 10^{13}\ h^{-1}\ M_\odot$) at the present epoch.

3. Our data provides a new constraint on the stellar-to-halo mass relation: $\log M_*/M_{\rm h} = -2.3 \pm 0.2$ at $M_{\rm h} = 10^{10.86}\ M_\odot$ ($h = 0.7$). We find that our result is in good agreement with the extrapolation of the SHMR previously derived by Martinez-Manso et al. (2015) based on a clustering analysis with an HOD modeling. In contrast, there still remains large differences in SHMRs based on different observations and/or analyses, which possibly indicates that different galaxy populations follow different SHMRs.

4. We find that the $M_1/M_{\rm min}$ (~ 5) ratio of our sample is lower than that as typically seen at the local Universe. Such a lower $M_1/M_{\rm min}$ ratio may indicates an enhancement of the accretion rate of subhalos at higher redshifts and/or the lack of time for merging onto the central galaxy

In this study, we established the correction scheme for the bias caused by the fiber allocation, using the angular correlation function of the photometric parent catalog and the sample of actually-observed galaxies (or their realistic mock samples). Such a technique may be essential for future surveys with the galaxy clustering such as Subaru/Prime Focus Spectrograph.

Chapter 6

Concluding remarks

In this thesis, we explored aspects of galaxy evolution based on the data from the FMOS-COSMOS survey, a large near-infrared spectroscopic galaxy survey carried out using Subaru/FMOS. From observations between 2012 March and 2014 February, we collected near-infrared spectra of ~ 3000 galaxies at $z \sim 1.6$ in the COSMOS field. The first catalog that includes 1153 objects has been made public[1].

In the first part of this thesis, we studied the intrinsic properties of star-forming galaxies at $z \sim 1.6$. We used a sample of 271 sBzK-selected galaxies with a robust Hα detection in the H-long spectra to quantify the relation between star formation rate (SFR) and stellar mass, i.e., the star-forming main sequence. Based on a subsample with J-long spectra, we measured the Balmer decrement (flux ratio Hα/Hβ) to evaluate the level of extinction towards nebular emission, which has been found to be comparable to those of local galaxies. We also found an important fact that the differential extinction between stellar and nebular emission is smaller than that typically seen at the Local Universe. In other words, the extinction towards nebular emission is less enhanced relative to the extinction towards stellar emission (UV continuum component), as compared to local galaxies. This has suggested a more uniform distribution of dust in galaxies. Our findings on the dust properties have provided an essential prescription and caveat for studying nebular line properties of high-z galaxies. Using our result on the dust extinction law, we derived SFRs from observed Hα flux, and established the star-forming main sequence at $z \sim 1.6$. We found that the slope and scatter are similar to those of the local relation, while the normalization is 10–20 times higher than than seen in local galaxies.

We further investigate the detailed physical conditions of the interstellar medium (ISM) of high-z galaxies. While there have been several efforts that inspect the ISM properties at high redshifts ($z > 1$), our study has the advantage of using a well-controlled large sample of 701 typical star-forming galaxies that well trace the star-forming main sequence. We used empirical and theoretical diagnostic diagrams based on the ratios of rest-frame optical emission lines, including Hα, [N II]λ6584, [S II]$\lambda\lambda$6717,6731, Hβ, and [O III]λ5007, to investigate the properties of H II gas in star-forming regions. Our data have confirmed that high-z star-forming galaxies are locate above the sequence of local galaxies on the BPT diagram on average, based on a larger data set than any of the past studies at similar redshifts. This offset on the BPT diagram obviously indicates that the typical excitation states of H II gas in high-z galaxies are much different from those seen in local galaxies. Comparing our sample with local galaxies at fixed stellar masses, we found that the offset is primarily caused by a significant enhancement of the [O III]/Hβ ratio seen in high-z H II regions. We also found an electron density, as twice or more as that of local galaxies, based on the [S II] doublet line ratios measured in the co-added spectra. Based on our comprehensive nebular diagnostics, we have advocated that these changes in emission line properties result primarily from a higher ionization parameter in high redshift galaxies, as supported by the offset in the [S II]/Hα ratio especially seen in the massive galaxies ($M_* \gtrsim 10^{10.6}\ M_\odot$). The comparison with the theoretical model also indicates the offset towards high ionization parameters at a given metallicity as compared to local galaxies, as well. We

[1] http://member.ipmu.jp/fmos-cosmos/FMOS-COSMOS.html

attribute an enhancement of the ionization parameter to higher star formation activities and lower metallicities in high-z galaxies.

We also measured the mass–metallicity (MZ) relation, and found that the most massive galaxies ($M_* \gtrsim 10^{11}\ M_\odot$) are fully chemically enriched, while lower mass galaxies have metallicities considerably lower than local galaxies at the same stellar masses, in agreement with past studies. We additionally applied a new theoretically motivated metallicity indicator that is based on the [N II]/[S II] ratio, and found that a trend of the MZ relation that is qualitatively consistent with that based on the conventional [N II]/Hα-based metallicity indicator. The observed evolution of the MZ relation can be well reproduced as a consequence of the gas consumption in a simple physically motivated model that rests on the universal relation between metallicity and gas-to-stellar mass ratio. Furthermore, we studied the SFR dependence of the MZ relation. Even though our data are not in agreement with the local fundamental metallicity relation, we found that the evolution of M_*–Z–SFR relation can be well reproduced by a simple model based on an idea that star formation in normal galaxies is immediately regulated by gas consumption, inflows, and outflows.

Lastly, we studied the large scale environments of star-forming galaxies by utilizing their spatial clustering. We used 516 star-forming galaxies at $1.43 \leq z \leq 1.74$ to measured a projected 'redshift-space' two-point correlation function, which shows a significant clustering at scales 0.05–20 h^{-1}Mpc with a correlation length $5.2 \pm 0.7\ h^{-1}$ Mpc. To investigate the connection between galaxies and their dark matter halos, we employed a halo occupation distribution model to interpret the observed correlation function. The one-halo term has been firmly measured with the transition scale of $\simeq 0.6\ h^{-1}$Mpc. Our data successfully constrained the physical parameters concerning the halos that host star-forming galaxies at $z \sim 1.6$. Based on these analysis, we found that, on average, our sample galaxies are hosted by halos of $M_{\rm h} \simeq 5 \times 10^{12}\ h^{-1} M_\odot$. According to the average assembly histories of halos, those halos eventually grow into halos of $\sim 2 \times 10^{13}\ h^{-1} M_\odot$ (galaxy group scale) at the present epoch. We measured a stellar mass-to-halo mass ratio, $M_*/M_{\rm h} \approx 5 \times 10^{-3}$ at $M_{\rm h} = 10^{11.9}\ M_\odot$, which encodes the integrated efficiency of the conversion of baryons into stars over the mass assembly history of the halo. While, at these redshifts, there still remains some differences in the stellar-to-halo mass relation (SHMR) from one study to another, our study provided a new measurement at relatively small halo mass scale less than $10^{12}\ M_\odot$ based on our deep spectroscopic survey. Our data is in good agreement with the extrapolation of the SHMR based on the HOD modeling in previous studies, while showing that galaxies with $M_* \sim 10^{9.6}\ M_\odot$ will continuously form stars with a high efficiency relative to the accretion rate of their host dark halos.

For this clustering measurement, we carefully took into account complicated biases concerning the fiber spectroscopy using multiple tests based on cosmological high-resolution N-body simulations. Generally, these careful treatments of the systematic effects are very important because the data statistics have amazingly been improved in recent galaxy surveys. The correction schemes validate in this study should be useful for future spectroscopic galaxy surveys.

With respect to future prospects, we would further push these studies by combining the data from the final FMOS observations and forthcoming follow-up observations. Now we are constructing a larger sample from all the observing runs that completes the full FMOS-COSMOS project. The later FMOS observations were mainly aimed at enlarging the survey area, and thus the sample size, collecting J-band spectra for galaxies with a positive Hα detection to cover Hβ and [O III], and improving the quality of spectra of faint sources to detect week lines such as [N II] from individual spectra. In particular, we intended to increase the sampling rate of the most massive galaxies ($M_* > 10^{11}\ M_\odot$).

Recently, there have been studies that investigate the detailed properties of the star-forming main sequence, and some of them have reported on a flattening (or turnover) of the sequence

at the massive end. Such features may be related to the quenching process of the star formation. Our larger sample will enable us to constrain the characteristics of the star-forming main sequence based on the Hα emission line with an accurate dust extinction correction. We are also planning optical spectroscopic following up the FMOS sample to cover [O II]$\lambda\lambda$3726, 3729 which are important diagnostic features to constrain the ionization parameter of the ionized gas, metallicity, electron density, and chemical composition (the oxygen-to-nitrogen abundance ratio).

These optical spectra also cover some of the metal absorption lines, such as Mg II$\lambda\lambda$2796, 2803, Fe IIλ2587, 2600. The accurate measurements of the line profile of these absorption lines and the [O III]λ5007 line permit us to investigate the existence and kinematics of the outflows, which play an important role in regulating the star formation and gas-phase metallicity of galaxies.

The larger sample also provides a measurement of the three-dimensional galaxy number density field based on the spectroscopic redshift with a large dynamic range of the density. We are also planning follow-up observations to collect the spectral data of galaxies of such *proto*-cluster regions with high sensitivity multi-object spectrographs (e.g., Keck/MOSFIRE). Combining the accurate measurements of the intrinsic galactic properties and the density field will permit us to study the environmental effects on galaxy evolution, including the star formation quenching and accelerated chemical evolution, and metal pollution of the intergalactic medium (IGM) from over dense regions.

In the near future, the next generation multi-object spectrographs, such as Subaru/Prime Focus Spectrograph and VLT/MOONS will make a breakthrough by enlarging the intermediate redshift galaxy sample by several orders of magnitude, as the SDSS had done with the large dataset of lower redshift galaxies in the last decade. Such a large sample is essential to explore the relations between a number of galactic observables. For example, the SDSS has established the relation between stellar mass, metallicity and SFR by using 10^5 galaxies at $z \sim 0$. With the forthcoming data sets, we can constrain such relations with a similar statistical accuracy at higher redshifts up to $z \sim 3$ or larger. These measurements across cosmic time are fundamentally important to constrain models of galaxy evolution by tracing the evolutionary histories of galaxy populations after the formation of the first stars.

In the next decade, the future huge eyes of human beings, such as ground-based TMT, LSST, GMT, SKA, and space JWST, SPICA, WFIRST, will penetrate the dark Universe much more deeply and widely, and push out the frontier of our view. Then, we will be able to reach the site of the formation of the first generation galaxies. Such observations will provide us with new insights not only on our understanding of the galaxy evolution, but also on our vision of the history of the Universe itself.

Appendix A

Chemical enrichment

A.1 Basic equations

Here, we summarize basic equations that describe the chemical evolution of a galaxy under some simple approximations. The following derivations are originally based on Schmidt (1963) and subsequent studies (Arnett 1971; Searle & Sargent 1972; Larson 1972). Tinsley (1980) presented a good review on this matter. To model the process of chemical enrichment of the ISM, it is necessary to introduce some assumptions and approximations for simplicity. We here make the *one-zone approximation* that supposes that materials ejected from stars and infalling gas instantaneously mix with the ISM and that its chemical composition is always uniform.

With star formation and gas inflow, the change of stellar and gas mass of a galaxy (M_* and $M_{\rm g}$) can be written as

$$\frac{dM_*}{dt} = \psi - E, \tag{A.1}$$

$$\frac{dM_{\rm g}}{dt} = -\psi + E + f \tag{A.2}$$

where ψ is the SFR, E is the total mass ejected from stars of all masses into the ISM per unit time and f is the *net* inflow rate (net mass of gas falling from outside the system under consideration). The ejection rate can be written in terms of the initial mass function (IMF), $\phi(m)$, and SFR as

$$E(t) = \int_{m_t}^{\infty} (m - w_m)\ \psi(t - \tau_m)\ \phi(m)\ dm \tag{A.3}$$

where τ_m is the life time of a star of mass m, and w_m is the remnant mass (i.e., mass locked in white dwarfs, neutron stars, or black holes). The lower limit m_t is the mass of a star with a lifetime $\tau_m = t$. Thus, a star that formed at time $t - \tau_m$ dies at time t, and all of stars with $m < m_t$ are still alive, while stars with $m > m_t$ already died.

We introduce Z as the metal abundance, which is defined as the mass fraction of metals to the total gas mass. For simplicity, we consider only primary elements, the production of which depends only on the mass of a star, but not on the initial chemical composition. The change of metal mass in the ISM ($M_Z = ZM_{\rm g}$) is expressed as

$$\frac{dM_Z}{dt} = -Z\psi + E_Z + Z_f f, \tag{A.4}$$

where E_Z is the total ejection rate of metals from stars, and Z_f is the metal abundance of infalling gas. Let p_m be the mass fraction of metals newly synthesized and ejected from a star of an initial mass m. The mass of a dying star can be separated into three parts; remnant w_m, newly synthesized and ejected metals mp_m, and the ejected *original* gas ($m - w_m - mp_m$). The returned gas can be considered to have the metal abundance at the formation time of a star

$t - \tau_m$. Thus, we obtain

$$E_Z(t) = \int_{m_t}^{\infty} [(m - w_m - mp_m)\ Z(t - \tau_m) + mp_m]\ \ \psi(t - \tau_m)\ \phi(m)\ dm. \tag{A.5}$$

For convenience, we define some parameters that depend only on models of the stellar evolution, but not on the current physical conditions of the system. The *return fraction* R is defined as the fraction of mass that is converted into stars and then returned to the ISM,

$$R \equiv \int_{m_1}^{\infty} (m - w_m)\ \phi(m)\ dm, \tag{A.6}$$

where m_1 is the present turnoff mass, which is usually taken to be 1 $M_\odot$. The *yield* y denotes the mass of metals newly synthesized in stars and ejected to the ISM per unit mass locked up in stars,

$$y \equiv \frac{1}{1 - R} \int_{m_1}^{\infty} mp_m\ \phi(m)\ dm. \tag{A.7}$$

Here, we make an approximation known as the *instantaneous recycling*, where stars are separated into two classes; less massive long-lived stars that are alive forever (longer than the timescale under consideration) or massive shot-lived stars that die immediately after their birth. This assumption is reasonable because the mass returned to the ISM is dominated by the contribution from short-lived stars, and their lifetime is much shorter than the timescale of galaxy evolution. Then we can rewrite Equations (A.3) and (A.5) as

$$E(t) = R\ \psi(t), \tag{A.8}$$

$$E_Z(t) = [RZ(t) + y(1 - R)]\,\psi(t), \tag{A.9}$$

where we use $1 - Z(t) \approx 1$. Substituting these in Equations (A.2), (A.2), and (A.4), we obtain

$$\frac{dM_*}{dt} = (1 - R)\psi, \tag{A.10}$$

$$\frac{dM_{\rm g}}{dt} = -(1 - R)\psi + f, \tag{A.11}$$

$$\frac{dM_Z}{dt} = -Z(1 - R)\psi + y(1 - R)\psi + Z_f f. \tag{A.12}$$

We have an equation for the metal abundance Z as

$$M_{\rm g}\frac{dZ}{dt} = y(1 - R)\psi + (Z_f - Z)f. \tag{A.13}$$

To derive its solution, we first assume the *closed box* model, where $f = 0$, so that the total mass of the system $M_{\rm tot}$ is conserved. From Equations (A.11) and (A.12), we have

$$M_{\rm g}\frac{dZ}{dM_{\rm g}} = -y. \tag{A.14}$$

With the initial conditions $M_{\rm g}(0) = M_{\rm tot}$ and $Z(0) = 0$ assumed, we have a simple solution

$$Z = y \ln \mu^{-1} \tag{A.15}$$

where $\mu = M_{\rm g}/M_{\rm tot}$ is the gas mass fraction of the system. Thus, the gas-phase metal abundance increases logarithmically as the gas fraction decreases. If the SFR is proportional to the gas mass

with a time-invariant coefficient, $\psi(t) = \varepsilon M_{\rm g}(t)$, we have simply

$$M_{\rm g}(t) = M_{\rm tot} \exp\left[-\varepsilon(1-R)t\right], \quad Z(t) = y\varepsilon(1-R)t, \tag{A.16}$$

where ε is called a star formation efficiency, and its inverse $\tau = 1/\varepsilon$ defines the timescale of gas consumption. Thus, in the closed-box model, the gas mass exponentially decreases, and the metallicity increases proportionally to time.

Next, we consider a case where the gas mass keeps its initial value, $M_{\rm g}(t) = M_{\rm g}(0) = M_{\rm tot}$ with infall f and star formation;

$$\frac{dM_{\rm g}}{dt} = -(1-R)\psi + f = 0. \tag{A.17}$$

In this case, we have a solution in terms of the gas fraction μ as

$$Z = y + (Z_0 - y)\exp(1 - 1/\mu), \tag{A.18}$$

where an unenriched infall ($Z_f = 0$) is assumed and Z_0 is the metal abundance at time $t = 0$. $Z \to y$ as $\mu \to 0$. If the SFR is proportional to $M_{\rm g}(t)$, $\psi(t)$ and f are constant. In this case, we have

$$\frac{dZ}{dt} = \frac{1}{M_{\rm g}}\frac{dM_Z}{dt} = \frac{y - Z}{\tau_{\rm gas}}, \tag{A.19}$$

where $\tau_{\rm gas} = [\varepsilon(1-R)]^{-1}$ is the timescale for the net gas consumption with the gas returning taken into account. We have a solution

$$Z = y + (Z_0 - y)e^{-t/\tau}. \tag{A.20}$$

This means that the metal abundance Z approaches an asymptotic value y at time $t \gg \tau_{\rm gas}$.

To derive these equations, we make a lot of approximations for simplicity. In reality, stars with different masses have different lifetimes. All heavy elements do not have the same production process, thus do not synthesized with the same rate. The production of individual elements depends on the chemical composition of the gas in different manners. In particular, at higher metallicity, the secondary production which is based on the amount of metals originally stored in stars becomes dominant for some elements (e.g., nitrogen). The SFR and inflow rate f must fluctuate both spatially and timely. In addition, the outflows of enriched gas from the system may play an important role. Yet still, these discussions provide us with a fundamental concept of the chemical enrichment of the ISM in galaxies.

A.2 Gas regulation model

We describe the model that is developed by Lilly et al. (2013). This model is used in §4.7.2. In this model, the star formation of a galaxy is instantaneously regulated by the gas mass, $M_{\rm gas}$, in a reservoir with the gas accretion and mass loss taken into account. Further, gas-phase metallicity (Z) can be predicted as a function of star formation rate (SFR) and stellar mass (M_*).

There has been a lot of studies on the so-called *main sequence* of star-forming galaxies out to $z \sim 2$ or more. In which, the SFR is tightly correlated with stellar mass of galaxies. In the most simple case, the main sequence has been expressed as SFR $\propto M_*^{1+\beta}$ or sSFR $\propto M_*^{\beta}$, where sSFR = SFR$/M_*$ is the specific SFR, which moderately decline with increasing stellar mass. With many studies, the slope β is known to be $\beta \sim -0.1$–-0.3 (Noeske et al. 2007; Daddi et al. 2007; Elbaz et al. 2007). Here, we choose $\beta = -0.1$ following Lilly et al. (2013).

Hereafter, we make the one-zone approximation and assume the instantaneous recycling. The derivation basically rests on the fundamental idea of the chemical enrichment described

in Appendix A.1. We define the reduced sSFR (rsSFR) that denotes net mass converted into long-lived stars. If we assume that some fraction R of the mass converted into stars (i.e., sSFR per unit M_*) is instantaneously returned to the interstellar medium (ISM), we can write

$$\mathrm{rsSFR} = (1 - R)\,\mathrm{sSFR}. \tag{A.21}$$

Lilly et al. take $R = 0.4$ from stellar population synthesis models (e.g., Bruzual & Charlot 2003). Generally, assuming a Chabrier (2003) IMF yields $R \approx 0.4$, while a Salpeter (1955) IMF is more weighted towards long-lived stars and yields a smaller return fraction $R \approx 0.27$ (Madau & Dickinson 2014).

We introduce a very simple gas-regulated model, where the instantaneous mass of the total gas in the galaxy is controlled by star formation, mass loss from the system, and gas inflow into the galaxy. The SFR is defined as a form proportional to the gas mass,

$$\mathrm{SFR} = \varepsilon M_{\mathrm{gas}}, \tag{A.22}$$

where ε is star formation efficiency (SFE) and its inverse denotes the gas consumption time scale,

$$\tau_{\mathrm{gas}} = \varepsilon^{-1}. \tag{A.23}$$

Letting μ be the gas-to-stellar mass ratio M_{gas}/M_*, we can write with Equation (A.22),

$$\mu = \varepsilon^{-1}\,\mathrm{sSFR}. \tag{A.24}$$

If the SFR is given as $\mathrm{SFR} = \varepsilon M_{\mathrm{gas}}^{\kappa}$, Equation (A.24) is generally written as

$$\mu = \left(\varepsilon^{-1}\mathrm{sSFR}\right)^{1/\kappa} M_*^{(1-\kappa)/\kappa}. \tag{A.25}$$

We introduce the mass loss Ψ and the gas accretion Φ. Because the outflow may be triggered by supernovae or stellar winds from massive stars, the mass loss rate should be correlated with the SFR. Hence, we assume the mass loss rate increases linearly with the SFR as;

$$\Psi = \lambda\,\mathrm{SFR} \tag{A.26}$$

where λ is a mass-loading factor. With the accretion rate Φ, we obtain the following mass conservation,

$$\begin{aligned} \Phi &= (1 - R)\ \mathrm{SFR} + \Psi + \frac{dM_{\mathrm{gas}}}{dt} \\ &= (1 - R + \lambda)\ \mathrm{SFR} + \frac{dM_{\mathrm{gas}}}{dt}. \end{aligned} \tag{A.27}$$

In the right-hand side of the upper equation, the first term denotes the decrement due to formation of long-lived stars, the second term is the mass loss, and the last term means the residual change in the total gas mass. Differentiating $\mu = M_{\mathrm{gas}}/M_*$ yields

$$\frac{d\mu}{dt} = -\frac{M_{\mathrm{gas}}}{M_*^2}\,(1 - R)\,\mathrm{SFR} + \frac{1}{M_*}\frac{dM_{\mathrm{gas}}}{dt}, \tag{A.28}$$

where we use $dM_*/dt = (1 - R)$ SFR. Thus, we obtain

$$\frac{dM_{\mathrm{gas}}}{dt} = \mu\,(1 - R)\ \mathrm{SFR} + M_*\frac{d\mu}{dt} \tag{A.29}$$

$$= \left(\mu\,(1 - R) + \varepsilon^{-1}\frac{d\ln\mu}{dt}\right)\mathrm{SFR} \tag{A.30}$$

where the change in the gas mass is related to the SFR in the galaxy. Further, with Equation (A.30), we can rewrite Equation (A.31) in an expression that links the inflow rate Φ and the SFR as follows

$$\Phi = \left((1-R)(1+\mu) + \lambda + \varepsilon^{-1} \frac{d\ln\mu}{dt} \right) \mathrm{SFR}, \tag{A.31}$$

where we use $(d\mu/dt)/\mu = d\ln\mu/dt$.

Now we derive the chemical enrichment in this model. The gas-phase metallicity (Z) is defined as the ratio of the mass of metals M_Z to the total gas mass $M_{\rm gas}$, i.e., $Z \equiv M_Z/M_{\rm gas}$. We define the yield y as the mass of metals synthesized in stars, then returned to the ISM per unit mass convert into long-lived stars. We assume that the infalling gas has metallicity $Z_{\rm in}$ and that the outflowing gas has the metallicity equal to the entire gas reservoir. In this case, we can express the change in the mass of metals as

$$\frac{dM_Z}{dt} = y(1-R)\,\mathrm{SFR} - Z(1-R)\,\mathrm{SFR} - Z\Psi + Z_{\rm in}\Phi \tag{A.32}$$

$$= y(1-R)\,\mathrm{SFR} - Z(1-R+\lambda)\,\mathrm{SFR} + Z_{\rm in}\Phi, \tag{A.33}$$

where we use $\Psi = \lambda \cdot \mathrm{SFR}$ (Equation A.26). Substituting Equation (A.31), we obtain

$$\frac{dM_Z}{dt} = \left(y(1-R) - (Z - Z_{\rm in})(1-R+\lambda) \right) \mathrm{SFR} + Z_{\rm in} \frac{dM_{\rm gas}}{dt}. \tag{A.34}$$

The change in metallicity Z is given by

$$\frac{dZ}{dt} = \frac{1}{M_{\rm gas}}\frac{dM_Z}{dt} - \frac{M_Z}{M_{\rm gas}^2}\frac{dM_{\rm gas}}{dt} \tag{A.35}$$

$$= \left(y(1-R) - (Z - Z_{\rm in})(1-R+\lambda) \right) \varepsilon - (Z - Z_{\rm in}) \frac{1}{M_{\rm gas}} \frac{dM_{\rm gas}}{dt}, \tag{A.36}$$

where we use Equation (A.22). Substituting Equation (A.30) into (A.36) yields

$$\varepsilon^{-1}\frac{dZ}{dt} = y(1-R) - (Z - Z_{\rm in}) \left(1 - R + \lambda + \varepsilon^{-1} \cdot \mathrm{rsSFR} + \varepsilon^{-1} \frac{d\ln\mu}{dt} \right). \tag{A.37}$$

By setting $dZ/dt = 0$, we have an equilibrium metallicity $Z_{\rm eq}$,

$$Z_{\rm eq} = Z_{\rm in} + \frac{y(1-R)}{(1-R) + \lambda + \varepsilon^{-1}(\mathrm{rsSFR} + d\ln\mu/dt)} \tag{A.38}$$

$$= Z_{\rm in} + \frac{y}{1 + \lambda(1-R) - 1 + \varepsilon^{-1}\left(\mathrm{sSFR} + (1-R)^{-1}\, d\ln\mu/dt\right)} \tag{A.39}$$

$$= Z_{\rm in} + \frac{y}{1 + \lambda(1-R) - 1 + \varepsilon^{-1}\left(M_*^{-1}\mathrm{SFR} + (1-R)^{-1}\, d\ln\mu/dt\right)}. \tag{A.40}$$

With Equation (A.24), Equation (A.40) can be written as

$$Z_{\rm eq} = Z_{\rm in} + \frac{y}{1 + \lambda(1-R) - 1 + \mu + (1-R)^{-1}\,\varepsilon d\ln\mu/dt}. \tag{A.41}$$

Here, we consider the timescale for the metallicity to reach an equilibrium value. Defining $\Delta Z = Z - Z_{\rm eq}$, which is the deviation from the steady state metallicity ($Z_{\rm eq}$), we obtain from

Equation A.37,

$$\varepsilon^{-1}\frac{d\Delta Z}{dt} = y\,(1-R) - (Z + Z_{\rm eq} - Z_{\rm in})\left(1 - R + \lambda + \varepsilon^{-1}\cdot{\rm rsSFR} + \varepsilon^{-1}\frac{d\ln\mu}{dt}\right) \quad (A.42)$$

$$\approx y\,(1-R) - (Z + Z_{\rm eq} - Z_{\rm in})\left((1-R)\,(1+\mu) + \lambda\right). \quad (A.43)$$

Here we set the last term to zero and use Equation (A.24). Then, substituting Equation (A.39) to eliminate $Z_{\rm eq}$, we have

$$\varepsilon^{-1}\frac{d\Delta Z}{dt} = -\Delta Z\left((1-R)\,(1+\mu) + \lambda\right), \quad (A.44)$$

or

$$\frac{d\ln\Delta Z}{dt} = -\left((1-R)\,(1+\mu) + \lambda\right)\tau_{\rm gas}^{-1}. \quad (A.45)$$

This indicates that the metallicity exponentially approaches the equilibrium value $Z_{\rm eq}$ with a timescale comparable or shorter than the gas consumption timescale. From Equation (A.31), we have the timescale to approach equilibrium,

$$\frac{\tau_{\rm gas}}{\left((1-R)\,(1+\mu) + \lambda\right)} \approx \frac{\rm SFR}{\Phi}\tau_{\rm gas} \leq \tau_{\rm gas}. \quad (A.46)$$

Lastly, we derive a convenient formulation for fitting observed $Z(M_*, {\rm SFR})$ relation. Lilly et al. assume both ε and λ are represented by a power-law of M_*,

$$\lambda = \lambda_{10}\left(M_*/10^{10}\ M_\odot\right)^a, \quad (A.47)$$

$$\varepsilon = \varepsilon_{10}\left(M_*/10^{10}\ M_\odot\right)^b. \quad (A.48)$$

Lilly et al. also suppose the following time dependence of ε and sSFR (i.e., redshift evolution of the main sequence):

$$\varepsilon \propto M_*^b t^{-1}. \quad (A.49)$$

$${\rm sSFR} \propto M_*^\beta t^{-2.2}, \quad (A.50)$$

where t is the cosmic epoch (Genzel et al. 2010). The term $d\ln\mu/dt$, thus, can be expressed as

$$\frac{d\ln\mu}{dt} = -\frac{1.2}{t} + (\beta - b)\,{\rm rsSFR}. \quad (A.51)$$

Thus, we obtain

$$Z_{\rm eq} = Z_{\rm in} + \frac{y}{1 + \lambda\,(1-R)^{-1} + \varepsilon\left((1+\beta-b)\,M_*^{-1}{\rm SFR} - (1-R)^{-1}\,1.2/t\right)}. \quad (A.52)$$

This parametrization is used in §4.7.2.

A.3 Universal metallicity relation

We describe an analytical model of chemical evolution of galaxies that is introduced by Zahid et al. (2014a). In this model, a universal relation between metallicity and stellar-to-gas mass ratio $M_*/M_{\rm gas}$ is considered as the underlying origin of the mass–metallicity (MZ) relation and its evolution. The formulation of this model is used in §4.6.3.

In this model, the MZ relation is parametrized as

$$12 + \log(\mathrm{O/H}) = Z_0 + \log\left\{1 - \exp\left[-\left(\frac{M_*}{M_0}\right)^{\gamma}\right]\right\}, \tag{A.53}$$

where Z_0 is the asymptotic value of the metallicity at the massive end, M_0 is the turnover mass at which the metallicity begins to saturate. At $M_* \lesssim M_0$, the metallicity declines with a power-law index γ. This formulation well explains observed characteristics of the MZ relation at different redshifts. In the following, the interpretation of this formulation is presented.

The gas-phase metallicity Z is defined as the ratio of the mass of metals in the gas (M_Z) and the hydrogen gas mass ($M_{\rm gas}$), i.e., $Z \equiv M_Z/M_{\rm gas}$. The change in metallicity with respect to stellar mass is given by

$$\frac{dZ}{dM_*} = \frac{d}{dM_*}\left(\frac{M_Z}{M_{\rm gas}}\right) = \frac{1}{M_{\rm gas}}\left(\frac{dM_Z}{dM_*} - Z\frac{dM_{\rm gas}}{dM_*}\right). \tag{A.54}$$

With the form of the MZ relation given by Equation (A.53), the metallicity increases with increasing stellar mass. Therefore, we require

$$\frac{dZ}{dM_*} > 0 \Leftrightarrow \frac{dM_Z}{dM_*} > Z\frac{dM_{\rm gas}}{dM_*}. \tag{A.55}$$

At low masses, metallicity tend to be small, so that the second term of Equation (A.54) is negligible. From observation, we have $M_{\rm gas} \propto M_*^g$ with $g \sim 0.5$ (Peeples et al. 2014). Therefore, at high masses, $dM_{\rm gas}/dM_* \propto 1/\left(M_*^{1-g}\right) \approx 1/\sqrt{M_*}$ should be small. Therefore, Equation (A.54) can be approximated by

$$\frac{dZ}{dM_*} \approx \frac{1}{M_{\rm gas}}\frac{dM_Z}{dM_*}. \tag{A.56}$$

This equation means that the chemical enrichment of a galaxy is dominated by the production of new metals through star formation rather than by the change in the gas reservoir.

Now we consider three processes that affect the chemical enrichment of a galaxy; star formation, gas accretion (inflow), and gas outflows. The star formation is characterized by star formation rate (SFR), and related to the change in M_* as $dM_*/dt = (1-R)$ SFR. Here, we assume that some fraction R of the mass converted into stars is promptly returned to the ISM. We define an yield Y as the mass of oxygen created in stars, then returned to the ISM per unit mass of gas that is converted into long-lived stars. The following derivation basically rests on the fundamental equations in Appendix A.1. The change in the mass of metals is given by

$$dM_Z = Y dM_* - Z(1-R)\,dM_* + Z_{\rm in} dM_{\rm in} - Z_{\rm out} dM_{\rm out}. \tag{A.57}$$

The first term denotes the metals newly provided into the ISM from the massive stars. The second-term is the decrement due to the conversion into long-lived stars. The third-term is metals supplied by the infalling gas with metallicity $Z_{\rm in}$ and an accretion rate $dM_{\rm in}$. The last-term indicates metals carried away by the outflows: $Z_{\rm out}$ is metallicity of the outflowing gas, and $dM_{\rm out}$ is the mass loss rate. Dividing Equation (A.57) by dM_*, we obtain

$$\frac{dM_Z}{dM_*} = Y - Z(1-R) + Z_{\rm in}\frac{dM_{\rm in}}{dM_*} - Z_{\rm out}\frac{dM_{\rm out}}{dM_*}. \tag{A.58}$$

We introduce a factor, combining the effects of outflows and inflows,

$$\zeta \equiv Z_{\rm out}\frac{dM_{\rm out}}{dM_*} - Z_{\rm in}\frac{dM_{\rm in}}{dM_*}. \tag{A.59}$$

If we assume that ζ is constant, substituting Equation (A.58) into (A.56) yields

$$\frac{dM_Z}{dM_*} \approx \frac{Y - \zeta - Z\,(1-R)}{M_{\rm gas}} = \frac{Y_{\rm net} - Z\,(1-R)}{M_{\rm gas}}, \tag{A.60}$$

where we define the *net* yield $Y_{\rm net} \equiv Y - \zeta$.

The relation between gas mass and stellar mass of star-forming galaxies is known to be reasonably expressed in a power-law form, as mentioned above:

$$M_{\rm gas} = G M_*^g. \tag{A.61}$$

In this case, we can solve Equation (A.60) as

$$Z(M_*) = \frac{Y_N}{1-R}\left\{1 - \exp\left[-\left(\frac{1-R}{1-g}\right)\frac{M_*}{M_{\rm gas}}\right]\right\} \tag{A.62}$$

where we impose the boundary condition, $Z(M_* = 0) = 0$. Taking the logarithm, we have

$$\log Z = \log\left(\frac{Y_N}{1-R}\right) + \log\left\{1 - \exp\left[-\left(\frac{1-R}{1-g}\right)\frac{M_*}{M_{\rm gas}}\right]\right\}, \tag{A.63}$$

which is the same form as Equation A.53. The asymptotic metallicity Z_0 is linked to the constant term, $\log\left[(Y_N)/1-R)\right]$. This states that the maximum metallicity in a galaxy is set by the net yield Y_N and the return fraction R. Comparing Equations (A.53) and (A.63) yields

$$\left(\frac{M_*}{M_0}\right)^\gamma = \frac{1-R}{1-g}\left(\frac{M_*}{M_{\rm gas}}\right) \approx \left(\frac{M_*}{M_{\rm gas}}\right) = \frac{M_*^{1-g}}{G}, \tag{A.64}$$

where we suppose that R and g are nearly equal ($R \sim g \sim 0.5$). Thus, the MZ relation is essentially related to a more universal relation between the metallicity and the stellar-to-gas mass ratio. This equation also states that the low-mass-end slope index of the MZ relation, γ, is related to the power-law slope of the relation between $M_{\rm gas}$ and M_* by $\gamma = 1 - g$, and that the turnover mass M_0 is related to the zero point G of the $M_{\rm gas}$–M_* relation by $M_0 = G^{1/\gamma}$. The turnover mass M_0 is the stellar mass at which the $M_{\rm gas}/M_*$ ratio is unity. This indicates that the redshift evolution of M_0, which decreases with time (see §4.6.3), is interpreted as a result of the gas consumption (i.e., decrement of G) with cosmic time.

Appendix B

Ionization equilibrium of nebulae

Here, we provide an brief overview of physics in nebulae. We refer readers to the text "Astrophysics of Gaseous Nebulae and Active Galactic Nuclei" (AGN^2; Osterbrock & Ferland 2006) for full details.

Emission nebulae result from the photoionization of a diffuse gas cloud by radiation from a hot young star or a cluster of such stars. The ionization equilibrium in such a nebula is characterized by the balance between the ionization by ionizing photons and the recombination of electrons with the ions. Let us suppose a pure hydrogen gas (since hydrogen is the most abundant element) surrounding a single hot star. The ionization equilibrium equation at an arbitrary point is given

$$n(\mathrm{H}^0)\int_{\nu_0}^{\infty}\frac{4\pi J_\nu}{h\nu}a_\nu(\mathrm{H}^0)d\nu = n_\mathrm{e}n_\mathrm{p}\alpha_A(\mathrm{H}^0,T) \tag{B.1}$$

where J_ν is the intensity of radiation (erg cm^{-2} s^{-1} str^{-1} Hz^{-1}) at the point in the gas cloud, ν_0 is the frequency corresponding the ionization potential of a hydrogen atom (13.6 eV), $a_\nu(\mathrm{H}^0)$ is the ionization cross section of H for photons with energy $h\nu$. The densities of neutral atoms, electrons, and protons are $n(\mathrm{H}^0)$, n_e, and n_p, respectively, and $\alpha_A(\mathrm{H}^0,T)$ is the recombination coefficient for all the energy levels of H. Therefore, the left-hand and right-hand sides of Equation (B.1) denote the number of neutral hydrogen atoms that are ionized and the number of protons that recombine with an electron per unit volume per unit time, respectively

In Equation (B.1), the radiation field can be divided into two contributions, from the exciting star $J_{\nu,\mathrm{star}}$ and from the re-emission due to recombinations of the ionized gas $J_{\nu,\mathrm{rec}}$,

$$J_\nu = J_{\nu,\mathrm{star}} + J_{\nu,\mathrm{rec}}. \tag{B.2}$$

Supposing the stellar radiation is isotropic, the intensity $J_{\nu,\mathrm{star}}$ is related to the luminosity density L_ν (per frequency interval) of the central star as

$$4\pi J_{\nu,\mathrm{star}} = \frac{L_\nu}{4\pi r^2}\exp\left[-\tau_\nu(r)\right], \tag{B.3}$$

where r is the distance at the point from the central star and $\tau(r)$ is the optical depth at r,

$$\tau_\nu(r) = \int_0^r n(\mathrm{H}^0,r')a_\nu dr'. \tag{B.4}$$

The number of ionizing photons emitted from the star per unit time $Q(\mathrm{H}^0)$ can be written as

$$Q(\mathrm{H}^0) = \int_{\nu_0}^{\infty}\frac{L_\nu}{h\nu}d\nu. \tag{B.5}$$

With respect to the other part from the recombinations of the ionized gas, we have

$$4\pi \int_{\nu_0}^{\infty} \frac{j_\nu}{h\nu} d\nu = n_{\rm p} n_{\rm e} \alpha_1(\mathrm{H}^0, T) \tag{B.6}$$

where j_ν is the emission coefficient for this radiation and α_1 is the recombination coefficient for the ground state (the principal quantum number $n = 1$). For an optically thin nebula, it is a good approximation to neglect this contribution from the radiation due to recombinations (Case A).

For an optically thick gas cloud (Case B), which is realized in typical H II regions in galaxies, no ionizing photons can escape, so that every ionizing photons generated due to the recombination is absorbed by neutral hydrogen. Supposing such ionizing photons are immediately absorbed very close to the point at which they are emitted ("on-the-spot" approximation), we have

$$J_{\nu,\mathrm{rec}} = \frac{\nu}{n(\mathrm{H}^0) a_\nu}. \tag{B.7}$$

With this approximation, from Equations (B.1), (B.3) and (B.6), we obtain

$$\frac{n(\mathrm{H}^0)}{4\pi r^2} \int_{\nu_0}^{\infty} \frac{L_\nu}{h\nu} a_\nu \exp\left[-\tau_\nu(r)\right] d\nu = n_{\rm p} n_{\rm e} \alpha_B(\mathrm{H}^0, T) \tag{B.8}$$

where $\alpha_B = \alpha_A - \alpha_1$ is the recombination coefficient for all the excited levels ($n \geq 2$). This means that, in an optically thick nebula, the ionizations due to the stellar radiation field are balanced by recombinations to excited levels of H. Electrons that directly falls back to the ground state emit ionizing photons, which immediately ionize another neutral hydrogen, thus do have no net effect on the overall ionization of the gas cloud. When electrons falling back to a excited level with $n \geq 2$ cascade down to the ground state, non-ionizing photons corresponding to transitions are emitted. Photons from the transition from $n \geq 3$ to $n = 1$ are also immediately absorbed by H atoms at the ground level, then the electron cascade again. Therefore, the luminosity of a Balmer series lines, which corresponds to the transitions from $n \geq 3$ to $n = 2$, of hydrogen reflects the number of ionizing photons in a nebula, thus they are used to probe the number of hot massive stars. Bright Hα emission (from $n = 3$ to $n = 2$) can be ubiquitously seen in H II regions. In contrast, the Lyman α photons undergo the resonance scattering (i.e., immediate absorption and re-radiation), while traveling a long distance in the galaxy. Thus, most such photons are absorbed by galactic dust, so that we usually do not see bright Lyman lines in star-forming regions. However, at high redshifts ($z \gtrsim 3$), we observe a number of Lyα emitters, which are usually expected to be dust-poor young, less massive galaxies.

When a hot star exists in a large homogeneous gas cloud, the star forms a spherical ionized region, within which hydrogen atoms are almost completely ionized. This region is called a *Strömgren sphere* (Strömgren 1939). Figure B.1 shows *Rosette Nebula*, which is the most notable example of a Strömgren sphere. Generally, the thickness of the transition region from an outer neutral region, which is approximately one mean free pass of an ionizing photon, is much thiner than the radius of the sphere (Strömgren radius, $R_{\rm s}$). Under the conditions of ionization equilibrium, the total number of ionizing photons emitted by the central star balances the total number of net recombinations within the ionized volume,

$$Q(\mathrm{H}^0) = \frac{4\pi}{3} R_{\rm s}^3 n(\mathrm{H})^2 \alpha_B \tag{B.9}$$

where we assume $n_{\rm p} = n_{\rm e} \approx n({\rm H})$. Thus, the Strömgren radius is given as

$$R_{\rm s} = \left[\frac{3Q({\rm H}^0)}{4\pi n(H)^2 \alpha_B}\right]^{1/3}. \tag{B.10}$$

Here, we introduce an parameter that characterizes the excitation state of ionized gas, the effective ionization parameter $q_{\rm eff}$,

$$q_{\rm eff} = \frac{Q_{\rm H^0}}{4\pi R_{\rm s}^2 n_{\rm H}} \tag{B.11}$$

which is defined as the ratio of ionizing photons and hydrogen atoms in the ionized sphere. Sometimes it is denoted by a dimensionless form $U = q/c$ where c is speed-of-light. The ionization parameter is also defined locally. Supposing a spherical gas shell surrounding a hot star, the ionization parameter is given at the inner face of the cloud (inner radius r) as

$$U = \frac{q}{c} = \frac{Q({\rm H}^0)}{4\pi r^2 cn(H)}. \tag{B.12}$$

The ionization parameter may be estimated from a ratio of lines of double- and single-ionized ions, such as [O III]/[O II] (Kewley & Dopita 2002; Nakajima & Ouchi 2014).

Figure B.1: Image of Rosette Nebular. The Hα emissions from the ionized gas cloud are shown in red. Image Credit & Copyright: Brian Davis (http://apod.nasa.gov/apod/ap120214.html)

The temperature in a static nebula is characterized by the equilibrium between heating by photoionization and cooling by recombination and through the radiation from ionized gas. As a result, An electron temperature of $T_{\rm e} \sim 5 \times 10^3$–$10^4$ K is ubiquitously realized in typical H II regions. The cooling is primarily attributed to collisional excitation of low-lying energy levels of abundant heavy ions, such as O^+, O^{++}, and N^+. Forbidden emission lines due to

radiative transitions between their excited levels and the ground level are widely seen in nebulae, such as [O II]$\lambda\lambda$3726, 3729, [O III]$\lambda\lambda$4959,5007, and [N II]$\lambda\lambda$6548, 6584. Free-free radiation or bremsstrahlung contributes subdominantly to cooling, in which a continuum spectrum is emitted.

In metal-free hydrogen gas (e.g., neutral intergalactic medium), the recombination cooling is the most important. As a consequence of the b heat balance, $T_{\rm e} \sim$ a few $\times 10^4$ K is usually seen.

Appendix C

The expanding Universe

The current cosmological models rely on the principle that the Universe is homogeneous and isotropic. This statement is, obviously, not exact because we can observe rich structures at a wide range of scales. Large galaxy surveys have shown that the large scale structures are basically traced by galaxies. However, looking at scales over a few $\times 100\ h^{-1}$Mpc, the Universe looks homogeneous enough and isotropic. Observations of the cosmic microwave background (CMB) have strongly supported the cosmological principle. Here, we see the basic properties of the smoothed space and time.

In 1915, Einstein had established the general theory of relativity, which the modern cosmology bases on. The evolution of spacetime is described by Einstein's equation,

$$G_{\mu\nu} \equiv R_{\mu\nu} - \frac{1}{2} g_{\mu\nu} R = \frac{8\pi G}{c^4} T_{\mu\nu} \tag{C.1}$$

where $G_{\mu\nu}$ is Einstein tensor, $R_{\mu\nu}$ is Ricci tensor, and R is Ricci scalar. The metric $g_{\mu\nu}$ describes the configuration of spacetime. $T_{\mu\nu}$ is energy-momentum tensor.

The most standard metric which satisfies the cosmological principle is given by

$$ds^2 = g_{\mu\nu} dx^\mu dx^\nu = -c^2 dt^2 + a^2(t) \left[\frac{dr^2}{1 - Kr^2} + r^2 \left(d\theta^2 + \sin^2 \theta d\phi^2 \right) \right], \tag{C.2}$$

which is called the Friedmann-Lemaître-Robertson-Walker metric (FLRW metric). The scale factor $a(t)$ describes the expansion of space, and is generally normalized as $a(t_0) = 1$ at the present epoch t_0. K describes the spatial curvature of the space. Under the cosmological principle, the energy-momentum tensor is given as the form of perfect fluid,

$$T^\mu_\nu = \mathrm{diag}(-\rho, p, p, p), \tag{C.3}$$

where, ρ is the energy density and p is the pressure. In the homogeneous isotropic spacetime, Einstein equation (C.1) can be written as

$$\left(\frac{\dot{a}}{a} \right)^2 = \frac{8\pi G}{3c^2} \rho - \frac{c^2 K}{a^2}, \tag{C.4}$$

$$\frac{\ddot{a}}{a} = -\frac{4\pi G}{3c^2} \left(\rho + 3p \right). \tag{C.5}$$

These equations state that space is unstable. If there is matter in the Universe, the space should shrink, otherwise expands while decelerating, due to gravity. Einstein, who believed that the Universe is stable, introduced *repulsion* term Λ against the attraction by gravity into his equation to maintain the stable space, which is referred to as the cosmological constant,

$$R_{\mu\nu} - \frac{1}{2} g_{\mu\nu} R = \frac{8\pi G}{c^4} T_{\mu\nu} - \Lambda g_{\mu\nu}. \tag{C.6}$$

Afterword, the expansion of the universe had been discovered by Edwin P. Hubble by measuring

the relation between radial velocity and distance of galaxies, and then Einstein has withdrawn the cosmological constant. Today, however, the cosmological constant is considered as one of the candidates of dark energy. Hereafter, we deal with the Einstein equation including Λ (Equation C.6), or the equivalent forms,

$$\left(\frac{\dot{a}}{a}\right)^2 = \frac{8\pi G}{3c^2}\rho - \frac{c^2 K}{a^2} + \frac{c^2\Lambda}{3}, \tag{C.7}$$

$$\frac{\ddot{a}}{a} = -\frac{4\pi G}{3c^2}(\rho + 3p) + \frac{c^2\Lambda}{3}. \tag{C.8}$$

The former equation is referred to as Friedmann equation. Eliminating $\ddot{a}$ from Equations (C.7) and (C.8), we obtain

$$\dot{\rho} + 3\frac{\dot{a}}{a}(\rho + p) = 0. \tag{C.9}$$

This can be derived from Equation (C.3), called fluid equation. If assuming an equation of state $p = p(\rho)$, we can determine the time evolution of the scale factor $a = a(t)$.

We introduce the comoving coordinates, which expand following the expansion of the space, and the concept of comoving distance. We consider two points separating by a comoving distance x in an isotropic space that expands uniformly. Let $d(t)$ be the physical separation between the two points at time t, we can write

$$d(t) = a(t)/a(t_0)x = a(t)x. \tag{C.10}$$

Here, we set the scale factor equal to unity at the present epoch t_0 and x to the physical distance measured at t_0. The relative velocity of these points due to the space expansion is expressed as

$$v = \dot{d}(t) = \dot{a}x = \frac{\dot{a}}{a}d = H(t)d, \tag{C.11}$$

where $H = \dot{a}/a$ is referred to as the Hubble parameter. At $t = t_0$, this equation is called Hubble's law, and $H_0 = H(t_0)$ is called the Hubble constant, which was introduced as a coefficient between the radial velocity and distance of galaxies. Currently, it is measured to be $H_0 = 67.74 \pm 0.46$ km s^{-1} Mpc^{-1} from the CMB observations (Planck Collaboration 2015). Historically, it had been difficult to constrain the Hubble constant, thus it has been conventionally written with an dimensionless parameter h, which is about unity, as

$$H_0 = 100h \text{ km s}^{-1} \text{ Mpc}^{-1}. \tag{C.12}$$

From Equation (C.7), the total energy density in the Universe without the cosmological constant and without curvature ($K = 0$) is given as

$$\rho_{\rm cr} = \frac{3c^2H^2}{8\pi G}. \tag{C.13}$$

This is referred to as the critical energy density. Now we define a dimensionless density parameter that measures the fraction of energy density ρ to the critical density as

$$\Omega \equiv \frac{\rho}{\rho_{\rm cr}} = \frac{8\pi G\rho}{3c^2H^2}. \tag{C.14}$$

The energy density ρ in Equation (C.7) can be separated into contributions from matter (non-relativistic matter) and radiation (relativistic matter), and further the matter component can be

separated into baryons and dark matter,

$$\Omega = \Omega_{\rm r} + \Omega_{\rm dm} + \Omega_{\rm b}. \tag{C.15}$$

Similarly, the contributions from the curvature (K) and the cosmological constant (Λ) are given as

$$\Omega_K = -\frac{c^2 K}{a^2 H^2}, \tag{C.16}$$

$$\Omega_\Lambda = \frac{c^2 \Lambda}{3H^2}. \tag{C.17}$$

Using these density parameters, the Friedmann equation (C.7) can be simplified as

$$\Omega + \Omega_K + \Omega_\Lambda = 1. \tag{C.18}$$

Values of the density parameters at the present day are usually denoted with index 0 (e.g., Ω_0, $\Omega_{\Lambda 0}$), which are constrained now from the CMB observations.

The equation of state for non-relativistic matter (dark matter and baryons) is given by $p = 0$ because the pressure is negligible relative to the energy density. From Equation (C.9), we have the time evolution of matter component as

$$\rho_{\rm m} \propto a^{-3}. \tag{C.19}$$

Similarly, the equation of state for relativistic matter (radiation component) is given by $p = \rho/3$, so that we have

$$\rho_{\rm r} \propto a^{-4}. \tag{C.20}$$

These dependence on the scale factor a state that the particle density declines by $1/V$ and that the energy of each relativistic particle declines by $1/a$ because its wavelength expands by a factor of a.

Taken together, the Friedmann equation at an arbitrary epoch is given with the density parameters at the resent day and the Hubble constant by

$$H^2(a) = H_0^2 \left(\frac{\Omega_{\rm m0}}{a^3} + \frac{\Omega_{\rm r0}}{a^4} + \frac{\Omega_{K0}}{a^2} + \Omega_{\Lambda 0} \right). \tag{C.21}$$

Due to the expansion of the Universe, the wavelength of light emitted from an object is stretched during traveling to an observer. Let $\lambda_{\rm emit}$ and $\lambda_{\rm obs}$ be the wavelengths of the light at the emission ($t = t_{\rm emit}$) and observation time ($t = t_{\rm obs}$), respectively. The ratio of these wavelengths is written using the scale factor a as

$$\frac{\lambda_{\rm obs}}{\lambda_{\rm emit}} = \frac{a(t = t_{\rm obs} = t_0)}{a(t_{\rm emit})} = \frac{1}{a(t_{\rm emit})} \equiv 1 + z. \tag{C.22}$$

where we are the observer and the scale factor is normalized as the present epoch ($t = t_{\rm obs} = t_0$). The parameter z is called a *redshift*, and it measures when the light was emitted and how far the object exists in the monotonically-expanding universe.

Appendix D

Theory of structure formation

So far, we have seen the evolution of the homogeneous isotropic Universe, from which however any structures do not form at all. In the real Universe, we see rich structures. In the paradigm of the standard cosmological model, all such structures originate from the quantum fluctuations input during the inflation, which we can see through the temperature fluctuations in the CMB. Fluctuations inscribed in the matter density field grow up through gravity, then form a variety of structures seen in the current Universe. We provide an overview of the evolution of matter density fluctuations and the formation of dark matter halos. In these processes, only gravity is important, and the effects of baryon physics can be negligible.

D.0.1 Linear perturbation theory

Considering the matter component as perfect fluid, its physical conditions are described by mass density field ϱ, pressure field p, and velocity field $\boldsymbol{v}$. In the case of non-relativistic matter, pressure is much smaller than the energy density ($p \ll \rho = \varrho c^2$). The gravitational potential ϕ of the density field ρ is given by a Poisson equation,

$$\Delta\phi = 4\pi G\rho. \tag{D.1}$$

We consider the evolution of fluid in the comoving coordinates, $\boldsymbol{r}$. The gravitational potential can be re-written as

$$\Phi = \phi + \frac{1}{2}a\ddot{a}|\boldsymbol{r}|^2, \tag{D.2}$$

where the additional term denotes the apparent force acting on the point $\boldsymbol{r}$ in the rest-frame. In the matter-dominant universe, from Equation (C.5), we have

$$\frac{\ddot{a}}{a} = -\frac{4\pi G}{3}\bar{\varrho}. \tag{D.3}$$

Thus, the Poisson equation in the comoving coordinate is given as

$$\Delta\Phi = 4\pi G a^2 \left(\varrho - \bar{\varrho}\right). \tag{D.4}$$

This means that, in comoving coordinates, only the inhomogeneous component of the density fluctuations contributes to the gravitational potential.

The evolution of the fluid obeys the continuity equation and Euler equation. In comoving coordinates, these equations are given as

$$\frac{\partial\varrho}{\partial t} + 3\frac{\dot{a}}{a}\varrho + \frac{1}{a}\nabla\cdot(\varrho\boldsymbol{v}) \quad : \quad \text{Continuity Eq.} \tag{D.5}$$

$$\frac{\partial\boldsymbol{v}}{\partial t} + \frac{1}{a}\left(\boldsymbol{v}\cdot\nabla\right)\boldsymbol{v} = \frac{1}{a}\nabla\Phi - \frac{1}{a\varrho}\nabla p \quad : \quad \text{Euler Eq..} \tag{D.6}$$

$$\tag{D.7}$$

Here, we define the density fluctuation δ as a function of time and location,

$$\delta(t, \boldsymbol{r}) = \frac{\varrho\,(t, \boldsymbol{r}) - \bar{\varrho}\,(t)}{\bar{\varrho}\,(t)}, \tag{D.8}$$

where $\boldsymbol{r}$ is the comoving coordinates and $\bar{\rho}$ is the mean density of the Universe at time t. The evolution of the dark matter fluctuation can be described by the equations of pressure-less fluid (i.e., $p = 0$). Considering very small density contrast $\delta \ll 1$, these equations can be linearized by neglecting the second-order terms, so that we obtain

$$\ddot{\delta} + 2\frac{\dot{a}}{a}\dot{\delta} = 4\pi G\bar{\rho}\delta. \tag{D.9}$$

In the flat matter-dominant universe (Einstein-de Sitter model), we have immediately a simple solution

$$\delta = At^{2/3} + Bt^{-1}, \tag{D.10}$$

where the first term is the growing mode and the second term is the decaying mode. The decaying mode rapidly decreases with time, thus it is not important in the structure formation. The growing mode have the same time dependence as the scale factor $a(\propto t^{2/3})$, so that the density fluctuations grow up proportionally to the scale factor ($\delta \propto a$).

In more general cases, the solution can be decomposed into the spatial and time dependent components as

$$\delta\,(\boldsymbol{r}, t) = D(t)\delta_0(\boldsymbol{r}), \tag{D.11}$$

where δ_0 is the density fluctuation at an arbitrary time. Two independent solutions of D are given as

$$D_+ \propto H\int_0^a \frac{da}{a^3H}, \quad D_- \propto H. \tag{D.12}$$

After the matter-radiation equality, the hubble parameter decreases with time, thus D_- gives the decaying mode. The solution with D_+ is the growing mode, and we call D_+ the linear growth factor.

D.0.2 Two-point statistics of matter fluctuations

Any cosmological models can only predict statistical properties concerning the realized matter fluctuations and/or galaxy distribution, but not any unique value at each point in the space theoretically. Two-point statistics are the most important quantities that characterize the large-scale distribution of matter, and thus the galaxy distribution.

The two-point correlation function ξ of a density field $\delta(\boldsymbol{r})$ is defined as

$$\xi(r_{12}) \equiv \langle\delta(\boldsymbol{r}_1)\delta(\boldsymbol{r}_2)\rangle\,, \tag{D.13}$$

where $r_{12} = |\boldsymbol{r}_1 - \boldsymbol{r}_2|$ and $\langle\cdots\rangle$ denotes an ensemble average. For discrete objects, the two-point correlation function measures excess of the probability of finding pairs of two objects as a function of separation.

In usual cases, it is convenient to describe stochastic fluctuations in Fourier space. Fourier transform of the density fluctuation $\delta(\boldsymbol{r})$ is given as

$$\tilde{\delta}(\boldsymbol{k}) = \int d^3r \exp\left(-i\boldsymbol{k}\cdot\boldsymbol{r}\right). \tag{D.14}$$

The ensemble average of $\tilde{\delta}(\boldsymbol{k})$ is given as

$$\left\langle \tilde{\delta}(\boldsymbol{k})\tilde{\delta}(\boldsymbol{k}')\right\rangle = \int d^3r_1 d^3r_2 \exp\left(-i\boldsymbol{k}\cdot\boldsymbol{r}_1 - i\boldsymbol{k}'\cdot\boldsymbol{r}_2\right)\xi(|\boldsymbol{r}_1-\boldsymbol{r}_2|) \tag{D.15}$$

$$= (2\pi)^3 {\delta_{\rm D}}^3(\boldsymbol{k}+\boldsymbol{k}')\int d^3r e^{-i\boldsymbol{k}\cdot\boldsymbol{r}}\xi(|\boldsymbol{r}|), \tag{D.16}$$

where $\delta_{\rm D}$ is the delta function,

$$\int d^3r e^{-i\boldsymbol{k}\cdot\boldsymbol{r}} = (2\pi)^3 {\delta_{\rm D}}^3(\boldsymbol{k}). \tag{D.17}$$

This holds due to the translational invariance of the universe. The integration in the right-hand side of Equation (D.16) can be written as

$$\int d^3 e^{-i\boldsymbol{k}\cdot\boldsymbol{r}}\xi(|\boldsymbol{r}|) = 4\pi\int_0^\infty r^2 dr \frac{\sin(kr)}{kr}\xi(r). \tag{D.18}$$

This is just a function of $k = |\boldsymbol{k}|$, which is ensured by the isotropy of the universe. Equation (D.18) is written as $P(k)$, called a *power spectrum*. Thus, we have

$$\left\langle \tilde{\delta}(\boldsymbol{k})\tilde{\delta}(\boldsymbol{k}')\right\rangle = \left\langle \tilde{\delta}^*(\boldsymbol{k})\tilde{\delta}(\boldsymbol{k}')\right\rangle = (2\pi)^3\delta_{\rm D}^3(\boldsymbol{k}-\boldsymbol{k})P(\boldsymbol{k}), \tag{D.19}$$

where we use $\tilde{\delta}^*(\boldsymbol{k}) = \tilde{\delta}(-\boldsymbol{k})$. A power spectrum and correlation function are related mutually as

$$P(k) = \int d^3 e^{-i\boldsymbol{k}\cdot\boldsymbol{r}}\xi(|\boldsymbol{r}|) = 4\pi\int_0^\infty r^2 dr\frac{\sin(kr)}{kr}\xi(r), \tag{D.20}$$

$$\xi(r) = \int \frac{dk}{(2\pi)^3} e^{i\boldsymbol{k}\cdot\boldsymbol{r}}P(|\boldsymbol{k}|) = \int \frac{k^2dk}{2\pi^2}\frac{\sin(kr)}{kr}P(k). \tag{D.21}$$

The power spectrum is the most fundamental quantity that statistically describes the density fluctuations in the Universe. The evolution of the power spectrum determines the fate of the fluctuations.

The mass fluctuation measures the excess of mass in a sphere relative to the average. The average mass in a sphere of a radius R is $M_R = 4\pi R^3\bar{\varrho}$. The mass fluctuation in a sphere with R at an arbitrary point (taken as the origin) is given as

$$\frac{dM_R}{M_R} = \frac{3}{4\pi R^3}\int_{|\boldsymbol{r}|\le R} d^3r\delta(\boldsymbol{r}) = \int d^3r W_R(|\boldsymbol{r}|)\delta(\boldsymbol{r}), \tag{D.22}$$

where W_R is a top-hat window function with a radius R;

$$\sigma^2(R) \equiv \left\langle\left(\frac{\delta M}{M}\right)^2\right\rangle = \int\frac{k^2dk}{2\pi^2}\tilde{W}^2(kR)P(k). \tag{D.23}$$

where $\tilde{W}$ is the Fourier transform of the window function W_R. In the Fourier space, the top-hat window function is written as

$$\tilde{W}(kR) = \int d^3r e^{-i\boldsymbol{k}\cdot\boldsymbol{r}}W_R(|\boldsymbol{r}|) = \frac{3}{(kR)^3}\left[\sin(kR) - kR\cos(kR)\right]. \tag{D.24}$$

The variance of the mass fluctuation smoothed within a sphere of $R = 8$ Mpc, σ_8, is commonly used for the normalization of the power spectra.

D.0.3 Initial condition and transfer function

In the expanding Universe, the density fluctuations evolve in response to scale k. The power spectrum at time t is related to the initial power spectrum $P_{\rm ini}(k)$ using the linear growth factor $D(t)$ and the transfer function $T(k,t)$, which describes the k-dependent growth within a hubble horizon, as

$$P(k,t) = T^2(k,t)\frac{D^2(t)}{D_{\rm ini}}P_{\rm ini}(k). \tag{D.25}$$

In 1970's, Harrison and Zel'dovich discussed what the initial power spectrum should be. Supposing that there is no characteristic scale, the power spectrum should have a power-law form

$$P_{\rm ini} = A_{\rm ini}k^{n_s}, \tag{D.26}$$

where n_s is called a spectral index and $A_{\rm ini}$ is a normalization factor. Further, if one assumes that the mass fluctuation corresponding to the hubble horizon at each time should be constant, the spectral index n_s should be unity;

$$P_{\rm ini} = A_{\rm ini}k. \tag{D.27}$$

The power spectrum given by this equation is called the *Harrison-Zel'dovich spectrum* (Harrison 1970; Zeldovich 1972), which is known to explain the structure of the Universe well. Most of inflation models predict a power-law initial power spectrum with $n_s \sim 1$. Observations of the CMB with the Planck satellite provided a constraint on the spectral index of $n_s = 0.968 \pm 0.006$ (Planck Collaboration 2015).

D.0.4 Spherical collapse model

So far, we have seen the evolution of the matter density fluctuation in the linear approximation. We now consider the gravitational collapse of a spherical region with a radius R and total mass M. Let ϱ_R be the mean density in the spherical region, thus $\varrho_R = 3M/(4\pi R^3)$. The equation of motion of this boundary is given as

$$\frac{d^2R}{dt^2} = \frac{GM}{R^2}. \tag{D.28}$$

In the expanding Universe, initially R have a positive (outward) velocity, i.e., $\dot{R} > 0$. If the initial velocity was lower than the escape velocity, this region eventually turns to the contraction. In this case, we obtain the solution (with parameter θ),

$$R = (GM)^{1/3}A^2(1-\cos\theta), \tag{D.29}$$
$$t = A^3(\theta - \sin\theta), \tag{D.30}$$

where A is an integral constant. In the Einstein-de Sitter universe, the mean matter density is given by $\bar{\varrho} = 1/(6\pi G t^2)$. Hence, the mean density fluctuation in the sphere is given as

$$\delta_R = \frac{\varrho_R}{\bar{\varrho}} - 1 = \frac{9GMt^2}{2R^3} - 1 = \frac{9}{2}(\theta - \sin\theta)^2(1-\cos\theta)^3 - 1. \tag{D.31}$$

This means that the sphere reaches the maximum radius at $\theta = \pi$, then turns to the contraction. At this turning point, the time and the radius are

$$t_{\rm turn} = \pi A^3, \quad R_{\rm turn} = 2(GM)^{1/3}A^2, \tag{D.32}$$

and the density fluctuation at this point is

$$\delta_{\rm turn} = \frac{9\pi^2}{16} - 1 \approx 4.55. \tag{D.33}$$

The sphere collapses at $\theta = 2\pi$, which corresponds to

$$t_{\rm coll} = 2t_{\rm turn} = 2\pi A^3. \tag{D.34}$$

The time $t_{\rm ff} = t_{\rm coll} - t_{\rm turn}$ is called a free-fall timescale, which is given with the mass density at the turning point $\varrho_{\rm turn} = 3M/(4\pi R_{\rm turn}^3)$ as

$$t_{\rm ff} = \pi A^3 = \frac{\pi}{2}\sqrt{\frac{R_{\rm turn}^3}{2GM}} = \sqrt{\frac{3\pi}{32G\varrho_{\rm turn}}}. \tag{D.35}$$

When $\delta \ll 1$, spherical collapse can be linearly described. As a fluctuation grows up, it gradually differs from the prediction from the linear theory. However, we can link the prediction from the linear theory to the non-linear value of the fluctuation. Expanding Equations (D.30) and (D.31) in terms of θ yields

$$\delta_R = \frac{3}{20}\theta^2 + \mathcal{O}(\theta^4), \quad t = \frac{A^3}{6}\theta^3 + \mathcal{O}(\theta^5). \tag{D.36}$$

These equations reproduce the linear growing mode of Equation (D.10), $\delta_R \propto t^{2/3}$, taking the lowest-order terms. Letting $\delta_{\rm L}$ be the linear fluctuation, we have

$$\delta_{\rm L}(t) = \frac{3(6t)^{2/3}}{20A^2}. \tag{D.37}$$

Substituting $t_{\rm turn}$ and $t_{\rm coll}$ yields

$$\delta_{\rm L}(t_{\rm turn}) = \frac{3(6\pi)^{2/3}}{20} \approx 1.06, \quad \delta_{\rm L}(t_{\rm coll}) = \frac{3(12\pi)^{2/3}}{20} \approx 1.69. \tag{D.38}$$

Namely, when the linear fluctuation δ_L reaches 1.69, the sphere collapses and its density becomes infinity.

So far, we consider a system that collapses and forms a singularity point with infinite density. However, in reality, the velocity dispersion such a the system cannot be negligible when the density increases. Thus, the collapsed sphere forms a gravitationally-bounded stable system with a finite size. We call this state the *virial equilibrium*, where the potential energy U is related to the kinetic energy K as $K = -U/2$. In the spherical collapse model, the sphere has the maximum radius $R_{\rm turn}$ and the kinetic energy is zero at the turning point. Thus, the total energy $E = U + K$ is given as

$$E = -\frac{3}{5}\frac{GM^2}{R_{\rm turn}}. \tag{D.39}$$

This total energy is conserved. When the sphere reaches virial equilibrium with a virial radius $R_{\rm vir}$, the potential energy is

$$U_{\rm vir} = -\frac{3}{5}\frac{GM^2}{R_{\rm vir}}. \tag{D.40}$$

From the virial theorem, we obtain $R_{\rm vir} = R_{\rm turn}/2$, and thus the mean density of the system is given as $\varrho_{\rm vir} = 3M/(4\pi R_{\rm vir}^3)$. Since the timescale required for the system to reach the virial equilibrium is approximately the same as the free-fall timescale, the density fluctuation is given

as

$$\delta_{\rm vir} = \frac{\varrho_{\rm vir}}{\bar{\varrho}(t_{\rm coll})} - 1 = \frac{3M/(4\pi R_{\rm vir}^3)}{(6\pi G t_{\rm col]})^{-1}} - 1 \approx 177. \tag{D.41}$$

Although we have seen a very simple case here, this provides us with a reasonable approximation for the real Universe. As demonstrated from N-body simulations, dark matter halos have the mean density that is about 200 times higher than the background density.

D.0.5 Press-Schechter theory

How many halos form in the Universe? This is an essential question. An analytical framework of deriving the halo mass function had been established by Press & Schechter (1974), called the Press-Shechter formalism, which extends the solution of the linear theory to the non-linear regime. According to the spherical collapse model, regions with $\delta_L(\boldsymbol{r}, t) > \delta_{\rm c} \approx 1.69$ will have collapsed by time t. Since the linear growth is expressed as $\delta(\boldsymbol{r}, t) = D(t)\delta_0(\boldsymbol{x})$ with the initial density fluctuation $\delta_0(\ll 1)$, we can rephrase this; regions with $\delta_0(\boldsymbol{x}) > \delta_{\rm c}/D(t)$ at the initial epoch will have collapsed. The linear growth factor $D(t)$ increases with time, thus $\delta_{\rm c}(t)$ decreases.

We assume that the initial matter fluctuation δ_0 obeys Gaussian statistics. This assumption has been observationally confirmed with a high degree of accuracy. If the fluctuations are enough small, the sphere with a radius R contains mass of $M = 4\pi\bar{\varrho}_0 R^3/3$, where $\bar{\varrho}_0$ is the mean density at the initial epoch. Next, let δ_M be the density fluctuation, based on δ_0, smoothed in the sphere of $R = (3M/\,4\pi\bar{\varrho}_0)^{1/3}$. This also obeys Gaussian statistics, thus its probability distribution function is given as

$$P\left(\delta_M\right) d\delta_M = \frac{1}{\sqrt{2\pi\sigma^2(M)}} \exp\left(-\frac{\delta_M^2}{2\sigma^2(M)}\right), \tag{D.42}$$

where $\sigma(M)$ is variance of δ_M.

In the context of the Press-Schechter formalism, we consider that a fluid parcel will be captured in an object of mass M when the mass fluctuation δ_M at that point exceeds $\delta_{\rm c}(t)$. Considering the Lagrange space, the fraction of regions with $\delta_M > \delta_{\rm c}(t)$ is given as a function of mass scale M as follows,

$$P_{>\delta_{\rm c}}(M) = \int_{\delta_{\rm c}(t)}^{\infty} P(\delta_M) d\delta_M = \frac{1}{\sqrt{2\pi}} \int_{\delta_{\rm c}(t)/\sigma(M)}^{\infty} e^{-x^2/2} dx. \tag{D.43}$$

Since the matter density is homogeneous in the Lagrange space, $\bar{\varrho}_0 P_{>\delta_{\rm c}}(M)$ denotes the amount of matter per unit volume that will have been captured in collapsed objects of mass more than M. Thus, the mass of matter that will have been captured in collapsed objects with mass between M and $M + dM$ is given as the difference between $\bar{\varrho}_0 P_{>\delta_{\rm c}}(M)$ and $\bar{\varrho}_0 P_{>\delta_{\rm c}}(M + dM)$. Letting $n(M)$ be the mass function, we obtain

$$\frac{dn(M,t)}{dM} = \sqrt{\frac{2}{\pi}} \frac{\bar{\varrho}_0}{M} \left|\frac{d\ln\sigma(M)}{d\ln M}\right| \frac{\delta_{\rm c}(t)}{\sigma(M)} \exp\left(\frac{\delta_{\rm c}^2(t)}{2\sigma^2(M)}\right). \tag{D.44}$$

Here, the factor of 2 is multiplied under the assumption that all the matter will have eventually collapsed. The Press-Schechter formalism is known to agree with results from cosmological N-body simulations well although it includes recipes that are not justified theoretically.

We consider a simple case that the variance of mass fluctuation has a power-law form $\sigma(M) \propto M^{-\alpha}$, which corresponds to a power-law power spectrum $P(K) \propto k^n$ with $\alpha = (n+3)/6$. In this case, Equation (D.44) becomes

$$n(M) = \frac{2}{\sqrt{\pi}} \frac{\bar{\varrho}_0 \alpha}{M_*^2} \left(\frac{M}{M_*}\right)^{\alpha-2} \exp\left[-\left(\frac{M}{M_*}\right)^{2\alpha}\right], \tag{D.45}$$

where M_* is defined by $\sigma(M_*/2^{1/(2\alpha)}) = \delta_c$. It means that the number density of halos exponentially decreases at $M > M_*$. In Figure 1.10, predictions from the Press-Schechter formalism are presented (dotted lines).

Appendix E

Some details relevant to the clustering analysis

Here, we provide details of our clustering analysis presented in Chapter 5.

E.1 Correction for the effects of fiber allocation

E.1.1 Mock samples from the ν^2GC simulation

We describe the construction of mock samples used to examine the correction scheme for the fiber allocation effects. The mock samples are constructed from the new numerical Galaxy Catalog (ν^2GC) cosmological simulation (Ishiyama et al. 2015). The middle size simulation (ν^2GC-M) that we use was conducted using 4096^3 particles with a mass resolution of $2.20 \times 10^8\ h^{-1}M_\odot$ in a comoving simulation box with each side length of 560 h^{-1}Mpc. We employ a halo/subhalo catalog at a scale factor $a = 1/(z+1) = 0.384871$ ($z = 1.598$), which is close to the median redshift of our spectroscopic sample ($z = 1.588$). Halos and subhalos in the catalog are identified using the Rockstar technique (Behroozi et al. 2013b), resolving subhalos with $M_{\rm h} \sim 10^{10}\ h^{-1}M_\odot$. This resolution is high enough for our purpose.

We select objects (halos and subhalos) from the catalog to create a sample that has a number density equal to the FMOS-parent sample ($n = 3.07 \times 10^{-3} h^3 {\rm Mpc}^{-3}$) and an amplitude of the projected correlation function similar to the observed correlation function (see Figure E.2 later in this Appendix). We construct the sample by extracting halos having a maximum circular velocity $V_{\rm max}$ greater than 170 km s^{-1} (physical) and subhalos having $V_{\rm max} > 160$ km s^{-1}. It is known that the observed shape and amplitude of the galaxy clustering can be reproduced better by a sample selected using a threshold for the highest $V_{\rm max}$ that a halo has had over its past history ($V_{\rm peak}$) or the $V_{\rm max}$ at the epoch when the satellite subhalo accretes into its host halo rather than the $V_{\rm max}$ at the epoch in which they are identified (Reddick et al. 2013). So far, however, such information is not available yet for this simulation. To roughly consider mass stripping effects of subhalos, we use the different threshold $V_{\rm max}$ for halos and subhalos here. The side and radial lengths of our survey volume over $1.43 < z < 1.74$ are $\sim 60\ h^{-1}$Mpc and $\sim 400 h^{-1}$Mpc, respectively. Hence, we divide the simulation box into 64 sub boxes on the x-y plane each having a volume of $70 \times 70 \times 560\ h^{-3}{\rm Mpc}^3$. Then, we convert the real space coordinates (x, y, z) into RA, DEC and redshift, taking into account the radial peculiar velocity of each halo or subhalo. We do not consider the redshift evolution between the redshift range of interest.

To realize the redshift distribution of the FMOS-parent sample in the mock samples (see Figure 5.7), we assign *photometric* redshifts by adding random fluctuation of ${\rm rms}(z_{\rm phot} - z_{\rm spec}) = 0.062$ onto the true observed redshift (including peculiar velocity) of each halo. Then we extract the objects from the same range of the photometric redshift as applied to the real data ($1.46 < z_{\rm phot} < 1.72$). This operation slightly reduces the amplitude of the angular correlation function of the mock samples, which is expected for the real data, compared with those extracted using

the true redshift. We apply the actual shape of the survey area (see Figure 5.1) for each sub-box mock. For those *Mock-parent* samples, we perform the FMOS fiber allocation to construct the *Mock-target* samples. Then we create the *Mock-spec-z* samples by extracting the same number of galaxies as that of the FMOS-spec-z sample ($N = 516$) from each Mock-target sample, so that all the objects have a true observed redshift within $1.43 < z < 1.74$.

E.1.2 Weighting scheme

We describe the correction scheme for the effects caused by the fiber allocation system of FMOS. In our survey, it was not achieved to observe all the galaxies in the input parent catalog. A sample of spectroscopically-observed galaxies is not a random subset of the input catalog due to observational effects. The most serious problem may be that the on-sky distribution of observed galaxies is biased in response to the characteristic scales of spatial separation and the movable area of the fibers. The FMOS fibers are uniformly embedded in the field-of-view and those fibers can move in a limited circular patrol area with 174 arcsec diameters (Akiyama et al. 2008b). These fibers are incidental to either of two spectrograph. In the cross-beam switching mode, a pair of fibers belonging to the same spectrograph is allocated to a galaxy to observe the object and sky in turn. Therefore, once a pair of fibers is allocated for one galaxy, the opportunity that its neighbor galaxies are observed at the same time decreases due to the lack of fibers and/or avoiding the fiber entanglement, while the patrol area can overlap with those of adjacent fibers. These limitations of the fiber allocation yield complicated biases and the distribution of observed galaxies on the sky is distorted from the intrinsic distribution. In particular, at small scales less or similar to the separation of fibers ($\sim 1\farcm6$), the sampling rates of galaxy pairs is suppressed, so that the clustering amplitude is reduced at the corresponding scales. In contrast, galaxy pairs with a separation several times larger than the fiber separation are easy to find, which might results in some amount of enhancement of the amplitude of correlation function at such scales. In addition, the sampling rate varies from place to place in the survey area because of the differences of the number of exposures among the four FMOS footprints and the existence of the small areas where the footprints are overlapped. Moreover, some broken fibers result in holes, where the sampling rate is reduced, around them in the spatial distribution of observed galaxies.

In order to correct for these intricate biases, we apply a weight for each galaxy–galaxy pairs in response to their angular separation (e.g., de la Torre et al. 2011; Durkalec et al. 2015). The weight function is defined as a ratio between the mean probability of finding pairs in the parent sample and the mean probability of finding pairs in the observed galaxy sample, and expressed with their angular correlation function:

$$f(\theta) = \frac{1 + \omega_{\rm par}(\theta)}{1 + \omega_{\rm tar}(\theta)} \tag{E.1}$$

where $\omega_{\rm par}(\theta)$ and $\omega_{\rm tar}(\theta)$ are the angular correlation functions of the Mock-parent and Mock-target samples, respectively. In this scheme, we implicitly assume that the photometric parent catalog is free from any artificial biases depending on the angular separation scale.

Figure E.1 (upper panel) shows the angular correlation functions of the FMOS-parent sample and FMOS-target sample. It is clear that the angular clustering amplitude of the FMOS-target sample is suppressed as compared to the one of the FMOS-parent sample at scales $\theta \lesssim 100$ arcsec, which is similar to the fiber separation. While we can define the weight function by directly taking the ratio between these angular correlation functions, the uncertainties are large especially at small scales. Therefore, we define the weight function that is applied for the analysis by using mock samples to achieve a reasonable statistical robustness.

For each of 64 Mock-parent samples described in Appendix E.1.1, we perform the FMOS Spine-to-Object allocation algorithm with the same configuration parameters as the real observations. We repeat the fiber allocation for all the H-long pointings (listed in 5.1), while removing the sources for which a fiber is allocated for the next step. The break down fibers, of which some are regularly out-of-order and the others are depending on the observing runs, are taken into account. Then we obtain the realistic Mock-target samples.

In Figure E.1 (upper panel), we show the angular correlation functions of the 64 parent and target mock samples, and their average. The mean angular correlation function of the parent and target mock samples are consistent with those of the data parent and target samples, respectively. As shown in the data, it is clear that the amplitude is reduced on average at scales $\theta \lesssim 100$ arcsec, corresponding to $r_{\rm p} \lesssim 2\ h^{-1}$ Mpc at $z \sim 1.6$. This decrease of the angular clustering amplitude is expected as the effect of the fiber allocation, i.e., the suppression of the opportunity of finding the close pairs by the fibers. Figure E.1 (lower panel) shows the weight function computed from the angular correlation functions ($\omega_{\rm par}$ and $\omega_{\rm tar}$) of each mock sample. For our study, we use the average function (thick solid line) calculated from the individual mock samples. The average weight function increases at angular scales of $\theta \lesssim 100$ arcsec and reaches $f(\theta) \sim 1.2$ at $\theta < 20$ arcsec at $\theta < 20$ arcsec, while it is slightly smaller than unity at scales of several hundreds arcsec. It likely implies the easiness of finding pairs with a separation several times larger than the fiber separation.

We examine if the correction scheme works well for our analysis by using the mock catalogs. In Figure E.2, we compare the average correlation functions $w_{\rm p}(r_{\rm p})$ of 64 Mock spec-z samples with (filled circles) or without (empty circles) the correction, to the average correlation function of Mock-parent samples (squares). The average amplitude of the Mock-spec-z samples without the correction is reduced at scales $r_{\rm p} \lesssim 2\ h^{-1}$Mpc compared to the average of the Mock-parent samples, while it is slightly enhanced at $r_{\rm p} \gtrsim 3\ h^{-1}$Mpc, as clearly seen in the lower panel. With the correction, in contrast, the observed $w_{\rm p}(r_{\rm p})$ is in good agreement with the true $w_{\rm p}(r_{\rm p})$ of the parent mock samples over the entire angular scale of interest. Therefore, we conclude that the proposed correction scheme based on the angular correlation functions works appropriately in our analysis.

E.2 Evaluating the effects of sample selection

We assess the effect of stellar mass completeness on our constraints of the HOD model by using a mock sample, which is constructed from the Bolshoi simulation (Klypin et al. 2011) by using a simple abundance matching technique (Kravtsov et al. 2004). The simulation traces 2048^3 particles with a mass resolution of $1.35 \times 10^8\ h^{-1}M_\odot$ in a cubic box with a side of $250\ h^{-1}$Mpc, resolving a halo of $10^{10}\ h^{-1}M_\odot$ with the Rockstar halo finding technique (Behroozi et al. 2013b). The volume of the simulation box is 19 times as large as our survey volume. We employ the public Rockstar catalog at $a = 0.38435$ ($z = 1.602$), which is the closest to our median redshift ($z = 1.588$). In this exercise, we use the cosmology used in the Bolshoi simulation $(\Omega_M, \Omega_\Lambda) = (0.27, 0.73)$.

To minimize the effects of the mass loss that subhalos have undergone, we use the peak maximum circular velocity ($V_{\rm peak}$) provided in the public catalog as the indicator of stellar mass of the galaxy hosted in the halo. Assuming a tight correlation between $V_{\rm peak}$ and stellar mass with no scatter, we chose the lower limit $V_{\rm peak}^{\rm lim}$ by matching the halo number density $n\,(> V_{\rm peak})$ to the number density of the M_*-limited galaxy sample (Table 5.2). Note that the number density is recomputed, as $n = 8.47 \times 10^{-3}({\rm Mpc}/h)^{-3}$, using the cosmology used in the simulation. In total, 132408 (sub)halos with $V_{\rm peak} > V_{\rm peak}^{\rm lim} \approx 165$ km/s are selected. For each subhalo, a stellar mass is assigned, keeping the relation $n\,(> V_{\rm peak}) = n\,(> M_*)$, to reproduce the stellar mass function of the M_*-selected galaxy sample (see Figure 5.6). We denote this mock catalog as

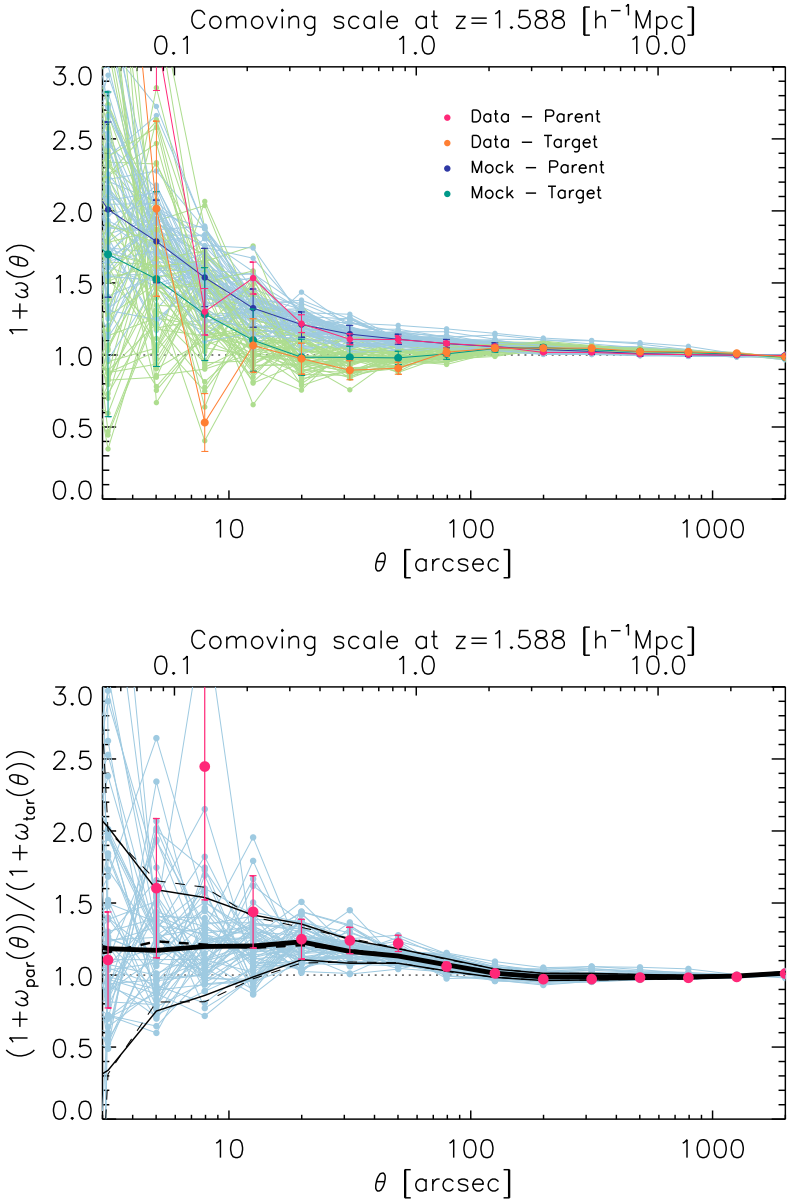

Figure E.1: Upper panel: angular correlation function $\omega(\theta)$ for the data and the mock samples. Red and yellow symbols show $1+\omega(\theta)$ the data parent and target samples, respectively. Blue and green symbols show the average of $(1+\omega(\theta))$ of the 64 mock parent and target samples, respectively, with the individual measurements. Lower panel: weight functions responding to the angular separation scale for the data (red) and the individual mocks (light blue). The average of the mocks is indicated by a solid thick line.

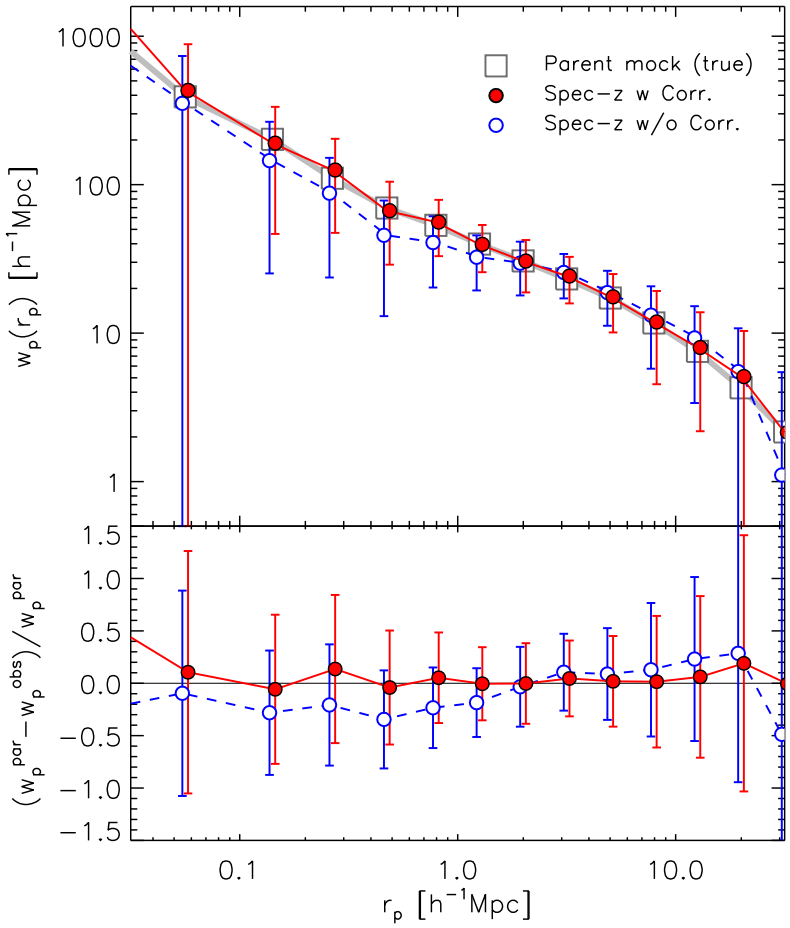

Figure E.2: Upper panel: projected two-point correlation functions from the mock samples. The average measurements of all 64 mock samples are shown with the error bars indicating their standard deviation. The filled and empty circles show the $w_{\rm p}(r_{\rm p})$ with and without the correction for the fiber allocation effect, respectively. The x-axis values of those data points are slightly shifted in opposite for the display purpose. The large squares with thick solid line shows the true $w_{\rm p}(r_{\rm p})$ computed for the Mock-parent samples. The error bars are not shown on the true $w_{\rm p}(r_{\rm p})$, since the statistical scatter is much smaller than those for the spec-z samples. Lower panel: difference between the true $w_{\rm p}(r_{\rm p})$ and the observed $w_{\rm p}(r_{\rm p})$ with or without the correction. Symbols are the same as the upper panel.

$V_{\rm peak}$*-limited* mock sample. From this sample, we construct the M_**-incomplete* mock sample taking into account the stellar mass incompleteness of the data. We construct the selected sample, corresponding to the FMOS-parent sample, by randomly selecting halos to reproduce the stellar mass function of the FMOS-parent sample as shown in Figure 5.6. Totally, 43777 (sub)halos are selected.

We measure the projected two-point correlation function of the selected halos, including peculiar velocity of halos along the line of sight. Figure E.3 shows the projected two-point correlation functions for the $V_{\rm peak}$-limited mock sample, the M_*-incomplete sample, and the FMOS-spec-z sample. We correct the correlation functions of the mock samples for the effect of the finite volume of the simulation box (see van den Bosch et al. 2013, for details). Note that $f_{\rm fake} \approx 0.1$ is assumed for the FMOS sample, which is the expected value from the HOD fitting (Table 5.4). It is shown that the clustering amplitude of the M_*-incomplete mock sample is slightly enhanced from the amplitude of the $V_{\rm peak}$-limited sample. This is not surprising because the M_*-selected mock sample is on average biased towards massive halos, which are more strongly clustered, as compared to the $V_{\rm peak}$-limited sample. This indicates that the mass-dependent incompleteness of an observed sample influences the observed galaxy clustering. However, as shown in Figure E.3, the difference is small compared to the uncertainties of the measurement, and the individual data points are consistent both with the M_*-incomplete and $V_{\rm peak}$-limited mock samples within 1σ errors.

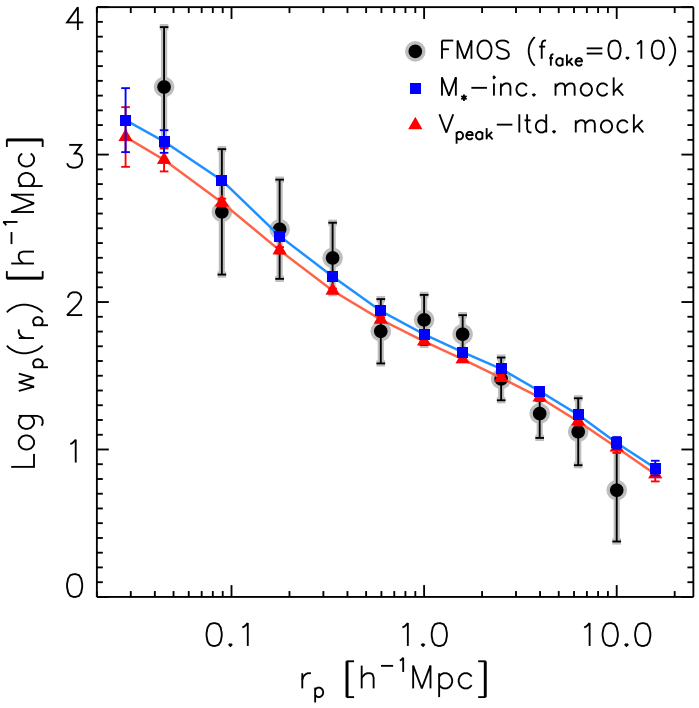

Figure E.3: Projected two-point correlation functions of the $V_{\rm peak}$-limited mock sample (red triangles), M_*-incomplete sample (blue squares), and the FMOS-spec-z sample with the contamination correction ($f_{\rm fake} = 0.10$; circles).

With the HOD model (Equations 5.24 and 5.25), we model the correlation function of both mock samples. Here we scale the covariance matrix by a factor of 19, which is the ratio of the effective comoving volume of the simulation box to the survey volume, and the uncertainty on the source number density to match the statistical uncertainties to those of the real data.

The parameter constraints are shown in Figure E.4 separately for the $V_{\rm peak}$-limited or M_*-incompleteness samples. We find that all the parameters are consistent within their 1 σ confidence level. Thus we conclude that the stellar mass incompleteness in our FMOS sample does not have any significantly impact on our results.

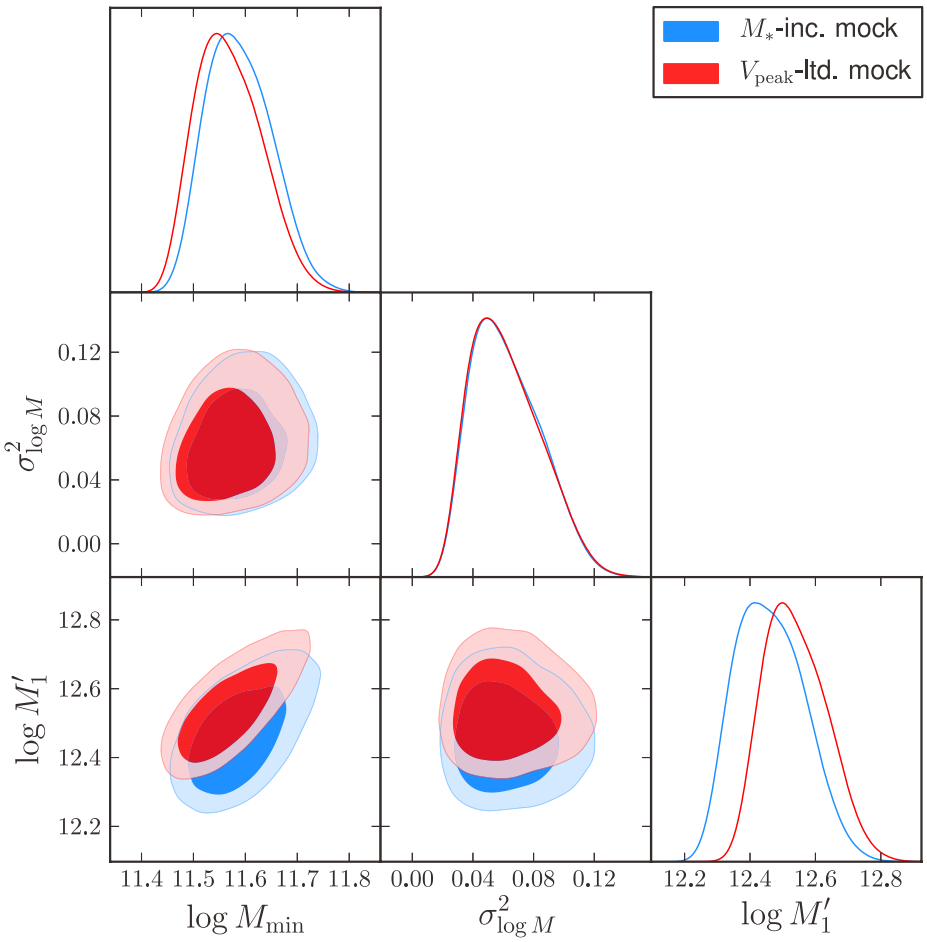

Figure E.4: Constraints of the HOD parameters ($M_{\rm min}$, $\sigma^2_{\log M}$, M'_1) for the $V_{\rm peak}$-limited (blue) and M_*-incomplete (red) mock samples.

E.3 Limitation on $\sigma_{\log M}$

We give the details of deriving the prior limitation on the HOD parameter, $\sigma_{\log M}$, as mentioned in §5.5.2. We use a stellar-to-halo mass relation (SHMR) derived by Behroozi et al. (2013a). The authors parametrized the evolution of the SHMR and its intrinsic scatter through the cosmic history ($0 < z < 8$). This denotes the standard deviation in $\log M_*$ of galaxies that inhabit halos of a given mass, and is expected to be $\sigma^{\rm int}_{\log M_*} = 0.23 \pm 0.04$ at $z = 1.588$. We then incorporate another scatter ($\sigma^{\rm sample}_{\log M_*}$) that is expected due to the sample selection at the threshold stellar mass. We select galaxies based on the best estimation of the stellar mass (and others such as $K_{\rm s}$, $z_{\rm photo}$), which essentially has an extended probability distribution function. Therefore, the lower edge of the *true* stellar mass distribution is smoothed with a typical uncertainty of individual stellar mass estimates. Computing the probability that a true parameter satisfies our selection criteria for each galaxy, we derive the realistic probability-weighted stellar mass distribution of our sample. Then, we find $\sigma^{\rm sample}_{\log M_*} = 0.09$ at our lower stellar mass limit. The total scatter in

$\log M_*$ of galaxies within halos of the threshold mass is given as

$$\sigma_{\log M_*} = \sqrt{(\sigma^{\rm int}_{\log M_*})^2 + (\sigma^{\rm sample}_{\log M_*})^2} = 0.24 \pm 0.04. \tag{E.2}$$

We then calculate the probability of finding a galaxy of the threshold stellar mass in a halo as a function of halo mass using the above SHMR and the intrinsic scatter:

$$P\left(\log M_*^{\rm lim}|M_{\rm h}\right) = \frac{1}{\sqrt{2}\pi\sigma_{\log M_*}} \exp\left(-\frac{\left(\log M_*^{\rm lim} - \log M_*(M_{\rm h})\right)^2}{2\sigma^2_{\log M_*}}\right) \tag{E.3}$$

where $M_*^{\rm lim}$ is lower limit stellar mass of our sample selection. The expected mean ($n = 1$) and mean square ($n = 2$) of halo mass to have a $M_*^{\rm lim}$ galaxy are given by

$$\langle(\log M)^n\rangle = \frac{\int P\left(\log M_*^{\rm lim}|M_{\rm h}\right) dn/dM\,(M_{\rm h}, z)\,(\log M_{\rm h})^n\, dM_{\rm h}}{\int P\left(\log M_*^{\rm lim}|M_{\rm h}\right) dn/dM\,(M_{\rm h}, z)\, dM_{\rm h}} \tag{E.4}$$

where dn/dM is a halo mass function at a given redshift. We find the dispersion in halo mass at our threshold stellar mass:

$$\sqrt{{\rm Var}\,(\log M)} = \sqrt{\langle(\log M)^2\rangle - \langle\log M\rangle^2} \approx 0.17 \pm 0.02. \tag{E.5}$$

The HOD parameter $\sigma_{\log M}$ related to the scatter derived above as $\sigma_{\log M} = \sqrt{2} \times \sqrt{{\rm Var}(\log M)}$. Therefore we apply on $\sigma_{\log M}$ a prior probability distribution function given by a Gaussian with a mean 0.24 and a standard deviation 0.03 (Equation 5.32). The derived value is supported by some previous studies (e.g., More et al. 2011).

Bibliography

Abazajian, K. N., Adelman-McCarthy, J. K., Agüeros, M. A., et al. 2009, ApJS, 182, 543

Abbas, U., de la Torre, S., Le Fèvre, O., et al. 2010, MNRAS, 406, 1306

Adelberger, K. L., Steidel, C. C., Pettini, M., et al. 2005, ApJ, 619, 697

Akiyama, M., Smedley, S., Gillingham, P., et al. 2008a, in Proc. SPIE, Vol. 7018, Advanced Optical and Mechanical Technologies in Telescopes and Instrumentation, 70182V

Akiyama, M., Smedley, S., Gillingham, P., et al. 2008b, in Society of Photo-Optical Instrumentation Engineers (SPIE) Conference Series, Vol. 7018, Society of Photo-Optical Instrumentation Engineers (SPIE) Conference Series

Alam, S., Albareti, F. D., Allende Prieto, C., et al. 2015, ApJS, 219, 12

Aller, L. H. 1942, ApJ, 95, 52

Aller, L. H., ed. 1984, Astrophysics and Space Science Library, Vol. 112, Physics of thermal gaseous nebulae

Andrews, B. H., & Martini, P. 2013, ApJ, 765, 140

Arnett, W. D. 1971, ApJ, 166, 153

Arnouts, S., & Ilbert, O. 2011, LePHARE: Photometric Analysis for Redshift Estimate, Astrophysics Source Code Library, ascl:1108.009

Babcock, H. W. 1939, Lick Observatory Bulletin, 19, 41

Baldry, I. K., Glazebrook, K., Brinkmann, J., et al. 2004, ApJ, 600, 681

Baldwin, J. A., Phillips, M. M., & Terlevich, R. 1981, PASP, 93, 5

Behroozi, P. S., Conroy, C., & Wechsler, R. H. 2010, ApJ, 717, 379

Behroozi, P. S., Wechsler, R. H., & Conroy, C. 2013a, ApJ, 770, 57

Behroozi, P. S., Wechsler, R. H., & Wu, H.-Y. 2013b, ApJ, 762, 109

Bell, E. F., Wolf, C., Meisenheimer, K., et al. 2004, ApJ, 608, 752

Benson, A. J., Cole, S., Frenk, C. S., Baugh, C. M., & Lacey, C. G. 2000, MNRAS, 311, 793

Berlind, A. A., & Weinberg, D. H. 2002, ApJ, 575, 587

Bertin, E., & Arnouts, S. 1996, A&AS, 117, 393

Bielby, R., Hill, M. D., Shanks, T., et al. 2013, MNRAS, 430, 425

Bielby, R. M., Gonzalez-Perez, V., McCracken, H. J., et al. 2014, A&A, 568, A24

Blanton, M. R., Hogg, D. W., Bahcall, N. A., et al. 2003, ApJ, 594, 186

Bond, J. R., Cole, S., Efstathiou, G., & Kaiser, N. 1991, ApJ, 379, 440

Bouché, N., Hohensee, W., Vargas, R., et al. 2012, MNRAS, 426, 801

Bouwens, R. J., Illingworth, G. D., Oesch, P. A., et al. 2011, ApJ, 737, 90

—. 2012, ApJ, 754, 83

Bouwens, R. J., Bradley, L., Zitrin, A., et al. 2014, ApJ, 795, 126

Bouwens, R. J., Illingworth, G. D., Oesch, P. A., et al. 2015, ApJ, 803, 34

Brinchmann, J., Charlot, S., White, S. D. M., et al. 2004, MNRAS, 351, 1151

Brinchmann, J., Pettini, M., & Charlot, S. 2008, MNRAS, 385, 769

Brusa, M., Fiore, F., Santini, P., et al. 2009, A&A, 507, 1277

Bruzual, G., & Charlot, S. 2003, MNRAS, 344, 1000

Bruzual A., G. 1983, ApJ, 273, 105

Bruzual A., G., & Charlot, S. 1993, ApJ, 405, 538

Bundy, K., Georgakakis, A., Nandra, K., et al. 2008, ApJ, 681, 931

Butcher, H., & Oemler, Jr., A. 1978, ApJ, 219, 18

Butcher, H. R., & Oemler, Jr., A. 1984, Nature, 310, 31

Cacciato, M., van den Bosch, F. C., More, S., Mo, H., & Yang, X. 2013, MNRAS, 430, 767

Calzetti, D., Armus, L., Bohlin, R. C., et al. 2000, ApJ, 533, 682

Capak, P., Aussel, H., Ajiki, M., et al. 2007, ApJS, 172, 99

Chabrier, G. 2003, PASP, 115, 763

Cid Fernandes, R., Stasińska, G., Schlickmann, M. S., et al. 2010, MNRAS, 403, 1036

Civano, F., Marchesi, S., Comastri, A., et al. 2016, ApJ, 819, 62

Clowe, D., Bradač, M., Gonzalez, A. H., et al. 2006, ApJ, 648, L109

Clowe, D., Gonzalez, A., & Markevitch, M. 2004, ApJ, 604, 596

Coe, D., Zitrin, A., Carrasco, M., et al. 2013, ApJ, 762, 32

Cole, S., & Kaiser, N. 1989, MNRAS, 237, 1127

Colless, M., Dalton, G., Maddox, S., et al. 2001, MNRAS, 328, 1039

Conroy, C., & Wechsler, R. H. 2009, ApJ, 696, 620

Conroy, C., Wechsler, R. H., & Kravtsov, A. V. 2006, ApJ, 647, 201

Cooray, A., & Sheth, R. 2002, Phys. Rep., 372, 1

Copetti, M. V. F., Mallmann, J. A. H., Schmidt, A. A., & Castañeda, H. O. 2000, A&A, 357, 621

Coupon, J., Kilbinger, M., McCracken, H. J., et al. 2012, A&A, 542, A5

Covey, K. R., Ivezić, Ž., Schlegel, D., et al. 2007, AJ, 134, 2398

Cowie, L. L., Barger, A. J., & Songaila, A. 2016, ApJ, 817, 57

Cresci, G., Mannucci, F., Maiolino, R., et al. 2010, Nature, 467, 811

Daddi, E., Cimatti, A., Renzini, A., et al. 2004, ApJ, 617, 746

Daddi, E., Röttgering, H. J. A., Labbé, I., et al. 2003, ApJ, 588, 50

Daddi, E., Dickinson, M., Morrison, G., et al. 2007, ApJ, 670, 156

Daddi, E., Bournaud, F., Walter, F., et al. 2010, ApJ, 713, 686

Dalcanton, J. J. 2007, ApJ, 658, 941

Davé, R., Finlator, K., & Oppenheimer, B. D. 2012, MNRAS, 421, 98

Davis, M., & Geller, M. J. 1976, ApJ, 208, 13

Dayal, P., Ferrara, A., & Dunlop, J. S. 2013, MNRAS, 430, 2891

de la Torre, S., Le Fèvre, O., Porciani, C., et al. 2011, MNRAS, 412, 825

de Lapparent, V., Geller, M. J., & Huchra, J. P. 1986, ApJ, 302, L1

Denicoló, G., Terlevich, R., & Terlevich, E. 2002, MNRAS, 330, 69

Dickey, J. M., & Lockman, F. J. 1990, ARA&A, 28, 215

Domgorgen, H., & Mathis, J. S. 1994, ApJ, 428, 647

Domínguez, A., Siana, B., Henry, A. L., et al. 2013, ApJ, 763, 145

Dopita, M. A., Kewley, L. J., Heisler, C. A., & Sutherland, R. S. 2000, ApJ, 542, 224

Dopita, M. A., Kewley, L. J., Sutherland, R. S., & Nicholls, D. C. 2016, Ap&SS, 361, 61

Dopita, M. A., Sutherland, R. S., Nicholls, D. C., Kewley, L. J., & Vogt, F. P. A. 2013, ApJS, 208, 10

Dressler, A. 1980, ApJ, 236, 351

Durkalec, A., Le Fèvre, O., Pollo, A., et al. 2015, A&A, 583, A128

Elbaz, D., Daddi, E., Le Borgne, D., et al. 2007, A&A, 468, 33

Ellison, S. L., Patton, D. R., Simard, L., & McConnachie, A. W. 2008, ApJ, 672, L107

Elvis, M., Civano, F., Vignali, C., et al. 2009, ApJS, 184, 158

Erb, D. 2008, in Astronomical Society of the Pacific Conference Series, Vol. 399, Panoramic Views of Galaxy Formation and Evolution, ed. T. Kodama, T. Yamada, & K. Aoki, 239

Erb, D. K., Shapley, A. E., Pettini, M., et al. 2006, ApJ, 644, 813

Evans, I. N., & Dopita, M. A. 1985, ApJS, 58, 125

Finkelstein, S. L., Papovich, C., Dickinson, M., et al. 2013, Nature, 502, 524

Finlator, K., & Davé, R. 2008, MNRAS, 385, 2181

Fioc, M., & Rocca-Volmerange, B. 1997, A&A, 326, 950

Fisher, K. B., Davis, M., Strauss, M. A., Yahil, A., & Huchra, J. P. 1994, MNRAS, 267, 927

Foreman-Mackey, D., Hogg, D. W., Lang, D., & Goodman, J. 2013, PASP, 125, 306

Förster Schreiber, N. M., Genzel, R., Bouché, N., et al. 2009, ApJ, 706, 1364

Foucaud, S., McCracken, H. J., Le Fèvre, O., et al. 2003, A&A, 409, 835

Gallego, J., Zamorano, J., Aragon-Salamanca, A., & Rego, M. 1995, ApJ, 455, L1

Garn, T., & Best, P. N. 2010, MNRAS, 409, 421

Geach, J. E., Smail, I., Best, P. N., et al. 2008, MNRAS, 388, 1473

Geach, J. E., Sobral, D., Hickox, R. C., et al. 2012, MNRAS, 426, 679

Genzel, R., Tacconi, L. J., Gracia-Carpio, J., et al. 2010, MNRAS, 407, 2091

Giovanelli, R., Haynes, M. P., & Chincarini, G. L. 1986, ApJ, 300, 77

Groth, E. J., & Peebles, P. J. E. 1977, ApJ, 217, 385

Groves, B., Brinchmann, J., & Walcher, C. J. 2012, MNRAS, 419, 1402

Guo, Q., White, S., Li, C., & Boylan-Kolchin, M. 2010, MNRAS, 404, 1111

Guo, Y., Koo, D. C., Lu, Y., et al. 2016a, ArXiv e-prints, arXiv:1603.04863

—. 2016b, ApJ, 822, 103

Hamilton, A. J. S. 1988, ApJ, 331, L59

Harikane, Y., Ouchi, M., Ono, Y., et al. 2015, ArXiv e-prints, arXiv:1511.07873

—. 2016, ApJ, 821, 123

Harrison, E. R. 1970, Phys. Rev. D, 1, 2726

Hartley, W. G., Lane, K. P., Almaini, O., et al. 2008, MNRAS, 391, 1301

Hartley, W. G., Almaini, O., Cirasuolo, M., et al. 2010, MNRAS, 407, 1212

Hayashi, M., Shimasaku, K., Motohara, K., et al. 2007, ApJ, 660, 72

Hayashi, M., Motohara, K., Shimasaku, K., et al. 2009, ApJ, 691, 140

Hayashi, M., Ly, C., Shimasaku, K., et al. 2015, PASJ, 67, 80

Herschel, W. 1785, Philosophical Transactions of the Royal Society of London Series I, 75, 213

Hopkins, A. M., & Beacom, J. F. 2006, ApJ, 651, 142

Ilbert, O., Capak, P., Salvato, M., et al. 2009, ApJ, 690, 1236

Ilbert, O., Salvato, M., Le Floc'h, E., et al. 2010, ApJ, 709, 644

Ilbert, O., McCracken, H. J., Le Fèvre, O., et al. 2013, A&A, 556, A55

Ishikawa, S., Kashikawa, N., Toshikawa, J., & Onoue, M. 2015, MNRAS, 454, 205

Ishiyama, T., Enoki, M., Kobayashi, M. A. R., et al. 2015, PASJ, 67, 61

Issa, M. R., MacLaren, I., & Wolfendale, A. W. 1990, A&A, 236, 237

Iwamuro, F., Moritani, Y., Yabe, K., et al. 2012, PASJ, 64, 59

Izotov, Y. I., Stasińska, G., Meynet, G., Guseva, N. G., & Thuan, T. X. 2006, A&A, 448, 955

Jenkins, A., Frenk, C. S., White, S. D. M., et al. 2001, MNRAS, 321, 372

Juneau, S., Dickinson, M., Alexander, D. M., & Salim, S. 2011, ApJ, 736, 104

Juneau, S., Bournaud, F., Charlot, S., et al. 2014, ApJ, 788, 88

Karim, A., Schinnerer, E., Martínez-Sansigre, A., et al. 2011, ApJ, 730, 61

Kartaltepe, J. S., Sanders, D. B., Silverman, J. D., et al. 2015, ApJ, 806, L35

Kashikawa, N., Yoshida, M., Shimasaku, K., et al. 2006, ApJ, 637, 631

Kashino, D., Renzini, A., Silverman, J. D., & Daddi, E. 2016, ApJ, 823, L24

Kashino, D., Silverman, J. D., Rodighiero, G., et al. 2013, ApJ, 777, L8

Kauffmann, G., Heckman, T. M., White, S. D. M., et al. 2003a, MNRAS, 341, 33

Kauffmann, G., Heckman, T. M., Tremonti, C., et al. 2003b, MNRAS, 346, 1055

Kennicutt, R. C., & Evans, N. J. 2012, ARA&A, 50, 531

Kennicutt, Jr., R. C. 1998, ARA&A, 36, 189

Kewley, L. J., & Dopita, M. A. 2002, ApJS, 142, 35

Kewley, L. J., Dopita, M. A., Leitherer, C., et al. 2013a, ApJ, 774, 100

Kewley, L. J., Dopita, M. A., Sutherland, R. S., Heisler, C. A., & Trevena, J. 2001, ApJ, 556, 121

Kewley, L. J., & Ellison, S. L. 2008, ApJ, 681, 1183

Kewley, L. J., Groves, B., Kauffmann, G., & Heckman, T. 2006, MNRAS, 372, 961

Kewley, L. J., Jansen, R. A., & Geller, M. J. 2005, PASP, 117, 227

Kewley, L. J., Maier, C., Yabe, K., et al. 2013b, ApJ, 774, L10

Kewley, L. J., Zahid, H. J., Geller, M. J., et al. 2015, ApJ, 812, L20

Kimura, M., Maihara, T., Iwamuro, F., et al. 2010, PASJ, 62, 1135

Klypin, A. A., Trujillo-Gomez, S., & Primack, J. 2011, ApJ, 740, 102

Koekemoer, A. M., Aussel, H., Calzetti, D., et al. 2007, ApJS, 172, 196

Kojima, T., Ouchi, M., Nakajima, K., et al. 2016, ArXiv e-prints, arXiv:1605.03436

Komatsu, E., Dunkley, J., Nolta, M. R., et al. 2009, ApJS, 180, 330

Köppen, J., & Edmunds, M. G. 1999, MNRAS, 306, 317

Koyama, Y., Kodama, T., Hayashi, M., et al. 2015, MNRAS, 453, 879

Kravtsov, A. V., Berlind, A. A., Wechsler, R. H., et al. 2004, ApJ, 609, 35

Kriek, M., Shapley, A. E., Reddy, N. A., et al. 2015, ApJS, 218, 15

Kroupa, P. 2001, MNRAS, 322, 231

Lamareille, F., Brinchmann, J., Contini, T., et al. 2009, A&A, 495, 53

Landy, S. D., & Szalay, A. S. 1993, ApJ, 412, 64

Lara-López, M. A., Bongiovanni, A., Cepa, J., et al. 2010a, A&A, 519, A31

Lara-López, M. A., Cepa, J., Bongiovanni, A., et al. 2010b, A&A, 521, L53

Lara-López, M. A., Hopkins, A. M., López-Sánchez, A. R., et al. 2013, MNRAS, 434, 451

Larson, R. B. 1972, Nature Physical Science, 236, 7

Le Fèvre, O., Vettolani, G., Garilli, B., et al. 2005, A&A, 439, 845

Leauthaud, A., Tinker, J., Behroozi, P. S., Busha, M. T., & Wechsler, R. H. 2011, ApJ, 738, 45

Leauthaud, A., Tinker, J., Bundy, K., et al. 2012, ApJ, 744, 159

Lee, H., Skillman, E. D., Cannon, J. M., et al. 2006, ApJ, 647, 970

Lee, J., & Shandarin, S. F. 1998, ApJ, 500, 14

Lehmer, B. D., Brandt, W. N., Alexander, D. M., et al. 2008, ApJ, 681, 1163

Lequeux, J., Peimbert, M., Rayo, J. F., Serrano, A., & Torres-Peimbert, S. 1979, A&A, 80, 155

Levesque, E. M., Kewley, L. J., & Larson, K. L. 2010, AJ, 139, 712

Li, C., Kauffmann, G., Jing, Y. P., et al. 2006, MNRAS, 368, 21

Lilly, S. J., Carollo, C. M., Pipino, A., Renzini, A., & Peng, Y. 2013, ApJ, 772, 119

Lilly, S. J., Le Fevre, O., Hammer, F., & Crampton, D. 1996, ApJ, 460, L1

Lilly, S. J., Le Fèvre, O., Renzini, A., et al. 2007, ApJS, 172, 70

Lin, L., Dickinson, M., Jian, H.-Y., et al. 2012, ApJ, 756, 71

Lisenfeld, U., & Ferrara, A. 1998, ApJ, 496, 145

Liu, X., Shapley, A. E., Coil, A. L., Brinchmann, J., & Ma, C.-P. 2008, ApJ, 678, 758

Lutz, D., Poglitsch, A., Altieri, B., et al. 2011, A&A, 532, A90

Ly, C., Lee, J. C., Dale, D. A., et al. 2011, ApJ, 726, 109

Ly, C., Malkan, M. A., Kashikawa, N., et al. 2012, ApJ, 747, L16

Macciò, A. V., Dutton, A. A., van den Bosch, F. C., et al. 2007, MNRAS, 378, 55

Madau, P., & Dickinson, M. 2014, ARA&A, 52, 415

Madau, P., Ferguson, H. C., Dickinson, M. E., et al. 1996, MNRAS, 283, 1388

Magdis, G. E., Daddi, E., Sargent, M., et al. 2012, ApJ, 758, L9

Maier, C., Lilly, S. J., Ziegler, B. L., et al. 2014, ApJ, 792, 3

Maier, C., Ziegler, B. L., Lilly, S. J., et al. 2015, A&A, 577, A14

Maiolino, R., Nagao, T., Grazian, A., et al. 2008, A&A, 488, 463

Mancini, C., Renzini, A., Daddi, E., et al. 2015, MNRAS, 450, 763

Mancini, C., Förster Schreiber, N. M., Renzini, A., et al. 2011, ApJ, 743, 86

Mandelbaum, R., Seljak, U., Kauffmann, G., Hirata, C. M., & Brinkmann, J. 2006, MNRAS, 368, 715

Mandelbaum, R., Slosar, A., Baldauf, T., et al. 2013, MNRAS, 432, 1544

Mannucci, F., Cresci, G., Maiolino, R., Marconi, A., & Gnerucci, A. 2010, MNRAS, 408, 2115

Mannucci, F., Salvaterra, R., & Campisi, M. A. 2011, MNRAS, 414, 1263

Maraston, C. 2005, MNRAS, 362, 799

Maraston, C., Daddi, E., Renzini, A., et al. 2006, ApJ, 652, 85

Markevitch, M., Gonzalez, A. H., Clowe, D., et al. 2004, ApJ, 606, 819

Markwardt, C. B. 2009, in Astronomical Society of the Pacific Conference Series, Vol. 411, Astronomical Data Analysis Software and Systems XVIII, ed. D. A. Bohlender, D. Durand, & P. Dowler, 251

Martinez-Manso, J., Gonzalez, A. H., Ashby, M. L. N., et al. 2015, MNRAS, 446, 169

Masaki, S., Hikage, C., Takada, M., Spergel, D. N., & Sugiyama, N. 2013, MNRAS, 433, 3506

Massey, R., Rhodes, J., Ellis, R., et al. 2007, Nature, 445, 286

Masters, D., & Capak, P. 2011, PASP, 123, 638

Masters, D., Faisst, A., & Capak, P. 2016, ArXiv e-prints, arXiv:1605.04314

Masters, D., McCarthy, P., Siana, B., et al. 2014, ApJ, 785, 153

McCracken, H. J., Capak, P., Salvato, M., et al. 2010, ApJ, 708, 202

McCracken, H. J., Milvang-Jensen, B., Dunlop, J., et al. 2012, A&A, 544, A156

McCracken, H. J., Wolk, M., Colombi, S., et al. 2015, MNRAS, 449, 901

Meneux, B., Guzzo, L., Garilli, B., et al. 2008, A&A, 478, 299

Meneux, B., Guzzo, L., de la Torre, S., et al. 2009, A&A, 505, 463

Miyaji, T., Griffiths, R. E., & C-COSMOS Team. 2008, in AAS/High Energy Astrophysics Division, Vol. 10, AAS/High Energy Astrophysics Division #10, 4.01

Miyatake, H., More, S., Takada, M., et al. 2016, Physical Review Letters, 116, 041301

Miyazaki, S., Komiyama, Y., Sekiguchi, M., et al. 2002, PASJ, 54, 833

Mo, H. J., & White, S. D. M. 1996, MNRAS, 282, 347

Momcheva, I. G., Lee, J. C., Ly, C., et al. 2013, AJ, 145, 47

More, S. 2013, ApJ, 777, L26

More, S., Miyatake, H., Mandelbaum, R., et al. 2015, ApJ, 806, 2

More, S., van den Bosch, F. C., & Cacciato, M. 2009, MNRAS, 392, 917

More, S., van den Bosch, F. C., Cacciato, M., et al. 2011, MNRAS, 410, 210

Moster, B. P., Naab, T., & White, S. D. M. 2013, MNRAS, 428, 3121

Moster, B. P., Somerville, R. S., Maulbetsch, C., et al. 2010, ApJ, 710, 903

Moustakas, J., & Kennicutt, Jr., R. C. 2006, ApJS, 164, 81

Moustakas, J., Kennicutt, Jr., R. C., Tremonti, C. A., et al. 2010, ApJS, 190, 233

Murray, G. J., Dodsworth, G. N., Content, R., & Tamura, N. 2008, in Proc. SPIE, Vol. 7014, Ground-based and Airborne Instrumentation for Astronomy II, 70145L

Nagao, T., Maiolino, R., & Marconi, A. 2006, A&A, 459, 85

Nakajima, A., Shioya, Y., Nagao, T., et al. 2008, PASJ, 60, 1249

Nakajima, K., & Ouchi, M. 2014, MNRAS, 442, 900

Nakamura, O., Fukugita, M., Brinkmann, J., & Schneider, D. P. 2004, AJ, 127, 2511

Navarro, J. F., Frenk, C. S., & White, S. D. M. 1997, ApJ, 490, 493

Newman, S. F., Buschkamp, P., Genzel, R., et al. 2014, ApJ, 781, 21

Neyman, J., & Scott, E. L. 1952, ApJ, 116, 144

Noeske, K. G., Weiner, B. J., Faber, S. M., et al. 2007, ApJ, 660, L43

Norberg, P., Baugh, C. M., Gaztañaga, E., & Croton, D. J. 2009, MNRAS, 396, 19

Norberg, P., Baugh, C. M., Hawkins, E., et al. 2001, MNRAS, 328, 64

—. 2002, MNRAS, 332, 827

Oesch, P. A., Bouwens, R. J., Illingworth, G. D., et al. 2013, ApJ, 773, 75

—. 2014, ApJ, 786, 108

Onodera, M., Daddi, E., Gobat, R., et al. 2010, ApJ, 715, L6

Onodera, M., Carollo, C. M., Lilly, S., et al. 2016, ArXiv e-prints, arXiv:1602.02779

Osterbrock, D. E., & Ferland, G. J. 2006, Astrophysics of gaseous nebulae and active galactic nuclei

Ouchi, M., Shimasaku, K., Okamura, S., et al. 2004, ApJ, 611, 685

Pagel, B. E. J., Edmunds, M. G., Blackwell, D. E., Chun, M. S., & Smith, G. 1979, MNRAS, 189, 95

Pagel, B. E. J., Edmunds, M. G., & Smith, G. 1980, MNRAS, 193, 219

Pannella, M., Carilli, C. L., Daddi, E., et al. 2009, ApJ, 698, L116

Pannella, M., Elbaz, D., Daddi, E., et al. 2015, ApJ, 807, 141

Peacock, J. A., & Smith, R. E. 2000, MNRAS, 318, 1144

Peeples, M. S., & Shankar, F. 2011, MNRAS, 417, 2962

Peeples, M. S., Werk, J. K., Tumlinson, J., et al. 2014, ApJ, 786, 54

Pérez-Montero, E., & Contini, T. 2009, MNRAS, 398, 949

Persic, M., & Rephaeli, Y. 2007, A&A, 463, 481

Pettini, M., & Pagel, B. E. J. 2004, MNRAS, 348, L59

Pilyugin, L. S., Vílchez, J. M., Mattsson, L., & Thuan, T. X. 2012, MNRAS, 421, 1624

Planck Collaboration. 2015, ArXiv e-prints, arXiv:1502.01589

Press, W. H., & Schechter, P. 1974, ApJ, 187, 425

Price, S. H., Kriek, M., Brammer, G. B., et al. 2014, ApJ, 788, 86

Reddick, R. M., Wechsler, R. H., Tinker, J. L., & Behroozi, P. S. 2013, ApJ, 771, 30

Reddy, N. A., Erb, D. K., Pettini, M., Steidel, C. C., & Shapley, A. E. 2010, ApJ, 712, 1070

Reddy, N. A., Erb, D. K., Steidel, C. C., et al. 2005, ApJ, 633, 748

Reynolds, R. J. 1984, ApJ, 282, 191

—. 1992, ApJ, 392, L35

Riess, A. G., Filippenko, A. V., Challis, P., et al. 1998, AJ, 116, 1009

Roche, N., Eales, S. A., Hippelein, H., & Willott, C. J. 1999, MNRAS, 306, 538

Rodighiero, G., Daddi, E., Baronchelli, I., et al. 2011, ApJ, 739, L40

Rodighiero, G., Renzini, A., Daddi, E., et al. 2014, MNRAS, 443, 19

Roseboom, I. G., Bunker, A., Sumiyoshi, M., et al. 2012, MNRAS, 426, 1782

Rubin, V. C., & Ford, Jr., W. K. 1970, ApJ, 159, 379

Rubin, V. C., Ford, W. K. J., & . Thonnard, N. 1980, ApJ, 238, 471

Rudie, G. C., Steidel, C. C., Trainor, R. F., et al. 2012, ApJ, 750, 67

Rykoff, E. S., Evrard, A. E., McKay, T. A., et al. 2008, MNRAS, 387, L28

Sabbadin, F., Minello, S., & Bianchini, A. 1977, A&A, 60, 147

Saito, S., Leauthaud, A., Hearin, A. P., et al. 2015, ArXiv e-prints, arXiv:1509.00482

Salim, S., Lee, J. C., Davé, R., & Dickinson, M. 2015, ApJ, 808, 25

Salim, S., Rich, R. M., Charlot, S., et al. 2007, ApJS, 173, 267

Salpeter, E. E. 1955, ApJ, 121, 161

Sanders, R. L., Shapley, A. E., Kriek, M., et al. 2015, ApJ, 799, 138

—. 2016, ApJ, 816, 23

Sargent, M. T., Daddi, E., Béthermin, M., et al. 2014, ApJ, 793, 19

Sargsyan, L. A., & Weedman, D. W. 2009, ApJ, 701, 1398

Schmidt, K.-H., & Boller, T. 1993, Astronomische Nachrichten, 314, 361

Schmidt, M. 1963, ApJ, 137, 758

Scoville, N., Aussel, H., Sheth, K., et al. 2014, ApJ, 783, 84

Searle, L., & Sargent, W. L. W. 1972, ApJ, 173, 25

Seljak, U. 2000, MNRAS, 318, 203

Shapley, A. E., Coil, A. L., Ma, C.-P., & Bundy, K. 2005, ApJ, 635, 1006

Shapley, A. E., Reddy, N. A., Kriek, M., et al. 2015, ApJ, 801, 88

Sheth, R. K., Mo, H. J., & Tormen, G. 2001, MNRAS, 323, 1

Sheth, R. K., & Tormen, G. 1999, MNRAS, 308, 119

Shim, H., Colbert, J., Teplitz, H., et al. 2009, ApJ, 696, 785

Shimakawa, R., Kodama, T., Steidel, C. C., et al. 2015, MNRAS, 451, 1284

Shioya, Y., Taniguchi, Y., Sasaki, S. S., et al. 2008, ApJS, 175, 128

Shirazi, M., Brinchmann, J., & Rahmati, A. 2014, ApJ, 787, 120

Silverman, J. D., Lamareille, F., Maier, C., et al. 2009, ApJ, 696, 396

Silverman, J. D., Kashino, D., Sanders, D., et al. 2015, ApJS, 220, 12

Smith, R. E., Peacock, J. A., Jenkins, A., et al. 2003, MNRAS, 341, 1311

Sobral, D., Best, P. N., Geach, J. E., et al. 2010, MNRAS, 404, 1551

Sobral, D., Best, P. N., Matsuda, Y., et al. 2012, MNRAS, 420, 1926

Sobral, D., Smail, I., Best, P. N., et al. 2013, MNRAS, 428, 1128

Speagle, J. S., Steinhardt, C. L., Capak, P. L., & Silverman, J. D. 2014, ApJS, 214, 15

Spergel, D. N., Bean, R., Doré, O., et al. 2007, ApJS, 170, 377

Springel, V., White, S. D. M., Jenkins, A., et al. 2005, Nature, 435, 629

Stasińska, G., Cid Fernandes, R., Mateus, A., Sodré, L., & Asari, N. V. 2006, MNRAS, 371, 972

Steidel, C. C., Strom, A. L., Pettini, M., et al. 2016, ArXiv e-prints, arXiv:1605.07186

Steidel, C. C., Rudie, G. C., Strom, A. L., et al. 2014, ApJ, 795, 165

Steinhardt, C. L., Speagle, J. S., Capak, P., et al. 2014, ApJ, 791, L25

Storey, P. J., & Zeippen, C. J. 2000, MNRAS, 312, 813

Stott, J. P., Sobral, D., Bower, R., et al. 2013, MNRAS, 436, 1130

Strateva, I., Ivezić, Ž., Knapp, G. R., et al. 2001, AJ, 122, 1861

Strömgren, B. 1939, ApJ, 89, 526

Taniguchi, Y., Scoville, N. Z., Sanders, D. B., et al. 2005, Journal of Korean Astronomical Society, 38, 187

Tasitsiomi, A., Kravtsov, A. V., Wechsler, R. H., & Primack, J. R. 2004, ApJ, 614, 533

Tinker, J., Kravtsov, A. V., Klypin, A., et al. 2008, ApJ, 688, 709

Tinker, J. L., Robertson, B. E., Kravtsov, A. V., et al. 2010, ApJ, 724, 878

Tinker, J. L., Weinberg, D. H., Zheng, Z., & Zehavi, I. 2005, ApJ, 631, 41

Tinker, J. L., Sheldon, E. S., Wechsler, R. H., et al. 2012, ApJ, 745, 16

Tinsley, B. M. 1980, Fund. Cosmic Phys., 5, 287

Tinsley, B. M., & Danly, L. 1980, ApJ, 242, 435

Tonegawa, M., Totani, T., Okada, H., et al. 2015, PASJ, 67, 81

Totsuji, H., & Kihara, T. 1969, PASJ, 21, 221

Tremonti, C. A., Heckman, T. M., Kauffmann, G., et al. 2004, ApJ, 613, 898

Trujillo-Gomez, S., Klypin, A., Primack, J., & Romanowsky, A. J. 2011, ApJ, 742, 16

Vale, A., & Ostriker, J. P. 2004, MNRAS, 353, 189

Valentino, F., Daddi, E., Strazzullo, V., et al. 2015, ApJ, 801, 132

van den Bosch, F. C., More, S., Cacciato, M., Mo, H., & Yang, X. 2013, MNRAS, 430, 725

van Zee, L., Salzer, J. J., Haynes, M. P., O'Donoghue, A. A., & Balonek, T. J. 1998, AJ, 116, 2805

Veilleux, S., & Osterbrock, D. E. 1987, ApJS, 63, 295

Villar, V., Gallego, J., Pérez-González, P. G., et al. 2008, ApJ, 677, 169

Vincenzo, F., Belfiore, F., Maiolino, R., Matteucci, F., & Ventura, P. 2016, MNRAS, 458, 3466

Wake, D. A., Whitaker, K. E., Labbé, I., et al. 2011, ApJ, 728, 46

Whitaker, K. E., van Dokkum, P. G., Brammer, G., & Franx, M. 2012, ApJ, 754, L29

Whitaker, K. E., Labbé, I., van Dokkum, P. G., et al. 2011, ApJ, 735, 86

Whitaker, K. E., Franx, M., Leja, J., et al. 2014, ApJ, 795, 104

Wild, V., Charlot, S., Brinchmann, J., et al. 2011, MNRAS, 417, 1760

Wink, J. E., Wilson, T. L., & Bieging, J. H. 1983, A&A, 127, 211

Wuyts, E., Kurk, J., Förster Schreiber, N. M., et al. 2014, ApJ, 789, L40

Wuyts, S., Labbé, I., Franx, M., et al. 2007, ApJ, 655, 51

Wuyts, S., Förster Schreiber, N. M., Lutz, D., et al. 2011, ApJ, 738, 106

Yabe, K., Ohta, K., Iwamuro, F., et al. 2012, PASJ, 64, 60

—. 2014, MNRAS, 437, 3647

Yabe, K., Ohta, K., Akiyama, M., et al. 2015, PASJ, 67, 102

Yamada, T., Kajisawa, M., Akiyama, M., et al. 2009, ApJ, 699, 1354

Yang, X., Mo, H. J., & van den Bosch, F. C. 2003, MNRAS, 339, 1057

—. 2008, ApJ, 676, 248

—. 2009, ApJ, 695, 900

Yates, R. M., Kauffmann, G., & Guo, Q. 2012, MNRAS, 422, 215

York, D. G., Adelman, J., Anderson, Jr., J. E., et al. 2000, AJ, 120, 1579

Zahid, H. J., Dima, G. I., Kewley, L. J., Erb, D. K., & Davé, R. 2012, ApJ, 757, 54

Zahid, H. J., Dima, G. I., Kudritzki, R.-P., et al. 2014a, ApJ, 791, 130

Zahid, H. J., Geller, M. J., Kewley, L. J., et al. 2013, ApJ, 771, L19

Zahid, H. J., Kewley, L. J., & Bresolin, F. 2011, ApJ, 730, 137

Zahid, H. J., Kashino, D., Silverman, J. D., et al. 2014b, ApJ, 792, 75

Zehavi, I., Zheng, Z., Weinberg, D. H., et al. 2005, ApJ, 630, 1

—. 2011, ApJ, 736, 59

Zeldovich, Y. B. 1972, MNRAS, 160, 1P

Zhao, D. H., Jing, Y. P., Mo, H. J., & Börner, G. 2009, ApJ, 707, 354

Zheng, Z., Coil, A. L., & Zehavi, I. 2007, ApJ, 667, 760

Zheng, Z., Berlind, A. A., Weinberg, D. H., et al. 2005, ApJ, 633, 791

Zwicky, F. 1933, Helvetica Physica Acta, 6, 110

—. 1937, ApJ, 86, 217